ROTORDYNAMICS OF TWIN SCREW PUMPS

A Dissertation

by

AMEEN ROSHDY ABOEL HASSAN MUHAMMED

Submitted to the Office of Graduate Studies of
Texas A&M University
in partial fulfillment of the requirements for the degree of

DOCTOR OF PHILOSOPHY

Approved by:

Chair of Committee,	Dara Childs
Committee Members,	Jim Morgan
	Gerald Morrison
	Alan Palazzolo
Head of Department,	Jerald Caton

May 2013

Major Subject: Mechanical Engineering

ABSTRACT

Twin-screw pumps are positive displacement machines. Two meshing screws connected by timing gears convey the fluid trapped in the screw chambers axially from suction to discharge and force it out against the back pressure. Because of the screw geometry, the circumferential pressure field around the screws is not balanced, resulting in net dynamic and static pressures applied on the rotors. The research work presented here aims at building and verifying a model to predict both: (1) the exciting lateral hydrodynamic forces produced by the unbalanced pressure field, and (2) the rotor response due to those forces. The model rests on the screw pump hydraulic models for predicting the pressure in the screw chambers as a function of the discharge pressure. These models are extended to predict the steady state dynamic pressure field as a function of the rotational angle of the rotor. The dynamic force resulting from the dynamic pressure field is calculated and applied to the rotor as a set of super-synchronous periodic forces. The structural model of the screw, although nonsymmetrical, was found to be accurately represented by an axisymmetric equivalent structure. The rotor response to the dynamic super-synchronous forces is calculated to predict the pump rotordynamic behavior.

The work in this dissertation presents: (1) the axisymmetric structural model of the rotors (2) the proposed dynamic pressure model, (3) the screw pump rotor response, (4) the experimental validation of the dynamic pressure model and rotor response.

The topic of twin-screw pump rotordynamics is absent from the literature. The original contribution of the work presented in this dissertation to the field of rotordynamics includes: (1) demonstrating the adequacy of an axisymmetric model for modeling the screw section, (2) developing a model for predicting the dynamic pressure field around the screws, (3) characterization of the dynamic forces (synchronous and its harmonics) applied at the screw pump rotors, (4) predicting the dynamic response of twin-screw pump rotors due to hydrodynamic forces, (5) measuring the axial dynamic pressure in two circumferential planes around the screws to verify pressure predictions, (6) measuring the dynamic response of twin-screw pump rotor.

DEDICATION

To my father, my mother and my brother

For all the time we had to be apart so I can finish this work

ACKNOWLEDGEMENTS

A common prayer told by all mothers in Egypt for their sons and daughters can be loosely translated “may your path be intercepted with good people who intend to do good deeds”. My mother seems to have special prayer powers, for my path has always been guided by extraordinary people who did uncountable good deeds for me, and whose support was indispensable for me to be where I’m now in life. I’m grateful for all the support I received in Egypt. Some of that support came from people I haven’t even met, but their generosity altered the path of my life. I’m grateful for my family, my teachers, my professors, and my scholarship sponsors.

In completing this work I received invaluable guidance from Dr. D. Childs. I’m very grateful that I was able to work closely with him for five years and I’m certain few people will ever get close to teaching me that much, not just about rotordynamics, but about life in general.

I’m also grateful for Dr. Morrison for kindly letting me use his test cell, and helping me indefinitely with the test rig.

I would also want to express my gratitude for my friends in the Turbomachinery Laboratory for all the time they spent helping me. Abhay Patil’s support was very important for the completion of the test rig and Emanuel Marsis helped me out with the Computational Fluid Dynamics work.

My constant gratitude goes to my father and my mother. They laid the foundation that my personality and everything that I do and stand for in life are based on.

I hope I will be, one day, one of the good people who are intercepting the path of others and supporting them without even meeting them. Only in this way will I be able to repay my debts.

TABLE OF CONTENTS

Page

Page

LIST OF FIGURES

Page

Page

Page

Page

Page

Page

LIST OF TABLES

Page

NOMENCLATURE

Symbol	Definition	Units
$A_{orifice}$	Area of the orifice opening the last chamber to discharge	L^2
A_r	The fraction of the annular space between the outer and inner diameter of the screw not blocked by the screw threads	
Acc	Leakage area of the circumferential clearance	L^2
a	Distance between the centers of the two rotors	L
B	Length of the screw land	
c	The celerity of sound in the working fluid medium	
$\mathbf{C}$	Damping matrix of the FE rotor/bearing system	
C_d	Coefficient of discharge for flow through the orifice from the discharge to the last chamber	
C_g	Coefficient of discharge for the gas flow through the orifice from the discharge to the last chamber	
$D_{o/p}$	Ratio of orifice to pipe diameter	
D_{out}/D_{in}	Outer/inner screw diameters	L
d_k	Diameter of the stiffness layer of the equivalent axisymmetric model	
D_m	Diameter of the mass layer of the equivalent axisymmetric model	M
e	Static rotor shaft deflection due to pressure loading	
$\boldsymbol{E_c}, \boldsymbol{E_s}$	Vectors of the magnitudes of the hydraulic forces for the sines and cosine terms	
F_r	Estimated radial forces from the pump differential pressure	F
F_x, F_y	Dynamic forces resulting from the unbalanced dynamic pressure field	F
$f_{R_{in}}, f_{R_{out}}, f_{cc}$	Friction factor for the flow across the inner and outer radii of the screw at the radial clearance and across the circumferential clearance	

Symbol	Definition	Units
f_t	Empirical fraction of the circumferential clearance slip to the total slip through all types of clearances	
$\boldsymbol{F_{ext}}$	Vector of externally applied forces to the rotor-bearing structural dynamic model	
G	Gyroscopic matrix of the FE rotor/bearing system	L
H	Horizontal distance between the inner radius of one rotor and the outer radius of the other rotor in the radial clearance	L
H_{max}	The maximum head rise above the absolute static pressure discharge head due to the flow of the air pocket through the orifice at the discharge	L
H_o	The absolute static pressure head at the discharge	L
H_{tv}	The head due to the velocity of the fluid accelerating out of the tank	L
H_{pv}	The velocity head imparted on the fluid due to its acceleration as it enters the pump	L
h	Screw pitch	L
K	Stiffness matrix of the FE rotor/bearing system	
K_d	Nondimensional ratio of the equivalent stiffness diameter of the axisymmetric model to the inner diameter of the screw	
L_s	Length of the screw section	L
M	Mass matrix of the FE rotor/bearing system	
$m_{R_{in}}, m_{R_{out}}, m_{cc}$	Blasius friction factor empirical exponent for flow across inner and outer radii of the radial clearance, and the flow across circumferential clearance respectively	
m_{sl}	Mass of a slice of the screw section	M
N	Number of screw threads	

Symbol	Definition	Units
$n_{R_{in}}, n_{R_{out}}, n_{cc}$	Blasius friction factor empirical coefficient for flow across inner and outer radii of the radial clearance, and the flow across circumferential clearance respectively	
N_f	Number of harmonic frequencies of the Fourier series transform of the dynamic forces	
N_{sl}	Number of slices of the screw pitch to estimate screw imbalance	
$N_{z_{sl}}$	Number of slices of the screw section to determine the number of the concentrated forces from the refined discretized mesh	
N_θ	Number of the rectangular elements of the discretized mesh in the polar direction	
N_z	Number of the rectangular elements of the discretized mesh in the axial direction	
n_e	Empirical factor of the roughness of the circumferential clearance for an eccentric screw	
n_{ch}	Number of chambers	
n_{stn}	Number of stations of the rotor-bearing finite element model based on Timoshenko beam theory	
P_i	Pressure in chamber i	F/L^2
$P_{i,\xi}$	Pressure value after the entrance loss in the circumferential clearance	F/L^2
P_{rot}	Three dimension array storing the pressure values as a function of the axial and circumferential locations on the screw and the thread terminal edge angle	
P_{atm}	Absolute atmospheric pressure	F/L^2
P_o	The absolute critical air pressure at the discharge	F/L^2
δp	Length of the rectangular element in the circumferential direction	L

Symbol	Definition	Units
Qcc_{lkg}	Axial leakage flow rate across circumferential clearance for a concentric rotor	
$Qcc_{lkg,\varepsilon}$	Axial leakage flow rate across circumferential clearance for an eccentric rotor	M/t
Q_{th}	Pump theoretical flow rate	M/t
$Q_{slp,i\to i-1}$	Total slip flow from chamber number i to chamber number $i-1$	M/t
$Q_{g,i}$	Gas flow rate in chamber i	M/t
Q_l	Liquid flow rate	M/t
Q_{in}	Actual multiphase flow rate at the pump inlet	M/t
$Q_{orifice}$	Flow rate through the orifice opening to discharge	M/t
$\boldsymbol{q_c}, \boldsymbol{q_s}$	Rotor translational and angular degrees of freedom response amplitude vectors to harmonic forces for the cosine and sine terms	
$\boldsymbol{q}$	Rotor's translational and angular degrees of freedom vector for Timoshenko beam FE model	
$\boldsymbol{Q_{static}}$	Rotor translational and angular degrees of freedom static response vector	
$\boldsymbol{Q_{dyn}}$	Time domain rotor translational and angular response to the harmonic forces excitation	
R_e	axial Reynolds number of the flow across the circumferential clearance	
R_{out}/R_{in}	Outer/inner screw radii	L
r_ε	Ratio of eccentric to centric axial leakage flow rate for circumferential clearance	
s	The radial distance between the inner diameter of one screw and the tip diameter of the other screw	L

Symbol	Definition	Units
Δt_{life}	The time period for the fluid in the chamber to be transported by one chamber position closer to the discharge	sec
$\boldsymbol{u_{sl}}$	Vector defining the displacement of the center of mass of a slice of the screw section from its center of geometry	m
$\forall_{L,i}$	Liquid volume in the i^{th} chamber	L^3
$\forall_{g,i}$	Gas volume in the i^{th} chamber	L^3
$\forall_{i+1\to i}$	Liquid slip volume from chamber $i+1$ to chamber i	L^3
$\forall_u$	Chamber volume	L^3
$\forall_{n_{ch}}$	Volume of the last chamber opening to discharge as a function of ϕ	L^3
Vcc_{lkg}	Velocity of the slip flow across the circumferential clearance	L/t
$\forall_{screw}$	Volume of the screw section	L^3
W	Bulk flow velocity for the flow across the radial clearance	L/t
y	Vertical coordinate across the line passing through the midpoint of the radial clearance	
z	Axial coordinate along the screw length	
z_u	Axial location of the concentrated force	L
δz	Length of the rectangular element in axial direction	L
β	Half the angle between the two liner edges	
ε	Ratio of the static rotor shaft deflection to the circumferential clearance height	
η_v	Pump volumetric efficiency	
δ_{cc}, δ_{rc}	Circumferential and radial clearance nominal height	L
θ_m	Rotating meshing line angle	
θ	Polar coordinate	
$\acute{\kappa}$	Effective bulk modulus of elasticity of the fluid-gas mixture	F/L^2
ν	Kinematic viscosity	L^2/t

Symbol	Definition	Units
ξ	Entry loss coefficient for the slip flow across circumferential clearance	
τ_{ry}, τ_{Ry}	Shear stress on the inner and outer radii of the screws for the flow across the radial clearance	F/L^2
ϕ	Angle between the line of centers and the screw thread terminal edge	
ψ_f	Fourier series phase angle of the harmonic forces	
Ω	Rotor rotational speed	rpm

Subscripts

i	Chamber number, 1 is the chamber closest to and isolated from suction and n_{ch} is the chamber closest to and isolated from discharge
s	Suction
d	Discharge

Acronyms

GVF	Gas Volume Fraction
HS	Horizontal Suction sensor
VS	Vertical Suction sensor
HM	Horizontal Middle sensor
VM	Vertical Middle sensor
HD	Horizontal Discharge sensor
VD	Vertical Discharge sensor

Formatting

Bold	**B** is a matrix
bold-italic	***b*** and ***B*** are vectors
italic	*b* and *B* are real-values

1. INTRODUCTION

The earliest version of screw pumps is the famous Archimedes' screw still in use for raising water. "Modern" twin-screw pumps have been used since the early 1950s. Historically, the domain of their applications was limited to high viscosity liquids and high temperature conditions such as asphalt transfer with temperature ranging from 150^{o}C to 275^{o}C and viscosities ranging from 0.02 to 1 Pa-s [1]. Since the early nineties, pump users realized that twin-screw pumps could be used successfully in multiphase applications to pump a mixture of liquid and gas [2]. While the available fluid dynamics models for predicting pump performance are relatively mature and widely acceptable, the literature is silent about pump vibrations and rotordynamics. The work proposed here is a first step to understand the rotordynamic behavior of twin-screw pumps and the dynamic forces they are subjected to.

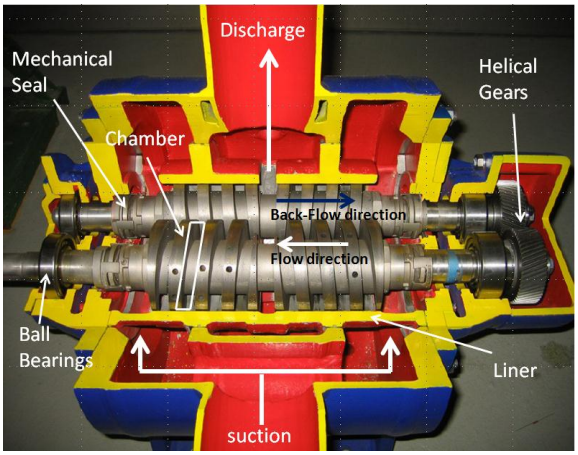

Figure 1 Screw pump cut-away section [3]

Figure 1 shows a cut-away section in a twin-screw pump and its main components. A glossary of twin-screw pump terminology is provided in Appendix A. The operating principle of twin-screw pump is different from centrifugal pumps. As a positive displacement machine, screw pump pressure head is achieved by trapping the fluid in a chamber and conveying it by the rotation of the screws to the discharge side where it is pushed out against the back pressure. Unlike centrifugal pumps, the pressure head is dependent on the pump back pressure while the rotational speed affects the flow rate only.

As shown in Figure 1, the suction flow is channeled to the opposite ends of the screws to eliminate thrust loading. The mechanical seals between the bearings and the pump are subjected to suction pressure.

In most screw pump designs, the screws are supported on roller-element bearings and connected via timing gears. Tight clearances separate the two screws from each other, and from the pump liner. Vetter and Wincek [4] identified the three different types of clearances around the screws shown in Figure 2. The circumferential clearance is between the screw lands and the pump liner. The radial clearance is between the screw land of one screw and the rotor of the other screw. The flank clearance is between the side walls of the screws. The clearances avoid metal-to-metal contact. Typical nominal clearance-to-radius ratios for the circumferential and radial clearances are in the range from 0.001 to 0.003.

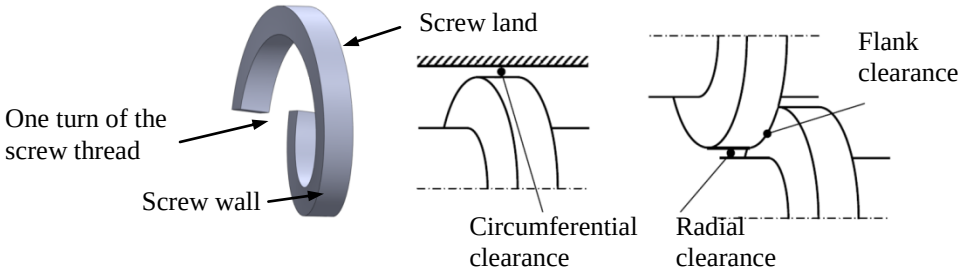

Figure 2 Types of clearances in twin-screw pumps [5]

The pump theoretical flow rate depends on the chamber volume and the running speed. However, because of the clearances around the screws, *slip flow* occurs from the discharge side to the suction side, which reduces the actual pump flow rate below its theoretical flow rate. The slip flow is the total leakage from one chamber to the chamber upstream through all the clearances connecting the two chambers.

From a rotordynamics point of view, screw pumps combine a number of interesting challenges. A complete rotordynamics model of screw pumps should address the following questions:

1. How should the asymmetric rotor structure be modeled?
2. What is the nature of the hydraulic forces on the rotor? How should they be modeled?

3. What are the fluid-structure-interaction forces in the tight clearances between the screw and the liner, and between the two screws?
4. What is the structural interaction between the two screws through the timing gears and through the housing?
5. How much damping is provided by the fluid in the tight clearances?
6. What is the effect of the presence of gas in the flow on the dynamic response?

The work proposed here does not attempt to answer all questions. It does provide an adequate model that can be used to predict the dynamic response of the pump. Such a model will be useful to elevate the screw pump rotordynamic analysis capability to par with conventional centrifugal turbo machines. With researchers and pump users voicing concerns about field vibration problems [2], and frequent premature seals and bearings failure [2,6], a rigorous baseline vibration analysis is necessary, especially for machines that are deployed sub-sea and expected to run for years without intervention.

A rotordynamic model of screw pumps will also be helpful for design purposes. The general conviction about screw pumps is that they are slow bulky machines running well below their first critical speed. However, with expanding domain of application in oil and gas to cover fluid mixtures with high gas content and less viscous fluids, running them at higher speed will soon be desired. A better understanding of the rotordynamic behavior in terms of determining the critical speeds, the exciting forces, and the steady state response, can contribute to refining the rotor design and operating speed for higher performance.

1.1 Literature review

Until relatively recently, screw pumps domain of application and advantages over centrifugal pumps were not fully appreciated by the pump user community especially in oil and gas business. Parker [1] discussed the set of limitations on centrifugal pumps that render twin-screw pumps more viable option under some circumstances. At conditions of high viscosity fluid (approximately greater than 0.1 Pa-s), low net positive suction head, or high entrained gas, twin-screw pumps have higher efficiency than their centrifugal pumps counterparts.

Little work was done on twin-screw pumps prior to the 1990s. Since then, the main thrust behind the surge in twin-screw pumps research is the move of the oil and gas business

towards offshore and deep sea reservoirs. Production technologies had to advance rapidly to meet the challenges of the new paradigm in oil and gas business. In a traditional production system, the liquid and gas phases in the crude are first separated, and then the pressure of each phase is increased using compressors for the gas and pumps for the oil and water. This traditional production method is not well suited for future expansion into deep sea wells, due to the large equipment footprint, and the long distance between the wellhead on the sea bed, and the pressure boosting station above surface. The longer the distance upstream of the pressure boosting station the higher the back pressure on the wellhead and the lower the recovery factor of the well. The shift to multiphase pumping seemed inevitable. Multiphase pumps can be installed on the sea bed next to the wellhead, thus reducing surface-equipment footprint and mitigating the back pressure on the wellhead [6]. Pump companies started to examine alternatives in multiphase technology, which triggered extensive research in twin-screw pumps. The bulk of the research effort in twin-screw pumps has been in characterizing their multiphase hydrodynamics and performance. This chapter is a literature survey of the screw pump fluid dynamics models and the published test results that validate them.

1.1.1 Eulerian-based models

The Eulerian approach to modeling twin-screw pumps approximates the geometrically complex pump chambers by a series of moving disks from suction to discharge. Both Vetter and Wincek [4] in 1993 and Prang and Cooper [7] in 2004 adopted this approximation independently. A schematic of the model is shown in Figure 3.

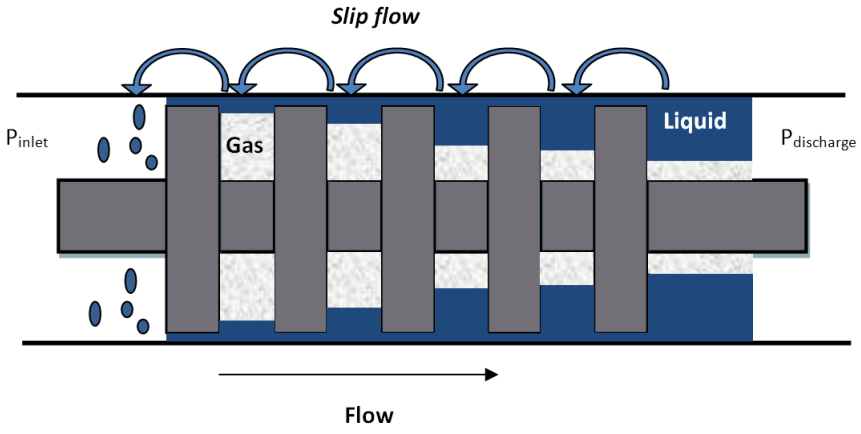

Figure 3 Screw pump represented as parallel disks [8]

The model inputs are the inlet and discharge pressures and the Gas Volume Fraction (GVF) at the suction in addition to the pump geometry and running speed. The model outputs are predictions for the steady state pressure in the chambers, the slip flow between chambers and the pump actual flow rate.

The GVF is the ratio of the gas flow rate to the total flow rate at suction

$$GVF = \frac{Q_{g,s}}{Q_l + Q_{g,s}} \quad (1)$$

Q_l and Q_g are the liquid and gas flow rates respectively. The subscript 's' is necessary to designate gas flow rate at suction, because the gas compressibility changes its flow rate from suction to discharge depending on the pressure. The liquid phase is incompressible, thus the liquid flow rate is constant throughout the pump.

Eulerian models [4,7] assume fully-developed steady state flow. They use isothermal ideal gas law to model the gas compression. The presence of the high heat-capacity liquid phase is assumed to absorb all heat generated from the gas compression without appreciable change in temperature. Experiments support this assumption up to a ~90% GVF [9].

Eulerian-based models also assume that all clearances connecting the chambers are filled with liquid phase only, due to the centrifugal effects of the screw rotation pushing away the higher density liquid phase to the circumference of the rotor. Although no experiment directly validated this assumption, it is widely believed that it holds up to a ~85% GVF. Pump performance at very high GVF is not predicted accurately by Eulerian based models.

Because of the isothermal-compression assumption, the Eulerian models do not include an expression of conservation of energy. They are entirely based on conservation of mass in addition to the ideal gas law in the multiphase case.

Vetter and Wincek [4] identified complex leakage paths including leakage from one screw to the other through the flank clearances. However, they reported a convenient experimental result that 80% of the slip flow occurs through the circumferential clearance alone. They estimated the contribution of each clearance type to the slip flow by applying an external pressure source to the discharge of a non-rotating pump and blocking one type of clearance at a time throughout the pump by synthetic resins. Prang and Cooper [7] later used this empirical result to simplify their model by solving for the axial leakage flow through the circumferential clearance. The slip flow was estimated using the 80% empirical constant in

[4]. They treated the circumferential clearance as an annular seal employing Moody friction coefficient for turbulent and laminar flow through smooth pipes. The laminar-turbulent transition region is handled by fitting a straight line to the friction at the turbulent region and extending it through the laminar region. The friction from the extended turbulent friction line is compared to the laminar friction value, and the laminar-turbulent friction is taken as the greater of the two values. Unlike Vetter and Wincek in [4], they included the effect of the Bernoulli entry losses of the axial leakage through the circumferential clearance.

The rotors are subjected to static pressure loading due to the unbalanced circumferential pressure field around the screws. Prang and Cooper explained the mechanism of the static pressure loading qualitatively in [7]. As shown in Figure 4, the helix angle of the screws causes a 'delay' in the pressure buildup around a segment of the circumference creating a net static pressure difference on the rotor.

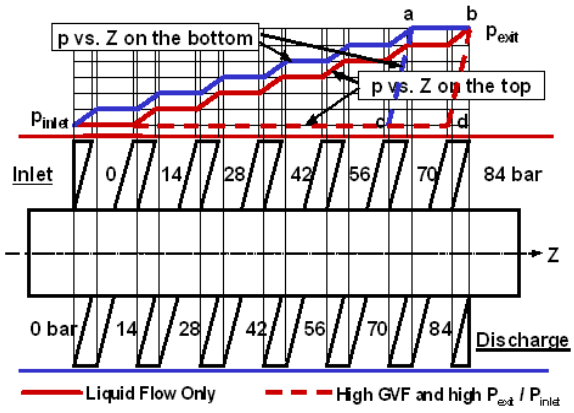

Figure 4 Axial pressure buildup [7]

Eq. (2) is a simplified estimation of the radial force F_r resulting from the unbalanced pressure around the screws [8,10].

$$F_r = h(D_{out} + D_{in}) \times \Delta P \tag{2}$$

h is the screw thread pitch. D_{out} and D_{in} are the outer and inner diameters of the screw respectively. ΔP is the total pressure difference across the pump.

F_r results in a deflection of the twin-screw pump rotors causing the rotors to be displaced a distance e from their centric position. The static rotor deflection e is an

important design parameter. The rotors have to be rigid enough to keep their deflection below the nominal circumferential clearance height δ_{cc} to avoid metal-to-metal contact.

The axial leakage through the circumferential clearance increases by a factor ranging from 1.2 to 2.5 of the concentric leakage flow depending on the eccentricity and the Reynolds number [4,7].

1.1.2 Lagrangian-based models

The Lagrangian approach for modeling a twin-screw pump treats the chamber as an open thermodynamic system transporting mass and energy and connected to other chambers through the different clearances. Unlike Eulerian models, the Lagrangian approach does not assume fully developed steady state flow; instead, they are based on a time-dependent application of the conservation of mass and energy equations.

Rausch et al. [11] were first to lay down a Lagrangian model for twin-screw pump. They formulated the problem as an initial and boundary value problem, the system is solved by time integration methods until steady state. They assumed an adiabatic chamber and neglected the kinetic energy and wall friction for the axial flow across the circumferential clearance. The multiphase model consisted of mass balance and energy balance based on ideal gas compression. Their single-phase model was simply an iterative solution of chamber pressure to satisfy a mass equilibrium for each camber. Single-phase pressure buildup is traditionally known to be linear due to the incompressibility of liquids. Their model did not include an expression for the pressure drop across the circumferential clearance as they neglected wall friction, but they mentioned that the circumferential clearance axial leakage flow was assumed to be liquid phase only. Their model predictions were not in good agreement with their test results at high speeds and high GVFs.

Rabiger [5,12] made a major contribution to the field by building what can be regarded as the most complete twin-screw pump model. His objective was to relax the assumption of a liquid-filled clearance flow to model pump operation at very high GVF (above 90%) where this assumption is no longer valid. In addition, his model included a 2-way fluid structure thermal interaction between the thermodynamic process in the chamber and a finite volume thermal model of the rotor and the liner to predict the rotor's thermal growth and its effect on the clearance.

Rabiger assumed an ideal gas for the compression process and thermal equilibrium between the two phases. He included both radial and circumferential clearance flows in his model but neglected the flow through the flank clearance since the experiment in [4] showed it only constitutes 5% of the total leakage. To model a two-phase flow across the circumferential and radial clearances, he assumed the liquid and gas phases have the same pressure, velocity and temperature as well as a homogenous density based on the relative density of each phase. The model is a system of ODEs expressing conservation of mass, energy and axial momentum. In that regard, his model is very similar to annular seal models with some modifications and simplifying assumptions to account for the presence of the gas phase. Both the friction and Bernoulli acceleration pressure drop were included.

1.1.3 Other modeling techniques

In addition to the previous two basic general modeling approaches, other work has been done in twin-screw pumps with different objectives or emphasis. Martin [13] developed a model to assist pump users in the oil and gas field to predict pump performance for operational purposes without the need for special information that pump designers might be unwilling to share, such as clearances and screw geometry. The model groups the resistance from all screw clearances into a single resistance coefficient, which is then estimated by a least-square curve fit to the water single phase pump curve supplied by the manufacturer. This approximation required multiple correction factors to match the experimental results.

Xu [3] extended Martin's model to account for high GVF keeping the same objective of gearing the model for pump users with minimum knowledge of screw geometry. Xu built both isothermal and non-isothermal models and assumed a two-phase axial leakage flow across the circumferential clearance. He further suggested and simulated a recirculation and reinjection of liquid directly into the chambers along the liner to enhance chambers' sealing.

Nakashima and Junior [14] built a thermodynamic model for twin-screw pumps using building blocks from process simulator program Hysys©. They assumed steady state and adiabatic flow with heat exchange only between the two phases. They assumed the flow in the clearances is only liquid, and neglected the effect of eccentricity from the pressure loading. Their chamber model was divided into separation, compression, pumping, and mixing processes and connected by single-phase flow in a pipe representing the clearances.

They solved the system iteratively until the inlet and outlet flows of all chambers are balanced.

The model by Feng et al. [15] is essentially a Lagrangian model. Their main contribution is in introducing the geometry of the screw profile in the model. Their integration scheme included a mathematical description of the rotor profile based on gear theory. A detailed discussion of the screw-pump rotor profile generation and the cutting tool design for screw thread manufacturing is given in Feng et al. [16]

Stosic et al. [17] investigated the applicability of screw compressors theory including profile generation and thermodynamic modeling to screw pumps. His chamber model was essentially Lagrangian. Screw compressors models and design concepts are generally more mature than screw pumps. Both machine types have some similar features. However, key differences in geometry and operation mechanism place a question mark on the validity of carrying screw compressor's knowledge into twin-screw pump domain directly.

In addition to hydrodynamic models, other researchers focused on different aspects of twin-screw pumps. Nakashima et al. [18] built an elaborate finite volume model for the heat transfer to the screw and the liner during a Loss-of-Prime (LOP) event when the pump loses pumping capacity, and all the fluid is recycled back from discharge. They concluded that even for a long LOP event (80 minutes), the temperature rise did not pose a serious problem.

1.1.4 Test results and performance characteristics of twin-screw pump

Most of the models discussed earlier were compared to experimental test results for validation. A typical twin-screw pump test program includes measurements of steady state pressure at discharge and suction and flow measurement for each phase at suction. Some test programs presented dynamic pressure measurements along the screw length in addition to static rotor deflection, but no results of dynamic rotor response or dynamic bearing forces are published in the literature. This section addresses the performance characteristics and operation modes of screw pumps, and then reviews the published test results.

The theoretical flow rate of twin-screw pumps depends on the screw geometry and the pump running speed as given by [7]

$$Q_{th} = 4\omega B A_r \left(D_{out}^2 - D_{in}^2\right) \quad (3)$$

ω is the running speed in rad/sec. A_r is the fraction of the annular space between the outer and inner diameters of the screw not blocked by the screw threads, D_{out} and D_{in} are the outer and inner diameters of the screw. The 4 in Eq. (3) is required because in twin-screw pumps each rotor has two screw sections [5]. B is the screw land width given by

$$B = \frac{h}{2N} \tag{4}$$

h is the screw pitch. N is the number of threads (h is illustrated in Figure 13).

While slip flow Q_{slp} occurs between every two adjacent chambers from the higher-pressure chamber downstream to the lower-pressure chamber upstream through the circumferential, radial and flank clearances, only the slip from the first chamber back to suction affects the pump flow rate [7]. The actual flow rate at the pump inlet is the difference between the theoretical flow rate and the slip flow from the first chamber back to suction.

$$Q_{in} = Q_{th} - Q_{slp,1\rightarrow s} \tag{5}$$

In Eq. (5) the subscript $(1 \rightarrow s)$ is appended to Q_{slp} to differentiate the slip between the first chamber and the suction chamber from the slip between other chambers. The chambers are numbered in ascending order from 1 to n_{ch}, where 1 is the chamber closest to and isolated from suction, and n_{ch} is the last chamber closest to and isolated from discharge. *Suction chamber* is the chamber communicating with the pump inlet. Similarly, *discharge chamber* is the chamber communicating with the pump outlet. Sections 3.3 and 3.4 will describe the process of opening the discharge and suction chambers to the pump's outlet and inlet and the pressure buildup in these chambers. P_{suc} is the pressure at pump inlet upstream of the suction chamber, and P_{dis} is the pressure at the pump outlet downstream from the discharge chamber.

Eq. (6) defines twin-screw pump volumetric efficiency as the ratio of the actual flow rate at the pump inlet to its theoretical flow rate.

$$\eta_v = \frac{Q_{in}}{Q_{th}} \tag{6}$$

The total efficiency of the pump includes the thermal, and mechanical efficiencies in addition to the volumetric efficiency as given by Schan [19]. However, the pump performance is generally characterized by η_v only.

Figure 5 is adopted from [5] and is very helpful to conceptually understand the effect of GVF on the axial pressure buildup profile.

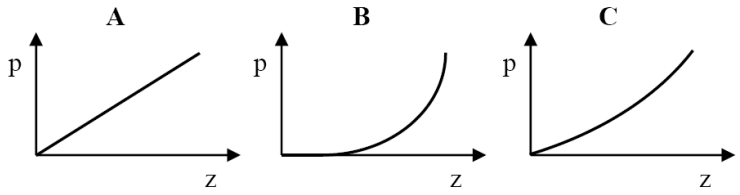

Figure 5 The effect of the GVF on the axial pressure buildup profile [5]

In Figure 5, *z* is the axial coordinate along the screw length. Case A applies when the inflow at the pump suction is predominantly liquid (GVF is below 10%). Case B applies for multiphase flow with enough liquid to seal the clearances (GVF is above 10% and below 90%). Finally case C applied for wet gas conditions where the flow at suction is predominantly gas and the flow across the clearances is a homogenous gas liquid mixture (GVF is above 90%). In case A the pressure profile increases linearly along the screw length because of the incompressibility of the liquid phase. In case B the pressure profile is parabolic due to the compressibility of the gas phase. Most of the pump head in case B is achieved in the chamber closest to discharge. A further increase of the GVF above 90% pushes the profile to become almost linear again as in case C.

The effect of GVF on the pump delivery performance is illustrated in Figure 6, which shows conceptual pump characteristic curves for cases A, B and C in Figure 5. For case A two separate pump curves are highlighted to distinguish between the pump performance at laminar and at turbulent clearance flow conditions. Prang and Cooper [7] investigated the difference between the two operation modes by varying the viscosity of the working fluid. They noted that for a highly viscous fluid – traditionally the domain of screw pump application – the slip flow is laminar and it increases linearly with the pressure difference, hence the linear decrease in inlet flow rate with pump head. For a low viscosity fluid, turbulent flow dominates, and slip flow tends to vary with the square root of the pressure difference, hence the slightly concaved downward flow decline with pump head. They validated their model experimentally using high and low viscosity fluids. Their model predicted pump performance for the two viscosities satisfactorily.

As the GVF increases, the pump characteristic curve moves in the (I) direction from A to B in Figure 6. Prang and Cooper [7] explained this marked increase in volumetric efficiency in the light of the pressure buildup profile. The contribution of the first chamber to the total pump head in case B is less than it is in case A because of the parabolic buildup profile in case B compared to the linear buildup profile in case A as shown in Figure 5, (compare the pressure value at suction (z~0) for cases A and B in Figure 5). Since the only slip that reduces the pump inlet flow rate is the slip from the first chamber to suction, a lower pressure difference between the first chamber and suction results in less slip, hence more inlet flow rate and more volumetric efficiency according to Eqs. (5) and (6).

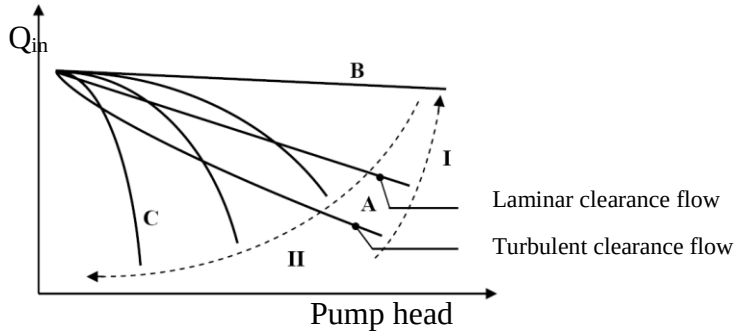

Figure 6 The effect of GVF on screw pump characteristic curve [5]

Increasing the GVF further in Figure 6 causes the pump curve to start decreasing again in the (II) direction from B to C. Rabiger [5] argues that at a GVF above 90%, the gas phase starts to infiltrate the circumferential clearances. At very high GVF (above 98%), the pump starts to act like a compressor, and a breakdown in the sealing between chambers results in a breakdown in the pump ability to deliver the wet gas mixture.

This trend in the twin-screw pump performance with varying GVF was reproduced in many independent test programs. In addition to the results presented by Prang and Cooper [7] , Vetter and Wincek [4] also presented pump performance and axial pressure buildup curves for 0, 10%, 50%, and 90% GVF. Their test results followed the trend. Their model was in a good agreement for GVFs lower than 90%, but showed consistent discrepancy for the 90% case. At 90% GVF the axial pressure buildup was still parabolic. The test results by Egashira et al. [20] show the same parabolic axial pressure buildup at 90% GVF. They also presented results for 0, 60%, 70%, 80% in addition to the 90% GVF. Vetter et al. [21]

pushed for higher GVF up to 98%. They were able to show the return-to-linear axial pressure buildup above the 90% GVF similar to case C in Figure 5. Their model was not in good agreement with the measurements at GVF above 90%. They attributed the discrepancy to the violation of the liquid-filled circumferential clearance assumption. As discussed earlier, Rabiger's [5] model relaxed that assumption allowing for a multiphase slip across the clearances. He conducted an extensive test program focusing only on GVF from 90-99%. The model and the test results were in good agreement for all GVFs.

Running speed ω has less an effect on the pump performance than GVF. In single-phase flow with GVF below 10%, it has almost no effect on the pressure buildup profile and consequently on the slip flow. The measurements by Egashira et al. [20] shown in Figure 7 for the slip flow versus pump differential pressure for three different speeds confirm the independence of slip flow from ω. Martin [13] also reported similar measurements and noted that this behavior implies that the axial leakage flow through the circumferential clearance is essentially insensitive to the coquette flow component. This characteristic of twin-screw pump is significant for improving its versatility, since it implies that the pump's volumetric efficiency increases with speed. Equation (3) indicates that the theoretical pump flow is a linear function of running speed. A slip flow that is constant with increasing ω indicates that running the pump faster increases the pump delivered flow without additional volumetric losses.

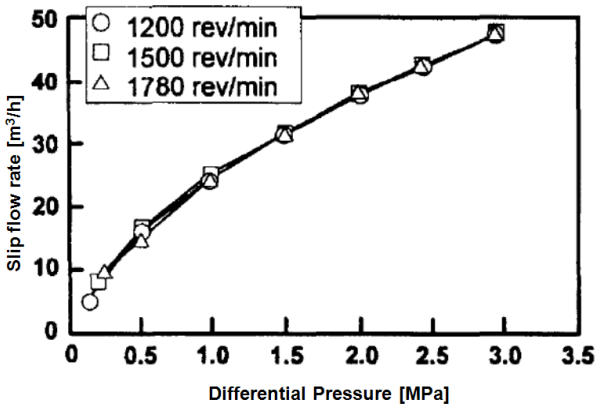

Figure 7 Single-phase (GVF = 0%) slip flow versus differential pressure [20]

This behavior is even more favorable in the multiphase case. Figure 8 shows the pump flow rate versus pump differential pressure for two running speeds from Prang and Cooper [7]. They noted that the inlet flow rate decreased more rapidly with increasing pump differential pressure for 900 RPM compared to 1500 RPM at a 95% GVF. The same behavior was reported in other published test results [4,21,13].

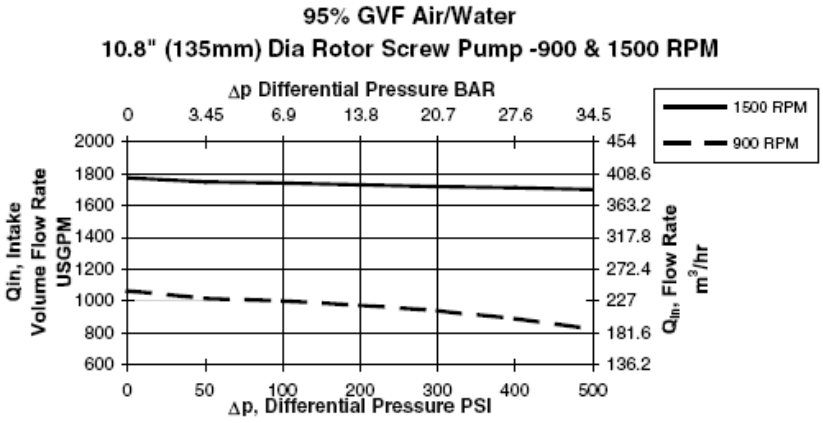

Figure 8 Flow rate versus pressure head at two running speeds [7]

This marked improvement in twin-screw pump volumetric efficiency with increasing running speed poses the question: What stops pump designers from building faster screw pumps? Prang and Cooper in [8] argue that pump designers prefer to keep the screw tip speed as low as possible to reduce wear due to solid particles trapped in the pump tight clearances. Martin argues in [13] that too fast operation might result in an incomplete filling of the suction chamber by the fluid, which reduces the overall efficiency of the pump. Despite of these two concerns, an undefined rotordynamic behavior is still a key issue to refine the pump design and improve its efficiency.

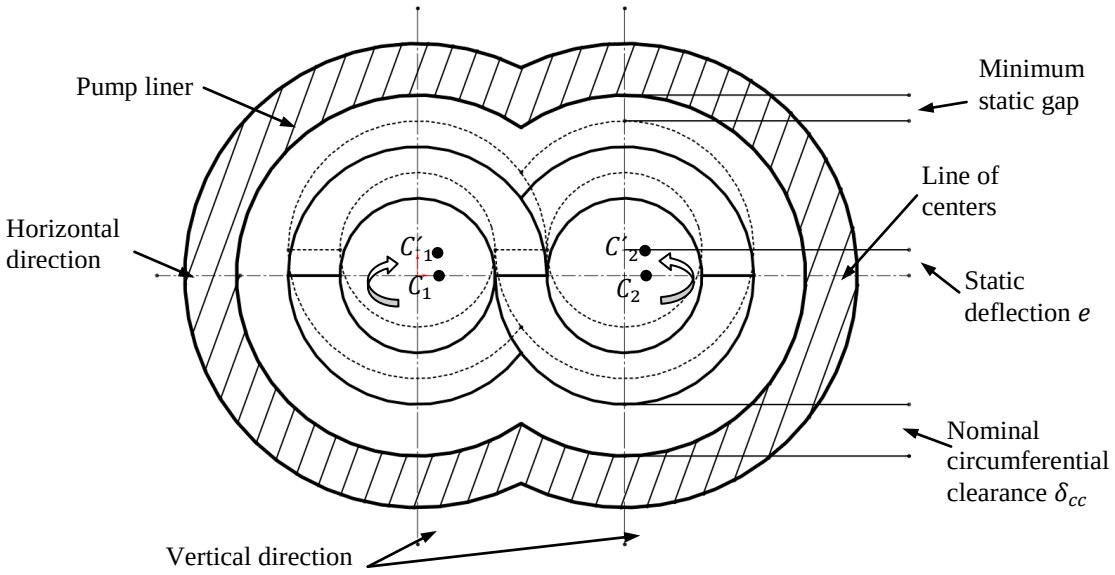

Figure 9 Schematic of screw deflection inside the liner

Figure 9 is a schematic of two screws inside a pump liner with the circumferential clearance exaggerated for visualization. The cross section is taken at the middle of the discharge. The centers of the two screws are at C_1 and C_2. The line passing through the centers C_1 and C_2 is referred to as the line of centers. The horizontal direction is along the line of centers and the vertical direction is perpendicular to it. The static hydraulic forces from the unbalanced pressure around the screws cause the centers of the screws to be displaced a distance e to C_1' and C_2'. A simplified estimation of the static forces was given by Eq. (2) from [7]. The nominal circumferential clearance δ_{cc} is the radial distance between the tip of the undeflected screw and the pump liner. The static gap is the distance between the tip of the deflected screw and the pump liner. Because measurements of shaft deflection are usually taken at the middle of the discharge section for accessibility, the minimum static gap is not measured directly; it is calculated as the difference between δ_{cc} and e.

Static gap measurements from Neumann [2] are shown in Figure 10 for single-phase and for 92% GVF. Neither the axial nor the circumferential locations of the gap measurements were reported in [2]. The gap decreased almost linearly with increasing pump differential pressure indicating a linear increase of the shaft deflection with increasing pump differential pressure. Neumann also measured the static radial reaction forces at the drive shaft bearing. He noted that although the force at the bearing for the 92% GVF is less than the force for the single-phase, the shaft deflection in the case of the 92% GVF is more than in

the single-phase case. He explained this contradiction qualitatively as a consequence of the axial pressure buildup. The linear axial pressure buildup for single-phase flow causes the effective hydraulic forces to be located at the middle of the screw section, while for the 92% GVF the parabolic axial pressure buildup pushes the effective hydraulic forces to the discharge side closer to the midspan of the rotor where it creates larger deflection.

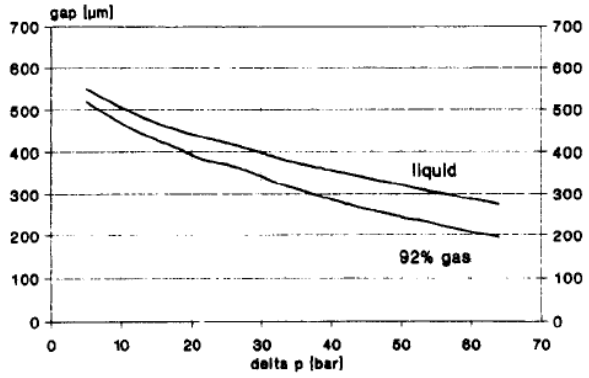

Figure 10 Static gap between the screw and pump liner [2]

Vetter and Wincek [4] showed similar results to Neumann [2]. They reported the static rotor deflection e at the rotor midspan in two planes. e was negligible in the horizontal direction and ~80% of δ_{cc} in the vertical direction. They noted that the deflection is a linear function of the pressure head, and that it is only slightly larger in the multiphase flow compared to the single phase. Their simple beam model and static force estimation under predicted e by ~25%.

Few test programs included dynamic pressure measurements. Vetter et al. [21] placed six dynamic pressure probes in the pump housing along the axial extent of the screw. All the probes were in one plane aligned with the line of centers of the rotors. The layout of the pressure sensors and the dynamic pressure measurements versus the rotor's rotation angle for 75% GVF are shown in Figure 11. Two screw lands pass by the sensor in the housing per rotation because the pump is double threaded. The parabolic axial pressure buildup is evident as most of the pressure head is achieved in the last chamber (sensor p_5).

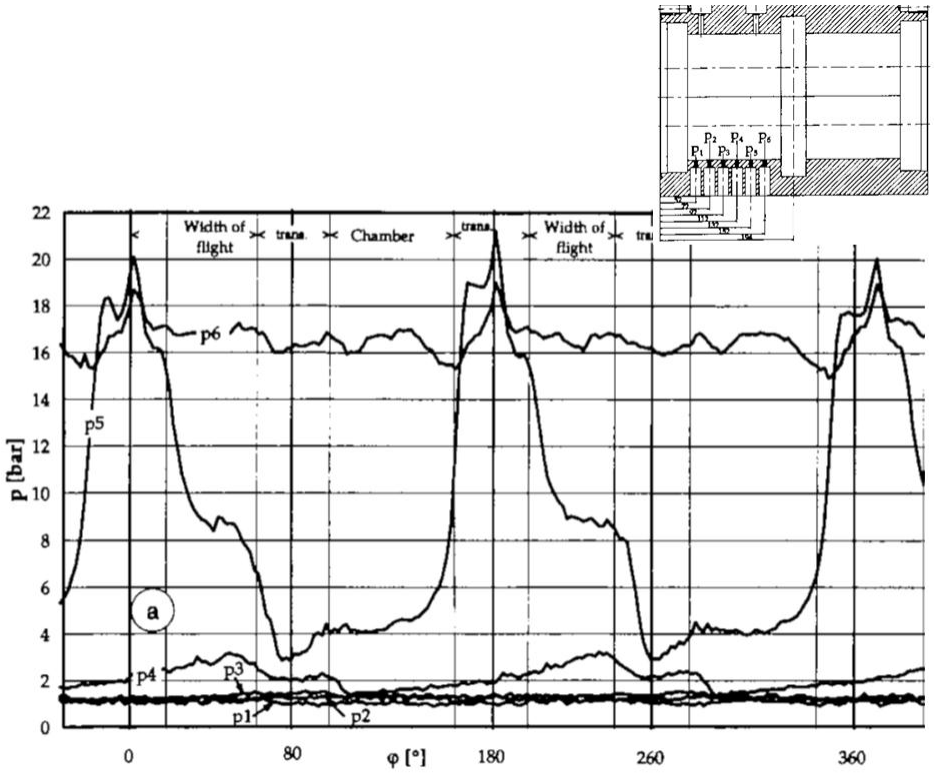

Figure 11 Dynamic pressure versus angle of rotation. 75% GVF [21]

The next two chapters will address a proposed new model for predicting the dynamic forces and the lateral twin-screw pump rotor response. Chapter 2 will address the dry structural dynamics of the machine. Chapter 3 will address the characterization of the unbalanced dynamic pressure field, the resulting forces and the rotor response. The last chapter is a description of the screw pump test rig.

The proposed model basis can be summarized in the following points:

1. Due to the helix angle of the screws, the circumferential pressure field around the rotors is not balanced [4,7].
2. The dynamic pressure measurements in Figure 11 show a periodic pressure field.
3. The unbalanced dynamic pressure field will create static forces as well as dynamic periodic forces. Therefore, the resulting exciting forces can be expressed as nonsynchronous harmonic force components and applied to the rotor structural model to predict its steady state dynamic response.

2. ROTORDYNAMICS MODEL OF TWIN-SCREW PUMP ROTOR

The rotordynamic analysis of twin-screw pump rotors is complicated by the asymmetry of the screw cross section, and by the interaction between the two rotors at the timing gears. This chapter is divided into three sections. The first section addresses the lateral structural rotordynamics of the twin-screw pump rotor. The second addresses the torsional rotordynamics, and the third addresses the torsional-lateral coupled rotordynamics.

2.1 Lateral structural rotordynamics of twin-screw pump rotor

Figure 12 is a simplified solid model of a typical single-thread screw rotor in a twin-screw pump. The rotor is for a 75 Kw pump running at 1750 rpm.

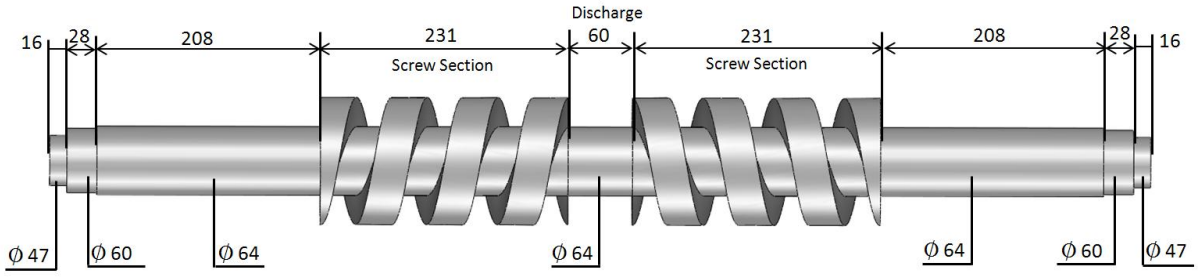

Figure 12 Solid model of a twin-screw pump rotor (dimensions in mm)

The screw section of the solid model and its cross sections are shown in Figure 13. L_s is the screw section length. D_{out} and D_{in} are outer and inner diameters of the screw thread respectively. h is the screw thread pitch. At any given axial location, the cross section of a single-thread screw is composed of the two half circles shown in Figure 13. The orientation of the two half circles cross section goes through a complete revolution in a pitch length.

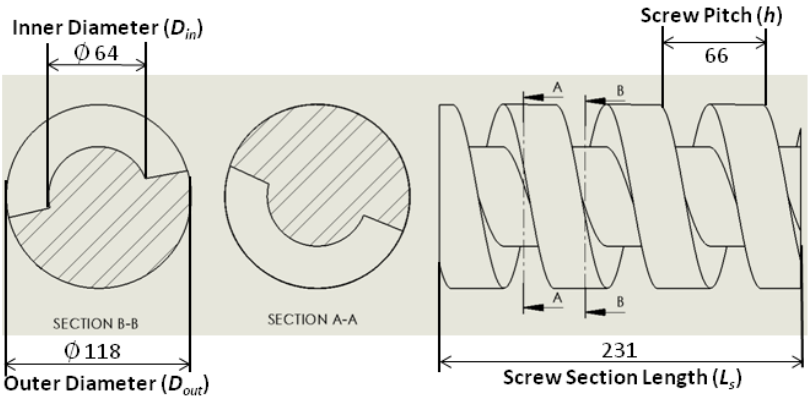

Figure 13 Screw section (dimensions in mm)

The asymmetry of the screw cross section does not lend itself to rotordynamic analysis. It requires a general Finite Element (FE) model rather than the simpler axisymmetric rotor model. Figure 14 shows the general FE mesh of the rotor in ANSYS©. The predicted first five free-free modes are shown in Table 1 in two lateral orthogonal directions.

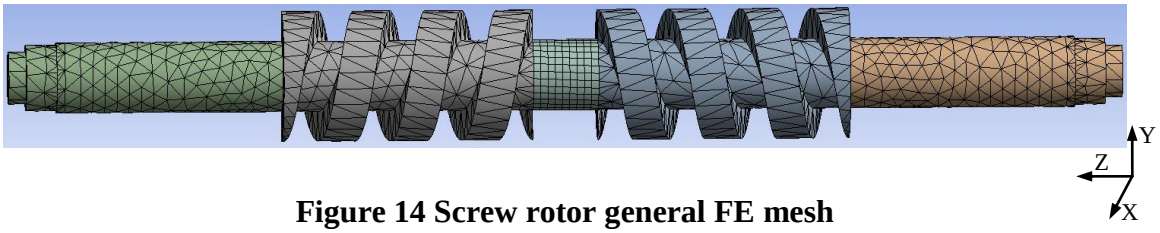

Figure 14 Screw rotor general FE mesh

Table 1 Screw rotor nonaxisymmetric free-free modes

Mode	Direction	
	X [Hz]	Y [Hz]
1st	277.99	278.58
2nd	674.71	673.91
3rd	1270	1267.3
4th	2014.5	2013.3
5th	2889.5	2886.9

Table 1 shows that the predicted free-free modes are almost identical in the X and Y directions. This convenient result implies that an equivalent axisymmetric model can be built to capture the structural dynamics of the geometrically asymmetric screw cross section. Figure 15 is a schematic of an axisymmetric rotor that is nominally equivalent to the general FE rotor shown in Figure 12 modeled in XLTRC2© using Timoshenko beams with circular cross section. The screw section is represented by two layers of different diameters. One layer captures the mass properties of the section, and the other layer captures the stiffness properties.

The mass layer is a cylinder with a length equals to the length of the screw section and a diameter (D_m) given by

$$D_m = 2\sqrt{\frac{V_{screw}}{\pi L_s}} \tag{7}$$

V_{screw} is the volume of the screw section. L_s is the axial length of the screw section. D_m is the circular radius that makes the volume of a cylinder with a length L_s equals to the volume of the screw section.

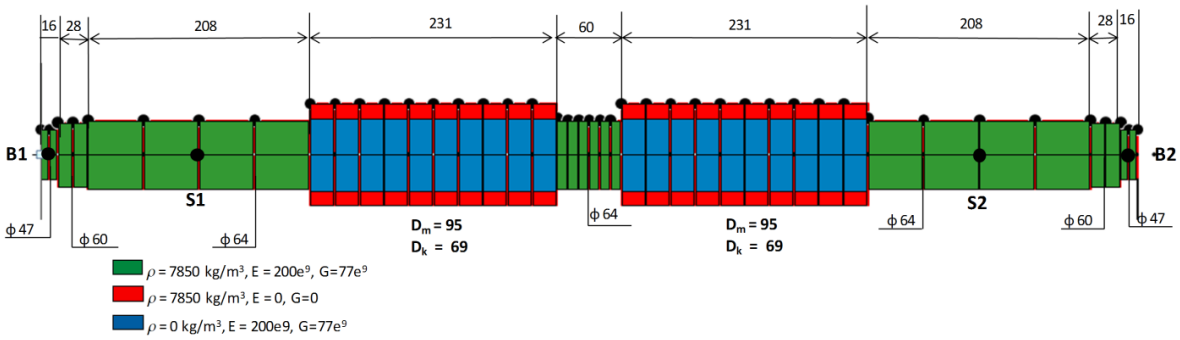

Figure 15 Screw rotor equivalent axisymmetric model (dimensions in mm)

The equivalent mass diameter of the axisymmetric model is 81% of the outer diameter of the screw thread. However, the difference between the transverse mass moment of inertia of the axisymmetric and general models is less than 1%. Including the production of inertia of the general model did not have any effect on the synchronous response of the axisymmetric model.

Unlike the equivalent mass diameter, the equivalent stiffness diameter of the axisymmetric model cannot be determined from the screw geometry. An equivalent circular cross section with the same moment of area of the two-half-circles cross section over estimates the free-free modes of the general model. The nondimensional ratio K_d defined in Eq. (8) is used to identify the stiffness properties of the screw section.

$$K_d = \frac{D_k}{D_{in}} \tag{8}$$

D_k is the diameter of the stiffness layer of the equivalent axisymmetric mode. D_{in} is the inner diameter of the screw. D_k is determined by varying K_r until the free-free modes of the axisymmetric model match the free-free modes of the general FE model to a satisfactory level. A comparison between the predicated free-free modes of the general FE and the nominally equivalent axisymmetric models is shown in Table 2. The values of D_m and D_k are shown in Figure 15. The values of D_{out} and D_{in} are shown in Figure 13. The small differences between the first five free-free modes of the two models confirm that the axisymmetric model is adequately equivalent to the general FE model. For matching purposes only the between-the-bearings section of the rotor is modeled. The complete model including the gear and coupling sections is presented in section 2.3 .

Table 2 Axisymmetric versus general FE free-free lateral modes

Mode	General FE ANSYS [Hz]	Axisymmetric XLTRC2 [Hz] $K_d = 1.08$	Error
1st	277.99	277.3	0.2%
2nd	673.91	670.2	0.6%
3rd	1267.3	1280.2	-1%
4th	2013.3	2030.1	-0.8%
5th	2886.9	2943.3	-2%

2.1.1 Screw cross section dynamic imbalance

While the asymmetric screw cross section can be adequately modeled by an axisymmetric circular cross section, the screw thread is not necessarily dynamically balanced. To investigate the effect of the cross section asymmetry on the dynamic imbalance

response, the pitch length (h) is sliced into N_{sl} pieces. The center of mass of each slice is displaced from the center of geometry of the rotor by the length of the vector $\boldsymbol{u_{sl}}$ given by

$$|\boldsymbol{u_{sl}}| = \frac{4(R_{out}^3 - R_{in}^3)}{3\pi(R_{out}^2 + R_{in}^2)} \quad , \quad \angle \boldsymbol{u_{sl}} = k\frac{2\pi}{N_{sl}} \qquad k = 0,1,2 \ldots , N_{sl} - 1 \tag{9}$$

R_{out} and R_{in} are the outer and inner screw radii respectively. The amount of the unbalanced mass for each slice (m_{sl}) is given by

$$m_{sl} = \rho \forall_{screw} \frac{h}{N_{sl} L_s} \tag{10}$$

ρ is the density of the screw section material. $\forall_{screw}$ is the volume of the screw section. h is the screw pitch. L_s is the axial length of the screw section. $N_{sl}$is the number of slices.

The rotor in Figure 12 has two screw sections. The thread of each screw section has 3.5 turns $(L_s = 3.5h)$. The screw thread pitch (h) was sliced in eight slices $(N_{sl} = 8)$. For each slice an imbalance equals $|\boldsymbol{u_{sl}}|m_{sl}$ was applied. The phase angle of the imbalance is the angle of the $\boldsymbol{u_{sl}}$ vector given in Eq. (9).

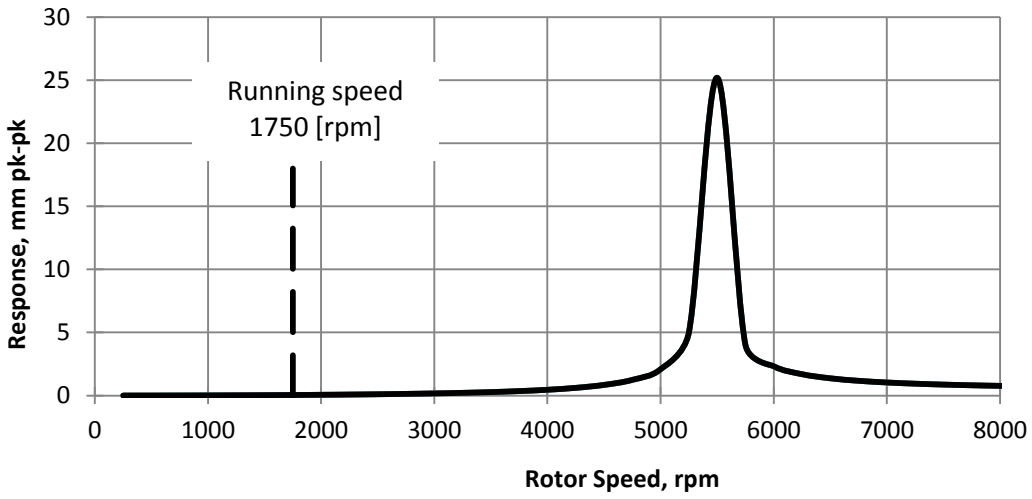

Figure 16 Response due to cross section imbalance

Figure 16 shows the predicted response due to the imbalance inherent in the thread geometry. No additional imbalances were applied. For Figure 15, the ball bearings are

isotropic and identical with a 6.1E7 [N/m] stiffness and 525 [N-s/m] damping located at points B1 and B2. The bearing parameters were estimated using XLTRC2© software package based on [22]. The large amplification factor (30.82) is due to the low damping in the bearings and the absence of damping along the rotor. The response at the critical speed is 25 mm peak to peak, confirming that the machine cannot pass the critical speed without appropriate dynamic balancing. However, the response at the running speed is 0.045 mm at the middle of the rotor and 0.028 mm at the seal at the suction sides S1 and S2 shown in Figure 15 which explains why the dynamic imbalance of a single-thread twin-screw pump might not be of a concern in the current application margins. The first damped mode is at 5513 rpm. The damped mode shape is shown in Figure 17. It is the typical bouncing mode of a simply supported beam with stiff bearings.

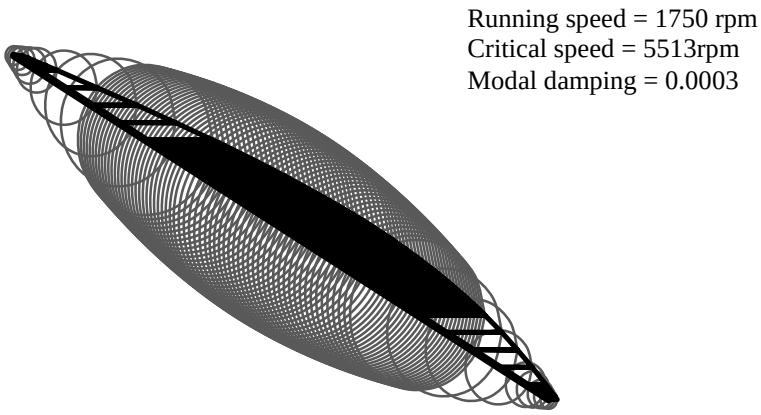

Figure 17 First damped mode shape

2.2 Torsional structural rotordynamics of twin-screw pump rotor

The screws in twin-screw pumps generally have smaller polar moment of inertia than the impellers in rotordynamic pumps. While this characteristic elevates the torsional natural frequencies of twin-screw pump rotors, other characteristics such as the gear connection, the long rotors, and the flexible couplings tend to decreases the torsional natural frequency of the whole drive train. Torsional analysis of turbomachines in general is becoming less of a

luxury due to the expanding use of Variable Frequency Drives, and twin-screw pumps are not an exception.

Similar to the lateral direction the screw threads can be treated as an axisymmetric structure in the torsional direction. The study of several screw geometries showed that the equivalent axisymmetric mass and stiffness diameters in the lateral direction are also applicable to the torsional direction. Table 3 compares torsional modes for the general FE rotor model shown in Figure 13 with the torsional modes for the axisymmetric rotor model shown in Figure 15 using the same equivalent mass and stiffness diameters of the lateral model.

Table 3 Axisymmetric versus nonaxisymmetric free torsional modes

Mode	General FE ANSYS© rpm	Axisymmetric XLTRC2 rpm $K_d = 1.08$	Error
1st	75306	75768	-0.61%
2nd	160224	157764	3.41%
3rd	188094	192540	-2.36%

The high values of the torsional modes in Table 3 compared to the running speed at 1750 rpm can be misleading. For matching purposes, the analysis is performed only for one rotor. In reality, the torsional system consists of a motor, coupling, and two rotors connected by timing gears as schematically shown in Figure 19. For a soft coupling, and including the gear tooth torsional stiffness, the system's first torsional mode can drop significantly as shown in Figure 18.

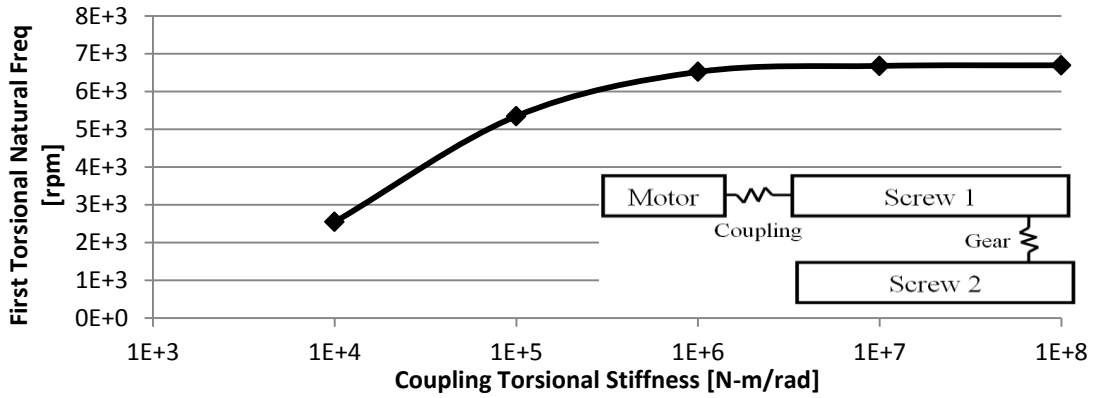

Figure 18 Effect of coupling stiffness on the first natural frequency of the system

2.3 Torsional-Lateral coupled rotordynamics of twin-screw pump rotors

Gears are a known source of torsional-lateral coupling. In many machines, the coupled and uncoupled dynamics are comparable. However, the layout of screw pumps especially for designs with long rotors and soft coupling can cause an appreciable interaction of the dynamics in the two directions. Rao et al. in [23] and Lee et al. in [24] both develop a finite element representation for two axisymmetric rotors connected by flexible gear tooth.

The system in Figure 19 consists of a motor, a coupling, two rotors, and a torsional lateral coupled gear connection. The mass and stiffness properties of the drive train components are listed in Table 4. The detailed dimensions of the screw rotor were shown in Figure 15.

Table 4 Mass and stiffness parameters of the twin-screw pump drive train

Mode	Mass Properties	Stiffness Properties
Motor	Mass = 180 [Kg] Ip =9 [Kg-m^2] It = 18 [Kg-m^2]	-
Coupling	Mass = 26.6 [Kg]	K_{Tor}= 1E4 [N/rad] K_{Lat}= 1E5 [N/m]
Gears	Radius = 43 mm Mass = 5.4 [Kg]	K_{tooth} =1E6 [N/rad]
Bearings	-	$K_{xx} = K_{yy}$ = 6.11E7 [N/m] $C_{xx} = C_{yy}$ = 5.25E2 [N-s/m]

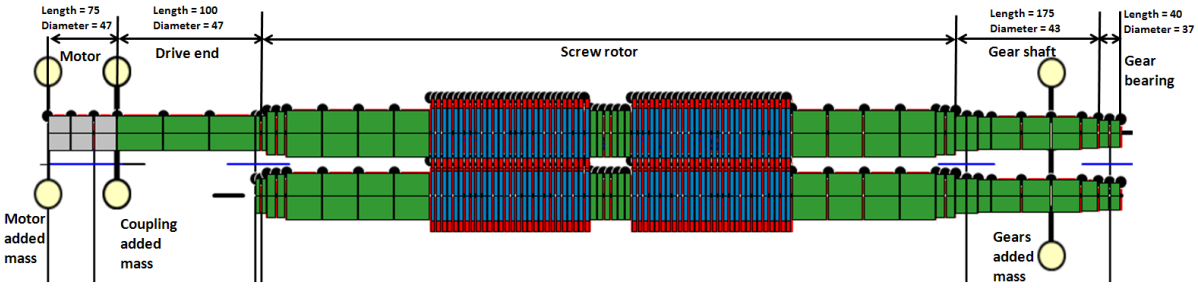

Figure 19 Twin-screw pump complete drive train model (dimensions in mm)

A comparison of the lateral, torsional and coupled lateral-torsional system's natural frequencies is shown Table 5.

Table 5 Lateral, torsional, and coupled system's natural frequency

Lateral rpm	Torsional rpm	Torsional/Lateral K_{GR}=1E6 [N/m]
5636 (BW)*	2271	1721 (BW)
5707 (FW)**	17000	3227 (FW)
5996 (BW)	…	5636 (BW)
6002 (FW)	…	5707 (FW)
…	…	5996 (BW)
…	…	6002 (FW)

*Backward critical speed, ** Forward critical speed

Without torsional lateral coupling each shaft vibrates independently with most of the energy going to the middle sections at the screws, and minimal energy going to the bearings and the gear section. The first two lateral mode shapes of the drive train are shown in Figure 20.

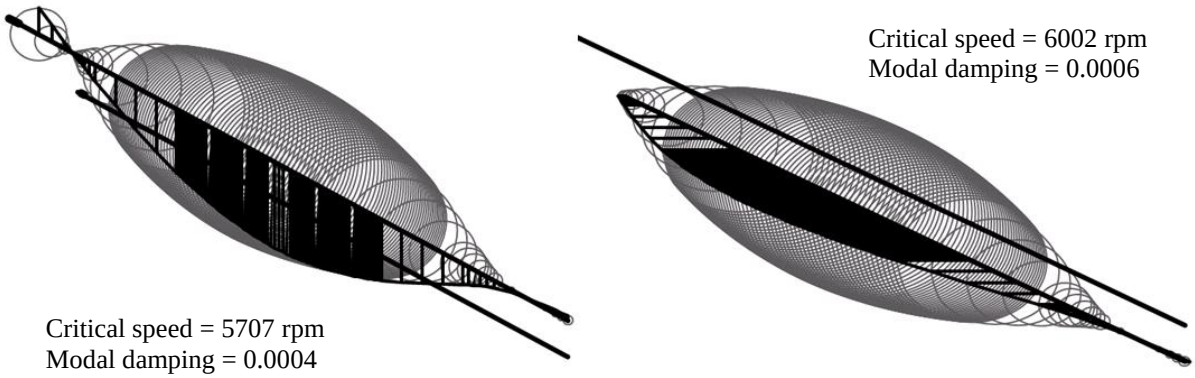

Figure 20 First two forward lateral mode shapes of the drive train

The coupling of the torsional and lateral dynamics adds a mode at a lower speed than the lateral dynamics alone as shown in Table 5. The torsional lateral first mode is at 3227 rpm, compared to 5707 rpm for the uncoupled lateral analysis. The coupled torsional lateral first mode shape is shown in Figure 21. The torsional part of the coupled mode is similar to the first uncoupled torsional mode shape (not shown) where the coupling and motor masses vibrate in an opposite direction to the rotors. The lateral part of the coupled mode on the other hand, is different from the first uncoupled lateral mode shape (shown in Figure 20). As evident in Figure 21 most of the energy of the mode goes to the gear section where the coupling between the lateral and torsional dynamics takes place. The rest of the modes are unaffected by the coupled dynamics.

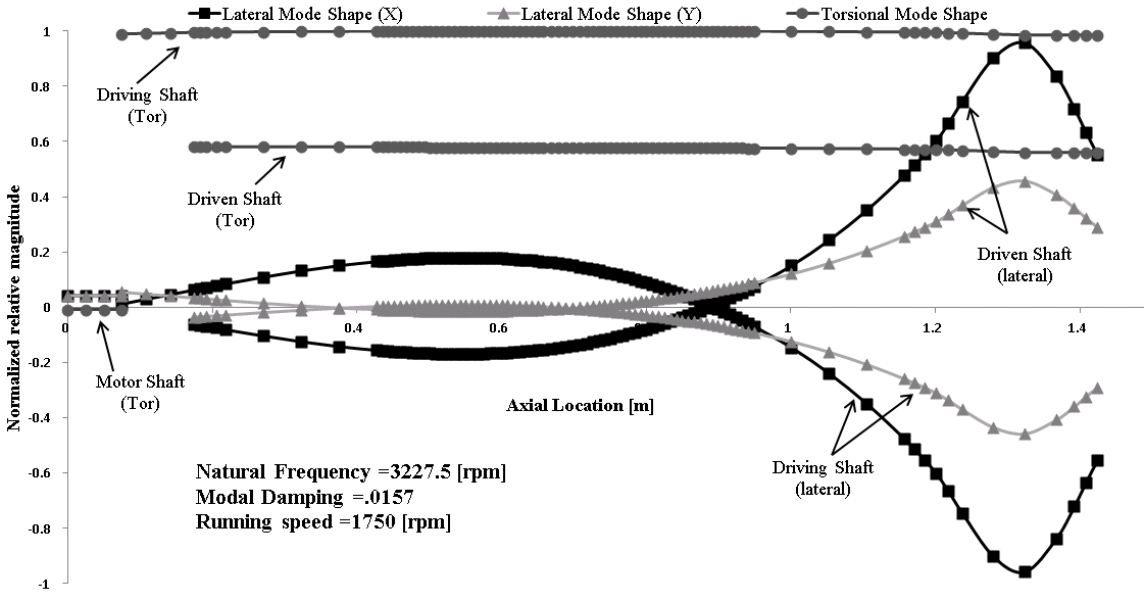

Figure 21 First forward torsional-lateral mode shape

For the analysis above, a soft coupling (1E4 N/rad) and a soft gear tooth (1E6 N/m) have been used to emphasize the effect of the vibration coupling and to stress that depending on the components and the design, the coupled dynamics might prove substantially different from the uncoupled. For the case at hand, the lowest mode that appeared due to the torsional lateral coupling is almost two times higher than the running speed at 1750 rpm. In other cases, the drop of the first critical coupled natural frequency could bring it closer to the running speed. Moreover, as will be discussed later, screw pumps are subjected to super-synchronous hydraulic harmonic forces. Therefore, accurate prediction of coupled critical speeds is required to avoid excitation near natural frequencies.

3. HYDRODYNAMIC FORCES IN TWIN-SCREW PUMPS

This chapter discusses the development of a hydraulic model of a twin-screw pump from a rotordynamic perspective. The dynamic pressure field around the screw as it rotates in a full revolution will be characterized to predict the resultant forces and response. The model rests on the steady state Eulerian hydrodynamic model first proposed by Vetter and Wincek [4] and later developed independently by Prang and Cooper [7]. Although the outcome of the analysis is a dynamic pressure of a transient nature (pressure field versus the rotor's rotational angle or time) the model is strictly steady state with results in the frequency domain.

The dynamic pressure characterization model is composed of the following three components: (1) The steady state hydraulic model that predicts the axial pressure distribution in the chambers and across the screw lands, (2) The model of the pressure buildup in the last chamber as it opens to the discharge, and (3) The extension of the axial pressure distribution to a pressure field around the screw and pressure field variation with respect to the rotational angle of the rotor. Section 3.1 introduces the adopted coordinate system and the geometry of the flow inside twin-screw pumps. Section 3.2 discusses the development of the steady state hydraulic model. The model for pressure buildup in the last chamber opening to discharge is addressed in section 3.3 Finally, the dynamic pressure model and the resulting dynamic forces are discussed in sections 3.5 and 3.6

3.1 Twin-screw pump geometry and coordinate system

Figure 22 defines the adopted coordinate system. The origin is taken at the center of the screw C_1 on the suction side. The X axis is in the direction of the line of centers $\overline{C_1C_2}$. The Y axis is perpendicular to it. The Z axis is along the axial direction of the screw section. θ is the polar coordinate measured from the line of centers counter clockwise. The mating of the two screws occurs at a line extending axially along the Z axis referred to as the *meshing-line*. The cross section shown in Figure 22 is at the discharge end at a screw section. The screw thread terminal edge shown on the cross section is the end of the screw thread profile. The angle between the line of centers and the screw thread terminal edge is referred to as the thread *terminal edge angle* and is denoted ϕ. The area outlined by the meshing of the two screws, the liner, and the screw thread terminal edge, is the area of the orifice opening to

discharge. The flow through the orifice opening to discharge and the pressure buildup in the last chamber are discussed in section 3.3

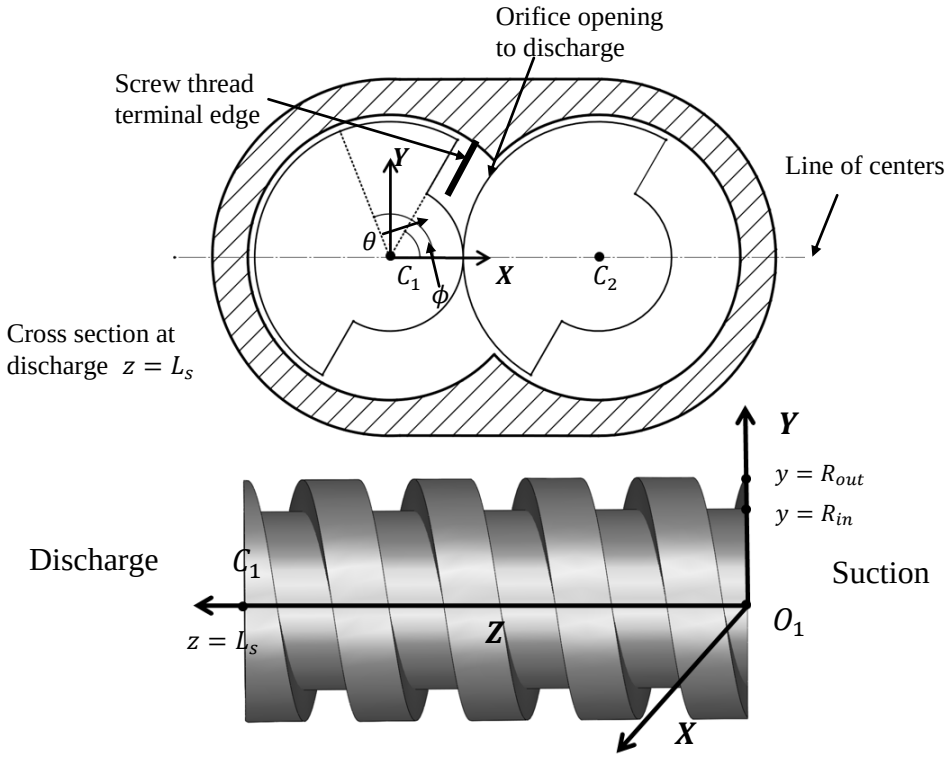

Figure 22 Coordinate system

The flow inside twin-screw pumps is complicated by the helix of the screw thread and the mating of the two screws together. However, correct visualization of the flow regions and the geometry of the pump is the key to follow the development of both the hydrodynamic and the dynamic force models.

Figure 2 introduced three types of clearances in twin-screw pump. The pressure distribution around the screws is affected by the pressure in the chambers and the pressure across the circumferential and radial clearances only. The flank clearance has no effect on the circumferential pressure distribution, and only a minor contribution to the chamber slip as validated by the experiment in [4].

Figure 23 shows a schematic of a single screw inside a pump liner. It highlights the region of the screw circumference bounded by the circumferential clearance and the region

bounded by the radial clearance. The two regions are separated by the liner edges. The angle between the liner edges is 2β. β is given by

$$\beta = \cos^{-1}\left(\frac{a}{2R_{out}}\right) \tag{11}$$

a is the distance between the centers of the two rotors given by

$$a = R_{out} + R_{in} + \delta_{rc} \tag{12}$$

R_{out} and R_{in} are the outer and inner radii of the screw. δ_{rc} is the nominal radial clearance as shown in the screw mating schematic in Figure 23.

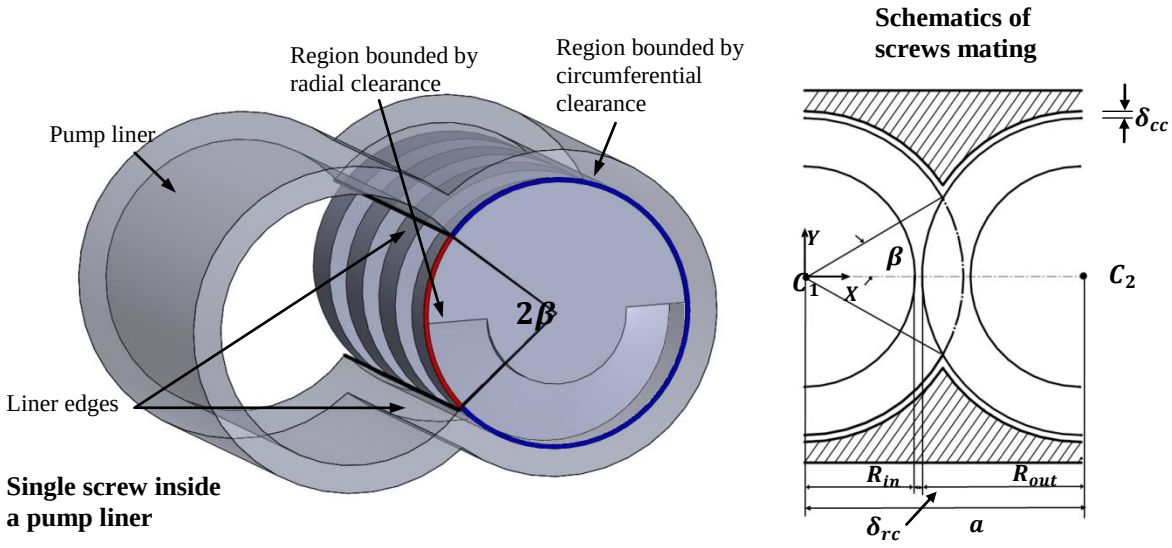

Figure 23 Circumferential and radial clearances regions and screws mating

Figure 24 shows the circumferential clearance flow region in 3D and unwrapped. The region is the volume between the screw land and the pump liner. The unwrapped geometry is the result of slicing the circumferential clearance flow region across the outer diameter of the screw. Axes Z and θ are the axial and polar coordinates respectively. The thickness of the region is the circumferential clearance nominal height δ_{cc}. The region width is the screw land width B given by Eq. (4). The circumferential clearance connects two adjacent chambers. The leakage from one chamber to the chamber upstream occurs through a cross section area A_{cc} and across the circumferential clearance width B. For concentric rotor A_{cc} is

$$A_{cc} = L_{cc}\delta_{cc} \tag{13}$$

L_{cc} is the circumferential clearance length given by

$$L_{cc} = 2(\pi - \beta)\sqrt{R_{out}^2 + \left(\frac{h}{2\pi}\right)^2} \tag{14}$$

h is the screw thread pitch. R_{out} is the outer radius of the screw. β is half the angle between the liner adeges defined in Eq. (11).

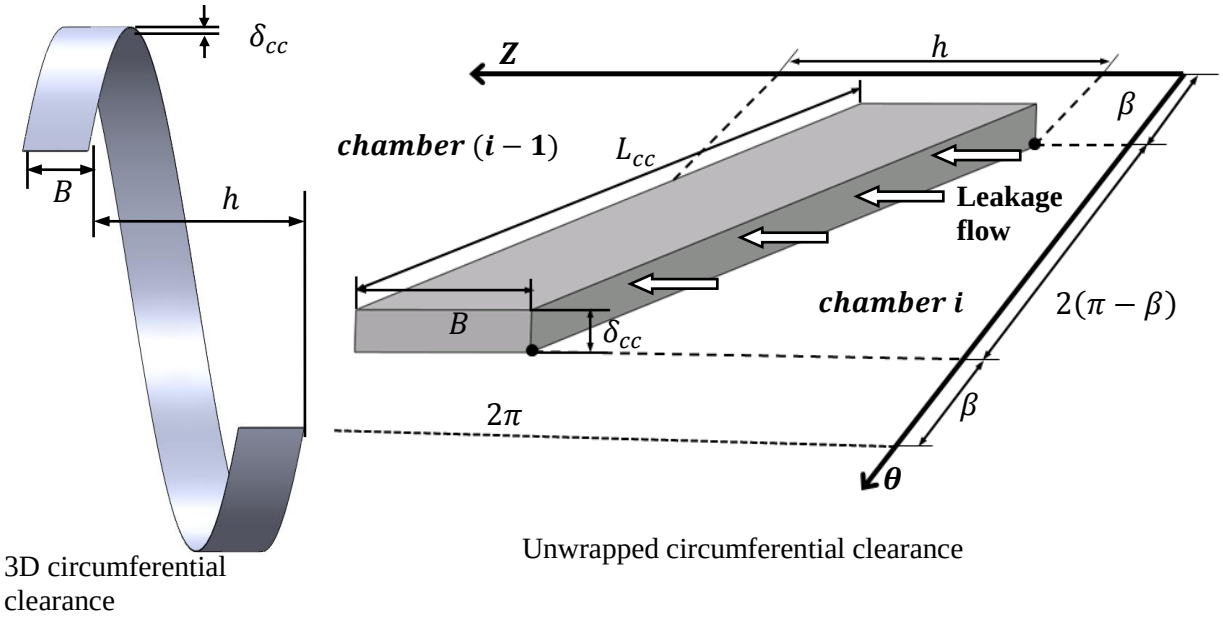

Figure 24 Circumferential clearance flow region

Figure 25 shows two meshing screws with the radial clearances between the outer and inner radii of the screws exaggerated for visualization. Planes A_1 and A_2 are parallel to the XY plane. The axial distance between the two planes is equal to the screw land width B. The half chamber shown in Figure 25 is the slice of the two screws between planes A_1 and A_2. The radial clearance is a line of length B at the contact between the outer radius of one screw and the inner radius of the other.

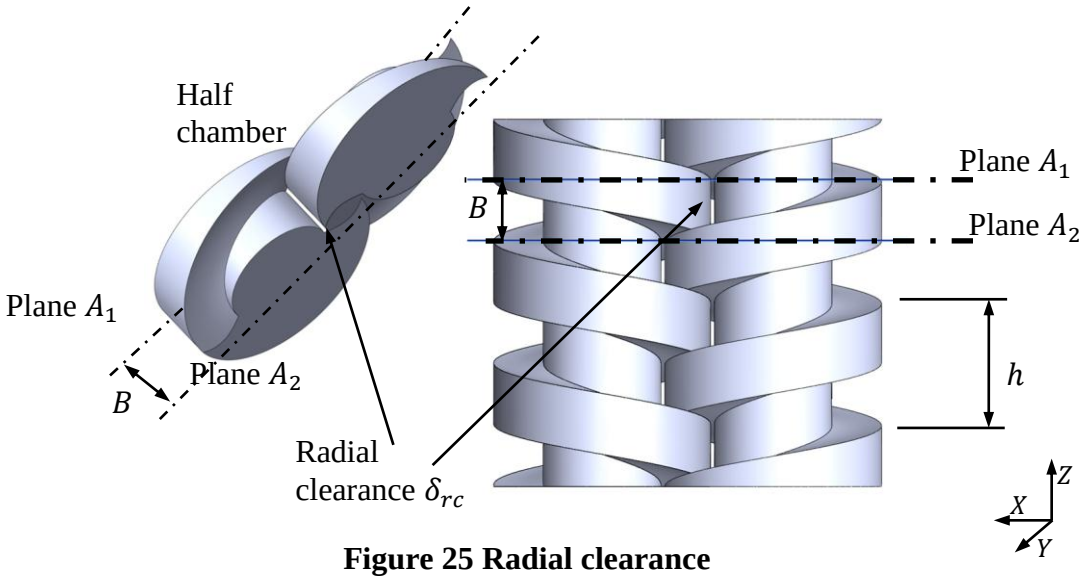

Figure 25 Radial clearance

The radial clearance flow region is the densely hatched area on the 2D schematic in Figure 26. The region is the volume created between the outer and inner radii of the screws; its width is B and its minimum thickness is δ_{rc} at the line of centers $\overline{C_1C_2}$ as shown in the 3D schematic in Figure 26.

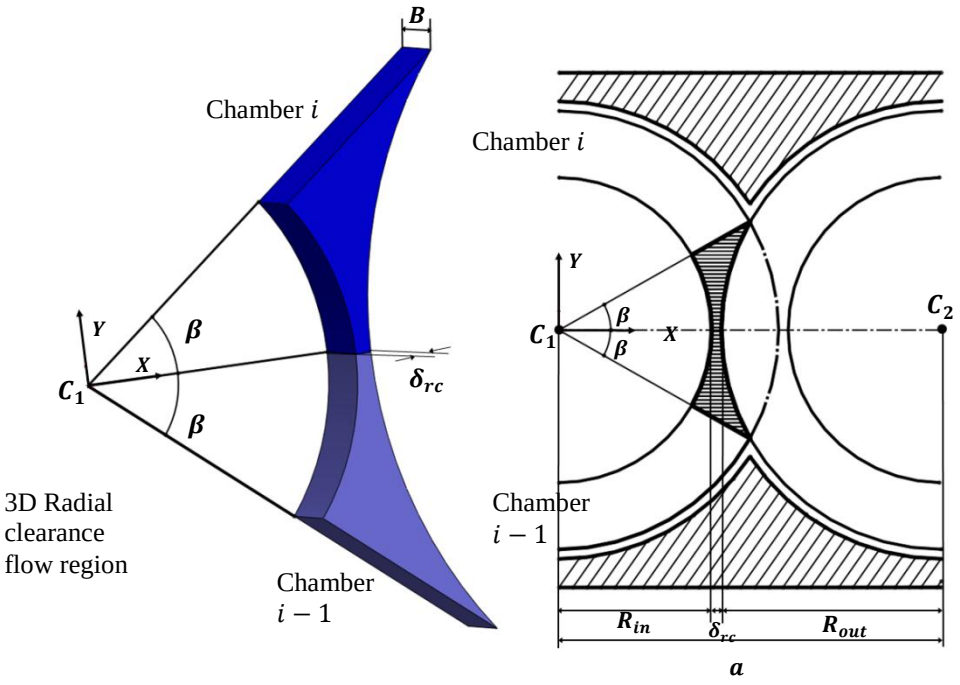

Figure 26 Radial clearance flow region

3.2 Steady state hydraulic model

The Eulerian hydraulic model of twin-screw pump [4,7] is a steady state model. It represents the pump as a series of disks moving continuously from suction to discharge as was shown previously in Figure 3. The pressure throughout each chamber is assumed constant. Each chamber is hydraulically connected to the chamber upstream and the chamber downstream by the circumferential clearance only. One end of the screw is subjected to the suction pressure while the other end is subjected to the discharge pressure.

The following is the list of the model assumptions:

(1) Fully-developed steady state flow.
(2) The flow in the clearances is only liquid phase.
(3) The axial leakage flow across the circumferential clearance is treated in a manner that is similar to annular-seal analysis.
(4) The total slip between two chambers through circumferential radial and flank clearances is estimated based on an empirical fraction of the axial leakage flow across the circumferential clearance to the chamber's total slip flow.
(5) The gas phase behaves ideally, and the compression is isothermal.
(6) The pressure throughout the chamber is constant.
(7) Constant pressure at suction (upstream of the screw section) and discharge (downstream of the screw section).

In the remainder of this section, the hydraulic model will be explained in details for both the single and multiphase cases. Some modifications have been made to the models from the literature in [4,7] and will be pointed out.

Chambers are numbered from 1 to n_{ch} as was introduced in Eq(5) . The axial velocity of the leakage flow across the circumferential clearance depends on the pressure difference between the two adjacent chambers, the friction across the circumferential clearance and the inlet pressure loss due to the sudden acceleration of the flow entering the clearance as given by [7]

$$Vcc_{lkg,i+1\to i} = \sqrt{\frac{P_{i+1} - P_i}{\frac{\rho_l}{2}(1+\xi) + \rho_l \frac{B}{\delta_{cc}} f_{cc}}} \tag{15}$$

P_{i+1} and P_i are the pressures in chambers $i+1$ and i. ρ_l is the density of the liquid phase. B is the length of the screw land as given by Eq. (4). δ_{cc} is the nominal circumferential clearance height. ξ is the entry loss coefficient. According to Childs [25] published values for ξ from measurements vary from 0 to 0.2. f_{cc} is the Fanning friction factor for the flow across the circumferential clearance.

Unlike Prang and Cooper [7] who used a Moody-based friction factor definition, a Blasius friction model [26] will be adopted here. The value of the friction factor for turbulent flow is dependent on the Reynolds number as given by

$$f_{cc} = n_{cc} R_e^{m_{cc}} \tag{16}$$

n_{cc} and m_{cc} are constants based on the surface roughness. R_e is the axial Reynolds number across the circumferential clearance given by

$$R_e = \frac{2Vcc_{lkg,i+1\rightarrow i}\delta_{cc}}{\nu} \tag{17}$$

ν is the kinematic viscosity of the liquid.

Since the friction factor is a function of Reynolds number and the Reynolds number is dependent on Vcc_{lkg}, the leakage-velocity calculation procedure is iterative. The flow chart of the algorithm of the procedure is shown in Figure 27. The procedure starts by assuming high value of the friction coefficient to calculate the leakage-velocity. The friction and leakage-velocity are iteratively calculated until the change in the leakage velocity value between two iterations falls below a desired percentage error.

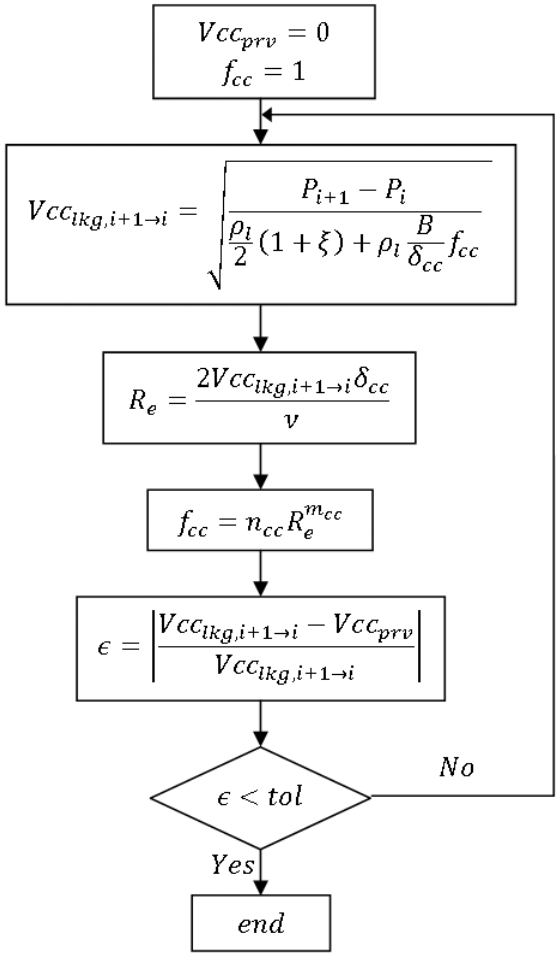

Figure 27 Iterative procedure for calculating axial-leakage velocity algorithm

Using Eq. (15) to describe the leakage velocity across the circumferential clearance discounts the effect of the coquette flow due to the screw rotation, and attributes the leakage to the pressure difference alone. A full annular-seal leakage model is outlined in Childs [25] based on axial and circumferential momentum equations in addition to continuity. He showed that for an initial circumferential velocity of the fluid entering the seal equals half the rotor surface velocity, the circumferential velocity of the fluid along the seal remains constant and generally has markedly less effect on the total leakage than the pressure driven flow, especially for a short seal (low length over diameter ratio). In the case of twin-screw pump, discounting the coquette flow effect is consistent with experimental data that show a slip flow that is independent of pump speed as discussed earlier in the literature survey.

The total slip flow rate from chamber $i + 1$ to the upstream chamber i is given by

$$Q_{slp,i+1\to i} = \frac{1}{f_t} \times Vcc_{lkg,i+1\to i} \times A_{cc} \tag{18}$$

f_t is the empirical fraction of the axial leakage flow through the circumferential clearance to the total slip between the two chambers through the flank, radial and circumferential clearances. According to [4], the estimated value of f_t from experiment is 0.8. Vcc_{lkg} is given by Eq. (15). A_{cc} is the leakage area of the circumferential clearance given by Eq. (13).

3.2.1 Single-phase screw pump hydrodynamic model

The single-phase hydrodynamic screw pump model is mainly an application of Eq. (18) to all screw chambers. Because the liquid phase is incompressible, the inflow to the chamber balances the outflow from the chamber as

$$Q_{slp,i+1\to i} = Q_{slp,i\to i-1} \tag{19}$$

Initially a linear pressure distribution in the chambers is assumed, then Eq. (18) is applied between each two adjacent chambers successively to calculate the in and out slip flow. The process continues iteratively with new calculated pressure buildup until Eq. (19) is satisfied for all chamber.

For a concentric rotor, the initial assumed linear chamber pressure distribution will satisfy Eq. (19). However, as discussed in the literature survey, the unbalanced circumferential pressure field around the screw creates hydraulic loading that deflects the rotor. The relative eccentricity of the rotor ε is the ratio of the static deflection e to the circumferential clearance nominal height δ_{cc} given by

$$\varepsilon(z) = \frac{e(z)}{\delta_{cc}} \tag{20}$$

e and ε depend on the axial position of the screw z since the static load creates a bent rotor profile as shown in Figure 28. The details for predicting the hydraulic forces and the resulting static deflection will be discussed in section 3.6

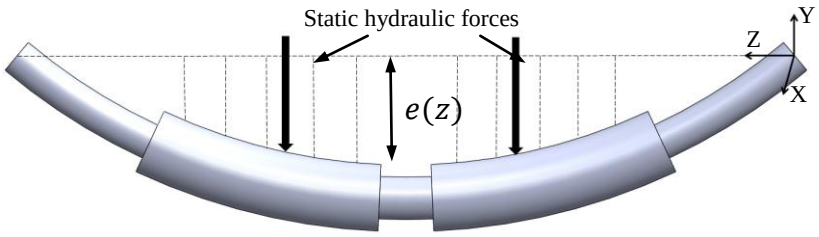

Figure 28 Bent screw rotor profile

To show the strong dependence of the axial leakage flow across the circumferential clearance Qcc_{lkg} on the nominal clearance height δ_{cc}, Prang and Cooper [7] approximated Qcc_{lkg} for laminar conditions by the Poiseuille flow equation between two parallel plates as in

$$Qcc_{lkg,i+1\to i} = \frac{(P_{i+1} - P_i)L_{cc}\delta_{cc}^3}{12\nu\rho B} \tag{21}$$

Tao and Donovan [27] conducted an experimental study and developed an analytical model for the flow in an eccentric narrow annulus with rotating and stationary boundaries. Vetter and Wincek [4] adopted their model to quantify the increase in the axial circumferential leakage flow due to rotor eccentricity.

Figure 29 is a schematic representation of the circumferential clearance annulus in the case of centric and eccentric rotor. The inner circle represents the screw and the outer circle represents the pump liner. The nominal circumferential clearance δ_{cc} and static deflection e are exaggerated for visualization.

$Qcc_{lkg,\varepsilon}$ is axial leakage flow through the circumferential clearance in the case of eccentric rotor. r_ε is the ratio of the eccentric to the centric circumferential leakage defined by

$$r_\varepsilon = \frac{Qcc_{lkg,\varepsilon}}{Qcc_{lkg}} \tag{22}$$

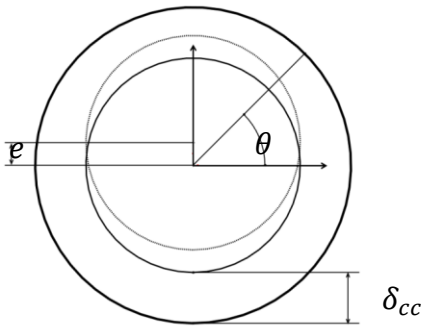

Figure 29 Schematic of eccentric annular flow across circumferential clearance

For laminar flow r_ε is given by [27]

$$r_\varepsilon = 1 + \frac{3}{2}\varepsilon^2 \tag{23}$$

For turbulent flow

$$r_\varepsilon = \frac{1}{\pi}\int_0^\pi (1 + \varepsilon\, cos\theta)^{\frac{3}{2-n_e}} d\theta \tag{24}$$

ε is the eccentricity as defined by Eq. (20). n_e is a factor related to the surface finish. n_e is equal to 0.25 and 0 for smooth and rough conditions, respectively. θ is the polar coordinate shown in Figure 29. The variation of r_ε with ε is shown in Figure 30.

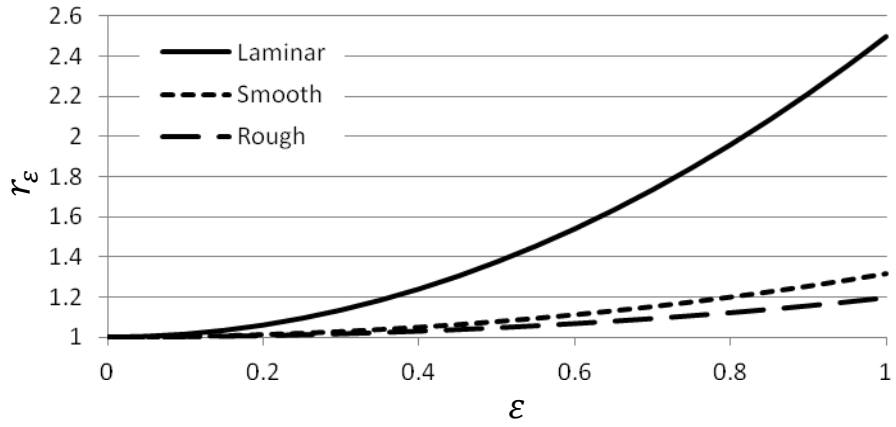

Figure 30 The increase in an annular-seal axial leakage flow due to eccentricity [27]

The CFD study in appendix B validates the applicability of the model in [27] to the circumferential clearance in twin-screw pumps.

3.2.2 Multi-phase screw pump hydrodynamic model

The multiphase hydrodynamic screw pump model accounts for the gas compression in the chambers. However, the slip flow is still modeled by Eq. (18) due to the liquid-filled clearances assumption.

Figure 31 is similar to the disc model of a screw pump with three chambers in addition to suction and discharge. $\forall_{L,s}, \forall_{L,d}$ are the liquid volume at the chambers open to suction and discharge respectively. $\forall_{L,i}$ is the liquid volume in the i^{th} chamber. Similarly for the gas volumes $\forall_{G,s}, \forall_{G,d}, \forall_{G,i}$

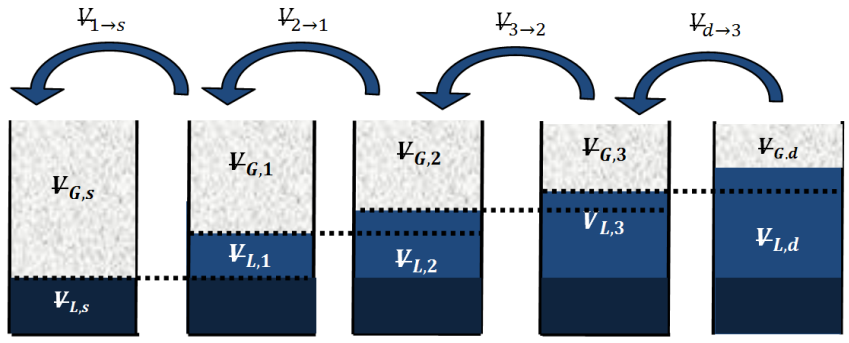

Figure 31 Gas phase compression in the chambers

Rabiger [5] defines the chamber life time as the time period for the fluid in the chamber to be transported by one chamber position closer to the discharge given by

$$\Delta t_{life} = \frac{2\pi}{N\omega} \tag{25}$$

N is the number of threads and ω is the rotational speed in rad/sec.

The liquid slip volume from one chamber to the chamber upstream over the period of chamber life time Δt_{life} is

$$\forall_{L,i+1\to i} = \Delta t_{life} \times Q_{slp,i+1\to i} \tag{26}$$

The volume occupied by liquid in the chamber just closing from the suction side can be found from the inflow Gas Volume Fraction (GVF) by

$$\forall_{L,s} = (1 - GVF) \times \forall_u \tag{27}$$

$\forall_u$ is the chamber volume given by

$$\forall_u = BA_r\left(D_{out}^2 - D_{in}^2\right) \tag{28}$$

The terms of Eq. (28) were defined earlier in Eq. (3) of Q_{th}.

As the chambers move axially from suction to discharge, their liquid level builds up. Because liquids are incompressible, the difference between the slip inflow from the chamber downstream and the slip outflow to the chamber upstream is the only source of the rise in the liquid level in the chamber. The increase in the chamber's liquid volume is balanced by the reduction in its gas volume due to the compressibility of the gas phase.

Because of the ideal gas and isothermal compression assumptions the gas volume in two chambers is related to their pressures by the ideal gas law

$$P_i = \forall_{g,i+1} \times \frac{P_{i+1}}{\forall_{g,i}} \tag{29}$$

P_i, and P_{i+1} are the pressures in chambers i and $(i+1)$. $\forall_{g,i}$ and $V_{g,i+1}$ are the volumes occupied by the gas in chambers i and $(i+1)$. The volume occupied by the gas and the volume occupied by the liquid add up to the chamber volume

$$\forall_u = \forall_{g,i} + \forall_{L,i} \tag{30}$$

Initially, the pressure in all chambers is assumed to be suction pressure, and the volume of the liquid in all chambers is assumed $\forall_{L,s}$ from Eq. (27). Starting from the discharge side, the liquid volume in each chamber is updated according to Eq. (26). The corresponding gas volume in the chambers is given by Eq. (30). The chamber pressure is updated from the ideal gas Eq. (29). The final chamber pressure distribution is used as the initial guess for the next iteration. The process concludes when the maximum difference in chamber pressures between two iterations falls below a desired tolerance. The flow chart of the algorithm is shown in Figure 32.

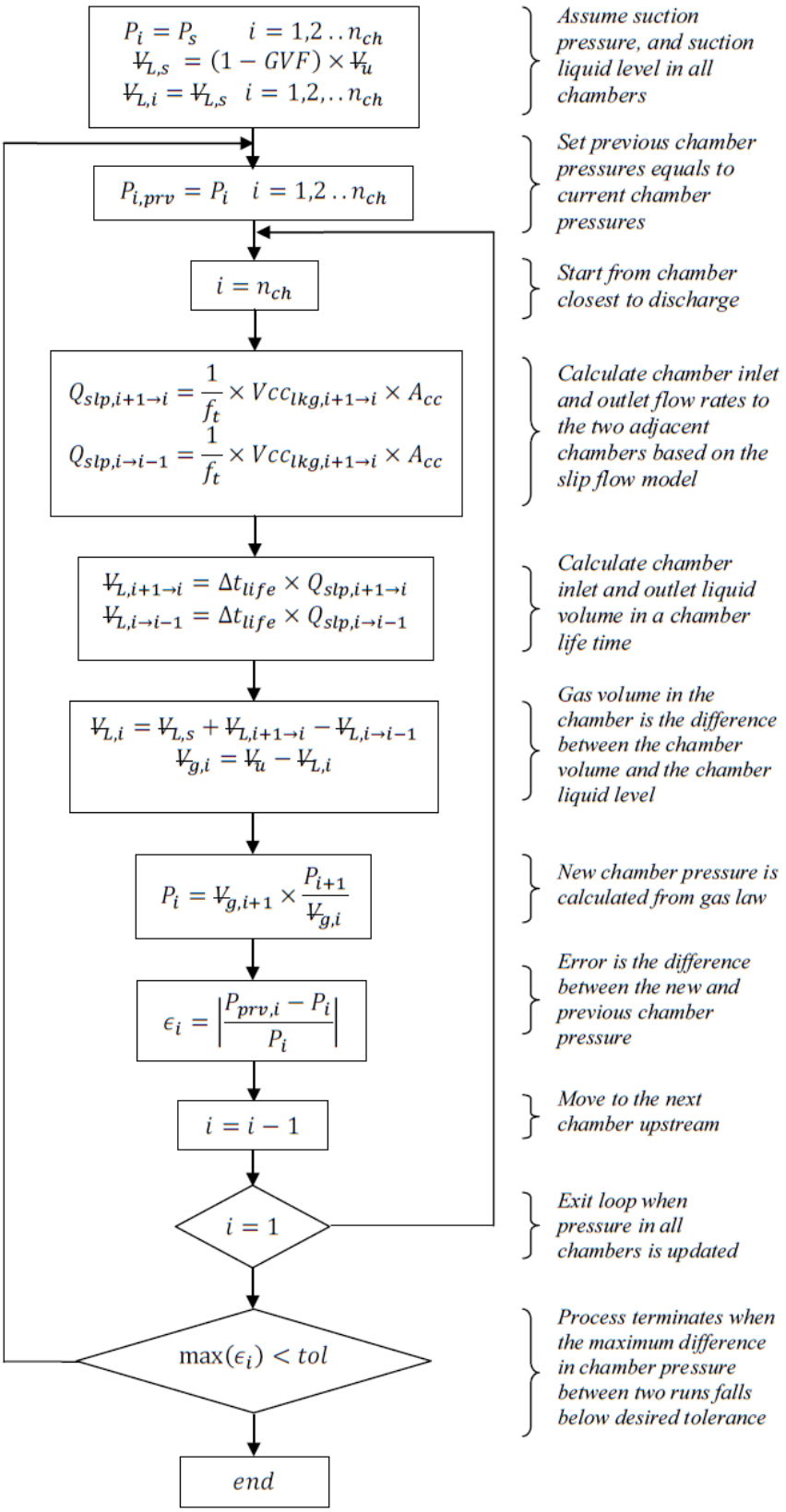

Figure 32 Twin-screw pump multiphase chamber pressure algorithm [28]

3.2.3 Steady state multiphase model validation against published results

To validate the model developed, the predictions in [21] were reproduced for 75%, 50%, and 25% GVF. The comparison between the developed model and test results is shown in Figure 33. The physical properties of the double threaded twin-screw pump tested by Vetter et. al in [21] is shown in Table 6. The shift from a close-to-linear pressure buildup in the case of 25% GVF to a parabolic curve in the case of 75% GVF is evident.

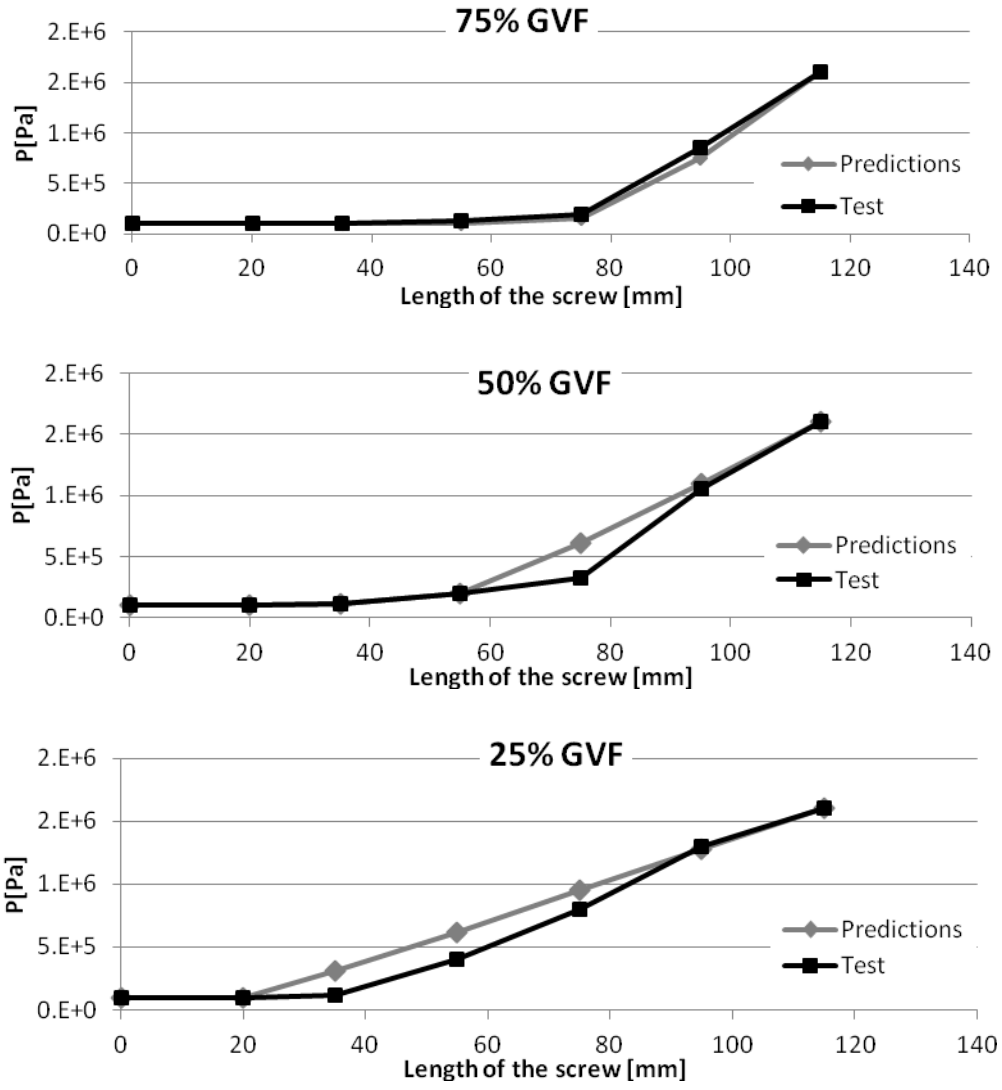

Figure 33 Axial pressure buildup (test results from Vetter et al. [21])

Table 6 Pump properties from Vetter et al. [21]

Screw outer diameter (D)	100 mm
Screw inner diameter (d)	70 mm
Screw pitch (h)	50 mm
Screw length (L_s)	120 mm
Number of threads (N)	2
Number of chambers	3.347
Circumferential Clearance height (δ_{cc})	187.5 [μm]
Nominal speed (Ω)	3000 rpm

3.2.4 Axial pressure distribution

The assumptions listed at the beginning of the section 3.2 state that the pressure in the chambers is taken to be constant, and the flow across the circumferential clearance can be modeled similar to an annular seal. Based on these two assumptions, the one-dimensional axial pressure buildup across the screw length will have a shape similar to the schematic shown in Figure 34.

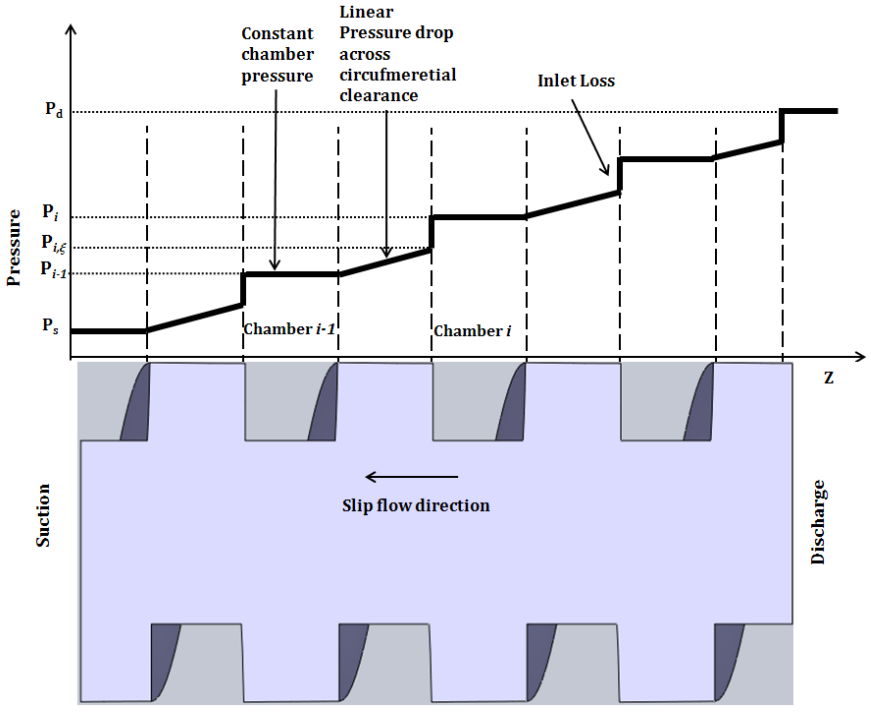

Figure 34 One dimensional axial pressure buildup

Eq. (15) included the term $\frac{\rho_l}{2}(1+\xi)$ to account for the effect of the inlet pressure loss due to the sudden acceleration of the flow through the tight circumferential clearance. The magnitude of the pressure drop due to the liquid acceleration is given by Bernoulli conservation of energy equation for incompressible flow

$$P_{i,\xi} = P_i - \frac{1}{2}\rho_l(1+\xi)Vcc_{lkg}^2 \tag{31}$$

P_i is the pressure in the chamber. $P_{i,\xi}$ is the pressure at the entrance of the circumferential clearance. ρ_l is the density of the liquid in. Vcc_{lkg} is the axial leakage flow through the circumferential clearance given by Eq. (15). ξ is the entry loss empirical coefficient ranging from 0 to 0.5 based on measurements [25].

3.2.5 Radial clearance pressure distribution model

The geometry of the radial clearance was discussed in section 3.1 Figure 26 showed that the flow region across the radial clearance is similar to the flow between two discs of radii R_{in} and R_{out} and thickness B, where R_{in} and R_{out} are the inner and outer radii of the screw, and B is the screw land width. In this subsection, a model is developed to describe the pressure distribution across the radial clearance.

Figure 35 shows a schematic of the flow in the radial clearance region. The center of rotor 1 is at C_1 rotating at ω_1, and the center of rotor 2 is at C_2 rotating at ω_2 where $\omega_1 = -\omega_2$. The X and Y axes were defined in section 3.1 The origin is taken at the center of rotor 1 at C_1. Line $\overline{Y_1Y_2}$ is the perpendicular line passing through the midpoint of the radial clearance δ_{rc}. The flow region is outlined by points B_1, B_2, B_3, B_4 where $\overline{B_1B_2}$ and $\overline{B_3B_4}$ are the horizontal lines passing through the intersection of lines $\overline{C_1B_0}$ and $\overline{C_1B_5}$ with $\overline{Y_1Y_2}$. The region is bounded axially (in the direction normal to the plane) by the walls of the screw of rotor 1 and extends for an axial length equals to the width of the screw land B.

The control volume (CV) is the hatched region defined by points P_1, P_2, P_3, P_4 and shown in 3D on top. The CV is enclosed between the arcs of the two rotors and the two horizontal lines $\overline{P_1P_2}$ and $\overline{P_3P_4}$. The lines are separated vertically by a small displacement Δy. The vertical distance from point Y_1 to the midpoint between the two horizontal lines is denoted y, and is the single spatial parameter that defines the location and dimensions of the CV. y varies between $[0, \overline{Y_1Y_2}]$.

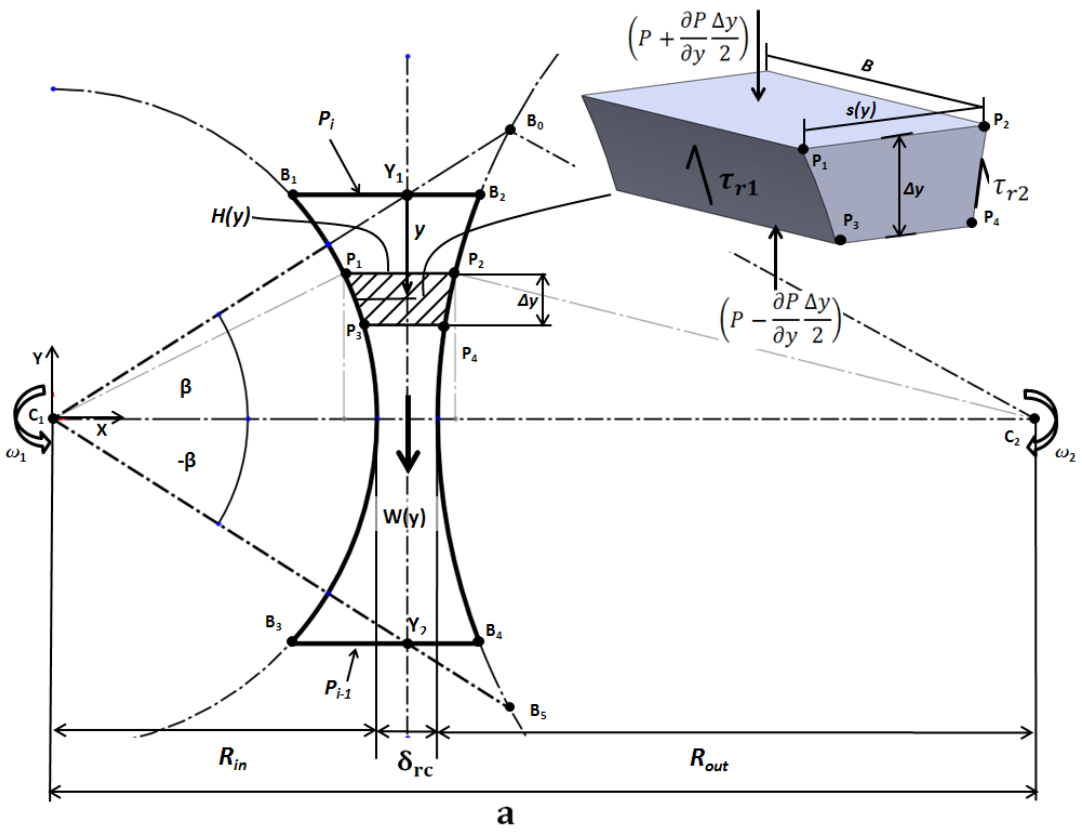

Figure 35 Radial clearance flow region (δ_{rc} exaggerated)

The clearance between the two rotors is denoted H and is a function of y

$$H(y) = a - \left(\sqrt{R_{out}^2 - (Y_1 - y)^2} + \sqrt{R_{in}^2 - (Y_1 - y)^2}\right) \tag{32}$$

Figure 36 shows the variation of H with y for the pump in [21] .The properties and dimensions of the pump were given earlier in Table 6.

H varies between maximum of $H(0) = 12\ [mm]$ at $y = 0$ corresponding to an angle $\beta = 31.6^o$ to minimum of $H(Y_1) = \delta_{rc} = 105[\mu m]$ at $y = Y_1$. With $\beta = 31.6$, the radial clearance covers 17.5% of the circumference of the screw.

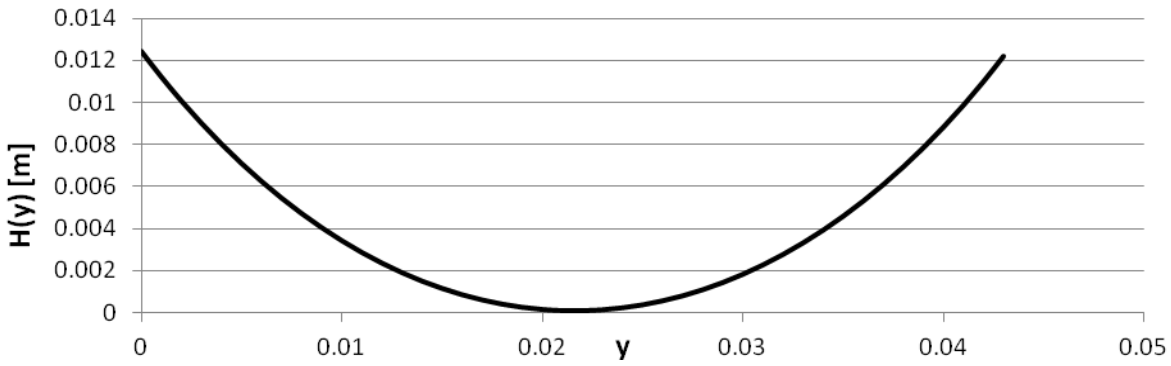

Figure 36 Distance between the outer and inner screw radii for the pump in [21]

The development of the model for the steady state pressure distribution across the radial clearance is based on Childs' zeroth order solution [29].

The radial clearance separates two chambers. Since the pressure in the chambers is assumed constant, the boundary conditions to the model are defined as the pressure of chamber i (P_i) on line $\overline{B_1B_2}$ and the pressure of the chamber $i-1$ (P_{i-1}) on line $\overline{B_3B_4}$ in Figure 35. The radial flow is assumed turbulent and is represented by a single bulk flow velocity $W(y)$ in the vertical direction. Applying the momentum equation from Reynolds transport theorem gives the expression of the pressure gradient with respect to y

$$\frac{dP}{dy} = \frac{-1}{H}\left[\rho\left(\frac{dH}{dy}W^2 + 2WH\frac{dW}{dy}\right) + \left(\tau_{R_{in}y} + \tau_{R_{out}y}\right)\right] \tag{33}$$

The bulk flow velocity derivative is evaluated from the continuity

$$\frac{dW}{dy}H + \frac{dH}{dy}W = 0 \tag{34}$$

The shear stress $\tau_{R_{in}y}, \tau_{R_{out}y}$ is defined from Hirs bulk flow model [25] as

$$\tau_{R_{in}y} = \frac{\rho_l f_{R_{in}} W_{R_{in}}^2}{2}, \qquad \tau_{R_{out}y} = \frac{\rho_l f_{R_{out}} W_{R_{out}}^2}{2} \tag{35}$$

ρ_l is the density of the liquid. The bulk velocities relative to the wall are

$$\begin{aligned} W_{R_{in}} &= W\frac{\sqrt{R_{in}^2 - (Y_1 - y)^2}}{R_{in}} + R_{in}\omega \\ W_{R_{out}} &= W\frac{\sqrt{R_{out}^2 - (Y_1 - y)^2}}{R_{out}} + R_{out}\omega \end{aligned} \tag{36}$$

The surface velocities of the rotor and screw are in the opposite direction to the bulk velocity W; hence the plus sign in Eq (36). Blaisus friction model [25] is used for $f_{R_{in}}$ and $f_{R_{out}}$.

$$f_{R_{in}} = n_{R_{in}} \left(\frac{2\rho_l H W_{R_{in}}}{\mu} \right)^{m_{R_{in}}}, \qquad f_{R_{out}} = n_{R_{out}} \left(\frac{2\rho_l H W_{R_{out}}}{\mu} \right)^{m_{R_{out}}} \tag{37}$$

$n_{R_{in}}, m_{R_{in}}, n_{R_{out}}, m_{R_{out}}$ are empirical constants related to the surface finish of the screw and rotors For smooth conditions $n_{R_{in}} = n_{R_{out}} = 0.08,$ and $m_{R_{in}} = m_{R_{out}} = -0.25.$

3.2.6 Radial clearance pressure distribution validation

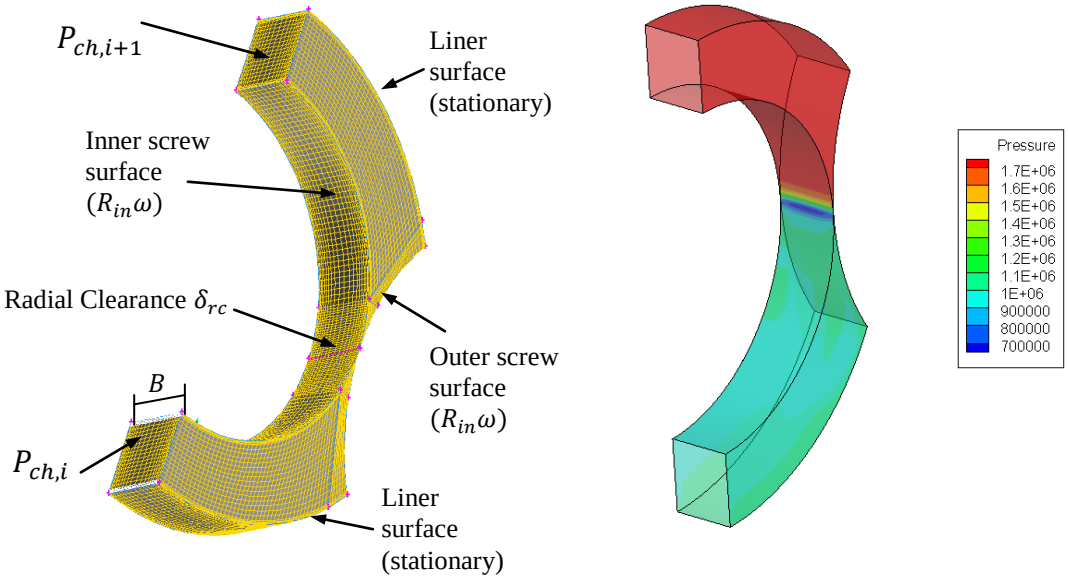

Figure 37 CFD Analysis of flow across circumferential clearance

The model in the previous subsection was validated against a Computational Fluid Dynamics (CFD) model of radial clearance flow. The CFD mesh and 3D pressure profile are shown in Figure 37. Similar to the model explained above, the radial clearance flow is modeled as a flow through two discs of radii R_{out} and R_{in} equal to the outer and inner radii of the screw respectively. The tips of the disks are separated by a tight gap equals to the nominal radial clearance δ_{rc}. The geometry is for one clearance of Vetter's pump introduced earlier in Table 6. The pressures of the chambers are set as boundary conditions on the

surfaces shown in Figure 37 (17.5, 10 bars). The figure also specifies the rotating and stationary surfaces and their speeds. The 3D pressure distribution in Figure 37 shows constant pressures in the chambers. The pressure drops as the fluid is squeezed through the clearance to a level below the pressure in the chamber downstream and then increases as the fluid expands.

Figure 38 shows a comparison between the CFD and the bulk-flow model predicted pressure profile across the $\overline{Y_1Y_2}$ line passing through the midpoint of the radial clearance. The line was shown schematically in Figure 35. The model used smooth friction coefficients. Running speed is 3000 rpm. The fluid is water. The minimum pressure occurred upstream of the minimum radial clearance by a distance equals to $4.4\delta_{rc}$ in the case of CFD and $2.41\delta_{rc}$ in the model. The model predicted leakage 5% less than the CFD leakage. The minimum pressure value was 6.41 bar, and 5.6 bar for the CFD and model, respectively. The dashed vertical lines in Figure 38 highlight the fraction of the profile affected by the pressure drop across the radial clearance. The rest of the profile is subjected to the chamber pressure.

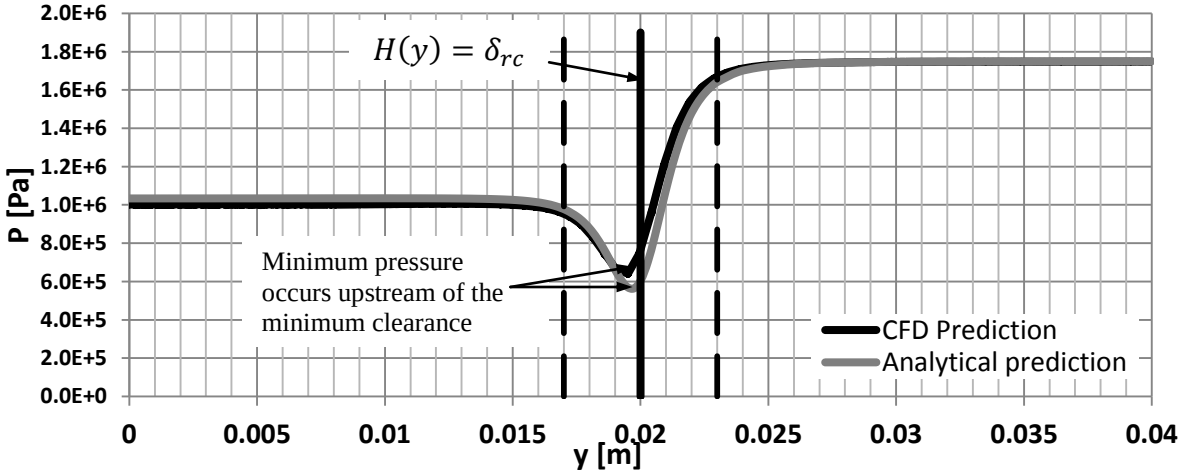

Figure 38 Predicted CFD versus analytical model pressure profile in the radial clearance

3.3 Discharge chamber

The process of opening the last chamber to discharge and communicating with the pressure downstream is a transient hydraulic process. While the development of the screw

pump rotordynamic model in this work is strictly for steady state operation, the characterization of the bulk pressure variation in the last chamber as it opens to the discharge is essential to describe the steady state pressure distribution around the screws as a function of the screw rotor's rotational angle.

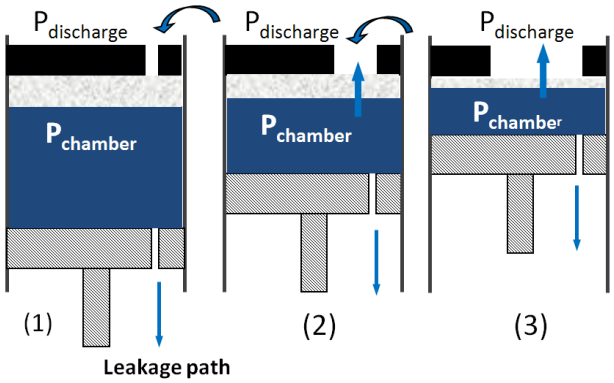

Figure 39 Conceptual model of the process of opening the last chamber to discharge

The exposure of the last chamber to the discharge pressure can be conceptually modeled as a positive displacement piston pushing a liquid-gas mixture against the discharge pressure through an orifice that is opening with the movement of the piston as shown in Figure 39. The solid model of two meshing screws inside a liner in Figure 40 is helpful to visualize the link between the piston action in Figure 39 and screws' rotation inside the twin-screw pump. The orifice is the area open to discharge and outlined by the screw thread terminal edge, the meshing-line with the other screw and the pump liner. As the screw rotates, the area of the orifice increases, and the volume of the last chamber decreases, giving rise to the positive displacement action. The leakage path shown in Figure 39 is the slip flow from the last chamber to the chamber upstream of it through circumferential, radial and flank clearances.

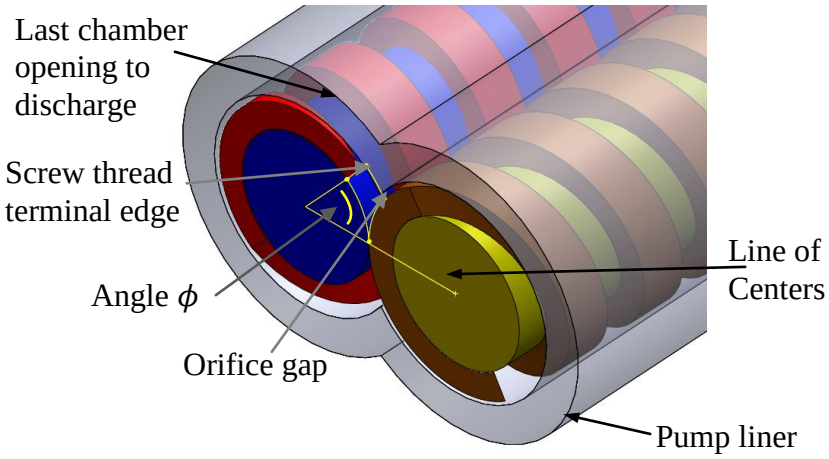

Figure 40 Meshing screws inside the liner

At the moment before the orifice opens, the pressure in the last chamber is lower than the discharge pressure. Once the orifice starts to open, liquid from higher pressure at the discharge side flows to the lower pressure in the chamber. The fluid accumulates in the chamber and pressure increases until equilibrium between the last chamber and discharge pressures is established. Finally, the chamber pressure remains equal to the discharge pressure, while the liquid-gas mixture in the chamber is pushed to the exit at a rate equals to the reduction in the chamber volume.

Manring in [30] developed a model for a process similar to the one described above for the axial-piston swash-plate hydrostatic pump. As with a twin-screw pump, the axial piston swash-plate pump is positive displacement and is characterized by an intermittent piston opening to discharge through an orifice that is changing in area. The objective in [30] was to find the instantaneous pressure in the piston chamber as a function of the rotation of the driving rotor to identify the ripples in the flow. A model similar to Marning's is adopted here to predict the instantaneous pressure in the last chamber in twin-screw pump as it opens to the discharge.

Eq. (38) captures the flow balance of the discharge chamber and relates it to the rate of pressure buildup through the effective bulk modulus of the fluid-gas mixture $\acute{\kappa}$.

$$\frac{dP(\phi)_d}{d\phi} = \frac{30}{\pi\omega}\frac{\acute{\kappa}}{\cancel{V}_{n_{ch}}(\phi)}\left(Q(\phi)_{orifice,d} - Q(\phi)_{(slp,d\to n_{ch})} + \frac{d\cancel{V}_d(\phi)}{d\phi}\right) \qquad (38)$$

P_d is the instantaneous pressure in the discharge chamber. ω is the rotational speed of the rotor in rpm. ϕ is the thread terminal edge angle defined in section 3.1 . $Q_{(slp,d\rightarrow n_{ch})}$ is the slip flow from the last chamber to the chamber upstream as given by Eq. (18). $\not{V}_d$ is the instantaneous volume of the discharge chamber. The effective bulk modulus of elasticity $\acute{\kappa}$ accounts for the presence of gas as given in [31]. $Q_{orifice,d}$ is the flow through the orifice opening to discharge.

The volume of the discharge chamber $\not{V}_d$ is a function of the thread terminal edge angle as in

$$\not{V}_d(\phi) = \not{V}_u - B\phi R_{in}(R_{out} - R_{in}) \tag{39}$$

$\not{V}_u$ is the chamber volume given by Eq. (28). B is the screw land width given by Eq. (4). R_{out} and R_{in} are the outer and inner screw diameters respectively.

The flow through the orifice $Q_{orifice,d}$ is modeled by the orifice equation given by

$$Q(\phi)_{orifice,d} = C_d A(\phi)_{orifice}\sqrt{\frac{2}{\rho_l}|P_{dis} - P(\phi)_d|} \tag{40}$$

P_{dis} is the discharge pressure at the pump outlet downstream from the discharge chamber. This outlet pressure is assumed constant. $P(\phi)_d$ is the instantaneous pressure in the discharge chamber. C_d is the coefficient of discharge associated with the orifice geometry. The instantaneous orifice area $A(\phi)_{orifice}$ is a function of ϕ (the shaded area in Figure 41) and is given by

$$\begin{aligned} A(\phi)_{orifice} &= \int_0^{\phi} s(\theta)d\theta \qquad && \phi \le \beta \\ A(\phi)_{orifice} &= A(\beta)_{orifice} + (\phi - \beta)(R_{out}^2 - R_{in}^2) \qquad && \phi > \beta \end{aligned} \tag{41}$$

R_{out} and R_{in} are the outer and inner radii of the screw. β is half the angle between the liner edges given by Eq. (11). $s(\theta)$ is the radial length between the inner radius of the screw opening to discharge and the tip of the other screw as shown in Figure 41. $s(\theta)$ is given by

$$s(\theta) = \frac{R_{out} \times \sin(\zeta)}{\sin(\theta)} - R_{in} \qquad \theta \neq 0$$
$$s(\theta) = \delta_{rc} \qquad \theta = 0 \tag{42}$$
$$\zeta = \pi - \theta - \sin^{-1}\left(\frac{a \times \sin(\theta)}{R_{out}}\right)$$

δ_{rc} is the radial clearance nominal height. ζ is the angle corresponding to θ on the other screw as shown in Figure 41. a is the distance between the centers of the two screws given by Eq. (12).

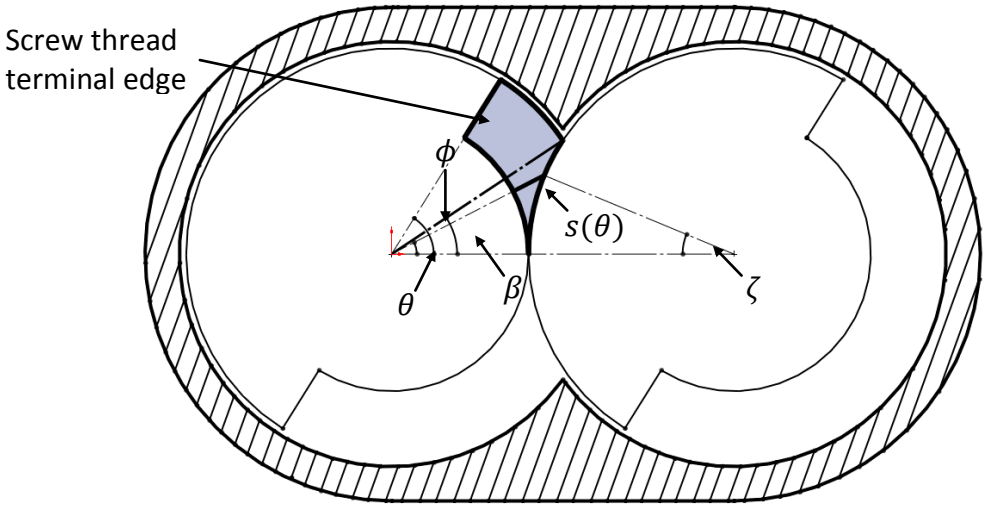

Figure 41 Orifice area

The coefficient of discharge (C_d) in Eq. (40) is an empirical constant that reduces the flow rate through an orifice below the maximum theoretical pressure-driven flow rate from Bernoulli due to the hydrodynamic losses. Rearranging Eq. (40) gives

$$C_d = \frac{Q(\phi)_{orifice}}{A_{orifice}\sqrt{\frac{2\Delta P}{\rho}}} \tag{43}$$

To find the coefficient of discharge, the actual orifice flow was estimated by a CFD analysis. Figure 42 is the velocity field of the fluid path from discharge to the last chamber only; no other parts of the pump were simulated. Pressure boundary conditions were set on the discharge and chamber sides, the model solves for the mass flow rate across the orifice. The calculated average value of C_d over a range of ϕ and differential pressures ΔP was 0.67.

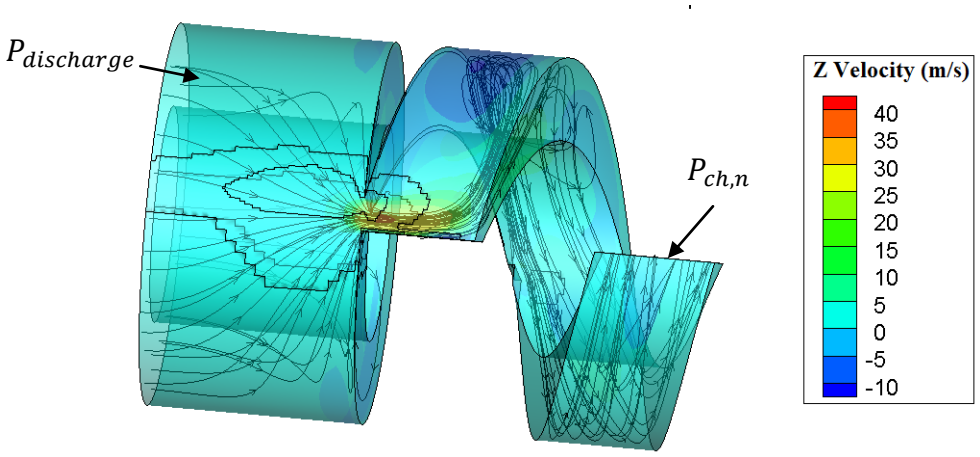

Figure 42 CFD velocity field of the flow through the gap opening to discharge

The predicted pressure buildup in the last chamber based on the model described by Eq. (38) for Vetter's pump in [21] (for 75% GVF) is shown in Figure 43.

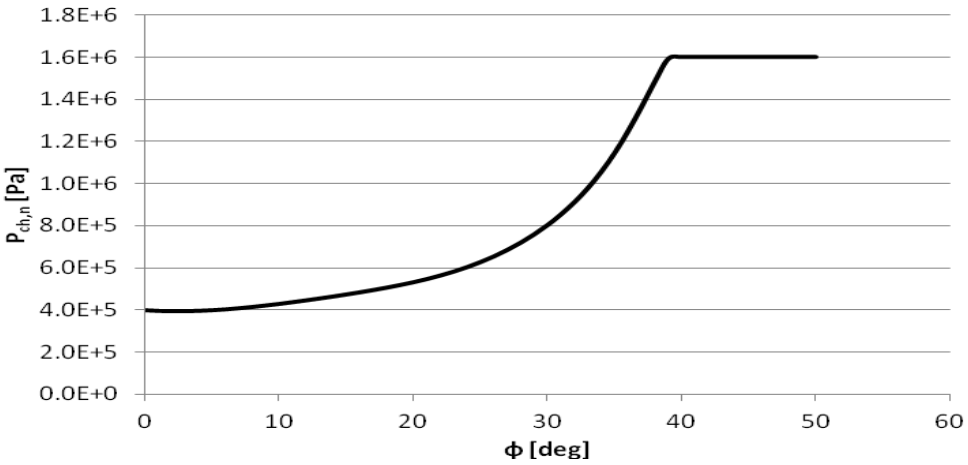

Figure 43 Prediction of discharge chamber pressure build up (75% GVF case in [21])

3.3.1 Multiphase flow through discharge orifice

The dynamic pressure measurements reported by Vetter et al. [21] in Figure 11 showed a spike of the pressure in the last chamber over the discharge pressure. This spike is best understood in the framework of transient hydraulics of multiphase flow. Tullis [32] explains that an air pocket passing through an orifice in a multiphase flow, causes a transient pressure rise. The difference in densities between the gas pocket and liquid phase results in an acceleration of the flow as the gas pocket passes the orifice and a sudden deceleration as

the liquid passes. The sudden reduction in velocity causes a pressure head. Martino et. al [33] ran a number of tests and compared their results favorably with the simplified model in Eq. (44) that predicts the maximum head rise ΔH_{max} in meters.

$$\Delta H_{max} = \left(\frac{c}{g}\right)\left(C_g\sqrt{\frac{2gH_o\rho_l}{\rho_g}\left(\frac{P_{atm}}{P_o}\right)^2 ln\left(\frac{P_o}{P_{atm}}\right)D_{o/p}^2}\right) \quad (44)$$

H_o is the absolute static pressure head at the orifice. P_o is the absolute critical air pressure at the discharge and P_{atm} is the absolute atmospheric pressure. C_g is the coefficient of discharge for the gas. $D_{o/p}$ is the ratio of the orifice to pipe diameter. ρ_g and ρ_l are the gas and liquid densities respectively. c is the water hammer celerity in the medium, and g is the acceleration of gravity. The pressure oscillation associated with the pressure spike is divided into a low frequency mild phase during the air release and a sudden pressure rise with water hammer characteristics when the liquid column reaches the orifice. Equation (44) is based on the classical water hammer equation, $\Delta H = \left(\frac{c}{g}\right)\Delta V$. ΔV is the velocity head. The second term in Eq. (44) is an estimation of the velocity head of the liquid column before going through the orifice. This relation is used to match the maximum pressure of the experimental results. Like other transient hydraulic phenomena, the only way to correctly estimate the uncertainties and empirical coefficients $(C_g, D_{o/p})$ is by extensive experimental investigation in the range of operation.

3.4 Suction chamber

Similar to the discharge chamber, a buildup of pressure takes place in the chamber closest to suction. While pressure at the pump discharge downstream from the screw section (P_{dis}) is controlled by the discharge valve only, the pressure at the suction upstream of the screw section (P_{suc}) is dependent on the piping, fittings, and flow velocity upstream of the pump. Chapter 3 in [34] discusses the flow conditions at twin-screw pump suction. Installations of twin-screw pump loops vary. Some installations include a booster pump at the suction to raise the fluid to the twin-screw pump suction level in case the pump suction is elevated, or overcome long suction pipe lines. Other installations depend on the screw pump's suction vacuum. As a positive displacement machine, a twin-screw pump develops

its suction abilities from moving the fluid to discharge, allowing room for fluid to be admitted to the suction side and into the screw chambers.

The schematic in Figure 44 is for a general loop of a twin-screw pump sucking fluid from a tank open to atmosphere without a booster pump. This type of loop is common in twin-screw pump applications. *Suction Lift* (SL) is the vacuum created by the twin-screw pump in the case of suction pressure below atmospheric. The majority of screw-pumps operate with suction lift of 1.7E4 Pa to 5E4 Pa. SL of 8.45E4 Pa is not uncommon [34]. The *Net Positive Suction Head Available* (NPSHA) is the absolute pressure head at the pump inlet. The NPSHA is calculated by summing up the head losses and gains upstream of the pump inlet. Losses include elevation, friction in the piping and hydraulic losses in the pipe fittings. The gage pressure at the pump suction upstream of the screw section P_{suc} is given by

$$P_{suc} = \rho g\left(\Sigma Elevation\ head - \Sigma Friction\ head - H_{tv} - H_{pv}\right) \quad (45)$$

The elevation head is the height of the liquid from an arbitrary datum. The friction head is the head loss due to the friction in the pipes and the fittings. It can be estimated using the Fanning or Darcy-Weisbach models. The tank velocity head H_{tv} is the flow rate over the area of the pipe. The pump velocity head H_{pv} is the pressure head loss due to the acceleration imparted on the fluid as it enters the pump suction. It can be estimated from the axial speed of the fluid inside the pump given by

$$H_{pv} = \frac{\rho}{2g}\left(N\frac{h\omega}{2\pi}\right)^2 \quad (46)$$

h is the screw thread pitch. ω is the pump running speed. N is the number of threads. g is the gravity acceleration. In a revolution the screw pushes the fluid an axial distance equal to the number of threads multiplied by the pitch length closer to the discharge. The various types of head losses (and gains) of a twin-screw pump suction are marked schematically in Figure 44 from an arbitrary datum.

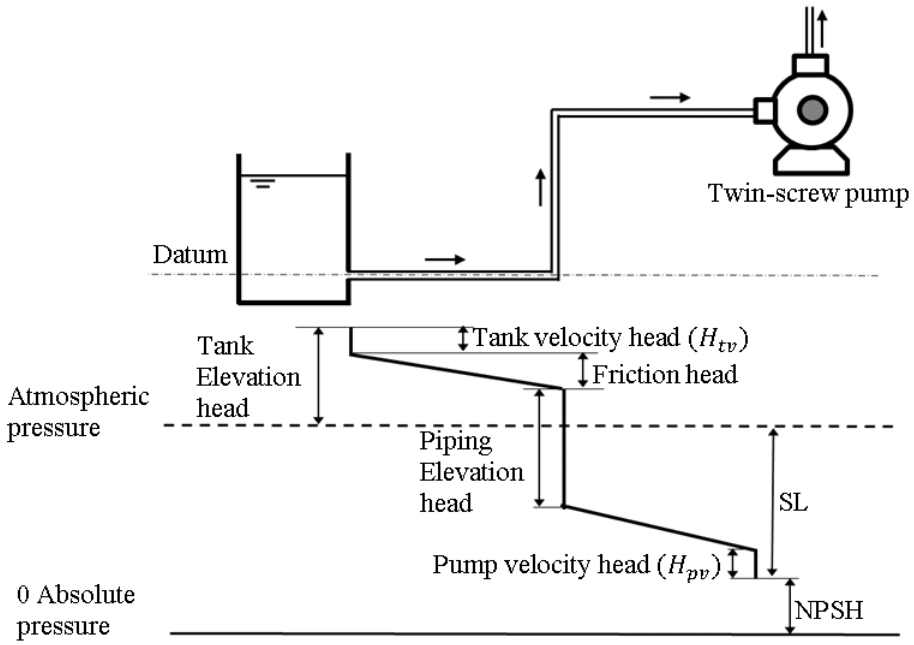

Figure 44 Relationship of hydraulic gradient, NPSH, and SL [34]

The sequence of the suction pressure buildup process is the opposite of the sequence of the process of discharge chamber pressure buildup shown in Figure 39. It can be described by an equation similar to Eq. (38) as in

$$\frac{dP(\phi)_s}{d\phi} = \frac{30}{\pi\omega}\frac{\acute{\kappa}}{V_s(\phi)}\left(Q(\phi)_{orifice,s} + Q(\phi)_{(slp,1\rightarrow s)} - \frac{dV_s(\phi)}{d\phi}\right) \tag{47}$$

The rotation of the screws causes the suction chamber to increase in volume, and the orifice between the suction chamber and the pump inlet to increase in area. The increase in the suction chamber volume creates a low pressure zone that draws flow from the higher pressure zones at the pump inlet and at the chamber downstream (chamber number 1). The flow from the pump inlet is through the orifice opening to suction. The flow from chamber 1 downstream is the slip flow through flank, radial and circumferential clearances. The orifice flow from the pump suction is given by an equation similar to Eq. (40) as in

$$Q(\phi)_{orifice,s} = C_d A(\phi)_{orifice}\sqrt{\frac{2}{\rho_f}|P_{suc} - P(\phi)_s|} \tag{48}$$

P_{suc} is the pressure at the pump inlet upstream of the screw section. P_{suc} is assumed constant and can be estimated from the pump suction loop as in Eq. (45). $A(\phi)_{orifice}$ is the same as

the in the case of discharge given by Eq (41). The coefficient of discharge C_d is given by Eq. (43), where the actual flow rate through the orifice is estimated by CFD similar to the discharge conditions.

The process of opening the first chamber to suction described by Eq. (47) helps in showing the effect of the slip flow from the first chamber to the suction chamber on reducing the pump's inlet flow rate below the pump's theoretical flow rate as given by Eq. (5). The slip flow from the first chamber competes with the inlet flow in filling the suction chamber causing a reduction in the pump volumetric efficiency.

The discharge chamber model in section 3.3 and the suction chamber model in this section provide the "boundary" values for the steady state model developed in section 3.3 . For each thread terminal edge angle ϕ, the pressures in the chambers opening to discharge, and the chamber opening to suction can be determined from Eq. (38) and Eq. (47) respectively. These pressure values are used to iteratively solve for the pressures in the chambers according to the algorithm in the flow chart in Figure 32. The pressure across the circumferential clearances is taken to drop linearly according to the annular seal model and the pressure across the radial clearances is described by the model in subsection 453.2.5 . The next section will discuss the extension of the axial distribution to a 2-dimensional pressure field around the screws, which can be later used to predict the dynamic forces acting on the rotors as will be discussed in section 3.6 .

3.5 Dynamic pressure field in screw pump

So far, the model treats the screw pump in one dimension. Each chamber is represented by a single one-dimensional constant pressure zone. To calculate a two-dimensional pressure field around the rotor, the helical screw geometry has to be considered.

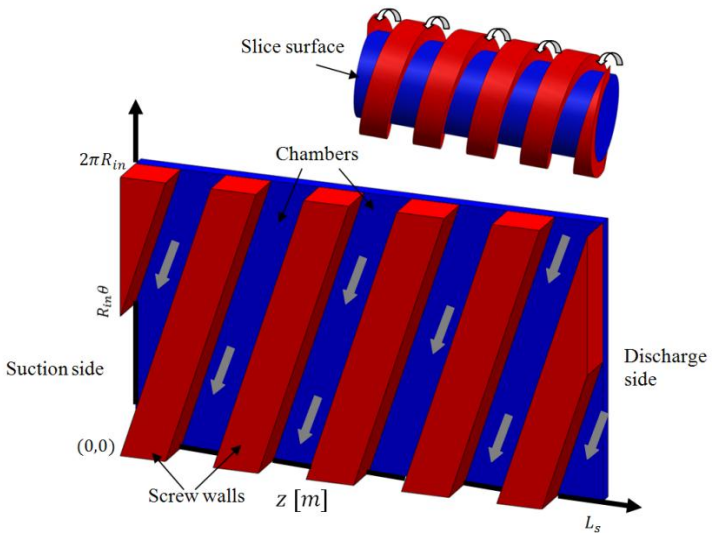

Figure 45 Unwrapped screw geometry

Figure 45 shows a solid model of a single screw (top) and an isometric view of an unwrapped screw (bottom). The unwrapped geometry is obtained by slicing the screw across the inner screw radius surface, so it can be unfolded and laid on a plane. Because the slicing is at the surface outlined by the inner screw radius, the walls of the helical screw threads project out of plane as 3D parallelograms. The horizontal axis Z is along the axial direction of the screw. The vertical axis denoted by coordinate $R_{in}\theta$ is along the polar circumference of the rotor as defined previously in section 3.1 . Coordinates 0 and $2\pi r$ on the vertical axis of the unwrapped geometry correspond to the same point on the screw. The arrows in Figure 45 illustrate that for a single screw not meshed with another screw, the discharge and suction sides are hydraulically connected. If liquid is pumped from the discharge side of a single screw, it will flow to the suction side without obstruction. It is the meshing of the two screws together that creates separate pressure zones (called chambers) and allow for the pressure buildup along the axial direction. The flow across the radial clearance at the meshing-line between the two screws was discussed in details in a previous section.

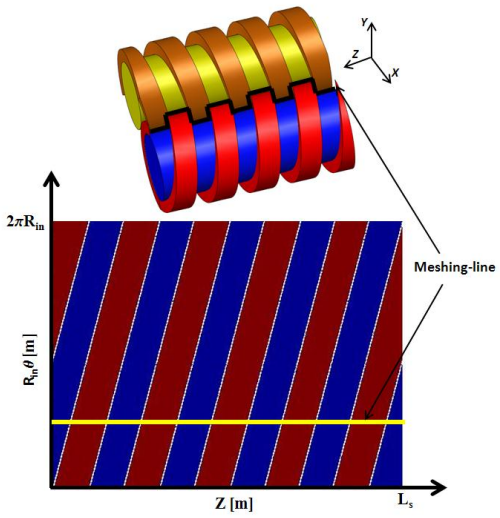

Figure 46 Meshing-line **projection on the unwrapped screw geometry**

Figure 46 shows the projection of the meshing-line on the 2D unwrapped geometry. The meshing-line plays a major role in the axial pressure build up and the pressure field distribution around the screws. A stationary observer will see a spinning rotor and a fixed meshing-line passing through the radial clearances between the screws. For an observer spinning with the rotor, the situation is reversed, the rotor is stationary and the meshing-line is spinning around the rotor circumference. Therefore, the rotation of the screw can be represented on the two dimensional unwrapped geometry by advancing the meshing-line on the vertical $R_{in}\theta$ axis.

Figure 47 is helpful to visualize the role of the meshing-line in screw rotation. The pictures on the left side are screen shots of a double-thread screw inside a pump with three marbles trapped in a chamber. The marbles emphasize the axial motion resulting from the rotation of the screws. The pictures on the right are the representation of the axial motion on the two dimensional unwrapped geometry. For an observer spinning with the rotor, the marbles are trapped between the two walls of the screws and the meshing-line, the rotor is stationary while the meshing-line is revolving around the rotor's circumference. In that scenario, it is the motion of the meshing-line around the circumference of the rotor that forces the marbles to move forward as illustrated on the 2D geometry in Figure 47.

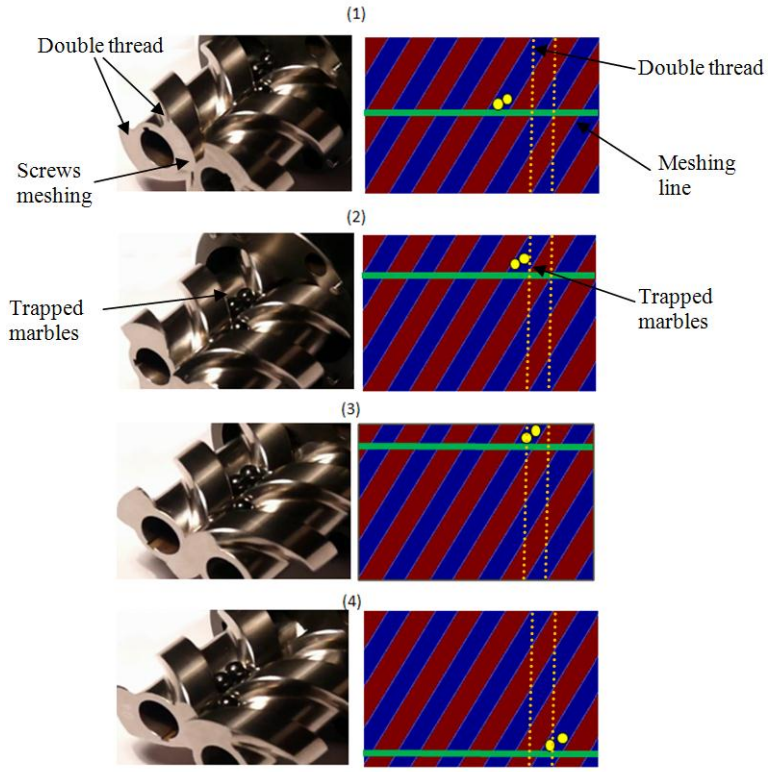

Figure 47 Screw rotation represented on the unwrapped geometry by advancing the meshing-line

Simulating the screw rotation by advancing the meshing-line across the screw circumference is equivalent to keeping the thread terminal edge angle ϕ fixed in space and rotating the reference frame. In Figure 48 C_1 and C_2 are the centers of the two screws. X, Y is the stationary reference frame (as was shown in Figure 22), x', y' is the rotating reference frame. The rotation of the x', y' frame is achieved by keeping screw 1 fixed in space and rotating the center of screw 2 (C_2) across a circle of radius $\overline{C_1C_2}$. The x' axis points in the direction of line $\overline{C_1C_2}$ as it rotates through the 360^0. The y'axis is perpendicular to x'. The *rotating* meshing-line *angle* (θ_m) is the angle between the rotating x' axis and the stationary X axis. The corresponding thread terminal edge angle (ϕ) is the angle between the x' axis and the terminal edge of screw 1 thread. Figure 48 shows two θ_m positions. In the first position, the rotating frame x', y' is aligned with the stationary frame X, Y and $\theta_{m,1} = 0$. In the second position, the x', y' has rotated an angle $\theta_{m,2} = 20^o$

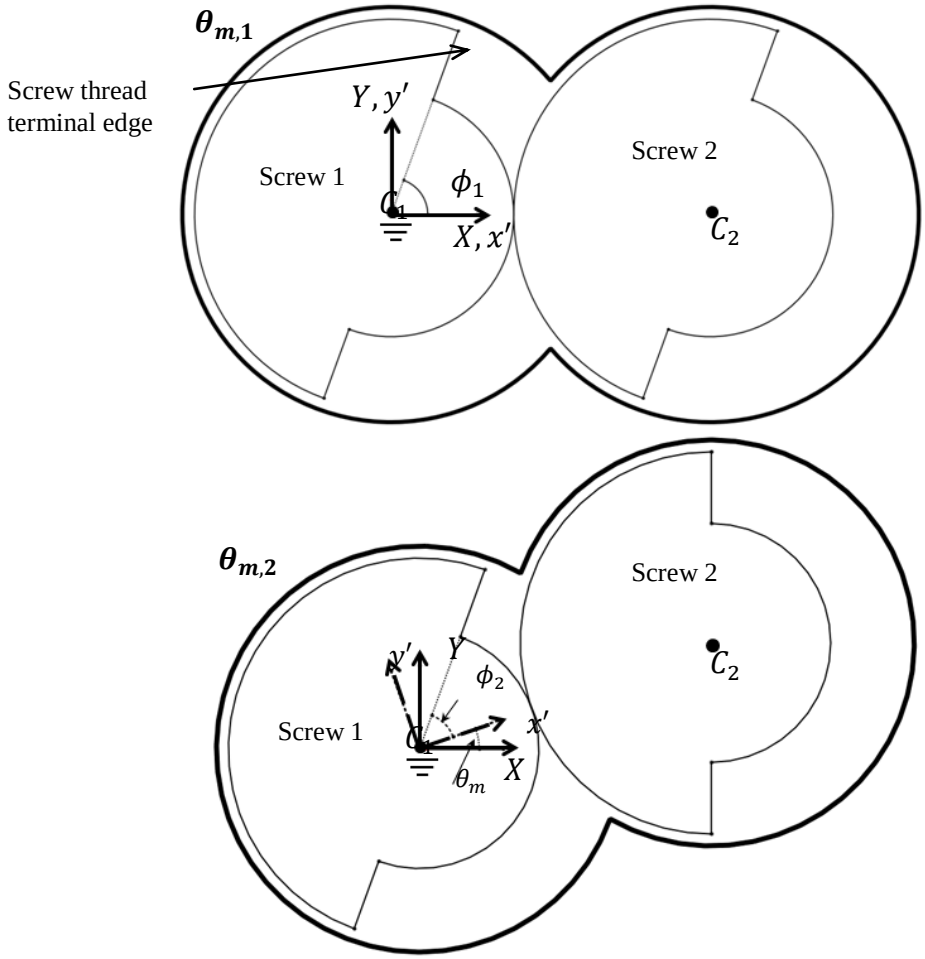

Figure 48 Rotating reference frame and *rotating* meshing-line ***angle*** $\boldsymbol{\theta_m}$

Having introduced the unwrapped 2D geometry of the screws, and the concept of advancing the meshing-line to represent the spinning of the rotor, revisiting the process of opening the last chamber to discharge is helpful to explain its sequence in the light of the new geometrical insights.

Figure 49 is a conceptual representation of the process of opening the last chamber to discharge in a single-thread screw pump on the unwrapped 2D geometry. At position (1), the last chamber (number 5) is completely open to discharge, and its volume is almost equal to the volume of the other chambers. The pressure in the chamber at this position equals to the discharge pressure. Chamber 4 is completely sealed from the discharge. In position (2), chamber 5 volume is reduced, and the trapped liquid is displaced to the discharge giving rise to the positive displacement action of twin-screw pumps. Chamber 4 is still completely

sealed and its volume is unchanged. In position (3), chamber 5 is further reduced in size, while chamber 4 is on the threshold of opening to the discharge. Finally, in position (4), chamber 5's size is further reduced, while chamber 4 starts to open to the discharge through an orifice created between the meshing-line and the screw thread terminal edge. Fluid flows from the high pressure discharge side to the lower pressure in chamber 4. As a result, the pressure in chamber 4 starts to rise until meshing-line reaches the point of position 1 again, and the process is repeated

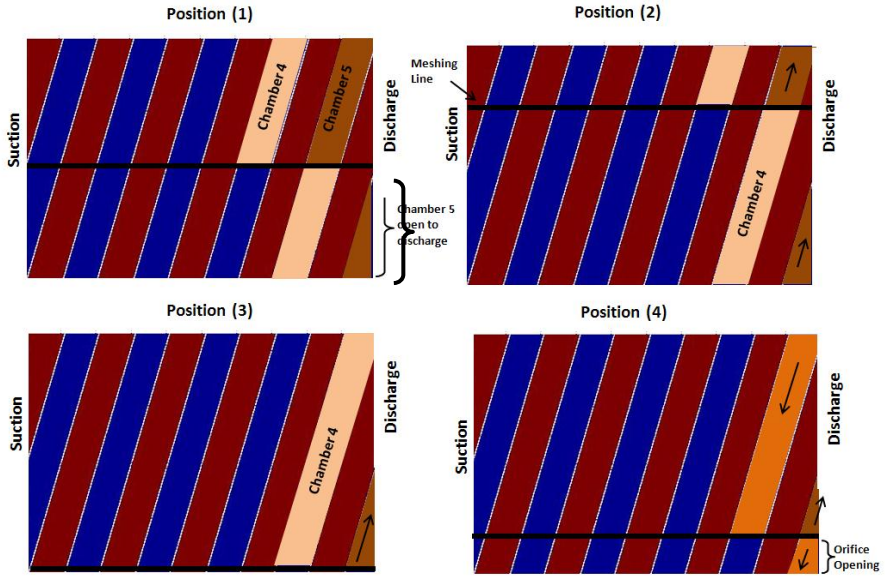

Figure 49 The sequence of chamber opening to discharge represented

3.5.1 Discretization of the unwrapped screw geometry

For the purpose of book-keeping, the unwrapped geometry is discretized into small rectangular elements in a two-dimensional mesh. The number of the rectangular elements is N_z in the axial direction and N_θ in the circumferential direction. A schematic of the mesh is shown in Figure 50. The horizontal and vertical axes are the indices of the rectangular elements in the axial and circumferential directions respectively. One screw thread is shown for illustration.

The length of the rectangular element in axial direction is δz given by

$$\delta z = \frac{L_s}{N_z} \tag{49}$$

L_s is the length of the screw section. N_z is the number of the rectangular elements in the axial direction .

The axial position of the i^{th} rectangular element is given by

$$z_i = i\ \delta z \qquad\qquad i = 1,2, \dots \dots N_z \tag{50}$$

The circumferential position of the j^{th} rectangular element is given by

$$\theta_j = k\ \frac{2\pi}{N_\theta} \qquad\qquad j = 1,2, \dots \dots N_\theta \tag{51}$$

While N_z is chosen arbitrarily for the desired mesh refine, N_θ is calculated to account for the inclination of the screw thread such that the screw thread edges lie on the edge of a rectangular element as highlighted by the black dots in Figure 50. N_θ is given by

$$N_\theta = \text{integer}\left(\frac{h}{\delta z}\right) \tag{52}$$

δs is the length of the rectangular element in the circumferential direction given by

$$\begin{aligned} \delta s &= \frac{2\pi R_{in}}{N_\theta} && \text{For an element in chamber} \\ \delta s &= \frac{2\pi R_{out}}{N_\theta} && \text{For an element on screw land} \end{aligned} \tag{53}$$

R_{out} and R_{in} are the outer and inner radii of the screw. The screw land is the surface area of the screw thread separated from the pump liner by the circumferential clearance.

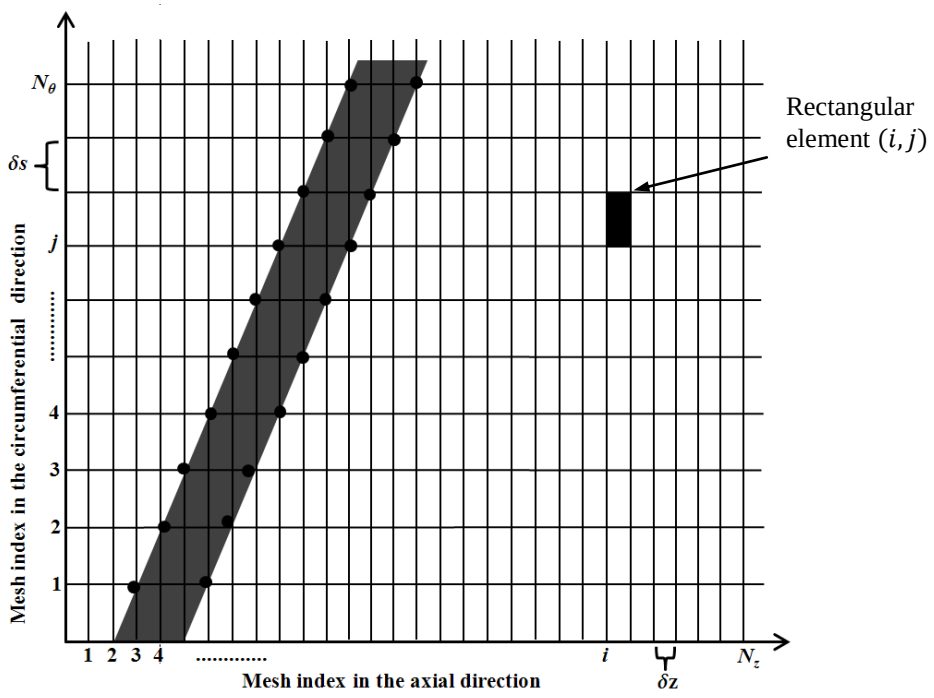

Figure 50 Discretized unwrapped geometry

To calculate the pressure field predictions during full rotation, the meshing-line is advanced along the circumferential direction of the mesh as described in the previous section. The *rotating* meshing-line *angle* (θ_m) is given by

$$\theta_{m,k} = k\,\frac{2\pi}{N_\theta} \qquad k = 1,2,\ldots\ldots N_\theta \qquad (54)$$

For every rotating meshing-line angle $(\theta_{m,k})$, the corresponding thread terminal edge angle (ϕ_k) is the angle between the meshing-line and the screw thread terminal edge. The thread terminal edge angle is used to predict the instantaneous pressure in the last chamber according to the discharge chamber model. The instantaneous pressure in the last chamber is used to predict the pressure in the other chambers from the steady state model. The pressure across the screw lands drop linearly as in Figure 34. The pressure value of each rectangular element is determined based on its axial position (z_i), circumferential position θ_j, and thread terminal edge angle (ϕ_k). A three-dimensional array $\boldsymbol{P_{rot}}(i, j, k)$ stores the pressure values for a complete rotation. z_i, θ_j and ϕ_k are related to the indices of P_{rot} i, j and k through equations (50), (51) and (54) respectively. Figure 51 is a visual representation of the three-dimensional P_{rot} array at two meshing-line angles. The unwrapped geometry in the figure is

discretized into 50 elements in the axial direction, and 10 elements in the circumferential direction. The screw lands are highlighted for visualization, in the program, a separate array will hold true/false values to differentiate discretized elements on screw lands from discretized elements on a chamber. The third dimension of the array relates to the location of the meshing-line. Position (a) in Figure 51 corresponds to a meshing-line at circumferential position 6, while Position (b) corresponds to a meshing-line at circumferential position 7. Two discretized elements are emphasized for visualization.

Because three-dimensional arrays are uncommon, they can cause confusion. A three dimensional array can be thought of as a vector of two dimensional arrays. For the schematic in Figure 51, the program will store 10 two-dimensional arrays, each array represents the pressure field distribution (axial and circumferential) at certain meshing-line angle. A 3D plot of $\boldsymbol{P_{rot}}$ will be shown in the next section for four different thread terminal edge angles.

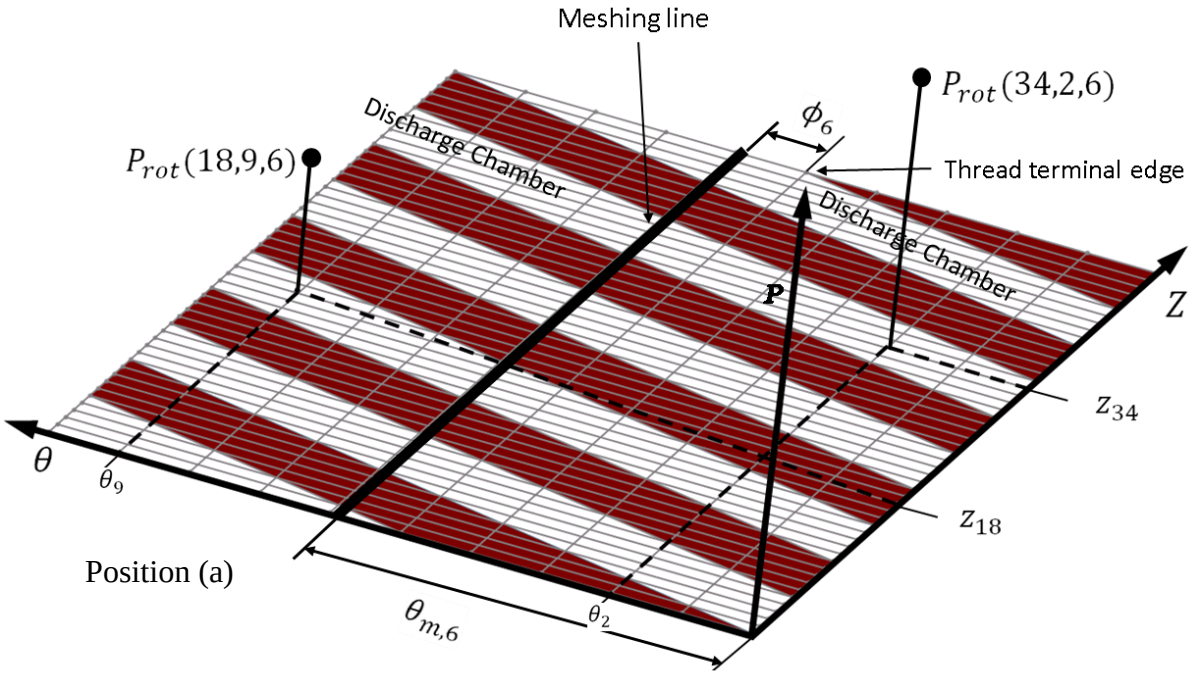

Figure 51 Schematic of the process of updating $\boldsymbol{P_{rot}}$

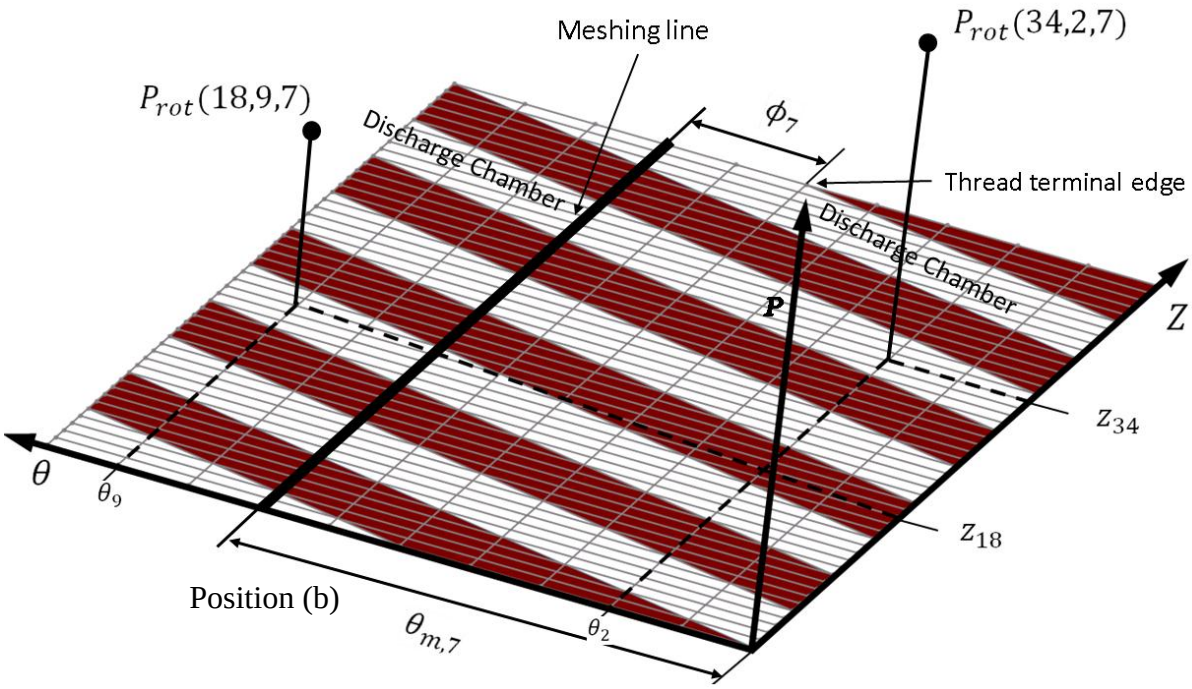

Figure 51 Continued

The flow chart of the algorithm of updating the dynamic pressure field is shown in Figure 52.

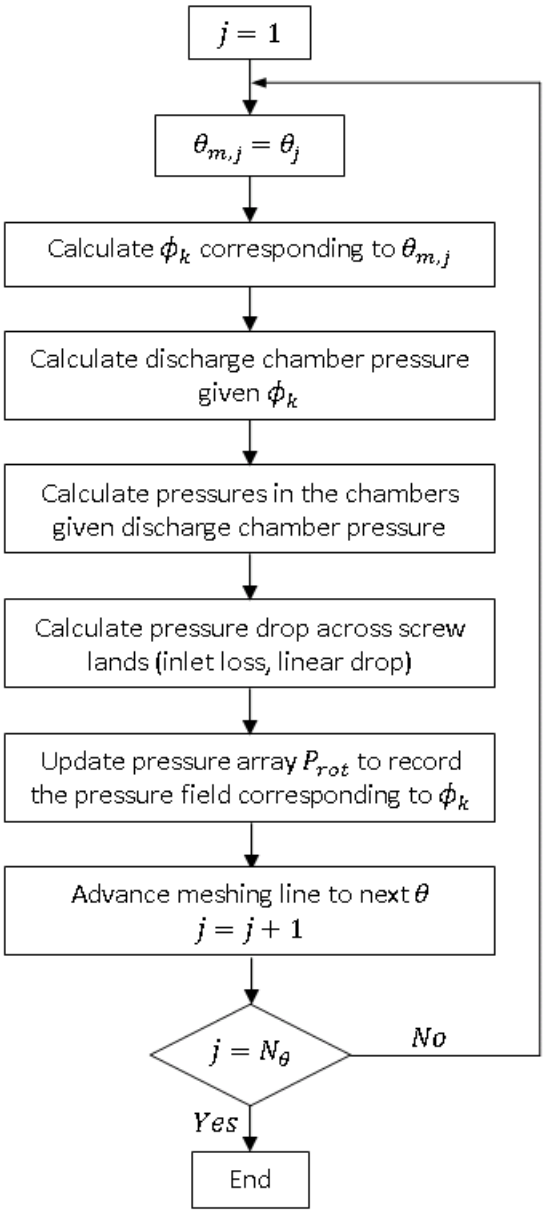

Figure 52 Dynamic pressure update algorithm

3.5.2 Dynamic pressure validation against published results

Vetter et al. [21] instrumented their pump with 6 dynamic sensors laid out axially in the XZ plane. Only one pressure reading is available around the rotor's circumference per axial location. Vetter's pump properties were listed Table 6**.** Figure 53 presents a comparison between dynamic pressure measurements from [6] and predictions from the model. The readings shown are for the fifth pressure sensor mounted in the housing at the

position of the last chamber (92 mm from suction). During a complete rotation, the sensor 'sees' the discharge pressure, chamber 3 pressure, and values in between on the circumferential clearance. Since the sensor is fixed in the housing opposite to the meshing-line, for a spinning observer, the model predictions is a record of the pressure values at a point following the meshing-line but lagging 180^{o}.

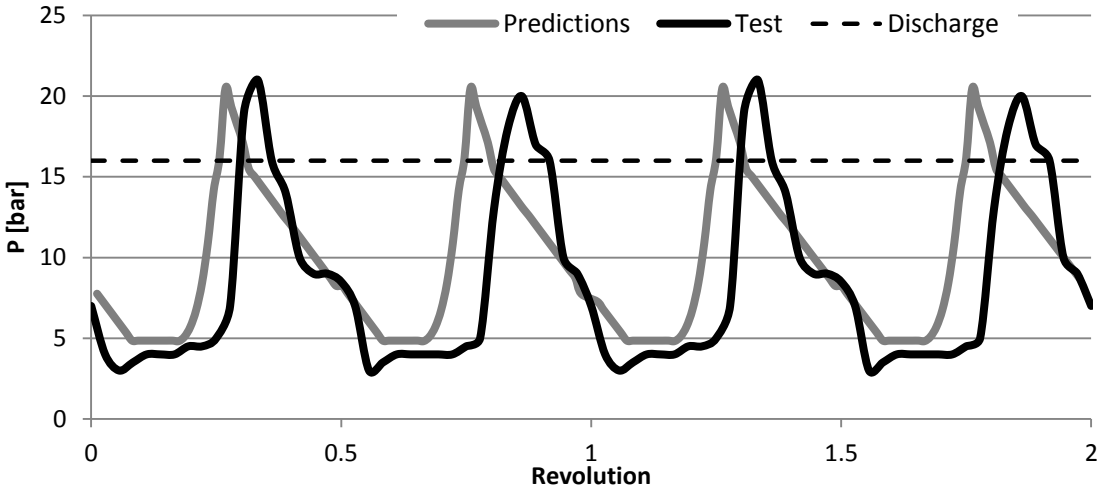

Figure 53 Prediction versus test results of dynamic pressure (GVF=75%) [21]

Figure 54 is the pressure field predictions shown in 3D for four thread terminal edge angle *s*. The axes of the horizontal plane are the axial direction and the unwrapped circumferential direction. The vertical axis is the pressure value corresponding to the radial and axial location on the screw.

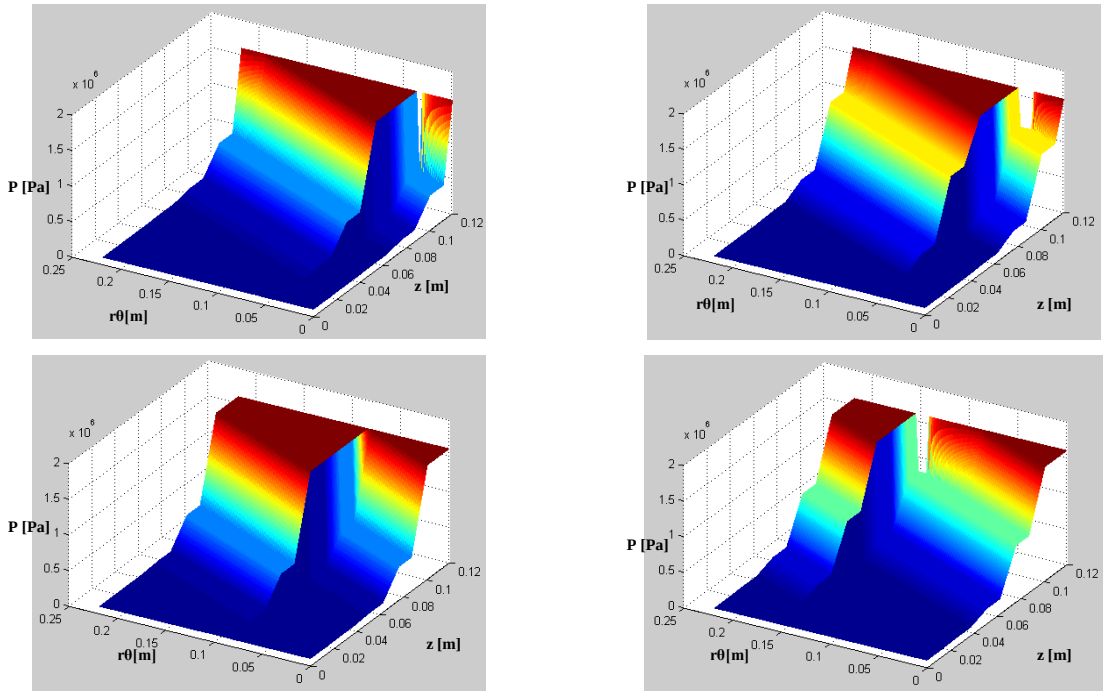

Figure 54 Two-dimensional pressure field predictions for the 75% GVF case in [21]

The spectrum of the dynamic pressure in Figure 53 is shown in Figure 55. The test spectrum is for the single revolution reported in [21]. The spectrum of the dynamic pressure predictions matches the spectrum of the reported test data closely. Because the pump is double threaded, the first harmonic appears at twice the running speed, the other harmonics are at four, six, eight, and ten times the running speed. The pressure at the zero frequency is the static unbalanced hydraulic pressure.

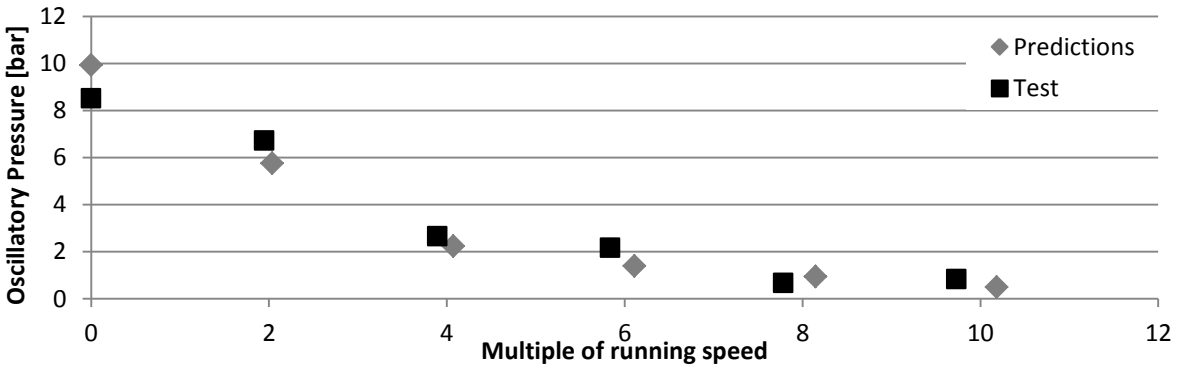

Figure 55 Dynamic pressure spectrum, predictions versus test results (75% GVF) [21]

3.6 Dynamic hydraulic forces acting on screw rotor

The output of the analysis in the last section is a dynamic pressure field as a function of the thread terminal edge angle. This section builds on the dynamic pressure field model, and ties it to the dry rotordynamic model to calculate the dynamic hydraulic forces and the dynamic rotor response.

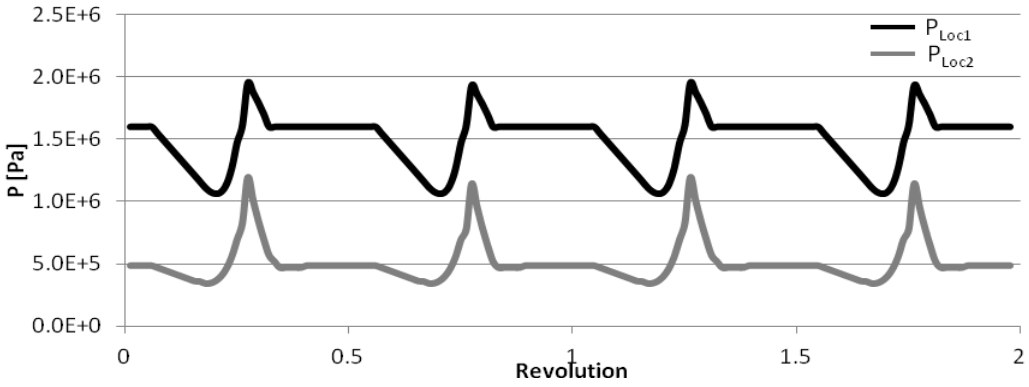

Figure 56 Dynamic pressure predictions along the Y axis for Vetter's pump [21]

Figure 53 compared the test results and predictions for pressure sensor number 5 of Vetter's pump in [21]. Sensor 5 was located axially at 92 mm from suction, and circumferentially at an angle $\theta = 180^o$. Figure 56 shows the dynamic pressure predictions for the same conditions at the same axial location but for two other circumferential locations, one at an angle $\theta = 270^o$ (denoted P_{Loc1}) and the other at an angle $\theta = 90^o$ (denoted P_{Loc2}). The difference between the predictions at the two locations $(P_{Loc1} - P_{Loc2})$ is the net dynamic pressure along the Y axis shown in Figure 58. A schematic of the sensors layout and the axes definition is shown in Figure 57.

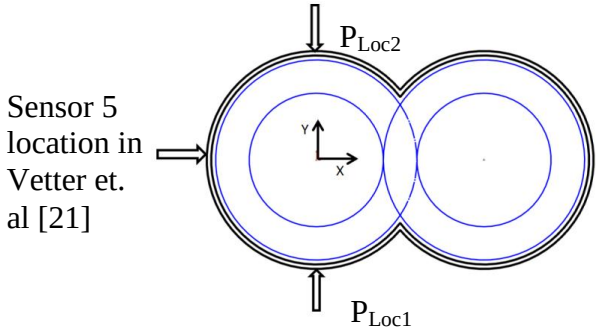

Figure 57 Circumferential layout of pressure prediction

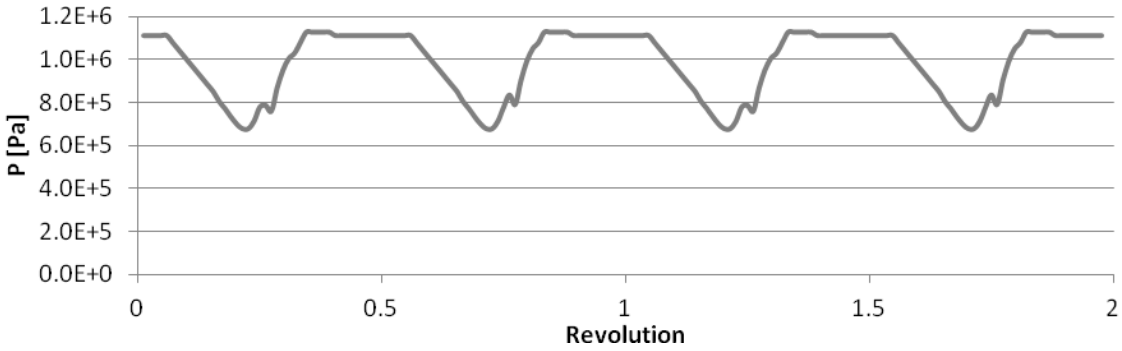

Figure 58 Net dynamic pressure along the Y axis ($P_{Loc1} - P_{Loc2}$)

Figures 56 and 58 give an insight about the hydraulic forces the rotors are subjected along the Y axis. The predictions show a net pressure pushing the rotor in the positiveY axis. This net pressure varies periodically between a maximum of 11.3 [bar] to a minimum of 6.7 [bar]. The helix angle of the screw results in an unbalanced circumferential pressure distribution and the rotation of the screws results in the periodic variation of the unbalance pressure field.

To predict the dynamic radial force through a complete revolution, the circumferential pressure is integrated at each axial position of the discretized unwrapped geometry mesh. The resulting force is projected along the X and Y axes. The integration is carried out by summing the recorded values of the dynamic pressure times the area of the rectangular element across the screw circumference for each thread terminal edge angle ϕ as given by

$$F_x(z_i,\phi_k) = \sum_{j=1}^{j=N_\theta} \boldsymbol{P_{rot}}(z_i,\theta_j,\phi_k)\,\delta z\delta s_j\, cos(\theta_i)$$
$$F_y(z_i,\phi_k) = \sum_{j=1}^{j=N_\theta} \boldsymbol{P_{rot}}(z_i,\theta_j,\phi_k)\,\delta z\delta s_j\, sin(\theta_i) \quad (55)$$

$\boldsymbol{P_{rot}}$ is the stored 3D array of the dynamic pressure as a function of the axial and circumferential locations of the rectangular element (i,j) on the discretized mesh corresponding to thread terminal edge angle ϕ_k. δz and δs are the lengths of the rectangular element in the axial and circumferential directions given by equations (49) and (53) respectively. N_θ is the number of rectangular elements in the circumferential direction as given by Eq. (52).

ϕ is related to time by the rotation speed of the rotor ω.

$$t = \frac{1}{\omega}(\phi_k - \phi_{t=0}) \qquad k = 1,2,\dots\dots N_\theta \quad (56)$$

$\phi_{t=0}$ is the initial rotor terminal edge angle at time equals zero. The initial ϕ can be determined experimentally by a phase marker on the shaft.

The forces in Eq. (55) can be expressed as a function of time instead of the rotor angle using Eq. (56) as in

$$F_x(z_i,(\omega t+\phi_{t=0})) = F_x(z_i,t) = \sum_{j=1}^{j=N_\theta} \boldsymbol{P_{rot}}(z_i,\theta_j,\phi_k)\,\delta z\delta s_j\, cos(\theta_i)$$
$$F_y(z_i,(\omega t+\phi_{t=0})) = F_y(z_i,t) = \sum_{j=1}^{j=N_\theta} \boldsymbol{P_{rot}}(z_i,\theta_j,\phi_k)\,\delta z\delta s_j\, sin(\theta_i) \quad (57)$$

The conclusion of Chapter 2 indicated that the rotor and the screw can be modeled as an axisymmetric structure. The structural dynamics of the rotor-bearing system can be modeled by mass (M), gyroscopic (G), damping (C), and stiffness (K), Finite Element (FE) matrices based on Timoshenko theory of rotating beams as defined in [35].

$$\mathbf{M}\ddot{\boldsymbol{q}} + (\mathbf{C}+\Omega\mathbf{G})\dot{\boldsymbol{q}} + \mathbf{K}\boldsymbol{q} = \boldsymbol{F_{ext}}(t) \quad (58)$$

$\boldsymbol{F_{ext}}(t)$ is the vector of the externally applied forces. $\boldsymbol{q}$ is the vector of the rotor-bearing system's degrees of freedom. Each station (stn) of the FE system has four degrees of

freedom; two translational degrees of freedom in the X and Y directions (R_X, R_Y respectively), and two angular around the X and Y axes (β_X, β_Y respectively) as

$$\boldsymbol{q_{stn}} = \{R_X, \beta_Y, R_Y, \beta_X\} \tag{59}$$

If the total number of stations of the FE rotor-bearing systems is n_{stn}, $\mathbf{M}$, $\mathbf{C}$, $\mathbf{G}$, and $\mathbf{K}$ have the dimension $[4n_{stn} \times 4n_{stn}]$. The degrees of freedom vector $\boldsymbol{q}$ has the dimension $[4n_{stn} \times 1]$.

To apply the external exciting hydraulic forces in Eq. (55) to the rotor-bearing system in Eq. (58), the axial location of each point of the discretized mesh z_i has to match the axial location of a station from the FE structural dynamic model. Since the number of the rectangular elements of the discretized mesh in the axial direction N_z is prohibitively larger than the number of FE stations along the screw section, the axial length of the screw section is sliced into number of slices ($N_{z_{sl}}$), and the hydraulic forces belonging to each slice are summed and taken to be applied as a concentrated dynamic force at the middle of the slice.

$$\begin{aligned} F_x(z_u, t) &= \sum_{i=(u-1)\times\frac{N_z}{N_{z_{sl}}}+1}^{i=u\times\frac{N_z}{N_{z_{sl}}}} F_x(z_i, t) \\ F_y(z_u, t) &= \sum_{i=(u-1)\times\frac{N_z}{N_{z_{sl}}}+1}^{i=u\times\frac{N_z}{N_{z_{sl}}}} F_y(z_i, t) \end{aligned} \tag{60}$$

$$u = 1,2 \dots N_{z_{sl}}$$

$N_z/N_{z_{sl}}$ is the number of the rectangular elements belonging to each slice. The number of the screw section slices $N_{z_{sl}}$ should be chosen such that the axial location of the concentrated dynamic forces from each slice z_u lies on a station from the FE structural model of the rotor-bearing system. The axial location z_u of the u^{th} concentrated force is given by

$$z_u = \frac{N_z}{N_{z_{sl}}}\left(\delta z(u-1) + \frac{1}{2}\right) \qquad u = 1,2 \dots N_{z_{sl}} \tag{61}$$

δz is the length of the rectangular element of the discretized mesh in the axial direction as given by Eq. (49)**.**

Because of the periodicity of the net pressure around the screws and consequently the net forces, the forces in Eq. (60) can be transformed in the frequency domain by Fourier series and be represented by set of harmonic frequencies. The time domain form of the Fourier series expansion of the concentrated dynamic forces along the rotor's axial direction is given by

$$F_{x,f}(z_u,t) = \sum_{f=1}^{N_f} \left|F(z_u)_{x,f}\right| \cos\left[fN\omega t + \Psi(z_u)_{x,f}\right]$$
$$F_{y,f}(z_u,t) = \sum_{f=1}^{N_f} \left|F(z_u)_{y,f}\right| \cos\left[fN\omega t + \Psi(z_u)_{y,f}\right] \quad (62)$$

N_f is the number of harmonic frequencies. $\left|F(z_u)_{x,f}\right|$ and $\Psi(z_u)_{x,f}$ are the magnitude and phase angle of the f^{th} harmonic frequency of the dynamic force at the axial position z_u in the X direction and similarly in the Y direction. The phase angle Ψ is with respect to time and ϕ equal zero. Time and angular position of the rotor are related through Eq. (56). N is the number of screw threads. ω is the rotational speed in rad/sec. The spectrum of the response of the pump studied for the work presented here showed up to eight harmonics. The forces in the X and Y directions in Eq. (62) are both expressed in cosine terms because they are the product of Fourier series analysis of the time domain forces in Eq.(60).

Using the rule of the cosine of the summation of two angles[1], the forces in the X and Y directions in Eq. (62) can be arranged as a summation of $[4 \times 1]$ vectors corresponding to the FE degrees of freedom per station in Eq.(59) as in

$$\boldsymbol{F}(z_u,t) = \begin{Bmatrix} \left|F(z_u)_{x,1}\right| \cos\left(\Psi(z_u)_{x,1}\right) \\ 0 \\ \left|F(z_u)_{y,1}\right| \cos\left(\Psi(z_u)_{y,1}\right) \\ 0 \end{Bmatrix} \cos(N\omega t) + \begin{Bmatrix} -\left|F(z_u)_{x,1}\right| \sin\left(\Psi(z_u)_{x,1}\right) \\ 0 \\ -\left|F(z_u)_{y1}\right| \sin\left(\Psi(z_u)_{y,1}\right) \\ 0 \end{Bmatrix} \sin(N\omega t) \quad (63)$$

[1] Cosine of the summation of two angles is given by, $\cos(a+b) = \cos(a)\cos(b) - \sin(a)\sin(b)$

$$+\begin{Bmatrix} |F(z_u)_{x,2}|\cos(\Psi(z_u)_{x,2}) \\ 0 \\ |F(z_u)_{y,2}|\cos(\Psi(z_u)_{y,2}) \\ 0 \end{Bmatrix}\cos(2N\omega t)$$

$$+\begin{Bmatrix} -|F(z_u)_{x,2}|\sin(\Psi(z_u)_{x,2}) \\ 0 \\ -|F(z_u)_{y,2}|\sin(\Psi(z_u)_{y,2}) \\ 0 \end{Bmatrix}\sin(2N\omega t)$$

$$+\begin{Bmatrix} |F(z_u)_{x,3}|\cos(\Psi(z_u)_{x,3}) \\ 0 \\ |F(z_u)_{y,3}|\cos(\Psi(z_u)_{y,3}) \\ 0 \end{Bmatrix}\cos(3N\omega t)$$

$$+\begin{Bmatrix} -|F(z_u)_{x,3}|\sin(\Psi(z_u)_{x,3}) \\ 0 \\ -|F(z_u)_{y,3}|\sin(\Psi(z_u)_{y,3}) \\ 0 \end{Bmatrix}\sin(3N\omega t)$$

$+ \ldots$

The complete external hydraulic harmonic forces vectors are constructed by assembling the vectors in Eq. (63) at the $N_{z_{sl}}$stations corresponding to the concentrated dynamic forces and zeros at all other stations as in

$$\boldsymbol{F_{ext}}(t) = \sum_{f=1}^{N_f} \boldsymbol{E_c}(f)\cos(fN\omega t) - \sum_{f=1}^{N_f} \boldsymbol{E_s}(f)\sin(fN\omega t) \tag{64}$$

$\boldsymbol{E_c}$ and $\boldsymbol{E_s}$ are the vectors of the magnitudes of the hydraulic forces for each harmonic excitation $f = 1$ to N_f in the cosines and sines. A sample of the first harmonic vector with the forces from two stations is shown in Eq. (65) for demonstration.

$$\boldsymbol{E_c}(1) = \begin{Bmatrix} 0 \\ \vdots \\ \left|F(z_u)_{x,1}\right| \cos\left(\Psi(z_u)_{x,1}\right) \\ 0 \\ \left|F(z_u)_{y,1}\right| \cos\left(\Psi(z_u)_{y,1}\right) \\ 0 \\ \vdots \\ \vdots \\ \left|F(z_u)_{x,2}\right| \cos\left(\Psi(z_u)_{x,2}\right) \\ 0 \\ \left|F(z_u)_{y,2}\right| \cos\left(\Psi(z_u)_{y,2}\right) \\ 0 \\ \vdots \end{Bmatrix} \cos(N\omega t) \tag{65}$$

For a rotor-bearing FE system with n_{stn} stations, vectors $\boldsymbol{E_c}$ and $\boldsymbol{E_s}$ in Eq. (64) have the dimensions $[4n_{stn} \times 1]$.

The particular solutions of Eq. (58) are assumed

$$\boldsymbol{q_f}(t) = \boldsymbol{q_{c,f}} \cos(fN\omega t) + \boldsymbol{q_{s,f}} \sin(fN\omega t) \qquad f = 1,2, \dots N_f \tag{66}$$

N is the number of threads. N_f is the number of harmonic forces. ω is the running speed. In Eq. (66) a response vector $\boldsymbol{q_f}$ corresponds to each harmonic excitation frequency f.

Substituting Eq. (66) in the left-hand-side of Eq. (58) and Eq. (64) for its right-hand-side and matching the sine and cosine terms, and rearranging

$$\begin{bmatrix} [\mathbf{K}] - (fN\omega)^2[\mathbf{M}] & fN\omega[\mathbf{C} + \omega\mathbf{G}] \\ -fN\omega[\mathbf{C} + \omega\mathbf{G}] & [\mathbf{K}] - (fN\omega)^2[\mathbf{M}] \end{bmatrix} \begin{Bmatrix} (\boldsymbol{q_{c,f}}) \\ (\boldsymbol{q_{s,f}}) \end{Bmatrix} = \begin{Bmatrix} \boldsymbol{E_c}(f) \\ -\boldsymbol{E_s}(f) \end{Bmatrix} \qquad f = 1,2, \dots N_f \tag{67}$$

Solving for the response vectors by inverting matrix on the left hand side

$$\begin{Bmatrix} (\boldsymbol{q_{c,f}}) \\ (\boldsymbol{q_{s,f}}) \end{Bmatrix} = \begin{bmatrix} [\mathbf{K}] - (fN\omega)^2[\mathbf{M}] & fN\omega[\mathbf{C} + \omega\mathbf{G}] \\ -fN\omega[\mathbf{C} + \omega\mathbf{G}] & [\mathbf{K}] - (fN\omega)^2[\mathbf{M}] \end{bmatrix}^{-1} \begin{Bmatrix} \boldsymbol{E_c}(f) \\ -\boldsymbol{E_s}(f) \end{Bmatrix} \qquad f = 1,2, \dots N_f \tag{68}$$

From linearity, the total dynamic response $\boldsymbol{Q_{dyn}}$ is the summation of all the harmonic response vectors from Eq. (68)

$$\boldsymbol{Q_{dyn}}(t) = \sum_{f=1}^{N_f} \boldsymbol{q_{c,f}} \cos(fN\omega t) + \boldsymbol{q_{s,f}} \sin(fN\omega t) \qquad f = 1,2, \dots N_f \tag{69}$$

The static response $\boldsymbol{Q_{static}}$ can be found from the rotor-bearing stiffness matrix [**K**] and the zero-frequency force component by

$$\boldsymbol{Q_{static}} = \mathbf{K}^{-1}\boldsymbol{F}_{f=0} \tag{70}$$

$\boldsymbol{F}_{f=0}$ is the static forces component from Fourier series expansion of Eq. (60). The static forces vector $\boldsymbol{F}_{f=0}$ is constructed in a manner similar to Eq. (65).

3.6.1 Dynamic forces and dynamic response results

A schematic diagram of the axisymmetric structure model of a rotor from Vetter's pump [21] is shown in Figure 59. The bearing's stiffness is 1.75E8 [N/m] located at B_1 and B_2. The bearing's stiffness coefficient was estimated using XLTRC2© software package based on [22]. The mass and stiffness diameters of the screw section are 86.6 mm and 68 mm respectively.

To apply the hydraulic asynchronous forces on the rotor, the 120 mm long screw is sliced into four axial slices as shown in Figure 59. Each slice is 30 mm long. The forces acting on the rectangular elements of the discretized mesh located within each slice are summed and taken to be applied at the center of the slice as explained at the beginning of this section. The forces on the two screw sections are identical and in phase.

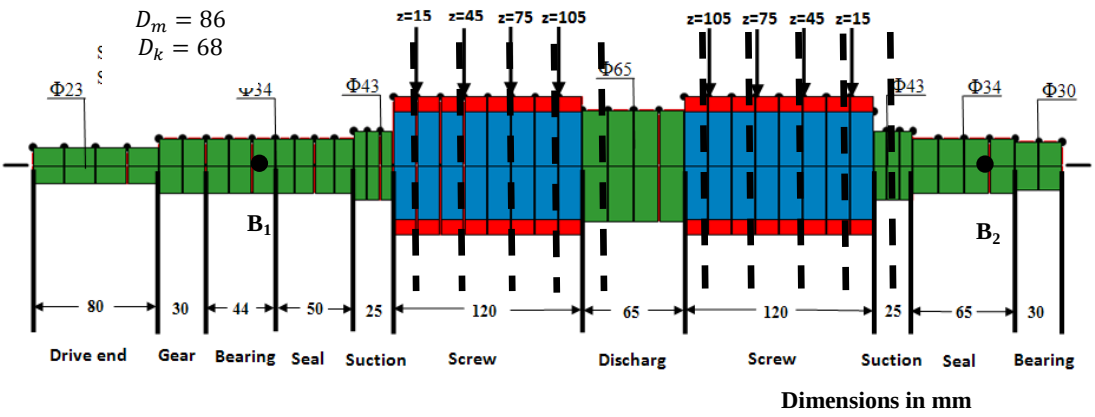

Figure 59 Axisymmetric structure model for double thread twin-screw pump in [21]

The forces in the X direction at the four axial locations in two complete revolutions are shown in Figure 60. The forces' spectrum is shown in Figure 61. The Y direction forces and spectrum are shown in Figure 62 and Figure 63. The X and Y axes were defined in section 3.1 .

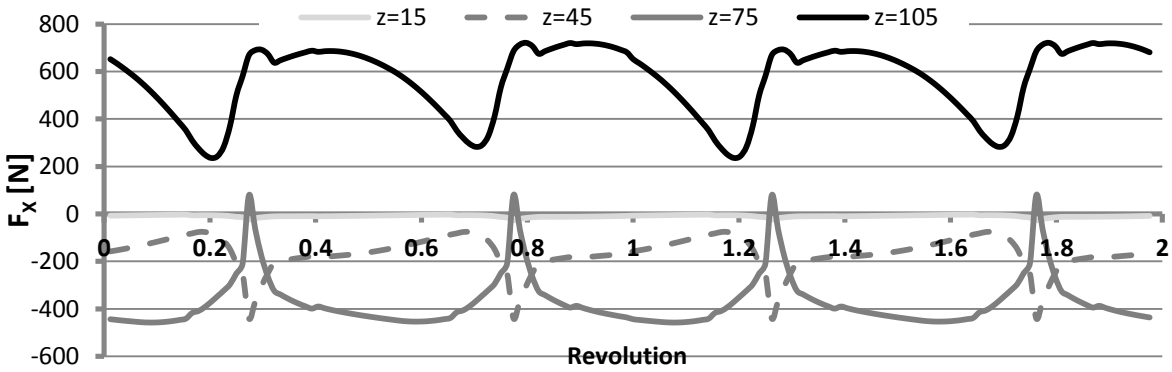

Figure 60 Predicted X direction hydraulic forces [(z) in mm from suction]

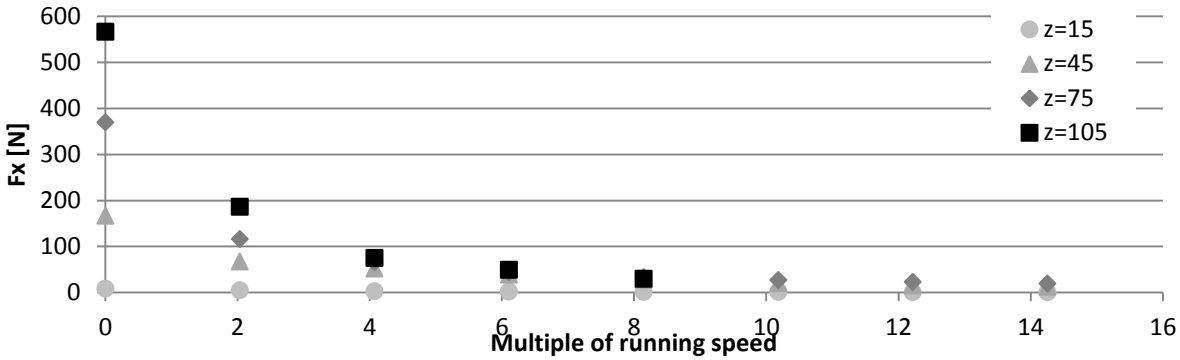

Figure 61 Predicted X direction force spectrum [(z) in mm from suction]

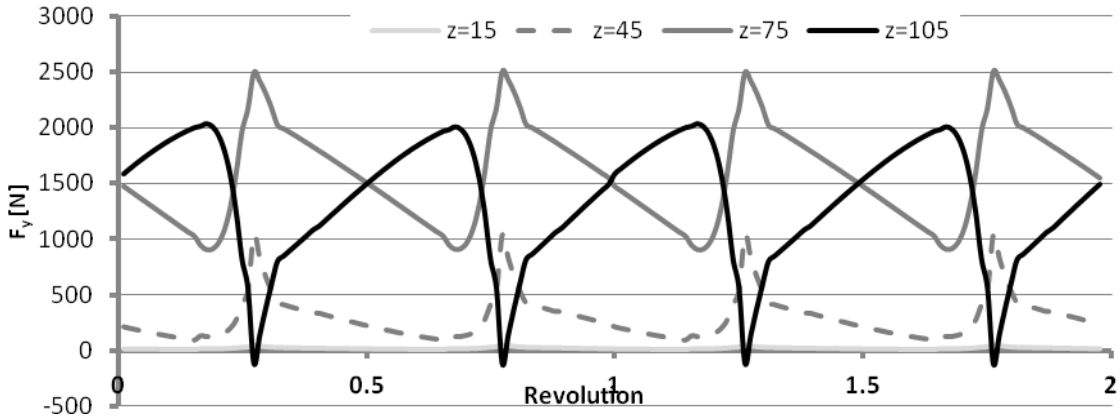

Figure 62 Predicted Y direction hydraulic forces [(z) in mm from suction]

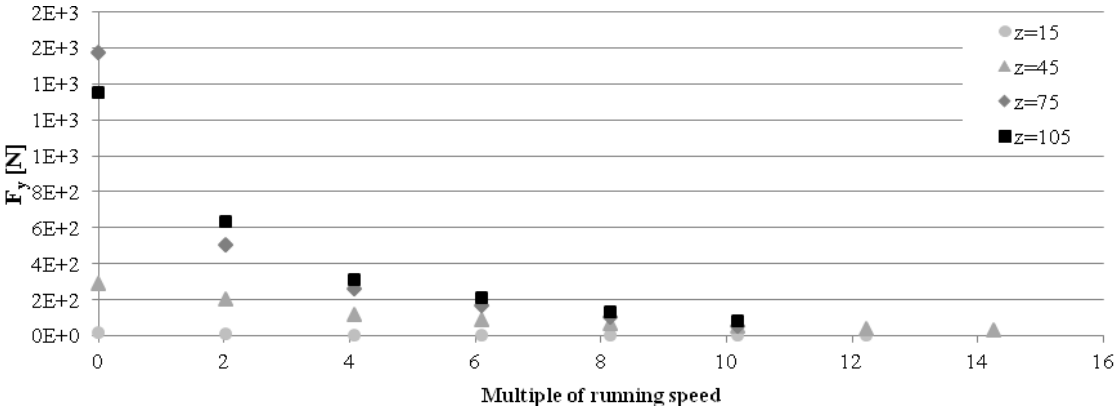

Figure 63 Predicted Y direction force spectrum [(z) in mm from suction]

Figure 64 shows the harmonic response spectrum in the Y direction. The response in the X direction was negligible compared to the response in the Y direction. The force in X direction at the axial location closest to discharge (z = 105mm) is in opposite direction of the forces at the other three axial locations. Therefore, the net effect of the X forces is almost cancelled out. Whereas, the forces in the Y direction are all negative, therefore there is a net unbalanced hydraulic (both static and dynamic) forces in this direction. These results are in line with the published static deflection test results in [4].

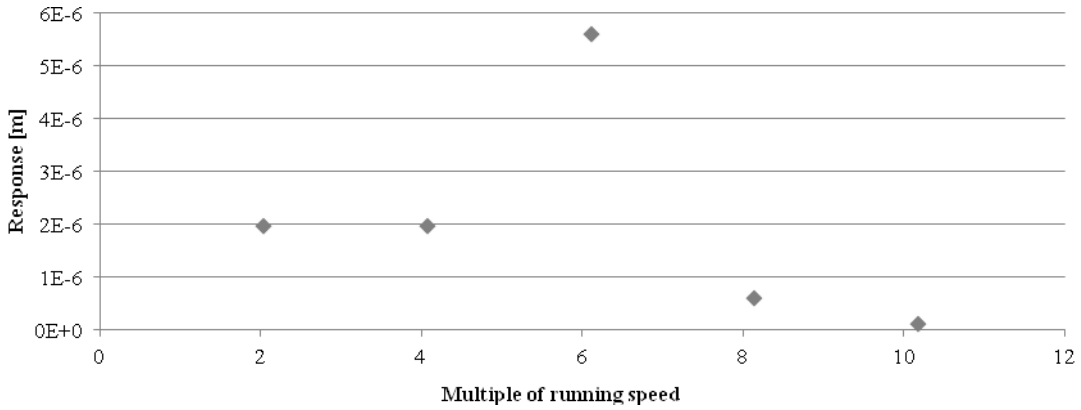

Figure 64 Super-synchronous dynamic response in the Y direction

The static rotor deflection at the discharge side of the screw is 1.6E-4 [m] (85% of the circumferential clearance). The maximum amplitude of the time domain response corresponding to the super-synchronous response in Figure 64 is 1.4E-5 [m] (10% of the circumferential clearance). The pump in [21] is double-thread. Double threaded screws are dynamically balanced, and no synchronous response at the running speed is predicted. In general, response to external unbalance can be calculated similar to conventional rotating machinery.

The magnitude of the first harmonic of the hydraulic forces at twice the running speed is around three times as high as the third harmonic at six times the running speed. However, the response due to the third harmonic is twice as much as the response due to the first harmonic, since the higher harmonic is closer to the first critical speed. This prediction shows that although the machine is operating subcritical, the harmonics of the hydraulic forces can cause excitation near the first natural frequency.

The model developed in this chapter is for one screw. Except for the coupling, the two screws in twin-screw pumps are structurally identical. Both screws are subjected to the same discharge and suction pressure conditions. The hydraulic forces developed on the two screws are equal in magnitude and direction but different in time phase. For the two screws to mate the threads have to be shifted by 180^o such that the chamber of one screw mates with the thread wall of the other screw. In addition to this shift, the terminal thread edges on the discharge side of the screw sections can be either in-phase or out-of-phase. Out-of-phase terminal thread edges help reducing the pulsation as the discharge from the screw sections take place at different points in time in a complete revolution. Because the phase shift between the two screws is related to geometry, it is constant throughout the screw section. For example two screws with the four terminal thread edges in phase would have all dynamic forces identical with 180^o shift. For the coordinate system defined in section 3.1 , the two rotors are displaced closer to each other for a positive horizontal static response, and away from each other for a negative horizontal static response. Both rotors are displaced in the same direction vertically.

4. BORNEMANN CLEAR PUMP TEST RIG

To test the model presented in the previous chapter, a twin-screw pump was instrumented with dynamic pressure sensors and proximity probes.

4.1 Pump facts and pump instrumentation

The clear-casing pump in Figure 65 was manufactured by Bornemann for demonstration purposes. The pump is a twin-screw single-thread with an acrylic casing.

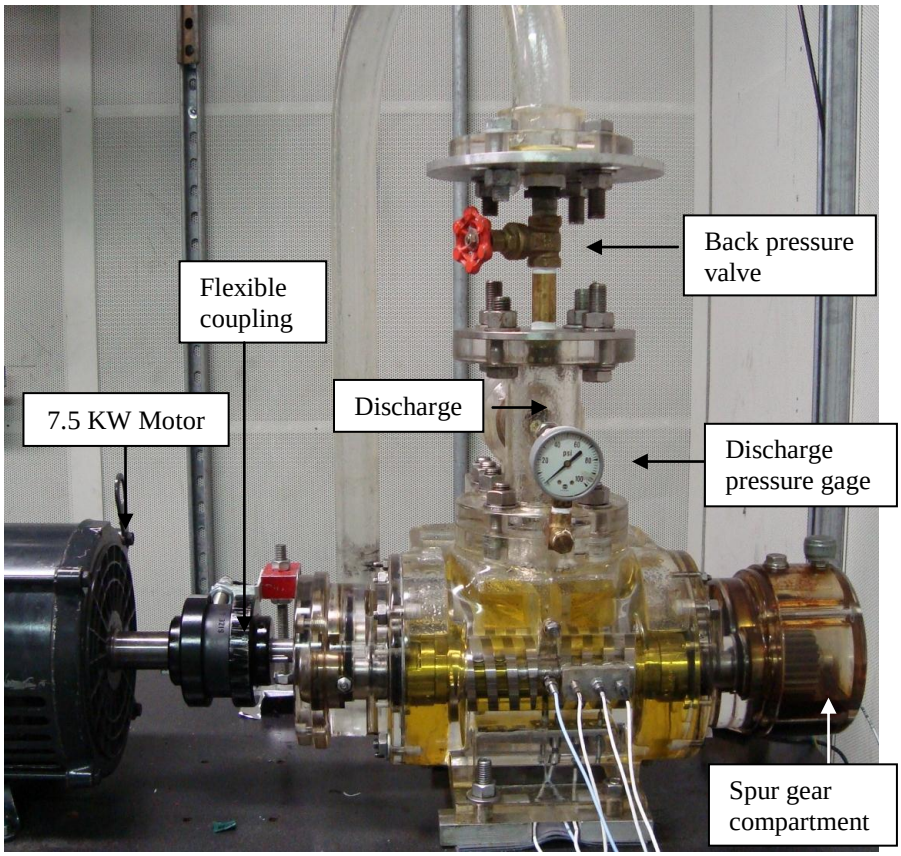

Figure 65 Bornemann clear-casing pump

The pump was fitted with a 7.5KW motor driven by a 37.2KW Variable Frequency Drive (VFD) and connected to the pump by a Lovejoy© S-flex coupling. The power is transmitted from the driving shaft to the driven shaft by spur gears immersed in lubricant oil in an external compartment. The pump's theoretical flow rate is ~0.6 liter per second at 1750 rpm. Originally the pump was not equipped with a back pressure valve since it was only

used for demonstration purposes. To run the experiment and validate the rotordynamic model, a 12.7 mm valve was installed at the discharge as shown in Figure 65. The discharge pressure is controlled by throttling the valve manually, while checking the discharge pressure gage to insure the pressure does not exceed 310 KPa. All test results are taken at 310 KPa discharge pressure.

The working fluid is oil (Viscosity = 0.2 Pa-sec at room temperature, Density =875 Kg/m^3). The pump loop is closed with its suction and discharge connected to a sealed oil tank located 0.8 meters below the suction level. The suction is immersed under the oil surface, and the discharge is above the oil surface. The pump loop is shown in Figure 66.

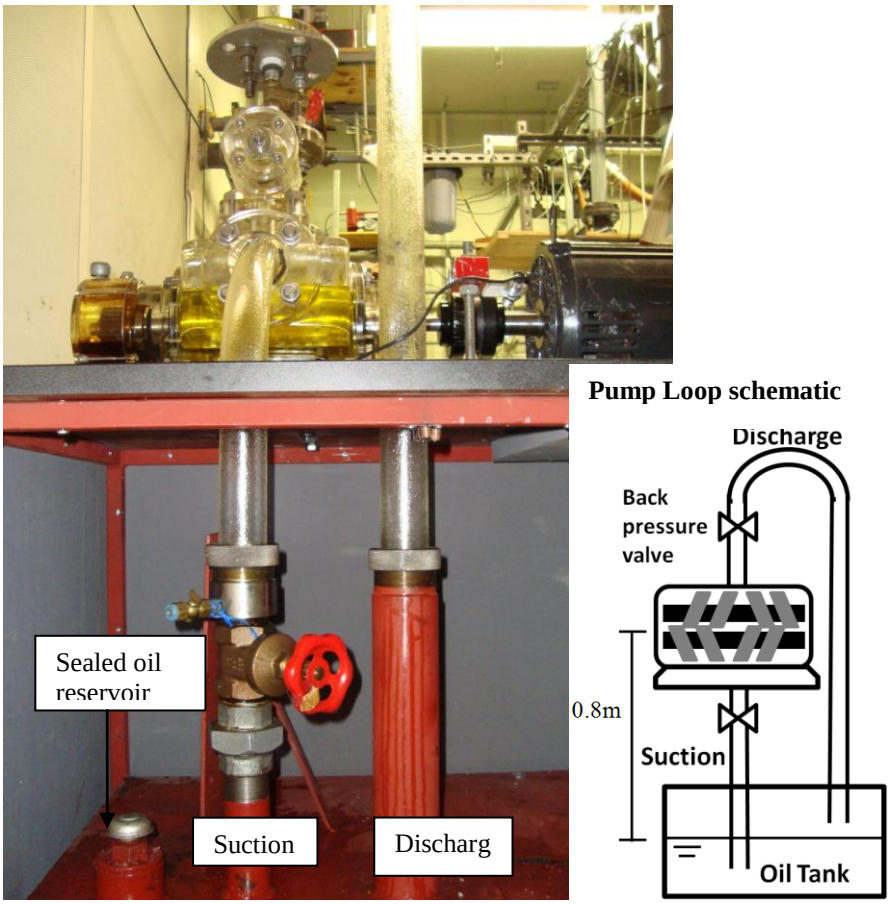

Figure 66 Clear-casing pump loop

The pump drawings are not available. Attempts to disassemble the pump to obtain accurate dimensions failed. To preserve the pump integrity, the author decided that the

fragile casing material might not withstand the process of disassembly. The rotor dimensions were measured through the clear casing and will be provided in section 4.2 . To measure the circumferential clearance, the discharge flange was removed and shims were inserted between the pump liner and the screw land. The circumferential clearance height δ_{cc} was estimated as the average of two shims thicknesses (largest-thickness shim admitted in the clearance and smallest-thickness shim not admitted in the clearance). δ_{cc} is equal to $90[\mu m]$. The ratio of the circumferential clearance height to the outer radius of the screw $\frac{\delta_{cc}}{R_{out}}$ is 0.0032, which is comparable to the range of twin-screw pumps clearance over radius ratios. The radial clearance δ_{rc} was calculated from the distance between the centers of the rotors. δ_{rc} is equal to 70 $[\mu m]$ with $\frac{\delta_{rc}}{R_{out}} = 0.00255$.

The pump was instrumented with the following sensors:

- 6 Dynamic pressure probes
- 2 Proximity probes
- Tachometer
- Air and liquid flow meters (for multiphase)

The dynamic pressure probes and proximities layout is shown in Figure 67. Three pressure probes are installed horizontally in the XZ plane, the other three are installed vertically in the XY plane. The probes are named according to their location, the names and abbreviations are shown in Figure 67. The axial distance between the probes in the horizontal plane is equals the pitch length h (16.7 mm), and likewise in the vertical plane. The vertical probes are displaced from the horizontal probes an axial distance equal to the screw land width B (8.35 mm) closer to discharge. The dynamic pressure sensors are arranged in this manner to give a better understanding of the pressures in the chambers and validate the assumption of constant chamber pressure in Chapter 3. The validity of this assumption can be checked by comparing the dynamic pressure measurements of each pair of sensors in the horizontal and vertical planes (HS versus VS, HM versus VM, and HD versus VD). With the vertical probes shifted axially the distance B, each pair of sensors should "see" the same chamber pressure for half the revolution.

To measure the dynamic pressure at the inlet of the screw, an additional dynamic pressure probe was installed in the suction compartment upstream of the screw.

The proximity probes are installed in the middle of the rotor at the discharge in the X and Y directions as shown in Figure 67. The tachometer is a noncontact optical type. It generates a single pulse per revolution corresponding to a reflective tape mounted on the coupling. The tape is approximately at the screw thread terminal edge aligned with the X axis. The signals from the sensors are amplified and read by a DAQ card at a sampling rate of 2K Hz.

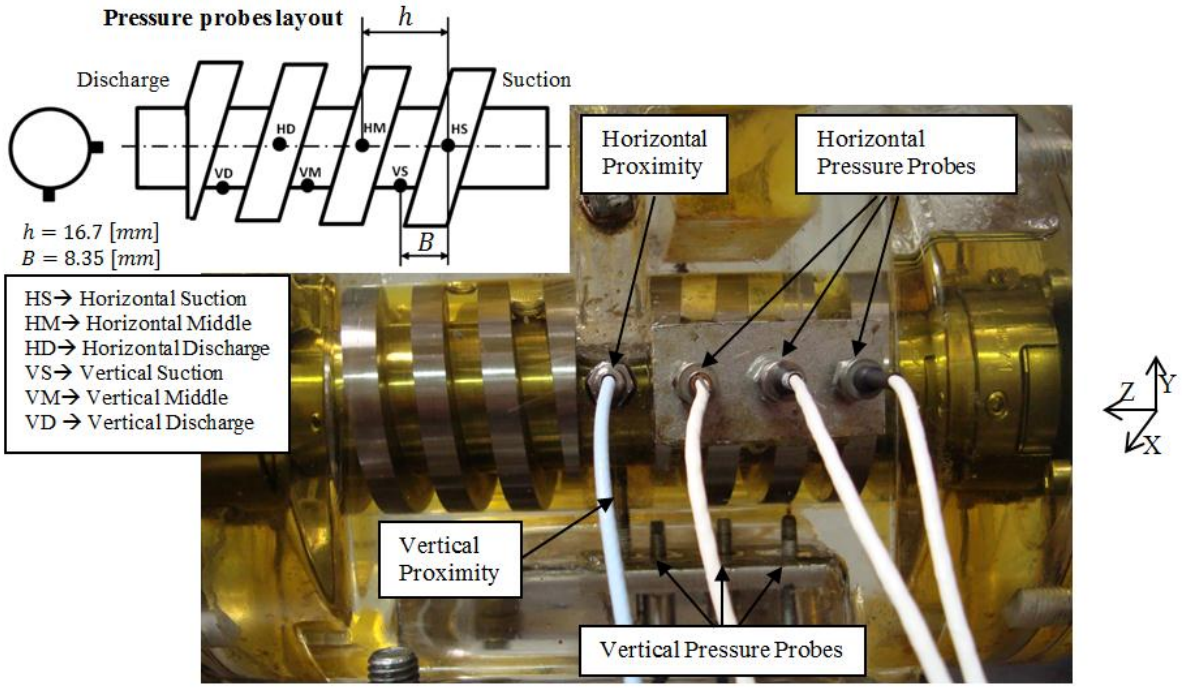

Figure 67 Sensors arrangement

4.2 Rotor structural model

A solid model with the dimensions of the rotor is shown in Figure 68. The rotor between-bearing span ($\overline{B_1B_2}$) is 0.37 m. The inner and outer radii of the screw section are 20 mm and 27.5 mm respectively.

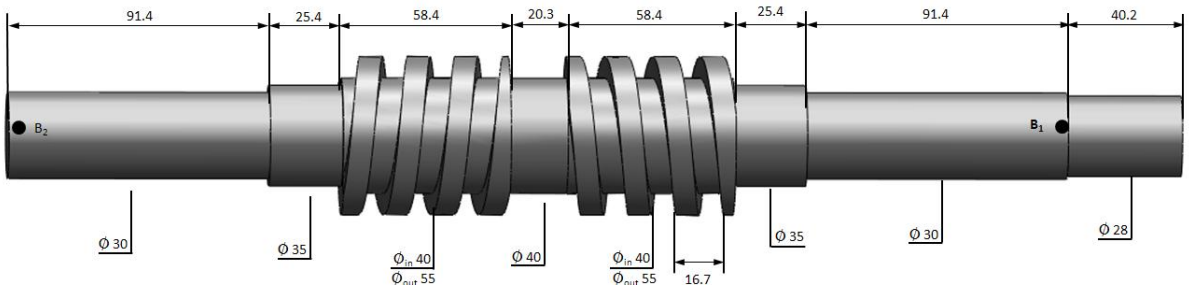

Figure 68 Rotor structural model (dimensions in mm)

An equivalent axisymmetric model of the rotor was built according to the procedure described in section 2.1 . The comparison between the axisymmetric and nonaxisymmetric free-free modes is shown in Table 7. The stiffness ratio K_d of the axisymmetric model defined in section 2.1 is 1.02. The equivalent mass diameter is 48.6 mm. The axisymmetric model schematic is shown on top of the graph in Figure 69.

Table 7Axisymmetric versus nonaxisymmetric free-free modes

Mode	Nonaxisymmetric ANSYS rpm	Axisymmetric XLTRC2 rpm	Error
1st	61448	62462	1.6%
2nd	135269	137772	1.8%
3rd	253888	260112	2.3%

The undamped critical speed map (UCS) for the clear-casing pump rotor is shown in Figure 69. Because of the short bearing span compared to the rotor diameter, the first UCS is 8.9 krpm in the stiff-rotor region (bearing stiffness 1.75E6 [N/m]) and 26.6 krpm in the stiff-bearing region (Bearing stiffness 1.75E8 [N/m]). The gear was modeled as an added mass (0.41 Kg) and an added inertia (4.02E-6 Kg-m^2 polar inertia, 6.19E-6 Kg-m^2 transverse inertia).

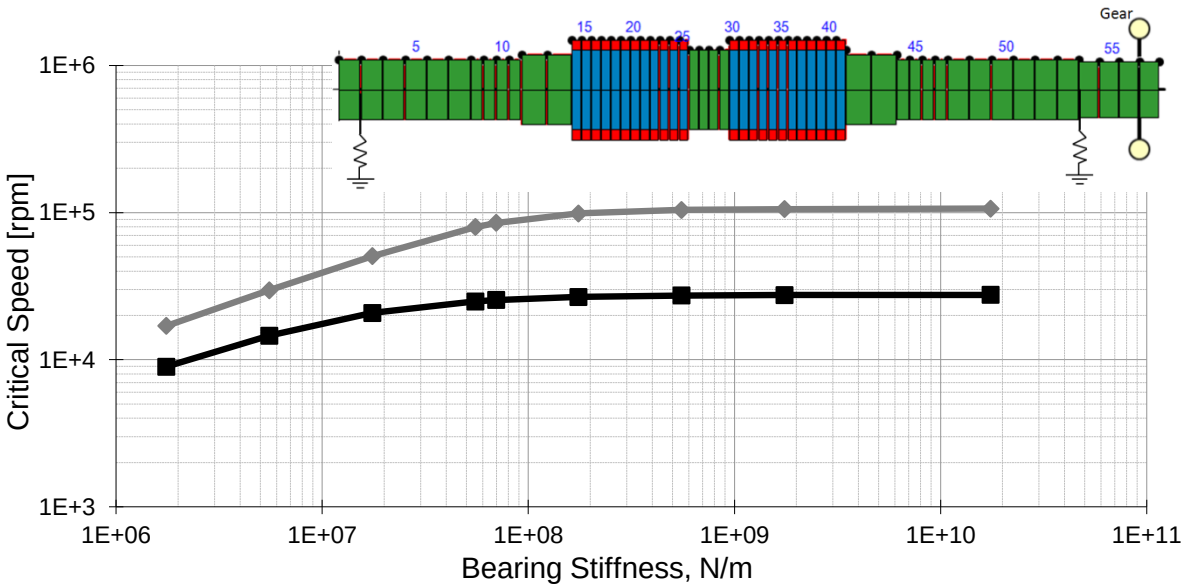

Figure 69 Undamped critical speed map for clear pump rotor

4.3 Bearing parameters identification

The clear pump rotors are supported on ball bearings. A complete model of the rotor has to include the bearing's stiffness and damping in addition to the rotor structure discussed in section 4.2 . There is more uncertainty associated with bearing's characteristics than with the rotor structure. The structure is only dependent on the rotor's geometry and material, whereas available models of ball bearings are – generally – less trusted. Moreover, the interaction between the bearing and the soft acrylic casing is expected to have a major effect on the bearing stiffness.

Attempts to run an impact test to determine the rotor-bearing system's natural frequency were unsuccessful. Because of the high stiffness of the system as predicted by the UCS map, the response to impact did not produce a signal large enough for analysis. With dynamic identification of the bearing's parameters precluded, static identification was the only viable option. In static identification, the rotor deflection from a known force is measured and the bearing stiffness is varied until the static response of the rotor-bearing model matches the measured deflection. This procedure is based on two underlying assumptions: (1) the structural model is accurate, which leaves the bearing stiffness as the

only unknown static property in the system and (2) the bearing stiffness is constant with rotor speed in the operating range. The bearing damping will be discussed in subsection 4.3.3

4.3.1 Static deflection experiment

Figure 70 shows the dead-weight fixture used to apply a known force on the rotor. The fixture is mounted on top of the pump through its discharge opening after removing the discharge pipe highlighted on the left-top view of the pump in the figure. The pump discharge is vertically aligned with the center distance between the two rotors. Therefore, to transfer the force from the dead-weight to the rotors, an inclined rod was fabricated with an angle 15^{o} as shown in the right-bottom picture in Figure 70. To secure the rod around the rotor and to prevent any slippage, the rod was welded to a bracket. The bracket has a slightly larger diameter than the rotor, so the force is assumed to be applied at one point.

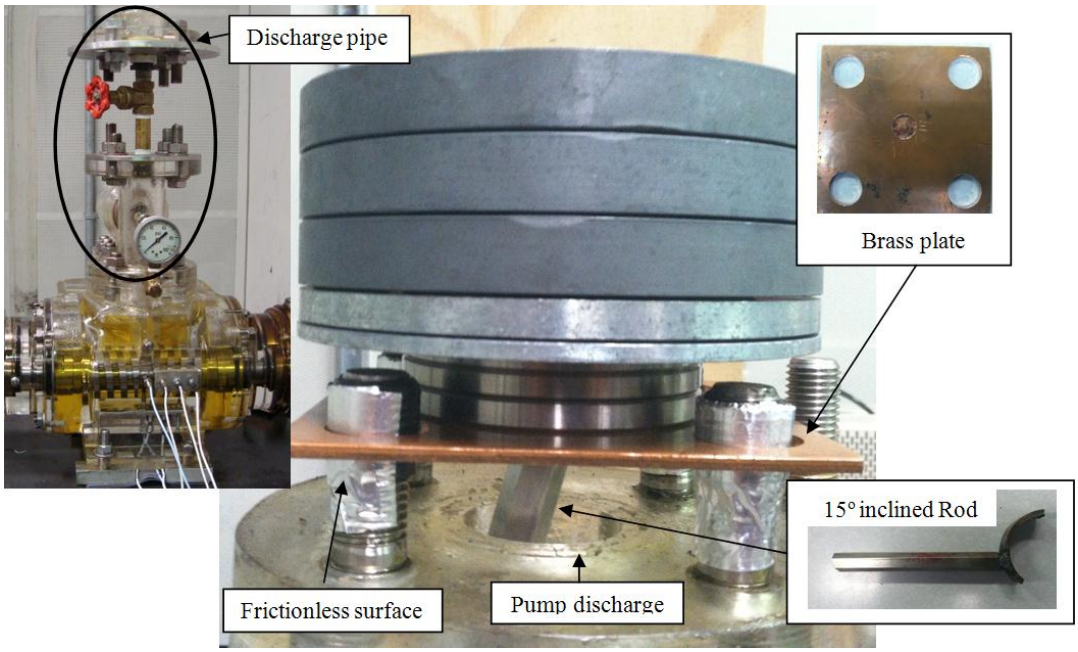

Figure 70 Dead-weight fixture for static deflection test

The dead-weights are placed on a brass plate shown in the right-top picture in Figure 70. The plate has a recess for the inclined rod to rest in. The horizontal force resulting from the inclination of the rod is supported by the bolts in the pump casing. The bolts are covered with smooth surface, and oiled to eliminate friction and insure all the vertical force is transferred through the connecting rod to the rotor and the bearings. The weights are

checked by a leveler in two directions to insure they rest horizontally on the plate. The free-body diagrams of the plate with the weights and the rod are shown in Figure 71. No moment is created because the weights rest directly on top of the connecting rod, the connecting rod is not rigidly attached to the plate, and the plate is not rigidly attached to the bolts in the pump casing.

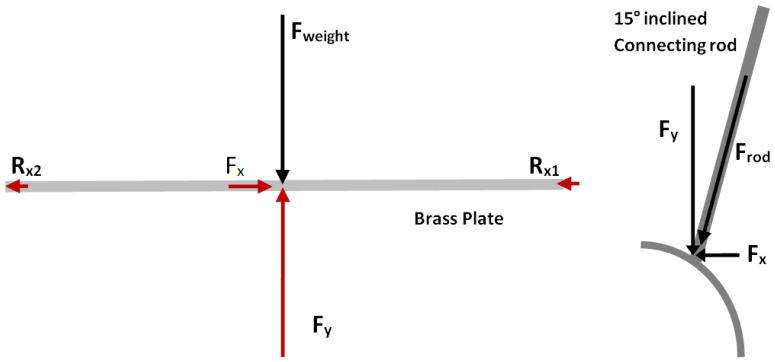

Figure 71 Dead weight fixture free-body diagram

The rotor deflection is measured in the vertical and horizontal directions by the proximity probes shown previously in Figure 67. The vertical forces and deflection results are shown in Table 8.

Table 8 Vertical static displacement results

Weight $[Kg]$	Vert Force $[N]$	Prox $[volt]$	Deflection $[\mu m]$
0.58	5.6898	7.436	0.4
0.865	8.4856	7.434	0.5
1.43	14.028	7.429	1.0
2.565	25.1626	7.42	1.8
3.7	36.297	7.411	2.5
4.835	47.4313	7.403	3.2
5.97	58.5657	7.393	4.1
7.105	69.7000	7.385	4.8
8.24	80.8344	7.3765	5.6
9.375	91.9687	7.368	6.3
10.51	103.103	7.36	6.9
13.345	130.9144	7.34	8.5
16.18	158.7258	7.32	10.1

Figure 72 shows the vertical force versus deflection curve. A straight line fits the curve with a goodness of fit R^2 value of 0.9972. The slope is 2E7 N/m (1.14E^5 lbs/in). It represents the combined rotor-bearing stiffness.

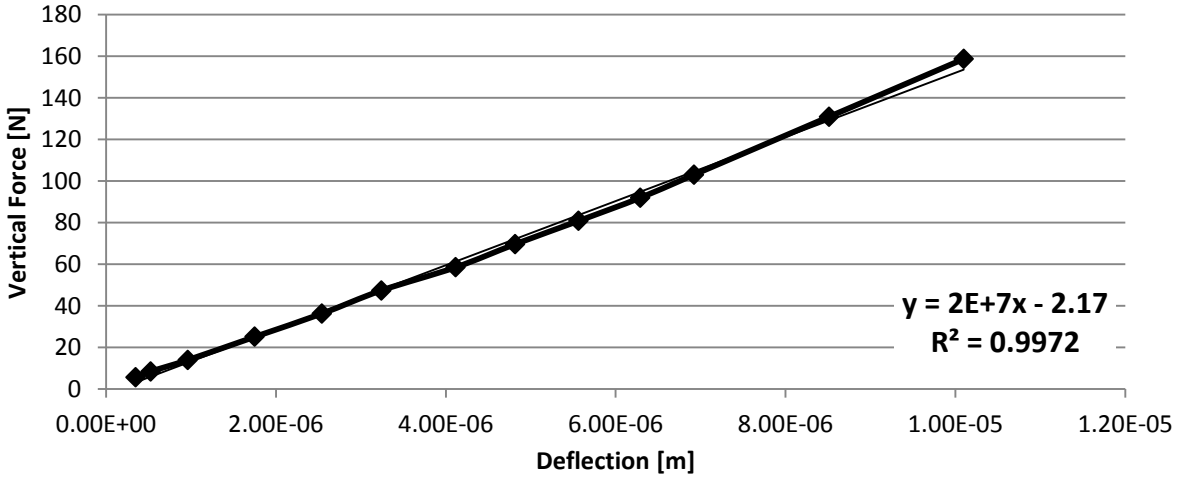

Figure 72 Vertical force vresus deflection from dead-weight test

4.3.2 Bearing stiffness

The bearing stiffness of the axisymmetric model shown schematically on top of the graph in Figure 69 was varied to match the static-deflection predictions to the measurements shown in Figure 72. The bearings' stiffness was estimated by matching the predicted static response with the measured static response. The best match is the stiffness that reduces the residual sum of squares of all the errors. Two bearings with symmetric stiffness 4.36E7 N/m were the best match to the static results as shown in Figure 73. The bearing stiffness predictions using XLTRC2© software based on [22] is 8.39E7 N/m. The difference between the predictions based on the static deflection experiment and the software predictions can be attributed to the soft casing which reduces the effective bearing stiffness.

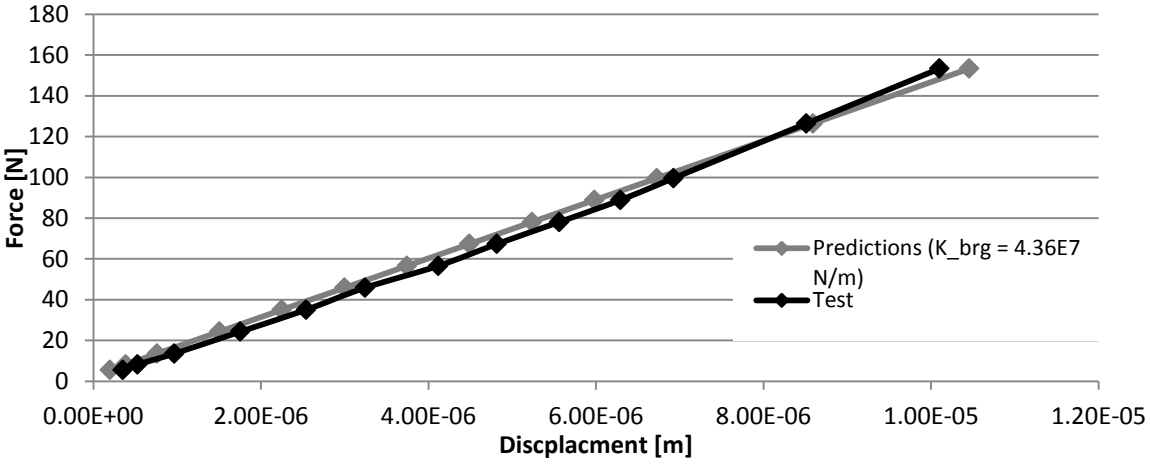

Figure 73 Static deflection measurements versus predictions

The vertical static deflected shape of the rotor for the 158.7 [N] force applied at mid span is shown in Figure 74. The deflection at the bearing is 1.87 [μm] 18% of the total mid span deflection 10 [μm]. The first undamped critical speed for bearings with 4.38E7 N/m stiffness is 24.75 krpm, 14 times the pump rated running speed.

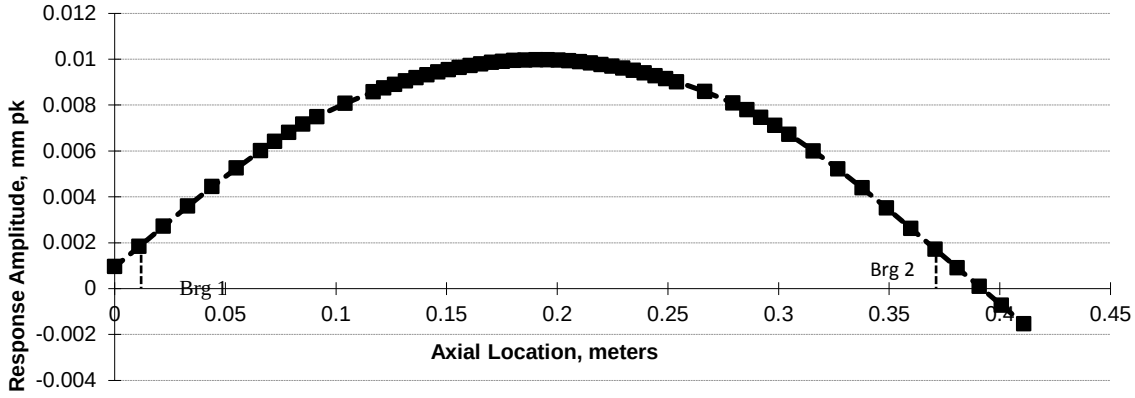

Figure 74 Vertical static deflected shape (vertical force 158 [N])

4.3.3 Bearing damping

Ball bearings are known to provide little damping. Some conservative designers ignore their damping contribution altogether. Moreover, the location of the bearings at the ends of the rotor where the first mode shape has the least amplitude is expected to reduce the effective damping of the ball bearings even further.

The empirical relation in Eq. (71) was provided by Kramer [36] for estimating the damping of roller-element bearings based on its stiffness.

$$C_b = (0.25\ to\ 2.5) \times 10^{-5} K_b \tag{71}$$

K_b is the ball bearing stiffness in N/m, C_b is the ball bearing damping in N-sec/m. The damping range corresponding to the predicted bearing stiffness is 175 to 1750 N-sec/m. The predicted damping from the XLTRC2© software is 525 N-sec/m. The ball bearing damping of the clear-casing pump will be taken as the average of the range in Eq. (71) as 963.2 N-sec/m. The next subsection will discuss the damped modes and the synchronous response to imbalance forces in addition to the effect of the damping on the imbalance response.

4.3.4 Damped mode shapes and imbalance response

Figure 75 shows the first damped mode shape for the equivalent axisymmetric model shown schematically in Figure 69. The two bearings are identical and symmetrical in the horizontal and vertical directions with stiffness and damping of $4.36E7\ N/m$ and $963\ N-sec/m$ respectively. The mode shape is the typical stiff-bearing cylindrical mode.

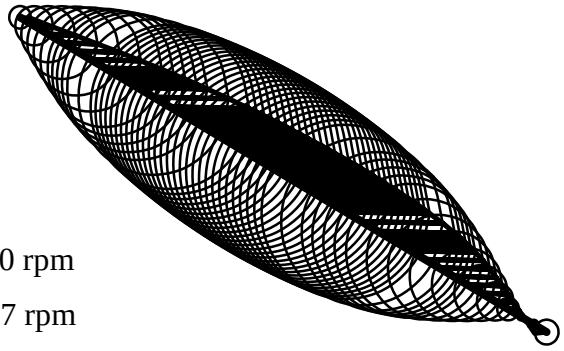

Running speed = 1750 rpm
Critical speed = 24277 rpm
Modal damping = 0.0064

Figure 75 First damped mode shape

Section 2.1.1 addresses the dynamic imbalance due to the asymmetry of the screw cross section. To include the effect of the screw cross-section imbalance, the pitch length h is sliced into N_{sl} pieces. The center of mass of each slice is displaced from the center of geometry of the rotor by the length of the vector $\boldsymbol{u_{sl}}$ given by

The values of the variables in Eq. (9) and (10) for the clear-casing pump screw are provided in Table 9. The calculated imbalance per slice $m_{sl}|\boldsymbol{u_{sl}}|$ is $8.307E^{-5}Kg-m$. The synchronous response to the screw cross-section imbalance at the midspan of the rotor is shown in Figure 76. The predicted response at the running speed (1750 rpm) is $0.013[\mu m]$.

Table 9 Screw cross-section imbalance properties

R_{out}	$0.0275\ [m]$
R_{in}	$0.02\ [m]$
ρ	$7850\ [kg/m^3]$
V_{screw}	$3.1527\ [m^3]$
h	$0.0167\ [m]$
N_{sl}	4
L_s	$0.058\ [m]$

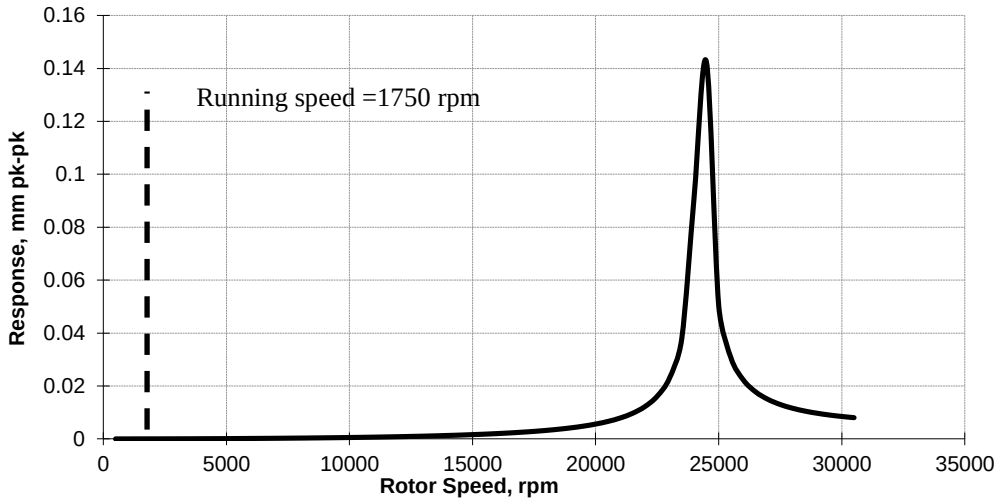

Figure 76 Synchronous response to screw-cross section imbalance

The graph in Figure 77 shows the variation of the midspan rotor imbalance response at 1,2,3 times the rated running speed with the bearing damping. The response shows that

the uncertainty associated with the bearing damping range in Eq. (71) is inconsequential to the rotor's synchronous response in the operating speed range.

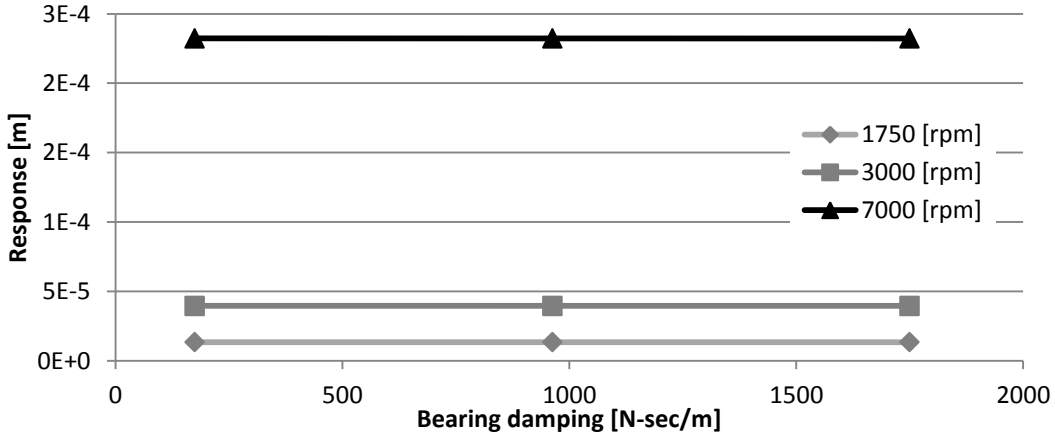

Figure 77 Effect of bearing damping on synchronous response

5. TEST RESULTS AND MODEL PREDICTIONS

In this chapter the single phase and low, medium and high GVF test results of the Bornemann clear-casing twin screw pump will be presented and compared to the predictions from the model presented in chapters 2 and 3. *Unless otherwise stated, all reported measurements in this chapter are taken at a discharge pressure of ~31.7E5 Pa (~45 psi) and a pump running speed of 1789 rpm.*

The chapter is organized in two sections. Section 5.1 addresses the single phase results, and section 5.2 addresses the multiphase results. In each section, first, the dynamic pressure measurements are presented and compared to predictions, then, the static and dynamic forces predictions are presented and the static and dynamic response measurements are compared to predictions.

The model in chapter 3 outputs static and harmonic forces in X and Y directions along the axial extent of the screw section. The predicted response is obtained by applying the resulting forces on the axisymmetric structural dynamics model of the screw rotor as detailed in section 3.6 . The development of the structural dynamics model was addressed in chapter 2. The rotor's dimensions and the bearing stiffness identification along with the resulting stiffness and mass diameters of the screw section for the clear-casing Bornemann pump were given in chapter 4. The hydrodynamic model of the clear-casing twin-screw pump used a discretized mesh with 200 elements along the axial direction ($N_z = 200$) and 58 elements along the circumferential direction ($N_\theta = 58$). N_z and N_θ were introduced in section 3.5.1 . The axisymmetric finite element (FE) model had 12 stations along the screw section. To apply the forces obtained from the refined discretized mesh, the screw section was sliced into four slices similar to section 3.6.1 . The forces from the hydrodynamic model located within each slice are summed and taken to be applied at the station located in the middle of the slice. The eight vertical forces are shown on the schematic in Figure 78. The axial locations of the forces are denoted Z1-Z4 (Z1 = 21 mm, Z2 = 21 mm, Z3=35 mm, Z4 = 49 mm measured from the suction side). Because the two screw sections are identical, the resulting static and dynamic forces are the same for both screw sections. In the reminder of the chapter, forces from only one section will be shown. The predicted responses are

calculated by applying the two identical set of four forces on the two screw sections of the FE model as shown in Figure 78.

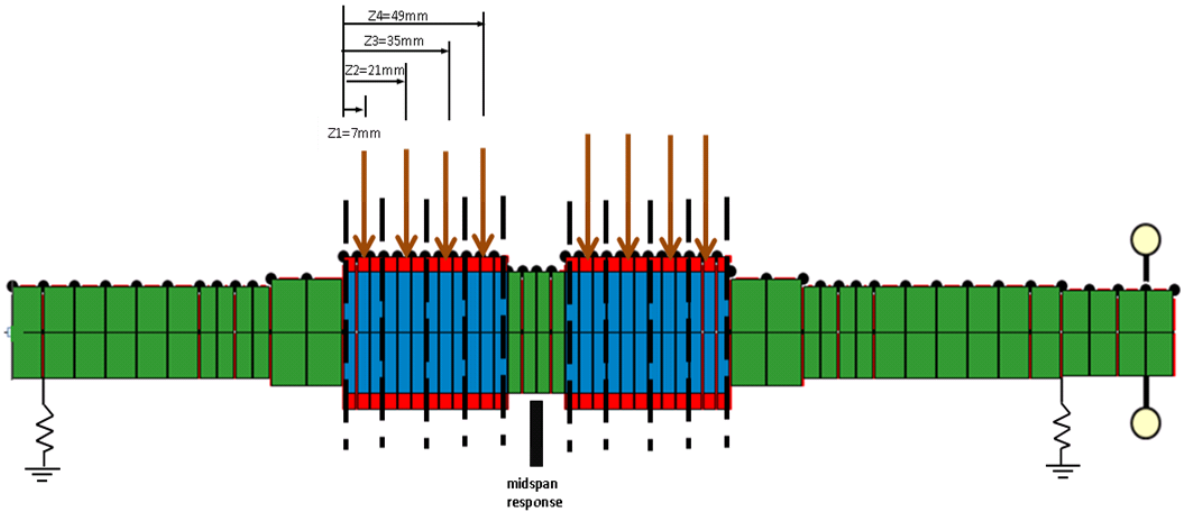

Figure 78 Predicted axial forces locations

5.1 Single phase results

This section will present the single phase results and predictions. In subsection 5.1.1 , the dynamic pressure measurements will be presented. A 12-second pressure history of the 6 installed pressure sensors shows that the dynamic pressures are stationary functions. Readings of four revolutions in the axial and circumferential directions will be shown to focus on the axial pressure buildup and the circumferential pressure distribution. Subsection 5.2.2 will compare the measured and predicted dynamic pressures in the time and frequency domains. The predicted static forces and the predicted and measured static response will be addressed in subsection 5.2.3 . Similarly, the predicted harmonic forces and the predicted and measured dynamic response in time and frequency domains will be addressed in subsection 5.2.4 . Finally, the measured response spectrum over a speed range from 900 rpm to 1800 rpm will be shown in subsection 5.1.4 .

5.1.1 Dynamic pressure measurements

After starting the pump, the discharge valve is throttled manually. The pressure gage on the discharge reads the steady state discharge pressure. A Few seconds after the discharge

pressure reaches the desired value (~31.7E5 Pa, ~45 psi), all the transients die out, and the dynamic pressure and response measurements are recorded for the duration of 12 seconds. The motor speed is maintained at a near constant 1789 rpm by the Variable Frequency Drive (VFD).

Figure 79 shows that the variation of the period of a revolution over the 12 second is minimal. The motor speed is equal to the inverse of one revolution period.

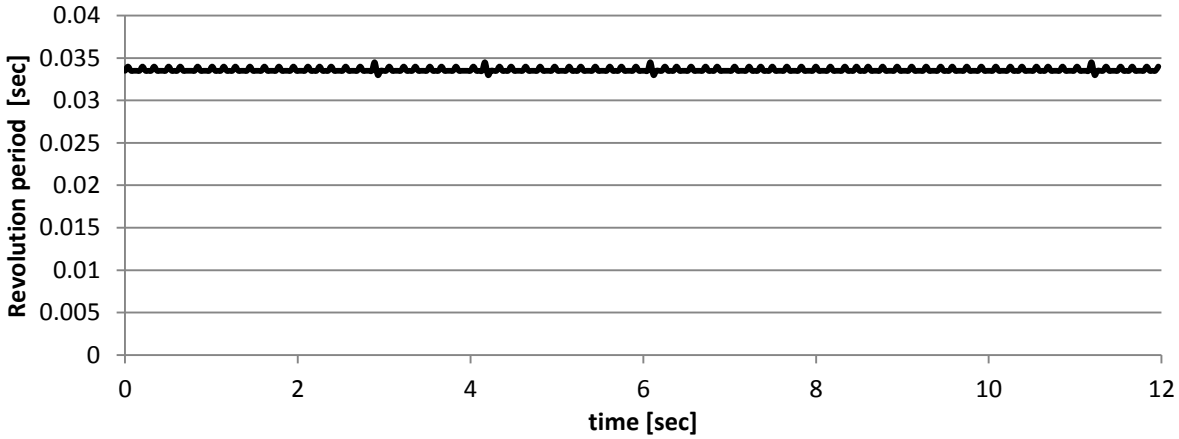

Figure 79 Revolution period at steady state operating conditions

Figure 80 shows the dynamic pressure from the six sensors. The single-phase steady state dynamic pressure shows only minor variation of the magnitude of the pressure oscillations in the 12 seconds period, confirming that the dynamic pressure signals are stationary. The discharge value at the vertical discharge (VD) pressure sensor (shown in Figure 80 (b)) is almost constant at ~31.7E5 Pa (~45 psi). The lowest value of the suction pressure at the horizontal suction (HS) pressure sensor is -0.86E5 Pa (-12.5 psi). The negative suction pressure (suction lift) was discussed earlier in section 3.4 .

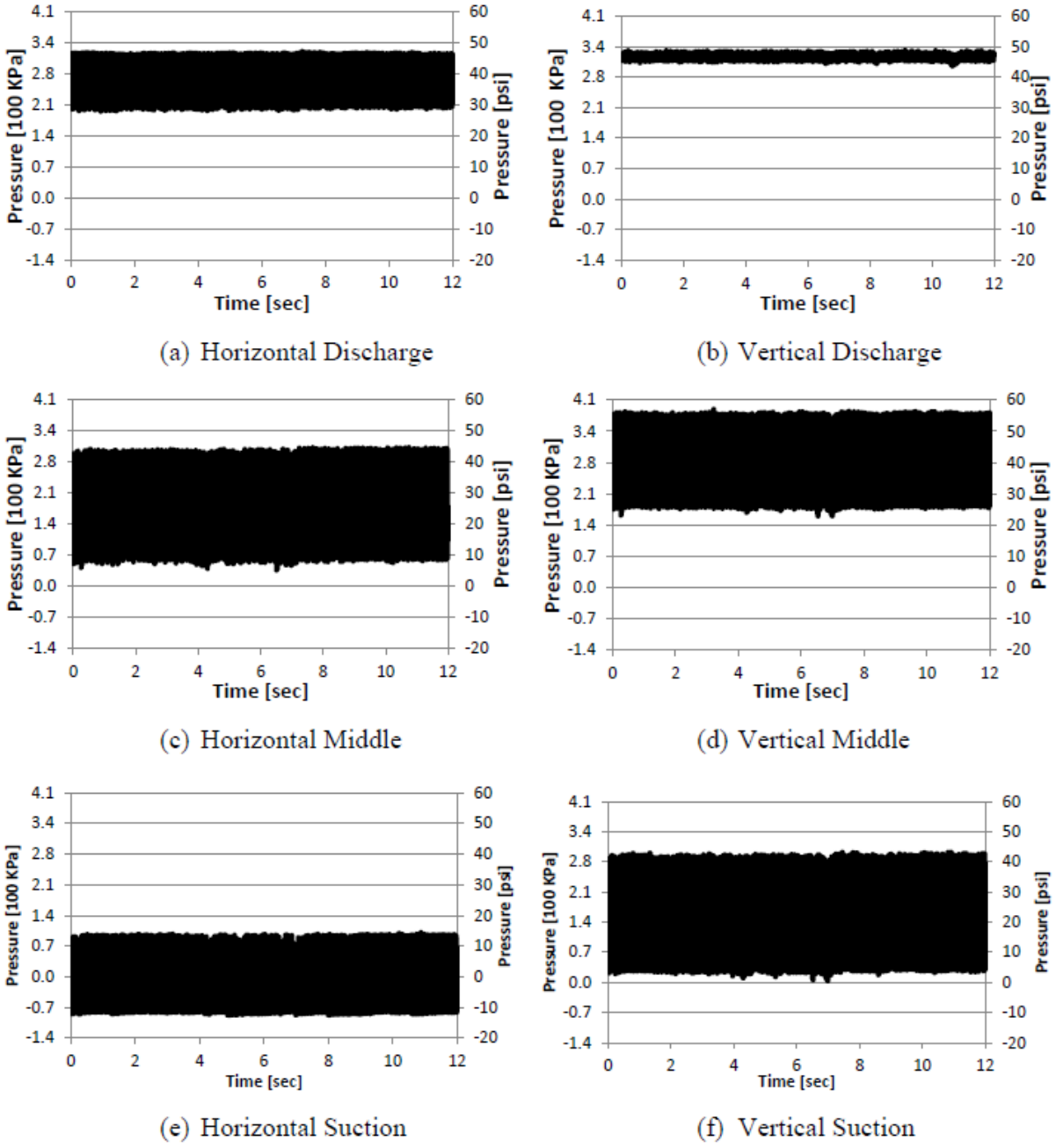

Figure 80 Single phase dynamic pressure

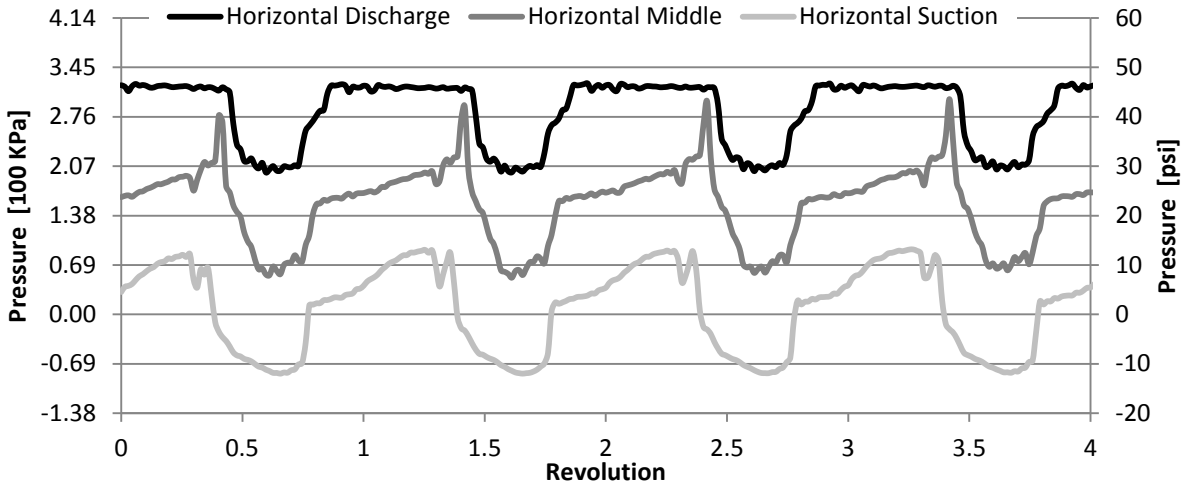

Figure 81 Measured dynamic axial pressure distribution in the horizontal ZX plane

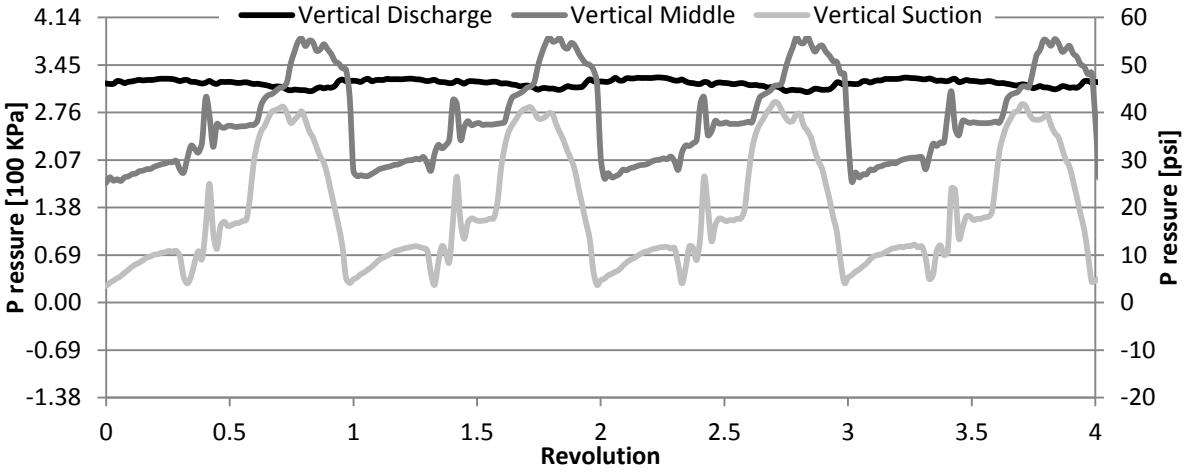

Figure 82 Measured dynamic axial pressure distribution in the vertical ZY plane

Four revolutions of the dynamic pressure are shown in Figure 81 for the horizontal plane and in Figure 82 for the vertical plane. The equal pressure rise achieved in each chamber confirms the linear pressure buildup characteristic of single phase flow as discussed earlier.

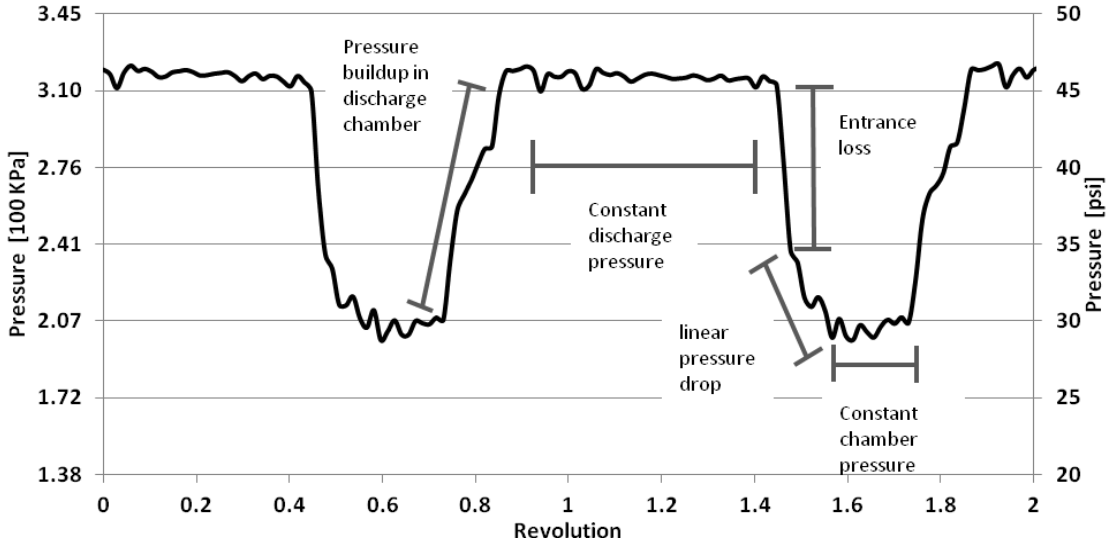

Figure 83 Dynamic events of the horizontal discharge pressure sensor

The different dynamic events discussed in details in the model in Chapter 3 are outlined on the horizontal discharge pressure readings in Figure 83. The sensor is exposed to the discharge pressure for 54% of the revolution. The pressure buildup in the discharge chamber takes ~12% of the revolution. The entrance loss takes ~66% of the total pressure difference between the discharge and the chamber upstream, the remaining 33% is taken by the linear pressure drop across the screw land. The entrance loss and the linear pressure drop were discussed in section 3.2.4 A schematic of the axial pressure distribution was shown in Figure 34.

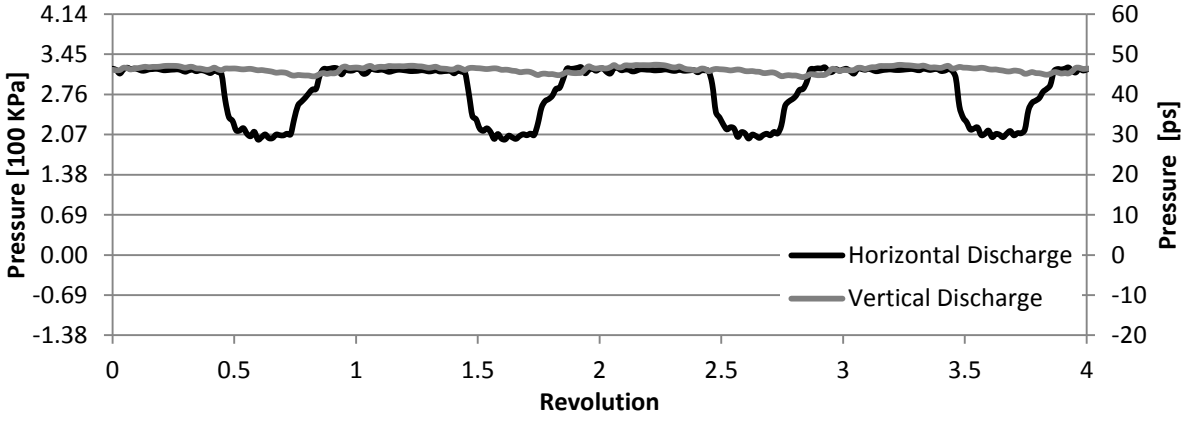

Figure 84 Horizontal versus vertical measured dynamic pressure at discharge sensors

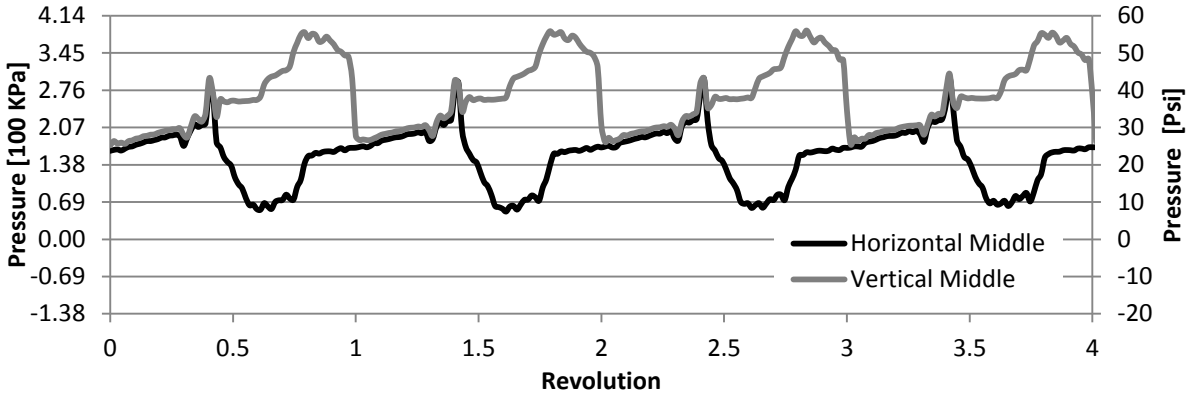

Figure 85 Horizontal versus vertical measured dynamic pressure at middle sensors

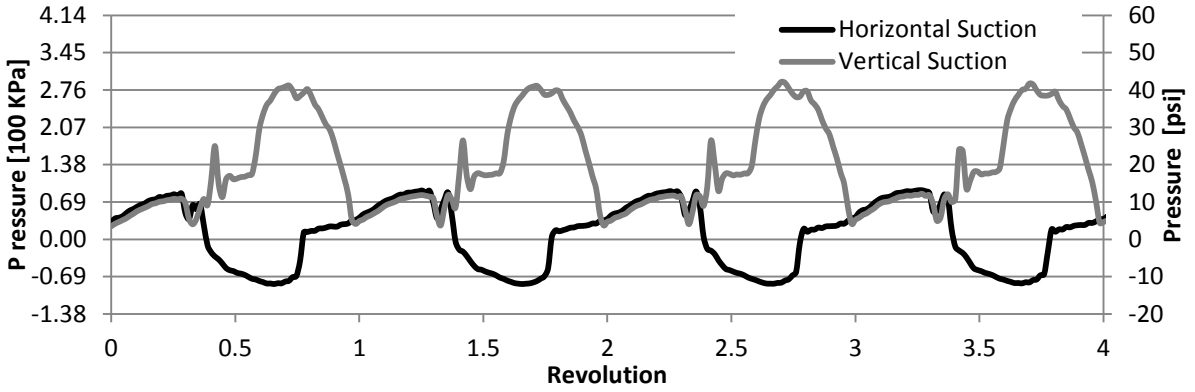

Figure 86 Horizontal versus vertical measured dynamic pressure at suction sensors

Figures 84-86 show the circumferential pressure distribution at suction, middle and discharge sensors. The vertical and horizontal sensors in the three axial locations show an overlap in pressure readings over half the revolution. The half-revolution vertical-horizontal pressure overlap is due to the displacement of the horizontal sensors for a length equal to the screw land width *B* closer to suction as shown in Figure 67. The pressure sensors in the vertical and horizontal directions read the same value when they are both exposed to the same chamber pressure. This pressure reading overlap confirms the constant-chamber pressure assumption of the model in Chapter 3. More discussion of the dynamic pressure measurements is provided in Appendix C by relating the dynamic pressure readings of the middle sensors to the orientation of the screw thread using 10 snapshots taken for the thread through the clear casing in a complete cycle.

The inlet dynamic pressure is shown in Figure 87 and compared to the readings of the horizontal pressure probes. As mentioned in Chapter 4, the inlet pressure probe is installed in the suction compartment to measure the oscillation of the suction pressure. The measurements showed low oscillation ranging from -10.8 KPa (-1.5 psi) to -15.6 KPa (-2.2 psi). The negative pressure is predicted from the pressure head losses in the pump loop as discussed in section 3.4 . The head loss is mainly due to the elevation of the pump above the oil reservoir as was shown in Figure 66. The Suction Lift of the pump due to its positive displacement action is evident in the drop of the Horizontal Suction pressure below the suction pressure to a value of -84 KPa (-12.1 psi). The positive displacement effect of the suction was modeled in section 3.4 . The low pressure oscillation in the suction compartment shown in Figure 87 and the low pressure oscillation of the discharge pressure downstream of the screw section as recorded by the Vertical Discharge (VD) sensor in Figure 82 both justify the constant, unperturbed boundary pressures assumption of the model stated in section 3.2 .

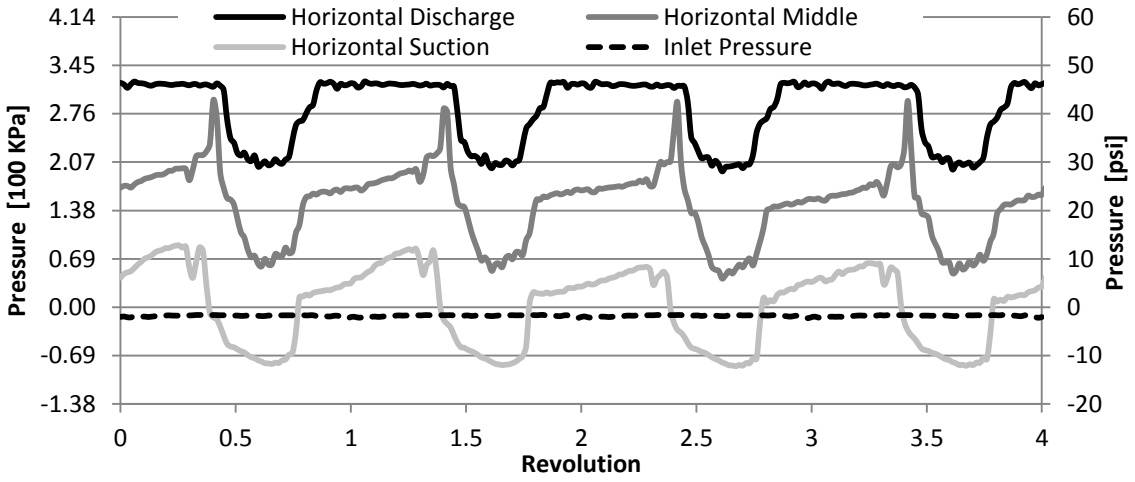

Figure 87 Inlet dynamic pressure

Figure 88 compares the predicted to the measured dynamic pressure in four revolutions from the six sensors. The measurements and predictions match satisfactorily for all sensors.

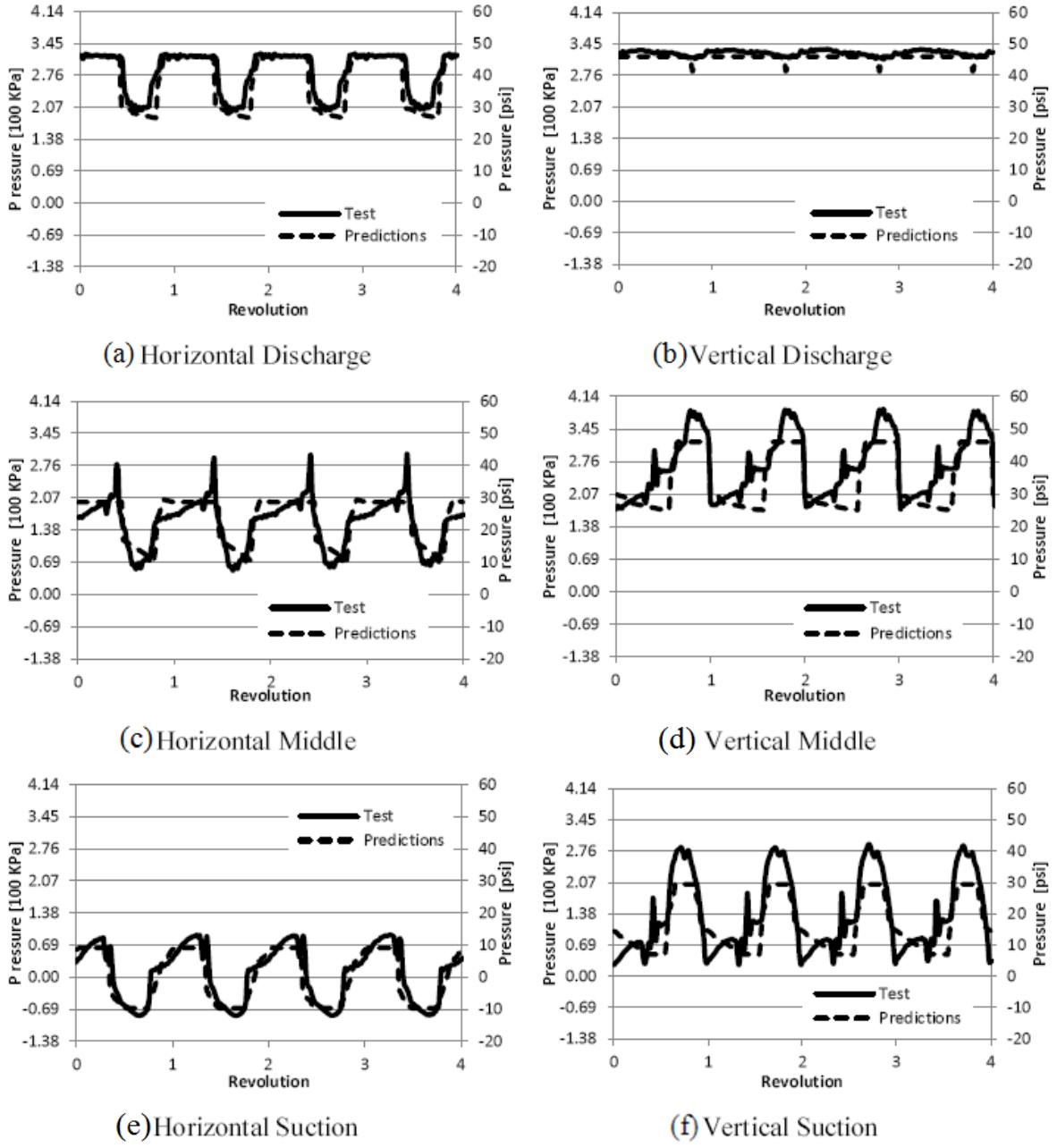

Figure 88 Measured versus predicted single phase dynamic pressure

In Figure 88, the vertical middle sensor shows a pressure spike over the discharge pressure that is not predicted by the single phase model. In the author's judgment, this pressure spike is due to the sudden communication of the last chamber with the discharge through the discharge orifice. The process was introduced and modeled in section 3.3 , however the model did not account for the transient pressure effects in single phase. The

pressure difference between the pump discharge and the discharge chamber causes a sudden flow into the discharge chamber. This flow is then stopped at the screw thread wall converting the velocity head into a pressure head and causing a transient increase in the dynamic pressure above the discharge pressure. The pressure spike is also reflected on the vertical suction sensor readings. More discussion of the pressure buildup sequence is provided in Appendix C.

Figure 89 shows the effect of the inlet loss coefficient ξ on the dynamic pressure predictions at the Horizontal Discharge (HD) sensor. Eq. (31) in section 3.2.4 relates the inlet loss coefficient to the pressure inlet loss due to Bernoulli's effect. Figure 89 compares the pressure predictions due to $\xi = 0.2, 0.25$ and 0.3. In general, the portion of the pressure drop taken by the inlet loss is larger than the portion taken by the friction across the screw land due to the short length of the screw land. The Length over diameter (L/D) ratio of the screw land to the screw diameter is 0.14. The inlet loss coefficient used for the model's predictions is 0.25. Figure 89 shows that the model is not sensitive to the inlet loss coefficient value.

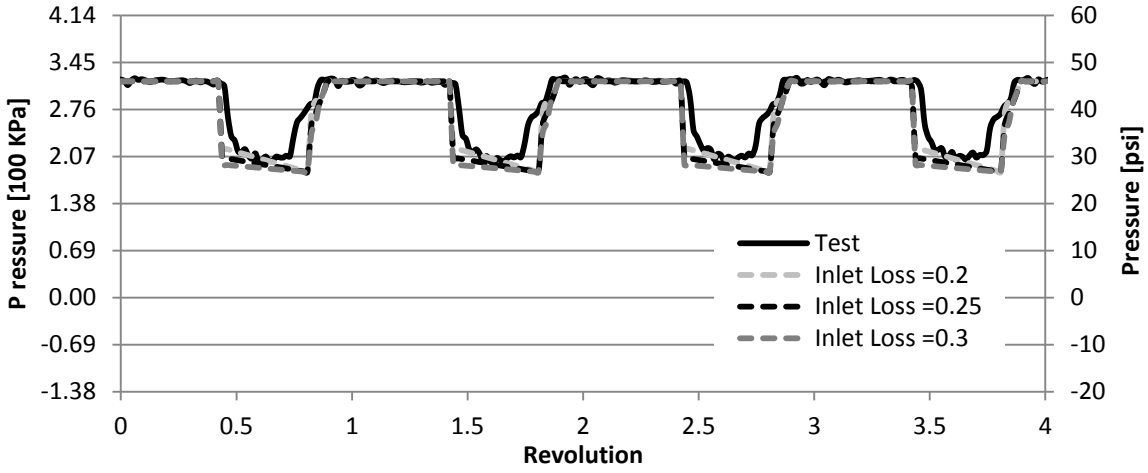

Figure 89 Effect of inlet loss on dynamic pressure predictions

Figure 90 compares the spectra of the measured and predicted dynamic pressures. As predicted by the model, the oscillating pressures are at integer multiples of the running speed. The results of the Vertical Discharge (VD) sensor are not shown as it reads a near-constant

dynamic pressure as shown in Figure 88. The spectra of the predicted and measured dynamic responses match satisfactorily for all remaining sensors.

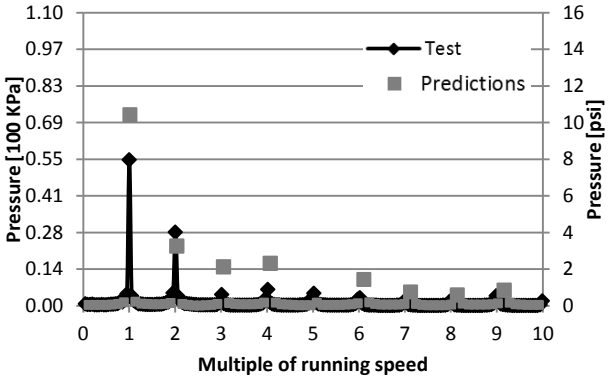

(a) Horizontal Discharge

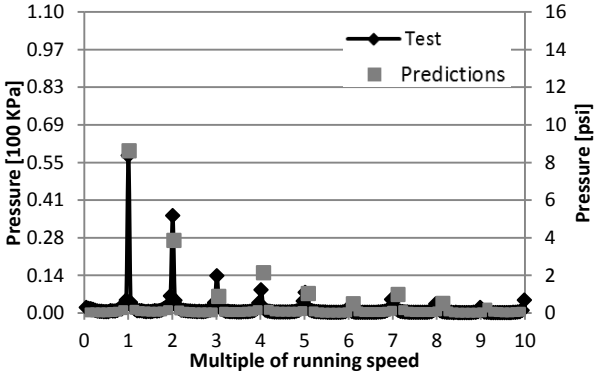

(b) Horizontal Middle

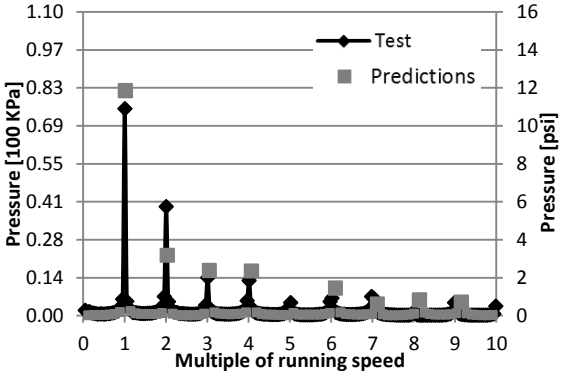

(c) Vertical Middle

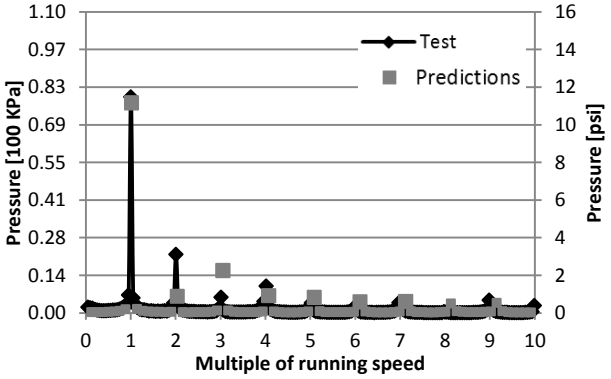

(d) Horizontal Suction

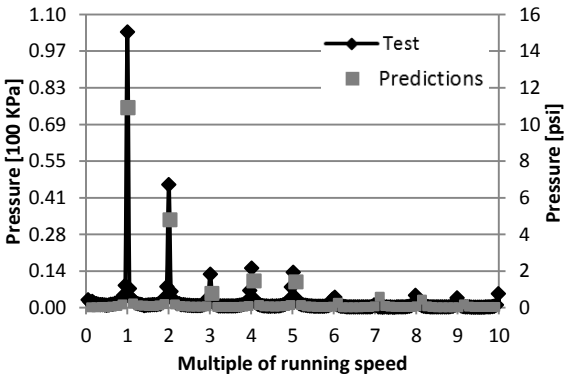

(e) Vertical Suction

Figure 90 Measured versus predicted dynamic pressure spectrum

To improve the accuracy of the calculations, the spectra of the measured pressure results are not calculated by running a Fast Fourier Transform (FFT) of the 12 second data

one time, instead, the FFT is calculated by a moving-window technique. The FFT is calculated for a window of 20 revolutions only, and the window is moved forward 10 revolutions at a time. Thus, each FFT calculation overlaps 10 revolutions with the previous calculation. The resulting spectrum is the average of the magnitudes of the FFT frequencies of all the windows. The variations in the 1x (synchronous) FFT magnitude over the entire 12 seconds span for the six sensors are shown in Figure 91. The low variation of the synchronous dynamic pressure component confirms that the dynamic pressure has no transient effects.

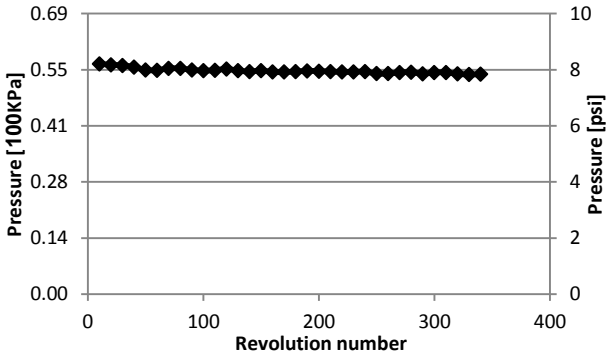

(a) Horizontal Discharge

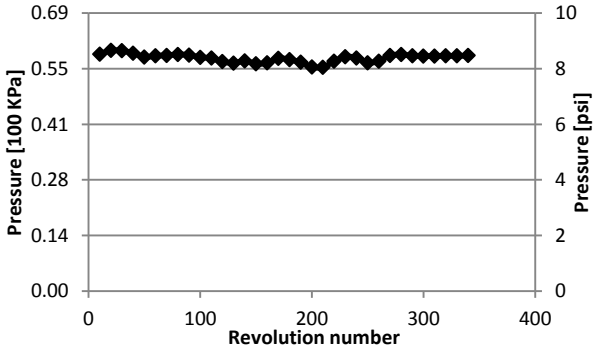

(b) Horizontal Middle

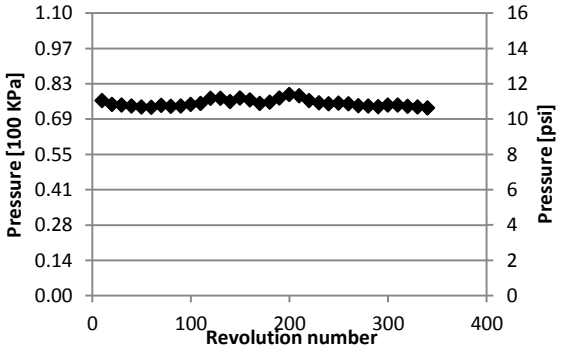

(c) Vertical Middle

Figure 91 Variation of 1x magnitude over the 12 seconds span

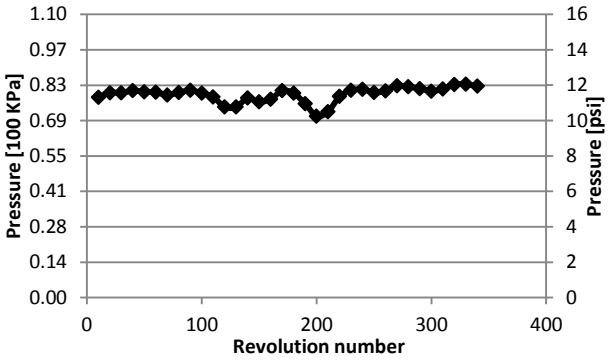

(d) Horizontal Suction

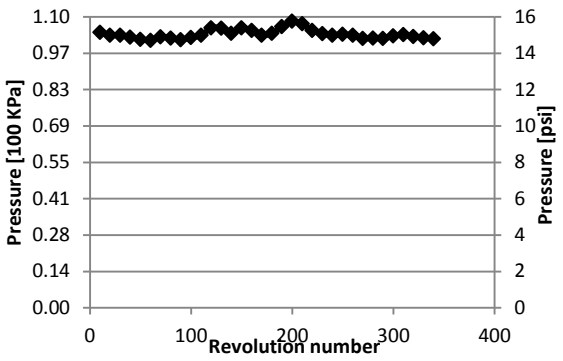

(e) Vertical Suction

Figure 91 Continued

5.1.2 Static response measurements versus predictions

Equation (2) is a crude estimation of the hydrostatic force F_r resulting from the unbalanced pressure field in the vertical direction. The equation uses the total pressure difference across the pump and an estimation of the "projected area". The equation is repeated here for convenience.

$$F_r = h(D_{out} + D_{in}) \times \Delta P \qquad (2)$$

h is the screw thread pitch. D_{out} and D_{in} are the outer and inner diameters of the screw respectively. ΔP is the total pressure difference across the pump. F_r is the radial force in the vertical direction.

Designers use this force estimation to insure the deflection from the rotors is below the circumferential clearance nominal height. Equation (72) from [37] approximates the static deflection of the rotor in the vertical direction by a static deflection of a simply supported beam with the estimated static force F_r from Eq. (2) applied at the mid span.

$$\delta_{static} = \frac{\frac{F_r}{\frac{3}{4}\pi E} L_{BS}^3}{D_{avg}^4} \qquad (72)$$

L_{BS} is the between-bearing span of the rotor. D_{avg} is an average representative diameter of the rotor. E is the modulus of elasticity.

The calculated estimated value of the force from Eq. (2) is 1.225 KN. The geometrical dimensions of the clear pump were given in Table 9. Static deflection based on the formula in Eq. (72) is 47.5 μm in the vertical direction.

The predicted static force axial distribution from the model is shown in Figure 92 in the vertical direction and in Figure 93 in the horizontal direction. The measured static deflection at the rotor's mid span is 34.02 μm in the positive vertical direction and 3.53 μm in the positive horizontal direction. The predicted static deflection at the rotor's mid span is 29.9 μm in the positive vertical direction and 3.38 μm in the positive horizontal direction. As mentioned at the end of Chapter 3, a positive vertical displacement indicates that the two rotors are displaced in the same direction (normal to the line of centers as shown in section 3.1), and a positive horizontal displacement indicates that the two rotors are displaced closer to each other. The prediction of the horizontal static forces in Figure 93 and the horizontal static deflection are in line with the results in [4] that also reported minimal static deflection in the horizontal direction for a double-thread twin-screw pump.

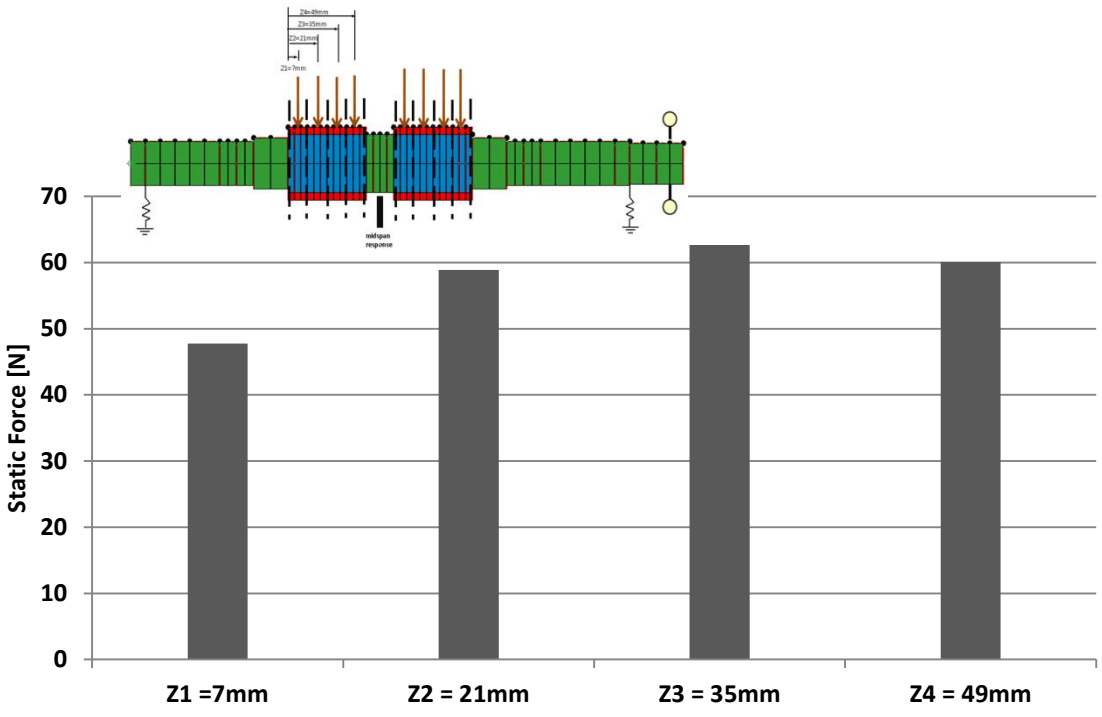

Figure 92 Predicted vertical static force axial distribution (axial location measured from suction)

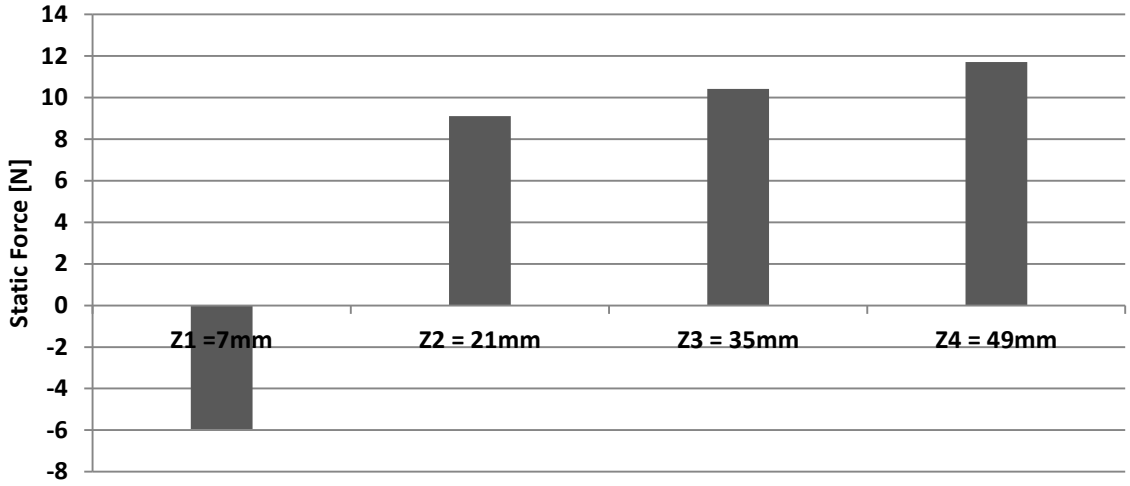

Figure 93 Predicted horizontal static force axial distribution (axial location measured from suction)

5.1.3 Dynamic response measurements versus predictions

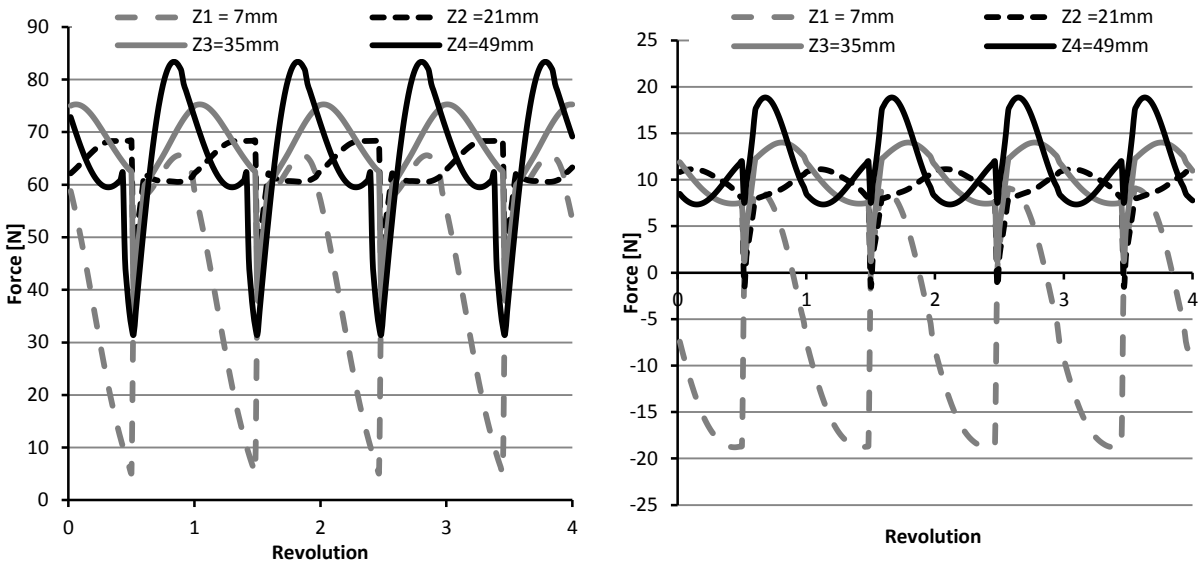

Vertical Force Horizontal Force

Figure 94 Predicted dynamic force components at four axial locations of the screw section

Figure 94 shows the predicted dynamic forces in the vertical and horizontal directions at the four axial locations shown earlier in Figure 78. The predicted range of force

oscillation in the horizontal direction is smaller than the predicted range of force oscillation in the vertical direction

Both the vertical and the horizontal predicted dynamic forces tend to have a larger range at the boundaries at the suction and discharge (points Z1, Z4 in Figure 94) than at the interior of the screw (points Z2, Z3 in Figure 94). The forces are created by the unbalanced circumferential pressure field. The boundaries are affected by the constant suction and discharge pressures. The unbalance in the circumferential pressure difference tend to be small when the boundary chambers are open to the discharge or the suction resulting in a low force, while higher unbalanced pressure is created when the boundary chambers are isolated from the discharge or the suction resulting in high forces. The difference between the low forces when the boundary chambers are communicating with the suction and discharge, and the high forces when the chambers are isolated from the suction and discharge increases the boundary forces range compared to the interior forces range. The difference between the boundary and interior forces is that for portion of the rotor's revolution, the boundaries of the screw are exposed to the constant circumferential pressure at the suction and discharge sides while the circumferential pressure at the screw interior is unbalanced throughout the rotor's revolution due to the thread walls.

The spectrum of the dynamic vertical force at location Z4=49 mm is shown in Figure 95 for the magnitude and Figure 96 for phase. The spectrum shows force magnitudes at integer multiples of the running speed. The spectra of the other three axial locations in the horizontal and vertical directions are similar to the Z4 spectrum. The phase angle is with respect to time equals zero and related to the response on the shaft by the phase marker. Section 3.6 discussed the calculations of the predicted response from the hydraulic harmonic exciting forces.

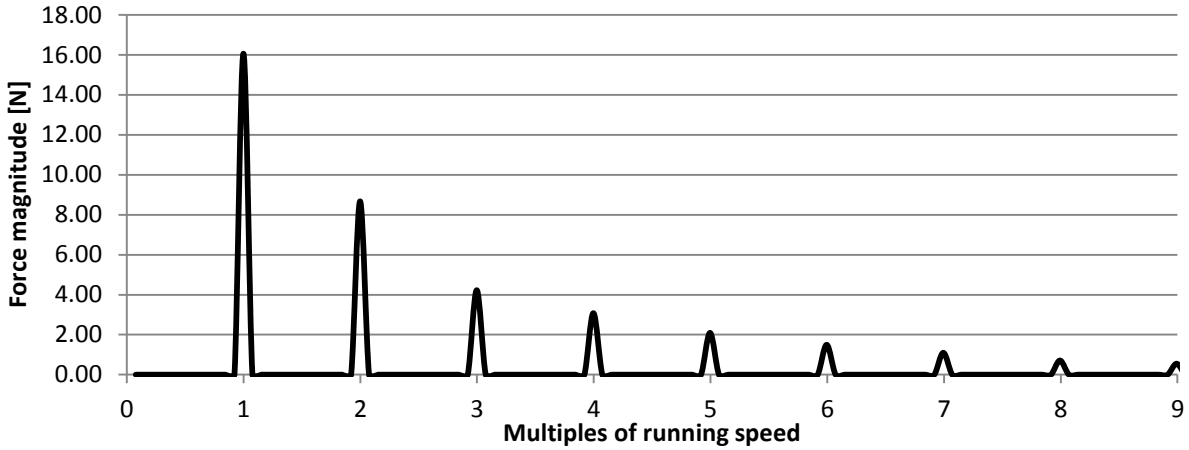

Figure 95 Dynamic vertical force magnitude spectrum at axial location Z4 = 49 mm

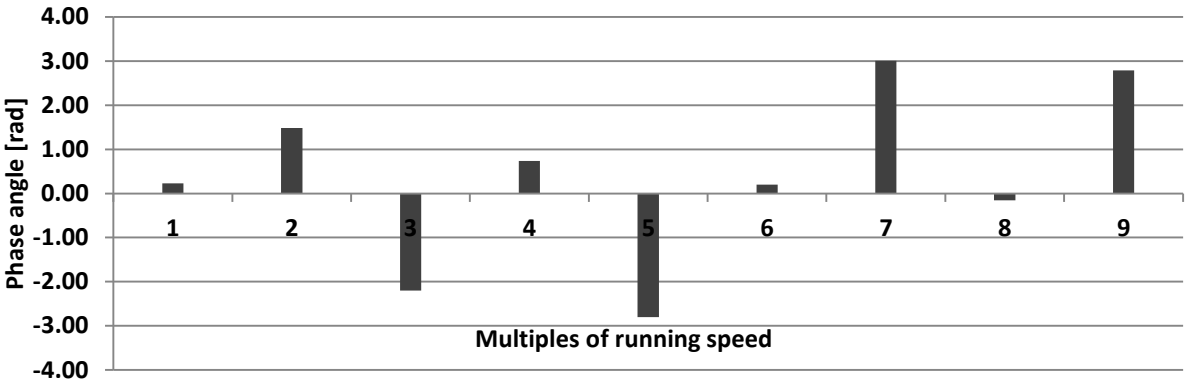

Figure 96 Dynamic vertical phase angle at axial location Z4 = 49 mm

Figure 97 and Figure 98 compare the measured and predicted dynamic responses in the vertical and horizontal directions at the mid span of the rotor. The predictions match the results closely. The predicted response is calculated by applying the harmonic forces at the eight axial locations of the screw sections as shown in Figure 78 to the rotor-bearing axisymmetric Finite Element (FE) model as was given by Eq. (69).

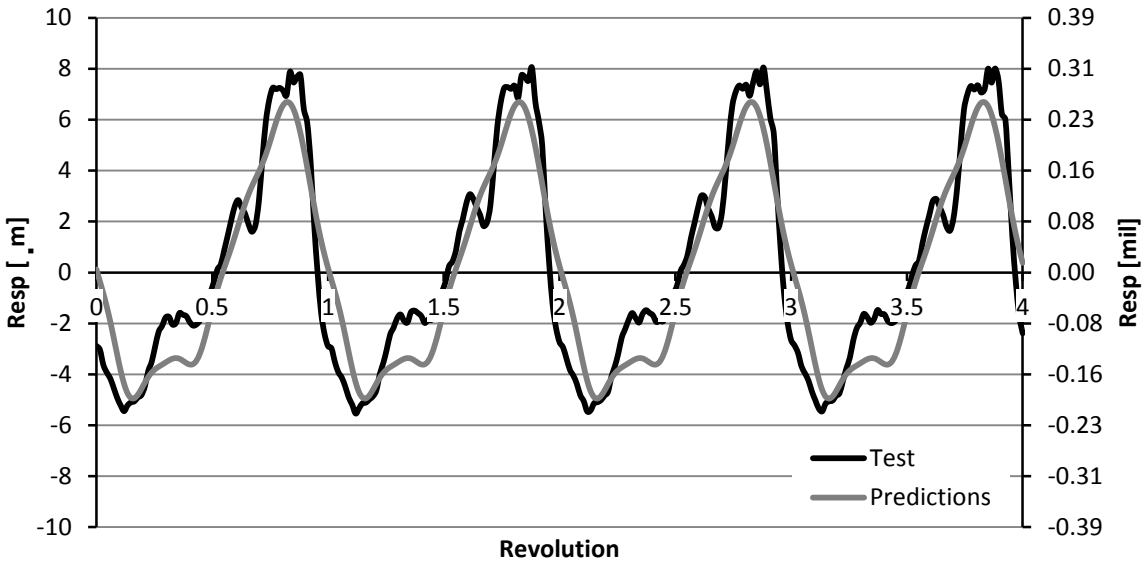

Figure 97 Measured versus predicted vertical dynamic response at mid span

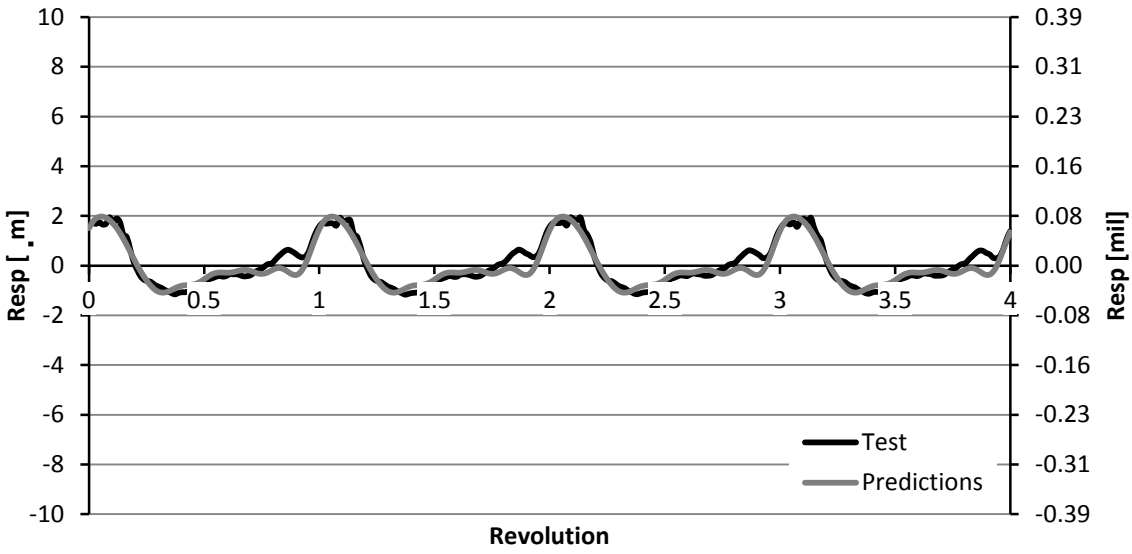

Figure 98 Measured versus predicted horizontal dynamic response at mid span

Figure 99 compares the measured and predicted orbits at mid span. The range of the orbit in the vertical direction is 15.2 μm and 3.8 μm in the horizontal direction. This "pinched" orbit is due to the difference between the exciting forces in the vertical and horizontal directions. The support bearings and structure are isotropic.

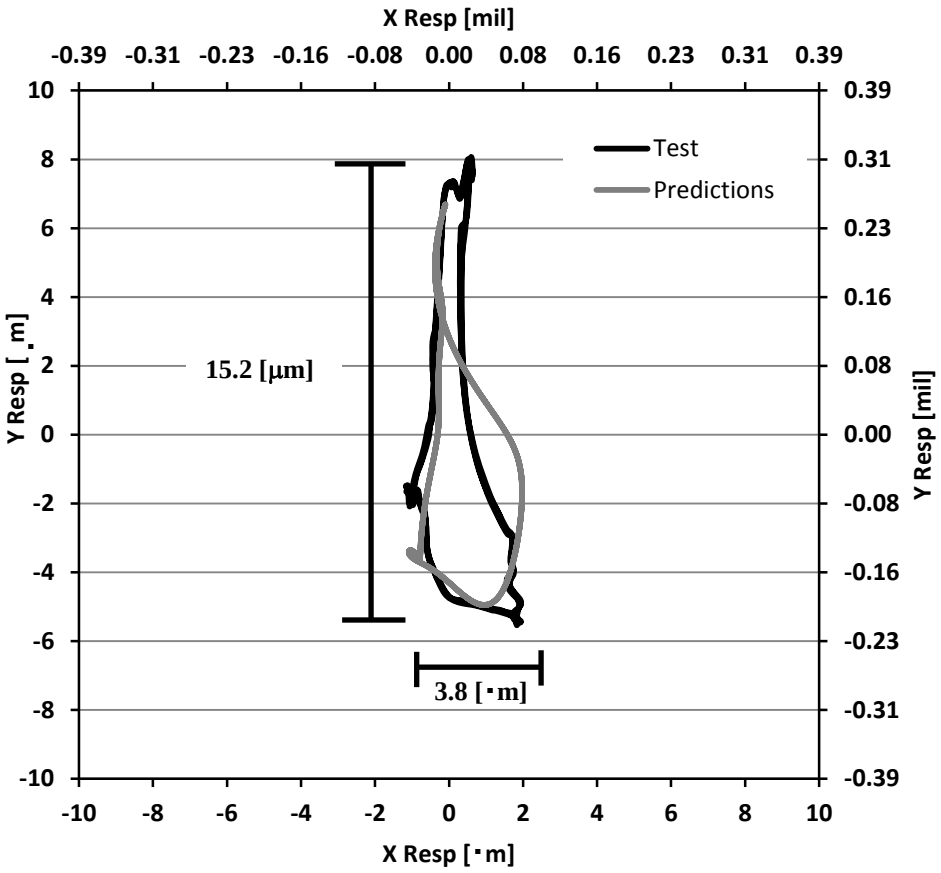

Figure 99 Measured versus predicted orbit at the mid span

Figure 100 and Figure 102 compare the dynamic spectrums of the vertical and horizontal responses. In the vertical direction, the predictions match the response component at the synchronous speed closely, but under predict the response component at two times the running speed by 50%. In the horizontal direction, the predictions match the measurements closely in all four first harmonics.

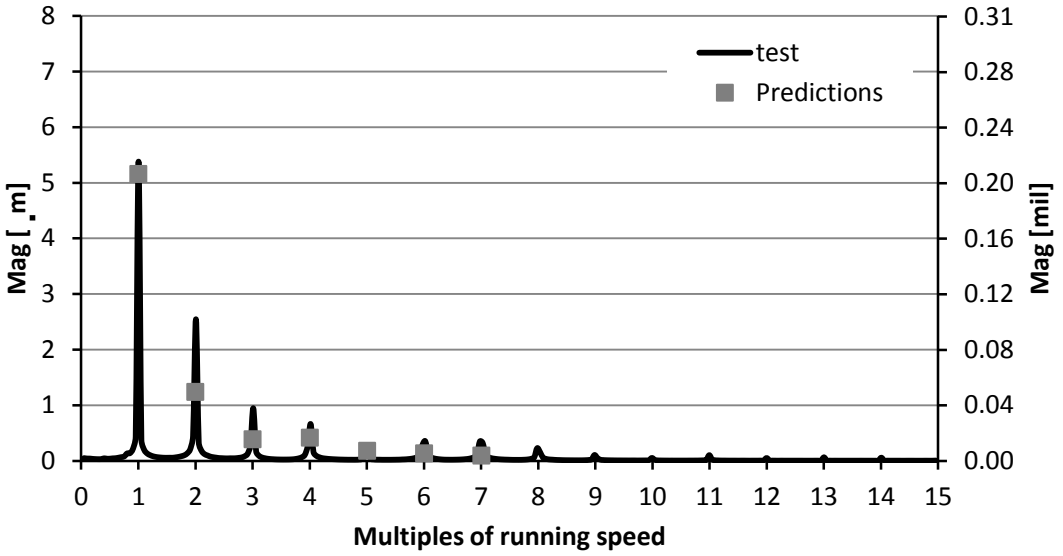

Figure 100 Measured versus predicted vertical dynamic response spectrum at the mid span

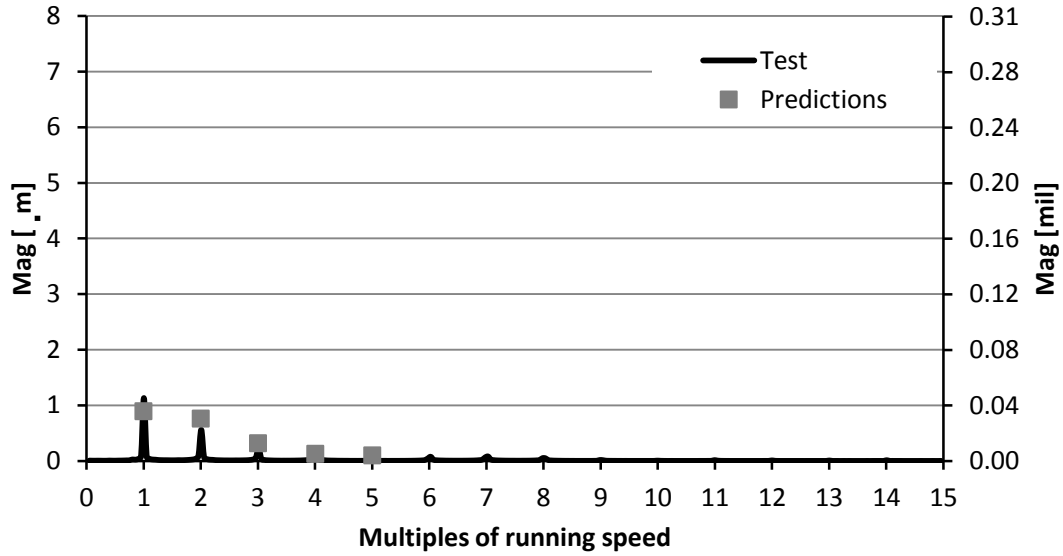

Figure 101 Measured versus predicted horizontal dynamic response spectrum at the mid span

5.1.4 Dynamic response variation with pump speed

To study the effect of change in running speed on the rotor response, the speed of the pump was varied from 900 rpm to 1800 rpm with 75 rpm steps. The spectrum in the water-

fall plot of the vertical response in Figure 102 is obtained in a similar manner to the FFT procedure described earlier at the end of section **Error! Reference source not found.**. The water fall plot shows distinct 1x through 9x frequency components.

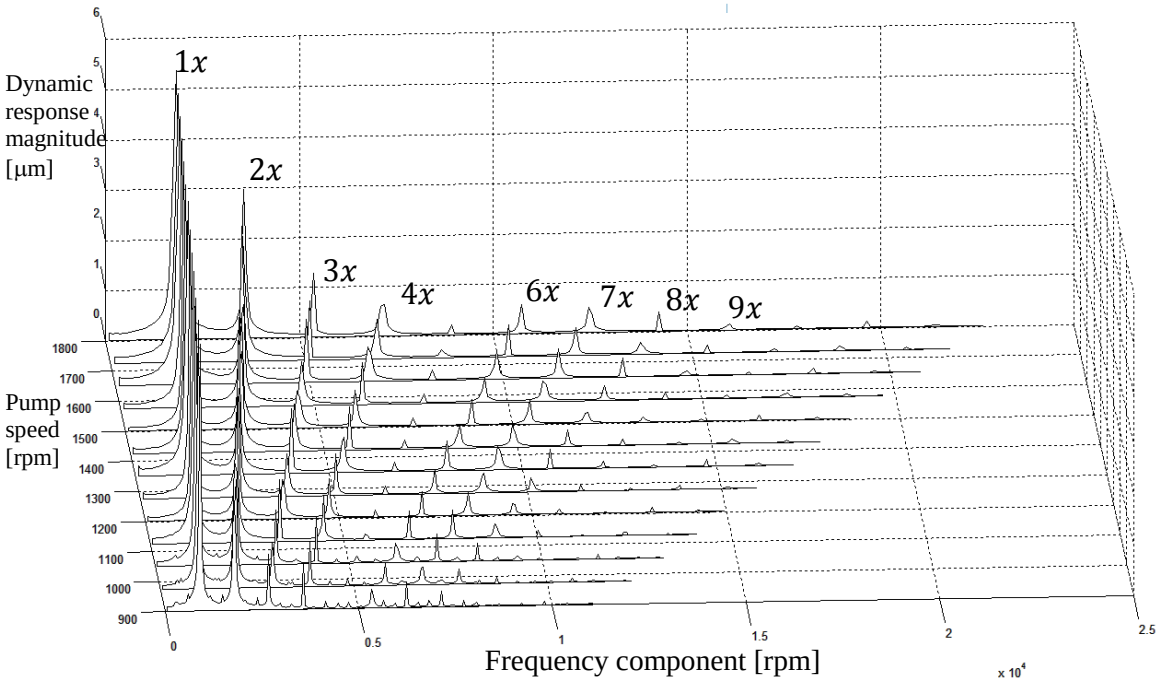

Figure 102 Water fall plot of the measured vertical response spectrum at the mid span

Each frequency spectrum corresponding to a pump running speed in Figure 102 is the result of a separate run. In each run the discharge pressure is maintained at ~31.7E5 Pa (~45 psi). Because of their working principle, the pressure head rise of twin-screw pumps is independent of the pump speed. The model in Chapter 3 predicted that the pressure field distribution (and consequently the resulting forces) do not depend on pump speed. The estimation of the mechanical imbalance and the natural frequency of the rotor-bearing system discussed in Chapter 4 confirm that the mechanical imbalance response is insignificant in the current speed range compared to the response from the unbalanced pressure field (refer to Figures 76 and 77 for imbalance response). Therefore, the model predicts that the response spectrum magnitude should not vary with pump speed in the current speed range.

The measurements shown in Figure 103 isolate the 1x response component from the water fall plot in Figure 102. The variation of the 1x magnitude with pump speed shows two

spikes at 1125 and 1350 rpm. The phase angle associated with the response remained constant throughout the speed range as shown in Figure 104 excluding the possibility of rotor-bearing-housing low natural frequency.

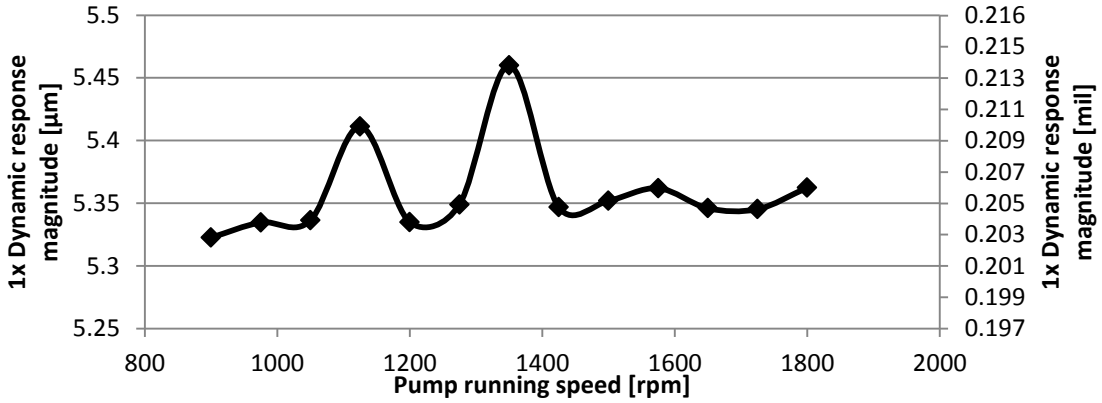

Figure 103 Synchronous response magnitude

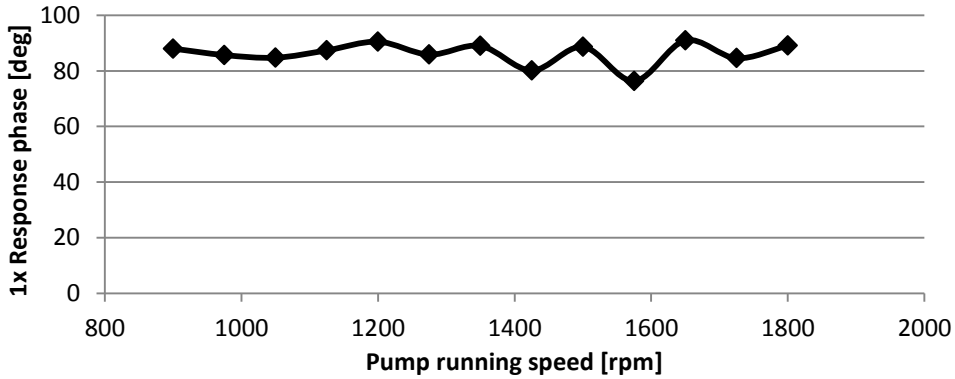

Figure 104 Synchronous response phase

Several single-phase flow runs at 1350 rpm pump speed were conducted to confirm that the response spike is an inherent dynamic characteristic of the system. All runs produced similar response spectra. The author has no explanation for this result.

A 12-second dynamic pressure at 1350 rpm is shown in Figure 105 for the sensors in the vertical (YZ) plane and in Figure 106 for the sensors in the horizontal (XZ) plane. Compared to the dynamic pressure at 1789 rpm shown in Figure 80, the 1350 rpm pressure

field shows more oscillations and more transient spikes as can be confirmed from the variation of the synchronous pressure component.

The vertical discharge pressure shows smaller oscillations compared to other sensors which excludes an excitation of a natural frequency of the downstream piping.

12-second dynamic pressure

Variation in synchronous pressure component

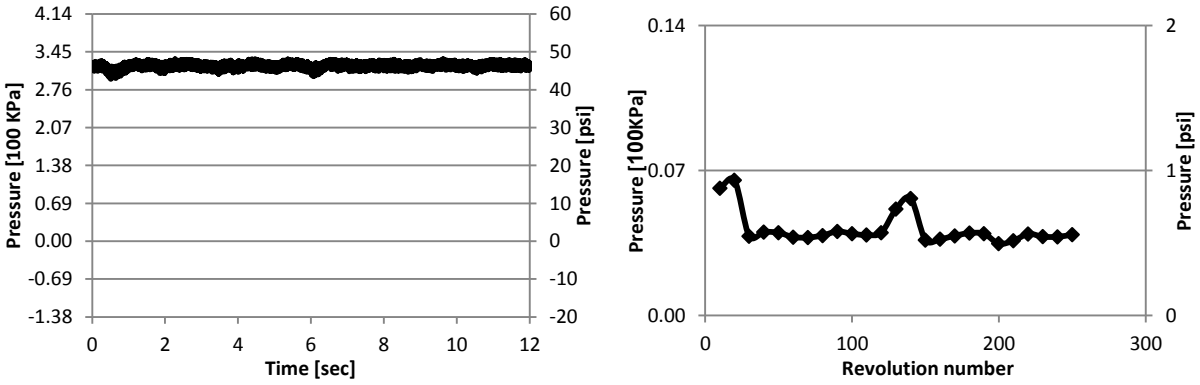

(a) Vertical Discharge

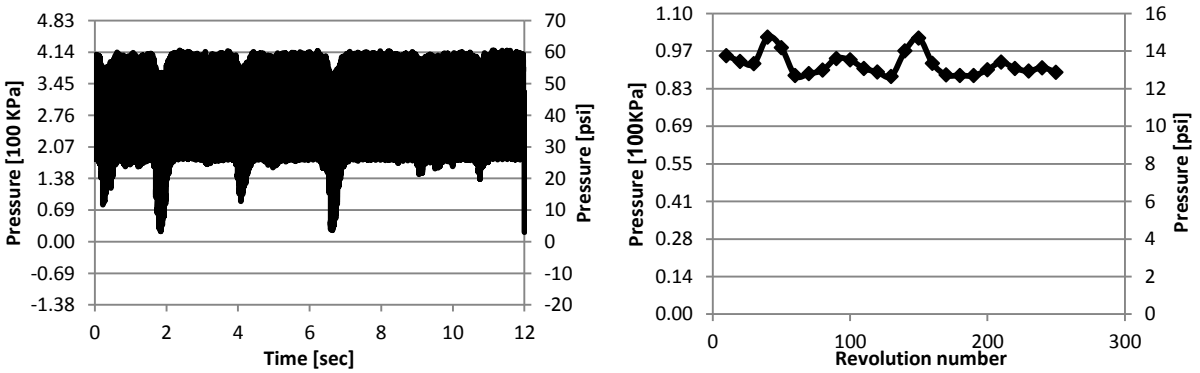

(b) Vertical Middle

Figure 105 Dynamic pressure and variation in synchronous pressure component of the vertical sensors at 1350 rpm

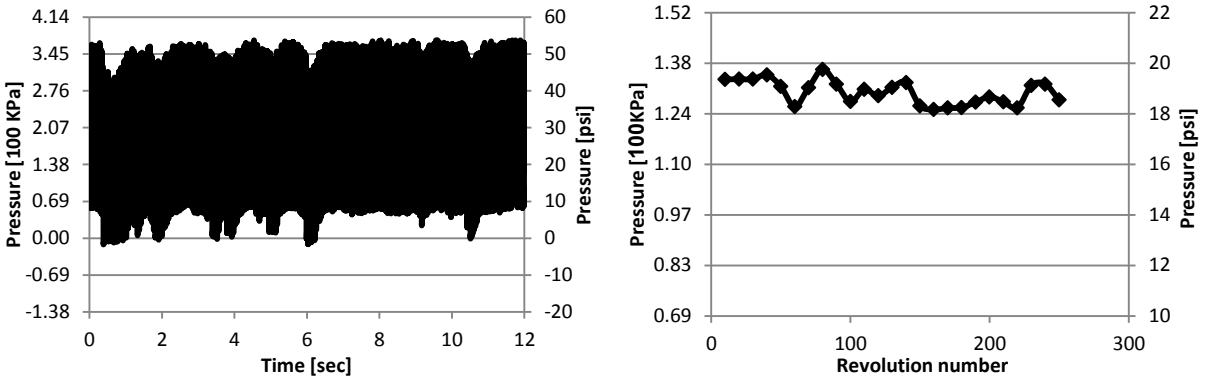

(c) Vertical Suction

Figure 105 Continued

12-second dynamic pressure

Variation in synchronous pressure component

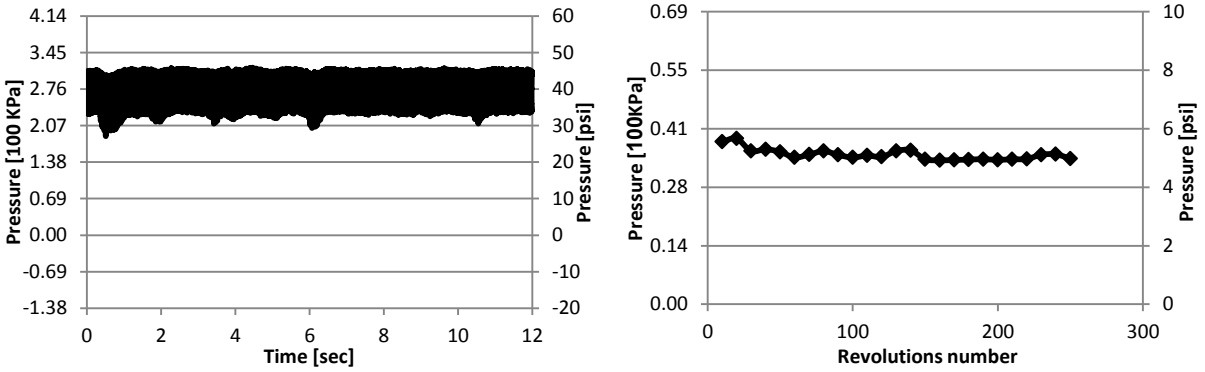

(a) Horizontal Discharge

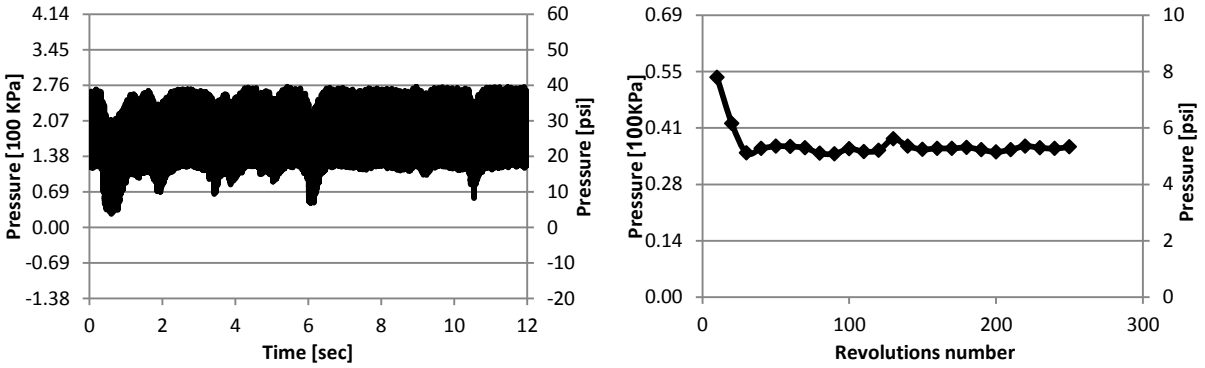

(b) Horizontal Middle

Figure 106 Dynamic pressure and variation in synchronous pressure component of the horizontal sensors at 1350 rpm

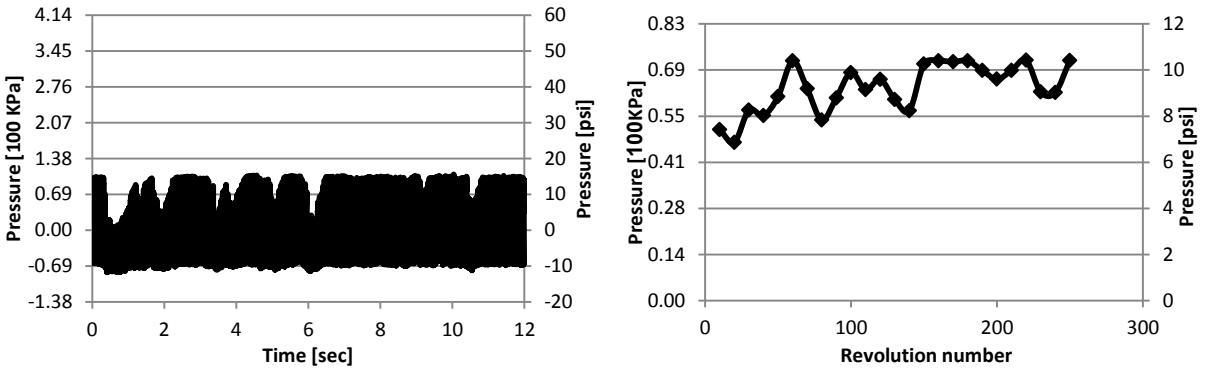

(c) Horizontal Suction

Figure 106 Continued

A rap test of the casing was conducted with the pump stationary to check for a casing mode in the operating range. An accelerometer was successively mounted on two spots of the casing in the vertical and horizontal directions, and several impulse excitations were applied to the casing at different directions. All measured casing modes were higher than the operating range, excluding the possibility of casing excitation or interaction as well. In the absence of reasonable explanation of the dependency of the pump response and the erratic pressure field at the two running speeds 1125 and 1350 rpm, this phenomenon needs further investigation with a different pump to determine if it is an inherent characteristic of twin-screw pumps, or if it is associated with specific operating conditions and pump design. No part of the model developed in chapter 3 predicts a dependence of the response or the pressure field on the pump running speed.

5.2 Multiphase results

This section presents the multiphase results and compares them to the predictions from the model. *In the rest of this section, the low GVF is 27%, medium GVF is 42% and high GVF is 65%. All runs are at the constant speed 1789 rpm and constant discharge pressure of ~31.7E5 Pa (~45 psi).* Subsection 5.2.1 presents the dynamic pressure measurements, the axial pressure buildup and circumferential pressure distribution of the three GVF ratios. Subsection 5.2.2 compares the dynamic pressure measurements to the pressure predictions in time and frequency domains for the three GVF ratios. Subsection 5.2.3 presents the prediction of the static forces and compares the predicted and measured static responses. Finally, the predicted dynamic forces and the measured and predicted

dynamic response orbits are presented in subsection 5.2.4 in the time and frequency domains.

Figure 67 introduced the locations and acronyms of the pressure sensors. The pressure sensor acronyms are reintroduced here and will be used in this section for brevity.

HS refers to Horizontal Suction sensor

HD refers to Horizontal Discharge sensor

HM refers to Horizontal Middle sensor

VS refers to Vertical Suction sensor

VM refers to Vertical Middle sensor

VD refers to Vertical Discharge sensors.

5.2.1 Dynamic pressure measurements

Figure 107 compares a 12-second dynamic pressure measurements of the three sensors in the horizontal direction for the low, medium and high GVF ratios. The results show more erratic transient oscillations compared to the single-phase pressure measurements in Figure 80.

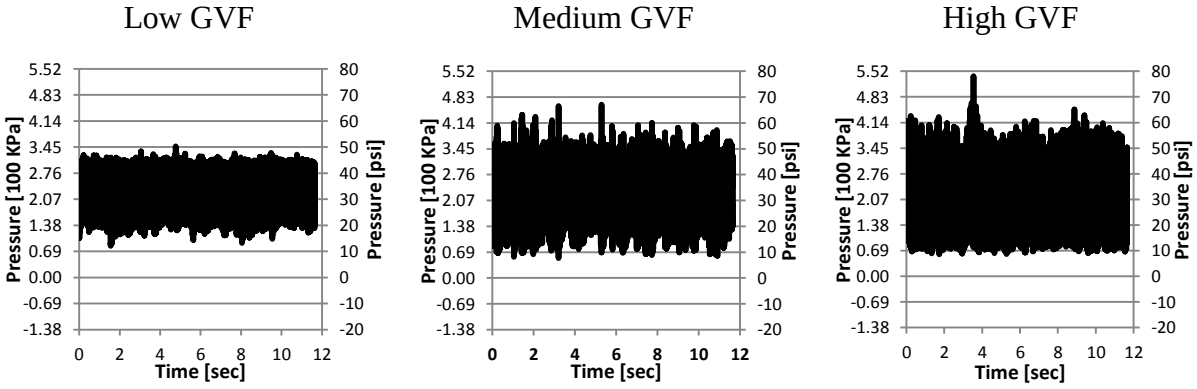

(a) Horizontal Discharge

Figure 107 12-seconds dynamic pressure measurements of the sensors in the horizontal direction along the ZX plane

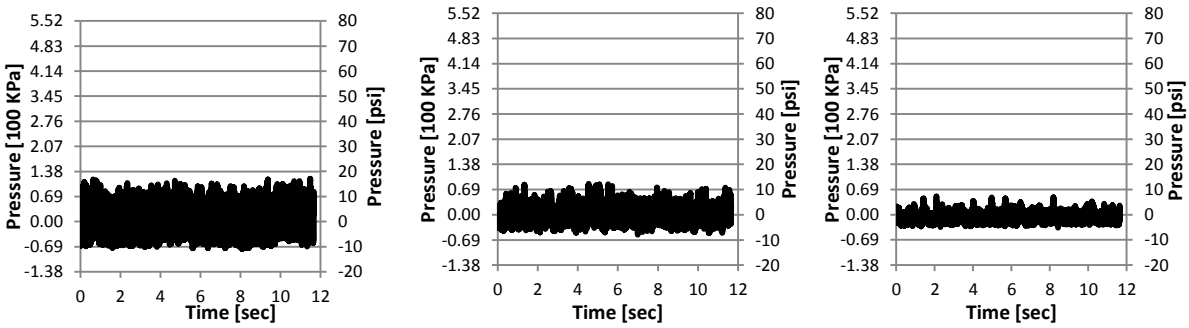

(b) Horizontal Middle

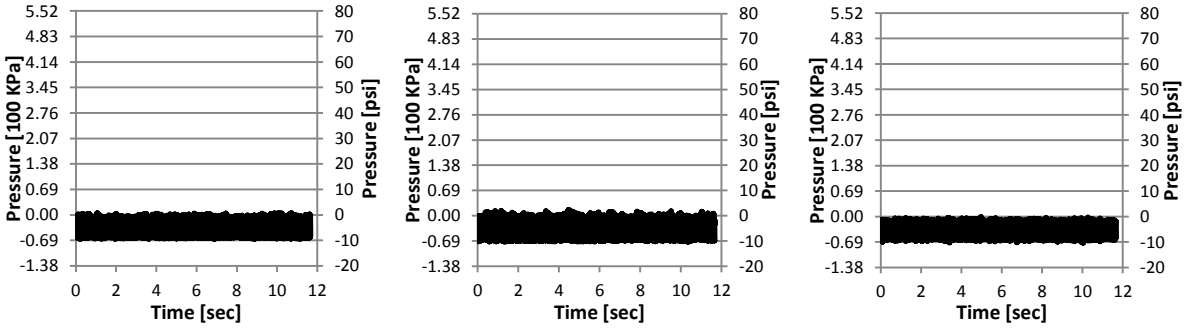

(c) Horizontal Suction

Figure 107 Continued

Figure 108 compares the variation of the synchronous component of the dynamic pressure along the duration of the 12-seconds. Compared to the single phase measurements shown in Figure 91, the multiphase shows higher variation in the synchronous dynamic pressure component.

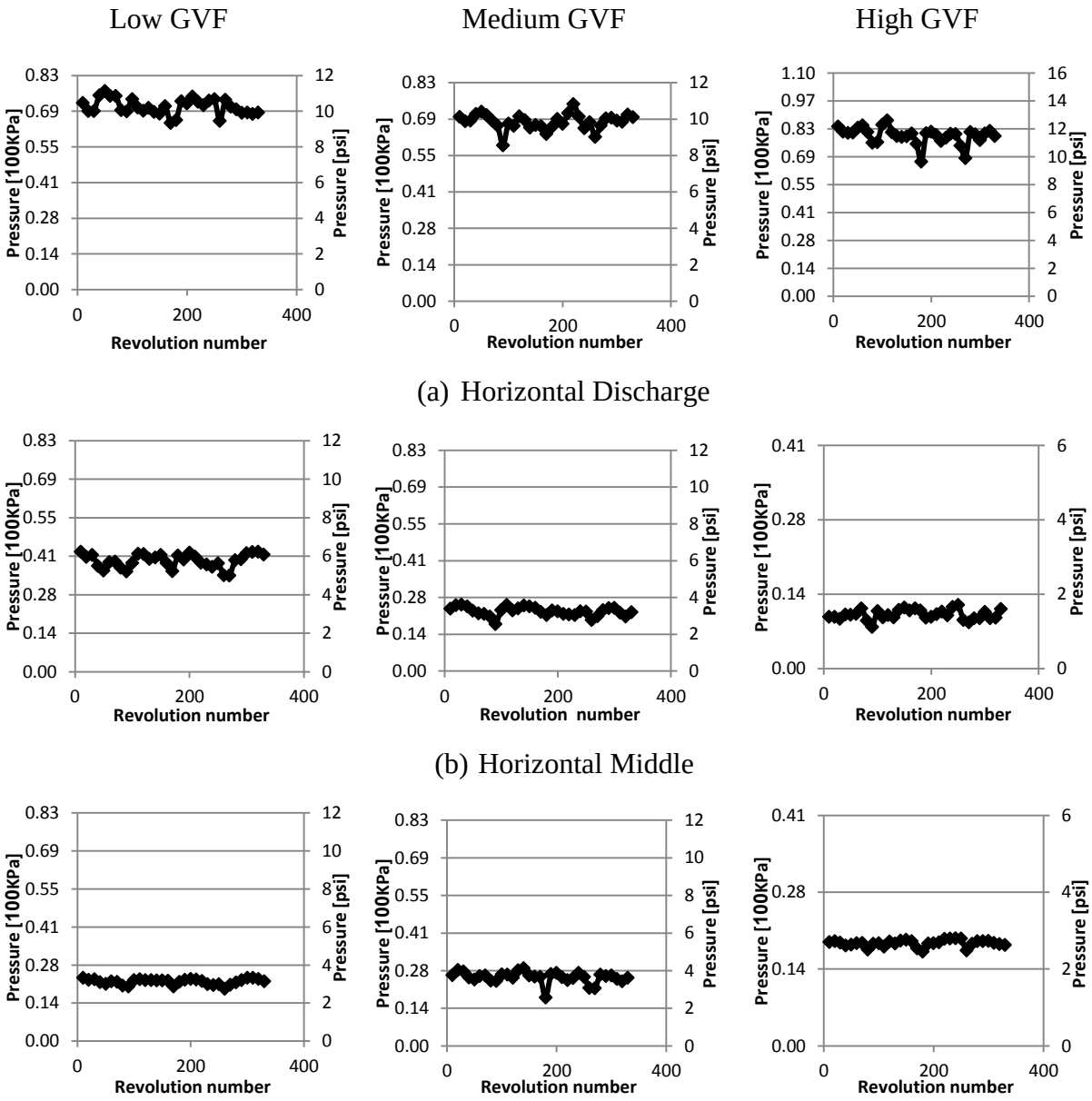

Figure 108 Variation of the synchronous pressure component of the dynamic pressure measurements of the sensors in the horizontal direction (XZ plane)

Similar to Figure 107 and Figure 108, the measurements of the sensors in the vertical direction (YZ plane) are shown in Figure 109 for the dynamic pressure and Figure 110 for the variation of the synchronous component of the pressure. The range of the transient variation in pressure at the vertical discharge sensor is ~1.38E3 kPa (~20 psi) for the high GVF ratio compared to ~0.2E3 kPa (~3 psi) in the case of single phase as shown in Figure

80. The larger range of pressure oscillation indicates that the discharge is affected by the dynamic pressure in the screws for high GVF ratio more than single-phase flow.

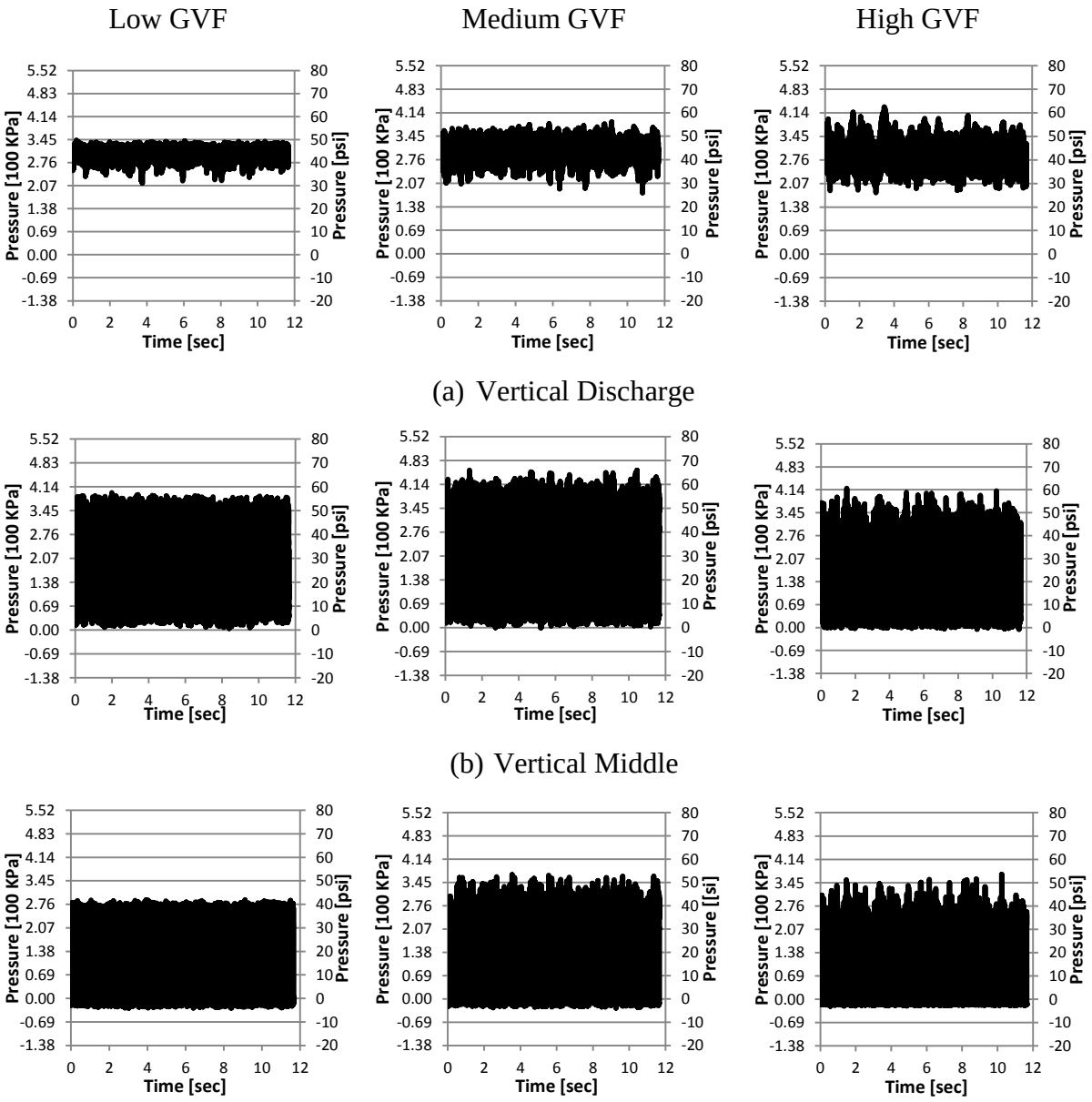

Figure 109 12-seconds dynamic pressure measurements of the sensors in the vertical direction along the YZ plane

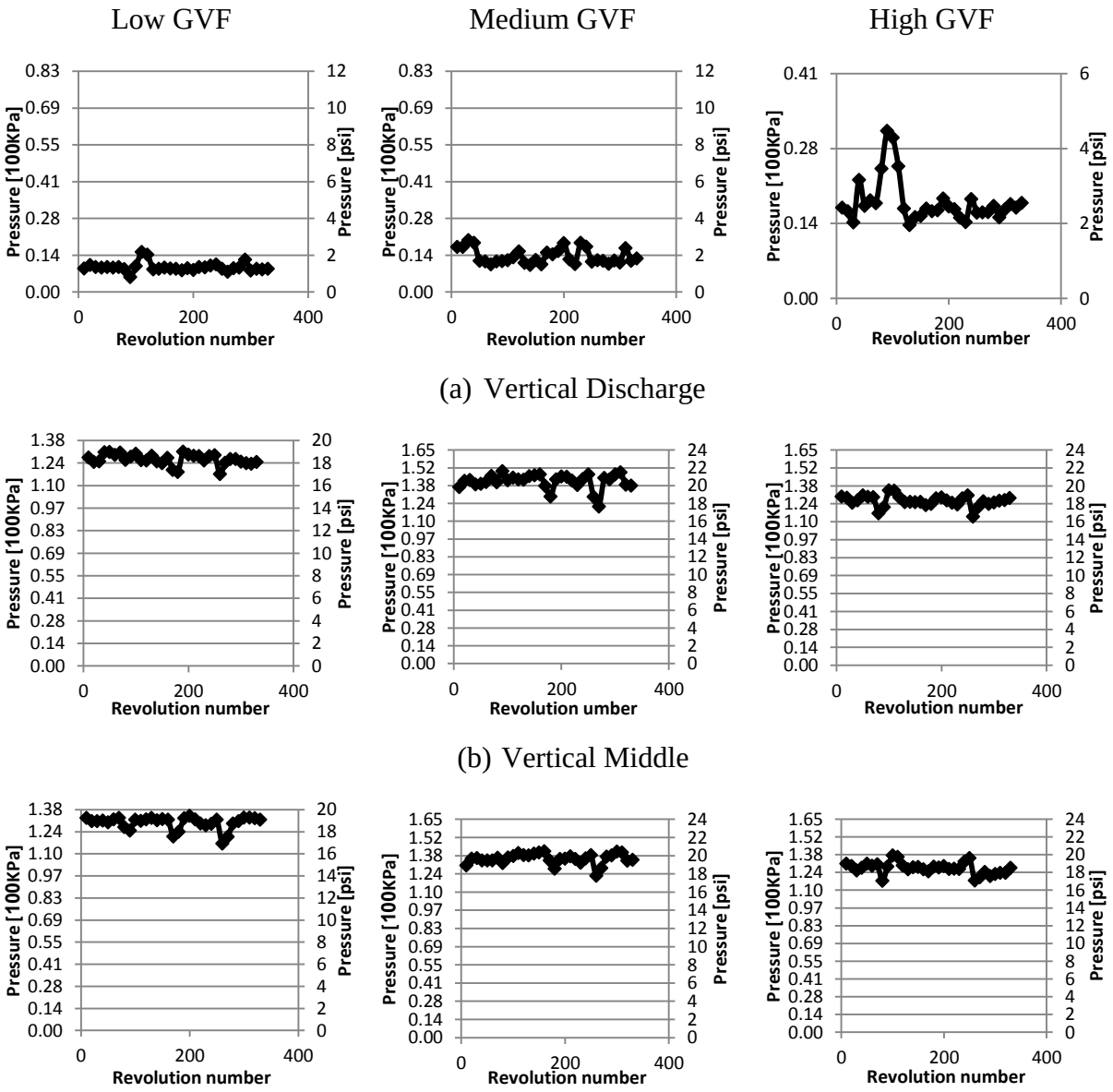

Figure 110 Variation of the synchronous pressure component of the dynamic pressure measurements of the sensors in the vertical direction (YZ plane)

The erratic oscillations of the time transient multiphase dynamic pressure measurements shown in Figures 107 and 109 compared to the stationary single phase dynamic pressure measurements shown in Figure 80 are likely due to the unsteady flow in multiphase operation. Figure 111 shows the dynamic pressure and spectra at the inlet compartment upstream of the screw suction. The erratic suction pressure measurements and

the noisy spectra indicate that the pressure oscillation in the multiphase operation is likely not related to rotordynamic phenomena.

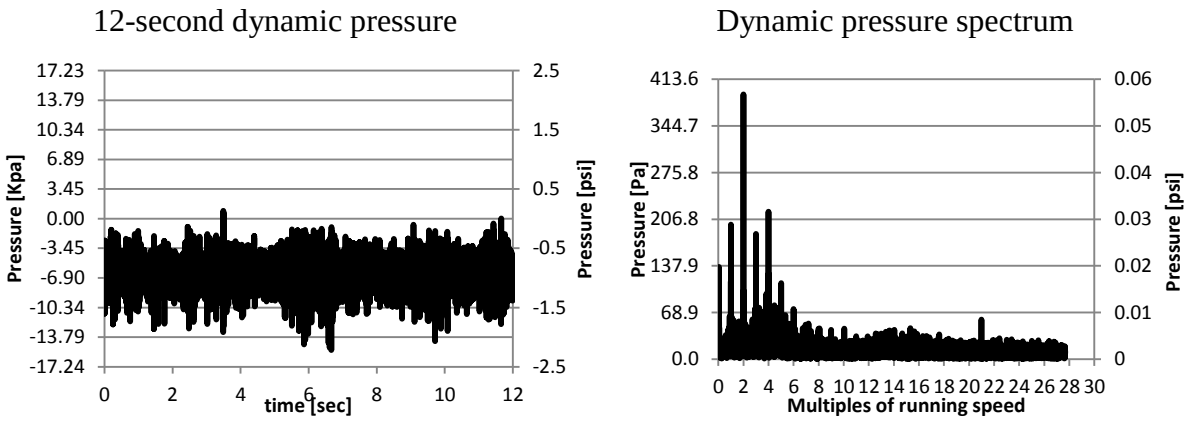

(a) Low GVF

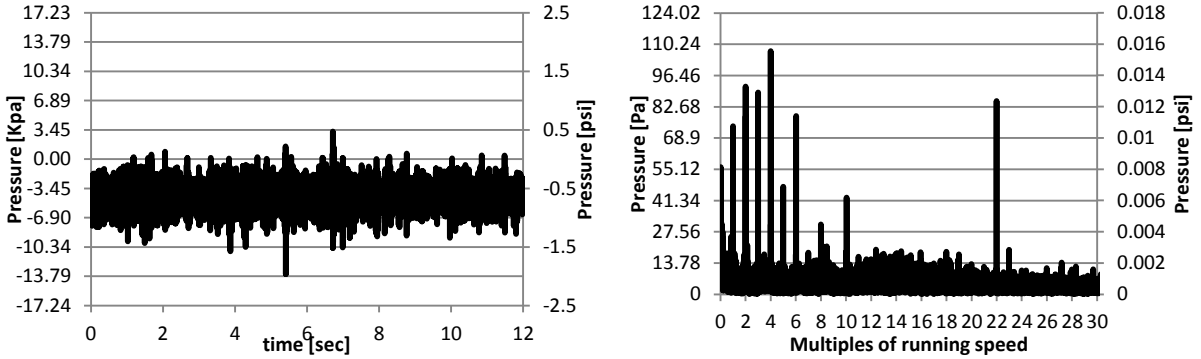

(b) Medium GVF

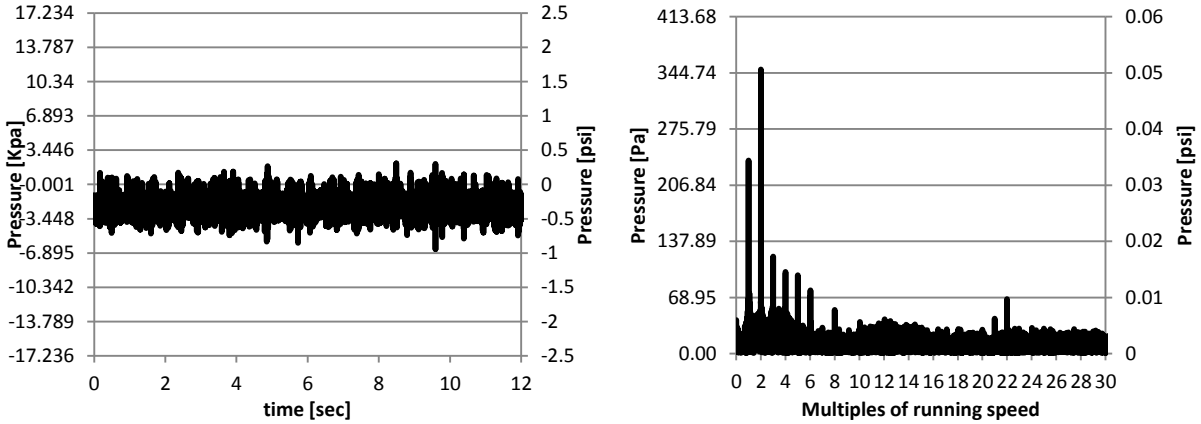

(c) High GVF

Figure 111 Dynamic inlet pressure and pressure spectra

Besides showing distinctively noisy pressure oscillations, the dynamic measurements and spectra in Figure 111 point to a possible low-frequency flow phenomenon related to the pump loop. Figure 112 shows the frequency components of the inlet pressure below half the running speed (1789 rpm). The frequency response shows a peak at 0.041 of the running speed (75 rpm).

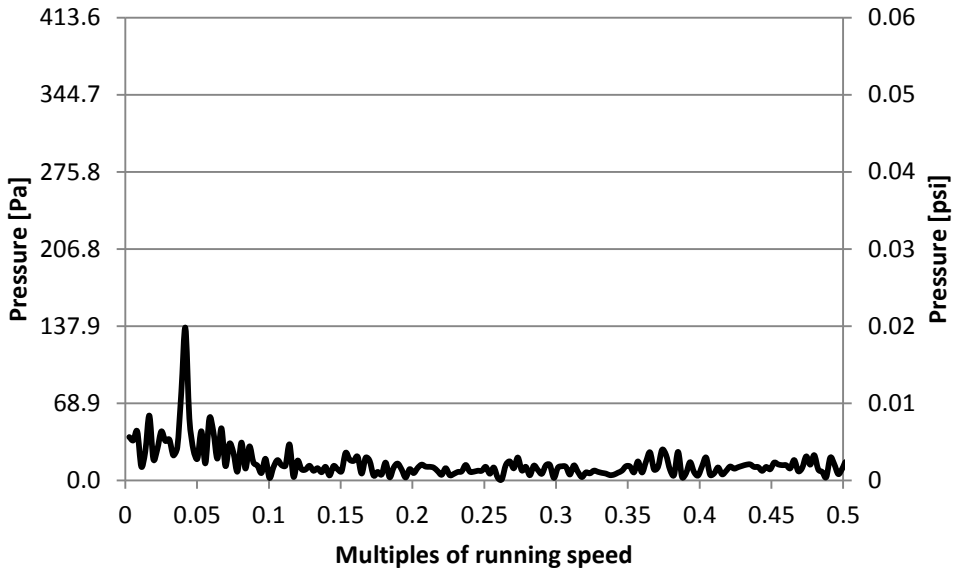

Figure 112 Low-frequency spectrum of the dynamic inlet pressure at low GVF

Although the measurements in Figure 111 and the low-frequency component in Figure 112 point at oscillation in the flow loop as a possible explanation for the ripples in the multiphase dynamic pressure measurements, the frequency of oscillation in Figure 112 is unrelated to running speed or pump rotordynamics. Note that the range of the suction ripples is within 10 KPa (1.5 psi), which supports the assumption of a constant boundary pressure at suction.

Figure 113 shows the dynamic axial pressure distribution for the three GVF ratios. The parabolic pressure buildup is evident from comparing the single phase results shown earlier in Figure 81and Figure 82 with the results in Figure 113. Most of the pressure head rise is achieved at the last chamber in the case of multiphase flow with high GVF.

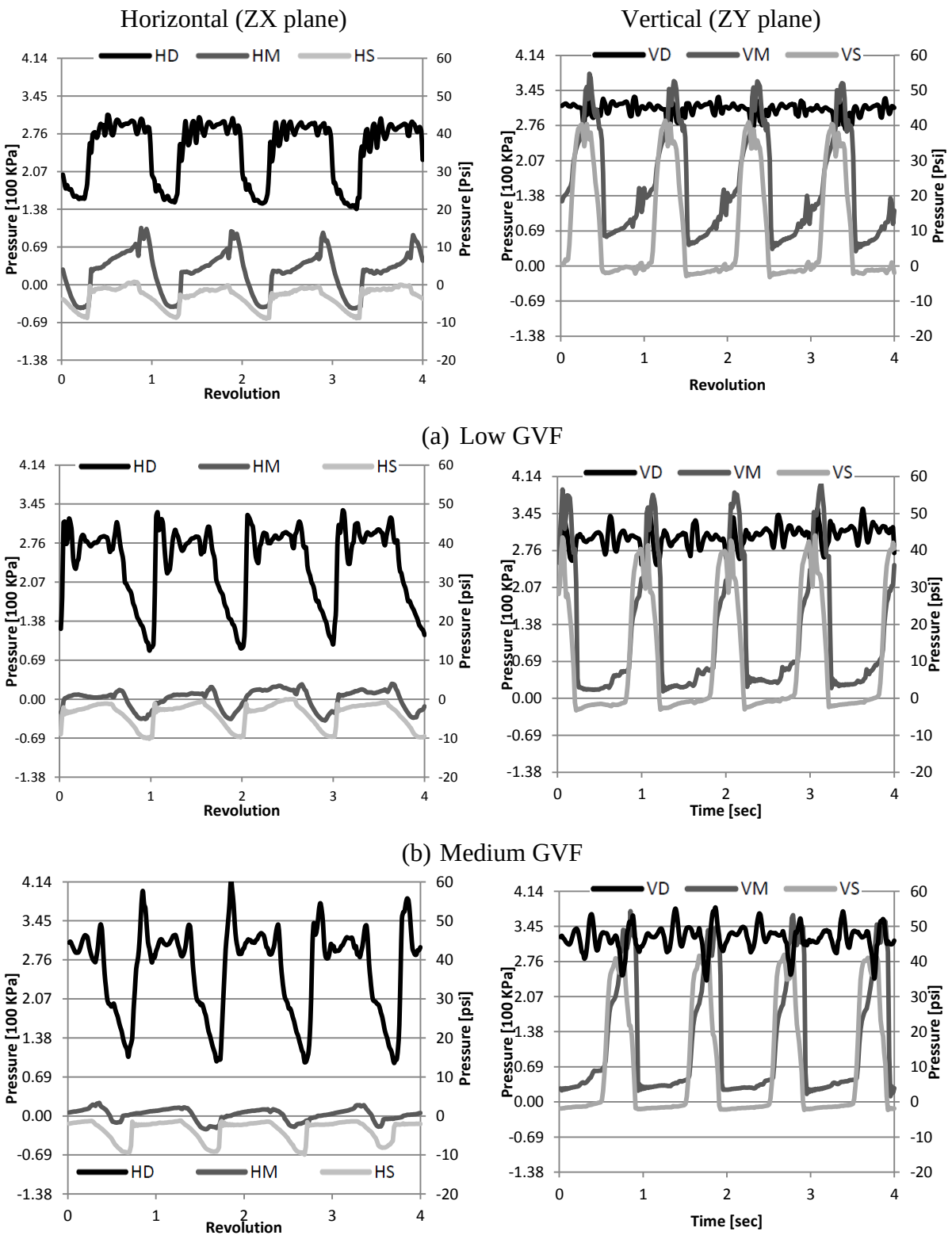

(a) Low GVF

(b) Medium GVF

(c) High GVF

Figure 113 Measured dynamic pressure axial distribution

Figure 114 shows the measured pressures at the discharge, middle and suction sensors for the low, medium and high GVF cases. With the exception of the increasing parabolic axial pressure distribution and the higher oscillation, the multiphase results show essentially similar dynamic pressure characteristics as the single phase.

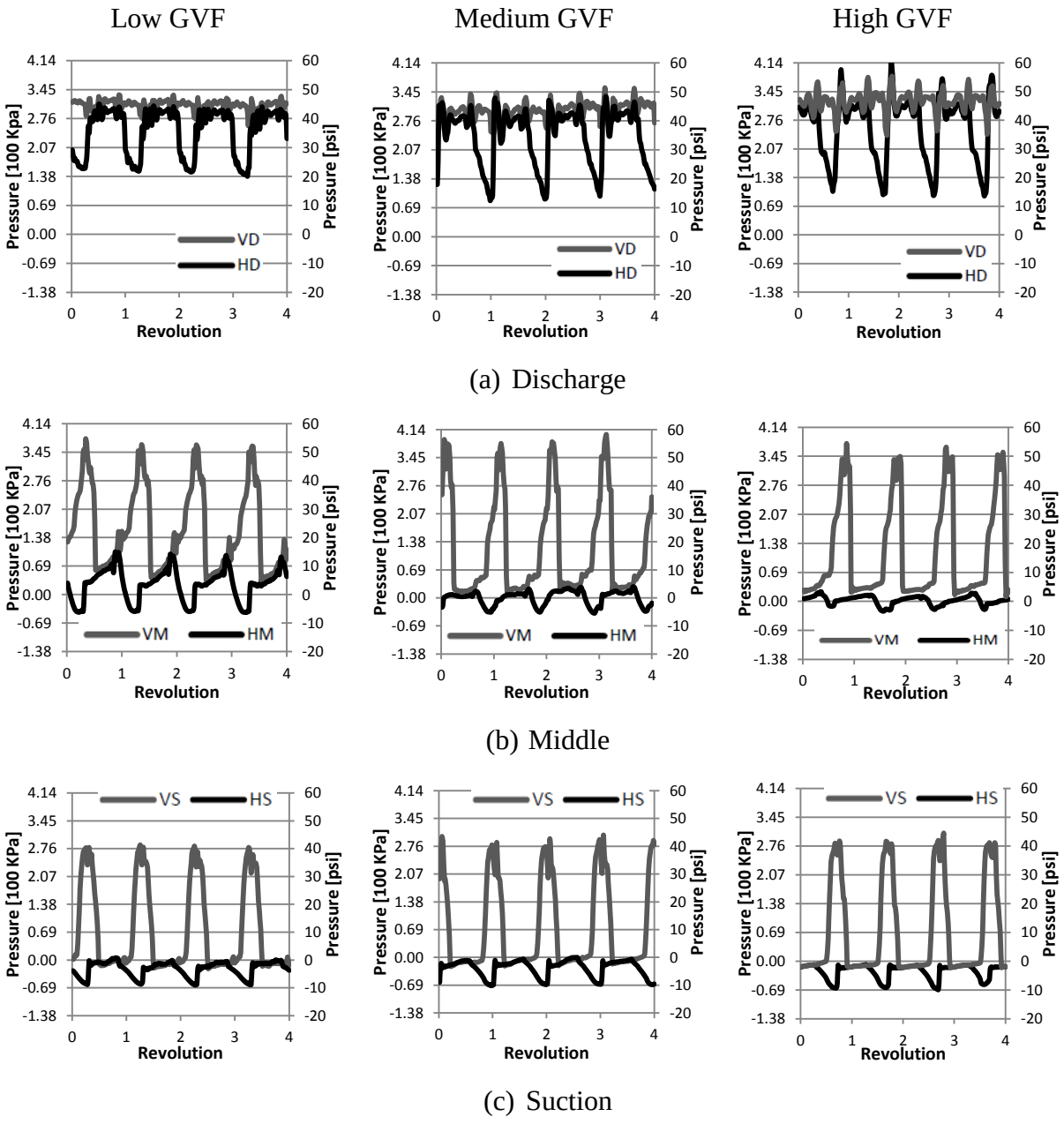

Figure 114 Measured dynamic pressure circumferential distribution

5.2.2 Dynamic pressure measurements versus predictions

Figure 115 compares the measured to predicted dynamic pressure of the horizontal sensors for the low, medium and high GVF. The predictions are generally in good agreement with the measurements. The predictions of the single phase model in Figure 88 show better agreement with measurements than the multiphase predictions shown in Figure 115.

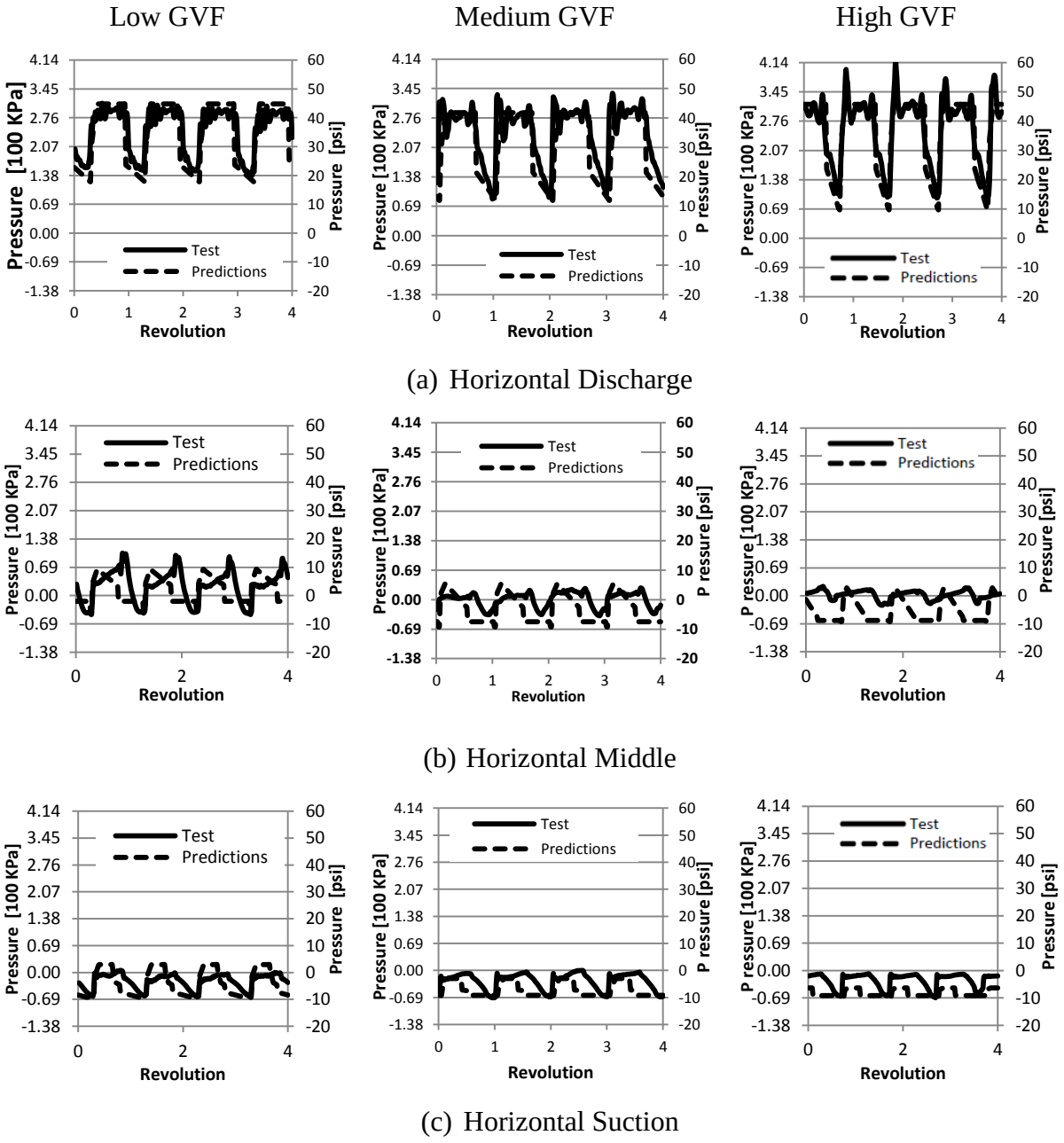

Figure 115 Horizontal dynamic pressure measurements versus predictions

Figure 116 compares the measured to predicted dynamic pressure of the vertical sensors for the low, medium and high GVF ratios. The model assumes the discharge pressure is constant. The discharge pressure measurements show ripples consistent with the opening and closing of the discharge chamber. The predictions at the middle sensors match the measurements closely for all three GVF ratios, while the predicted pressures at suction are consistently lower than the measured.

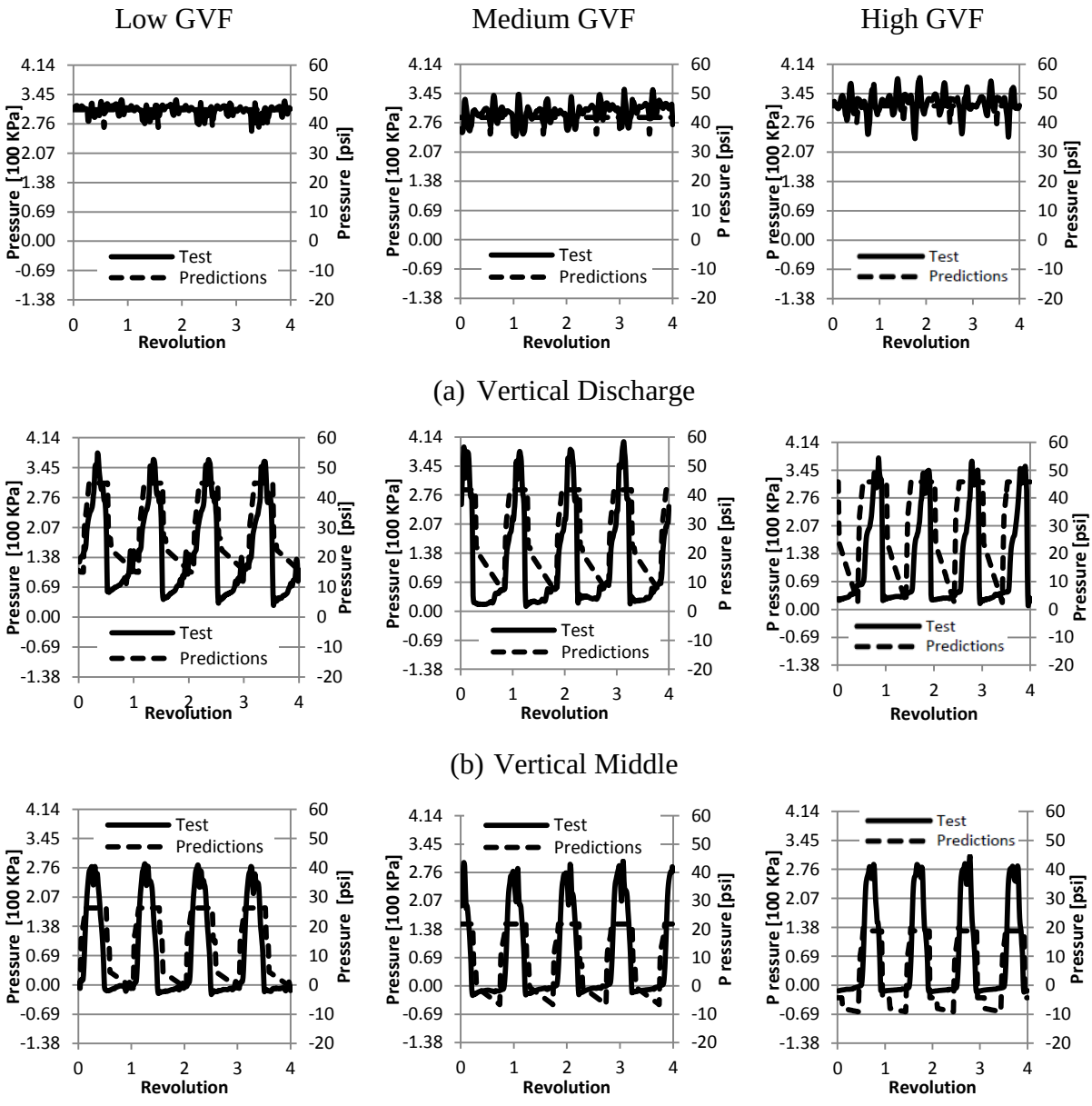

Figure 116 Vertical dynamic pressure measurements versus predictions

The measured and predicted spectra of the dynamic pressure at the six sensors are compared in Figures 117 118 and 119 for low, medium, and high GVF respectively. In general, the predictions match the measurements satisfactorily. The $2x$ component in the vertical direction is consistently under-predicted, but the synchronous component is closer to the measurements. In the horizontal direction the synchronous component is consistently over-predicted, and the component at twice the running speed is consistently under-predicted.

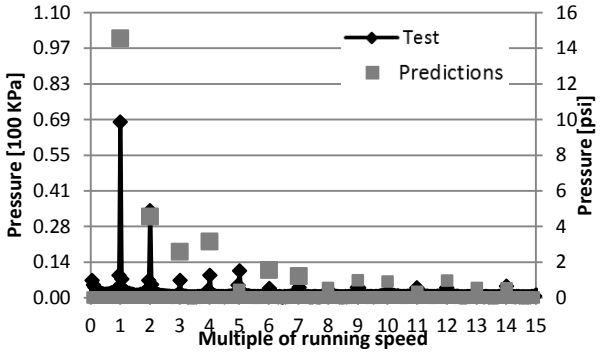

Horizontal Discharge

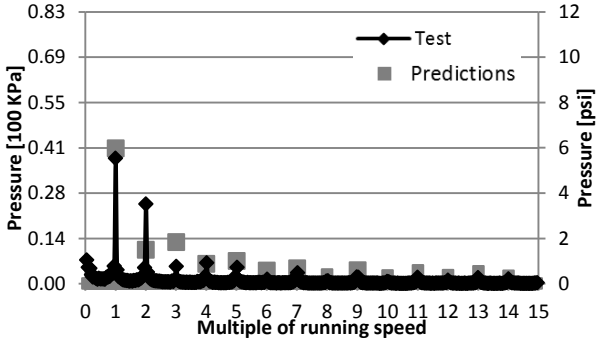

Horizontal Middle

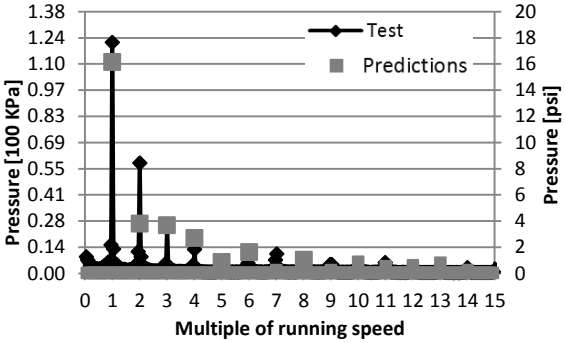

Vertical Middle

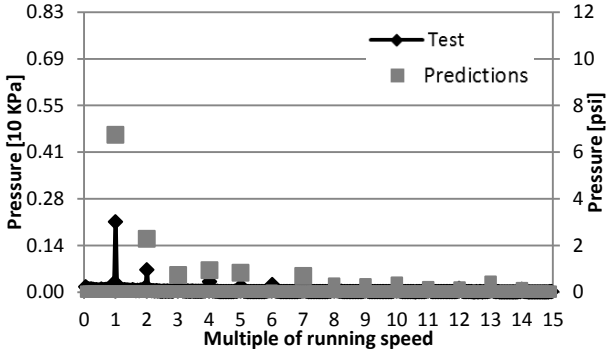

Horizontal Suction

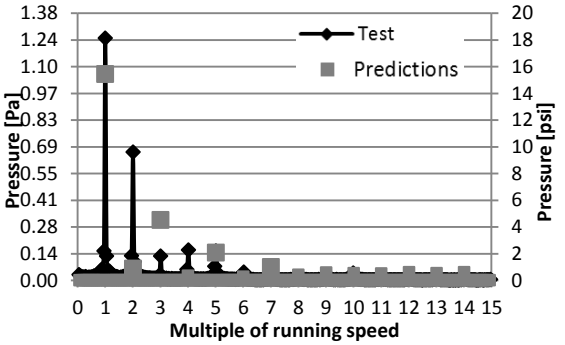

Vertical Suction

Figure 117 Dynamic pressure spectra measurements versus predictions (Low GVF)

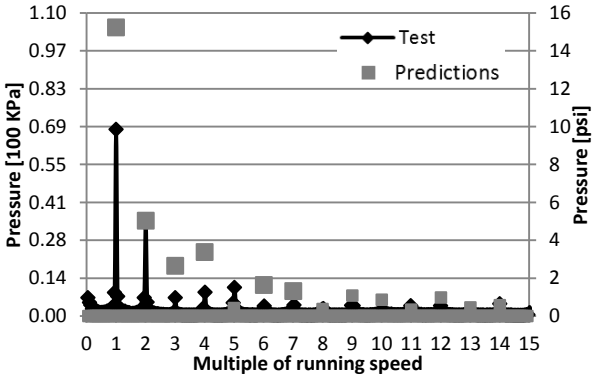

Horizontal Discharge

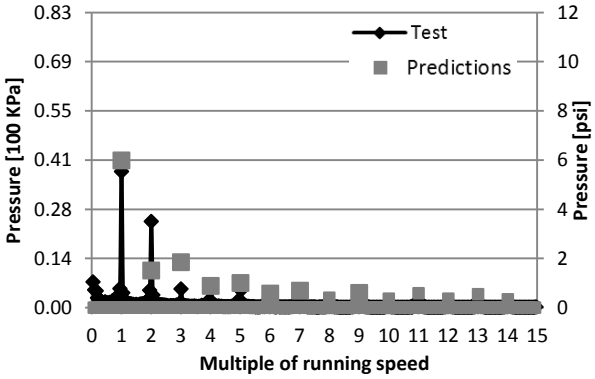

Horizontal Middle

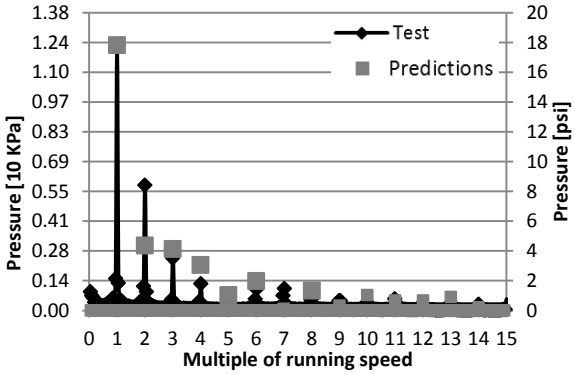

Vertical Middle

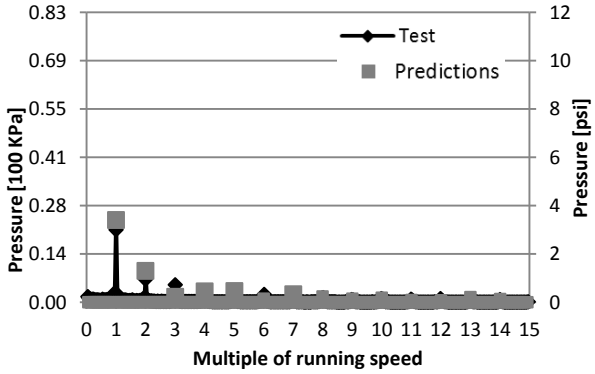

Horizontal Suction

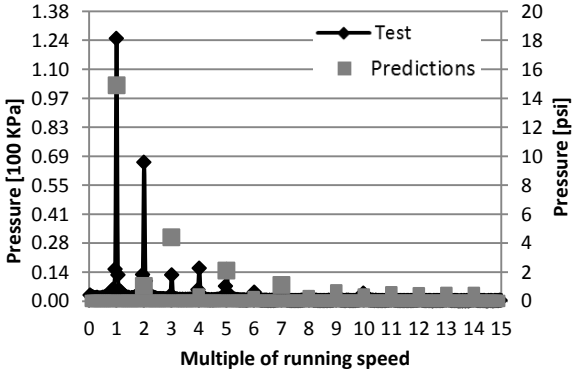

Vertical Suction

Figure 118 Dynamic pressure spectra measurements versus predictions (Medium GVF)

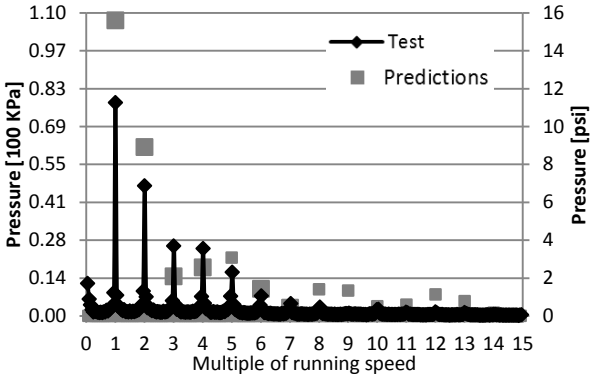

Horizontal Discharge

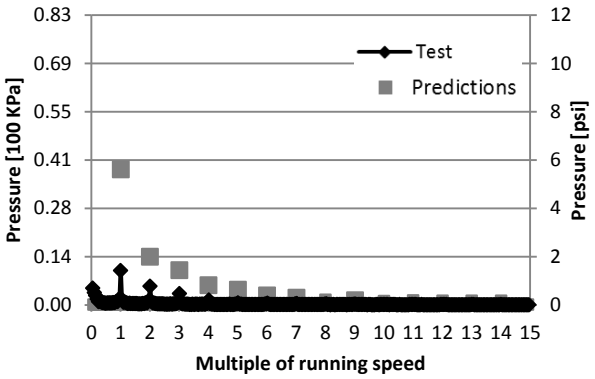

Horizontal Middle

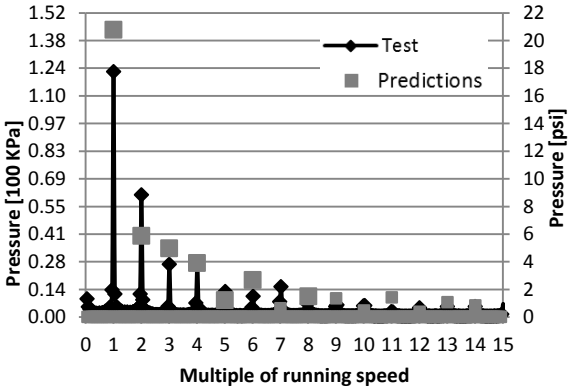

Vertical Middle

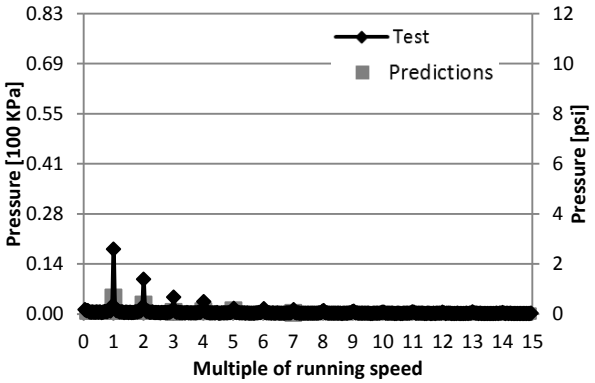

Horizontal Suction

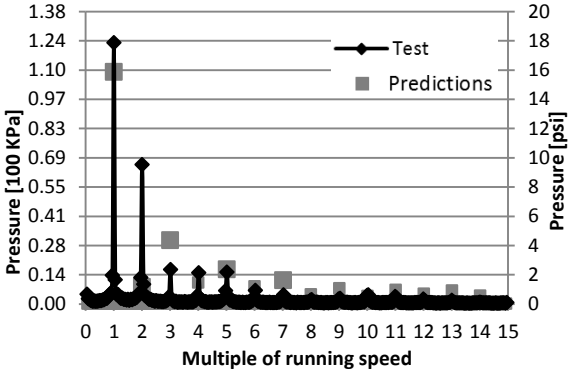

Vertical Suction

Figure 119 Dynamic pressure spectra measurements versus predictions (High GVF)

5.2.3 Static response measurements versus predictions

Figure 120 compares the predicted axial vertical static force buildup for the single phase, low GVF, medium GVF, and high GVF. The axial force buildup is roughly constant in the case of the single phase and becomes increasingly parabolic with increasing the GVF.

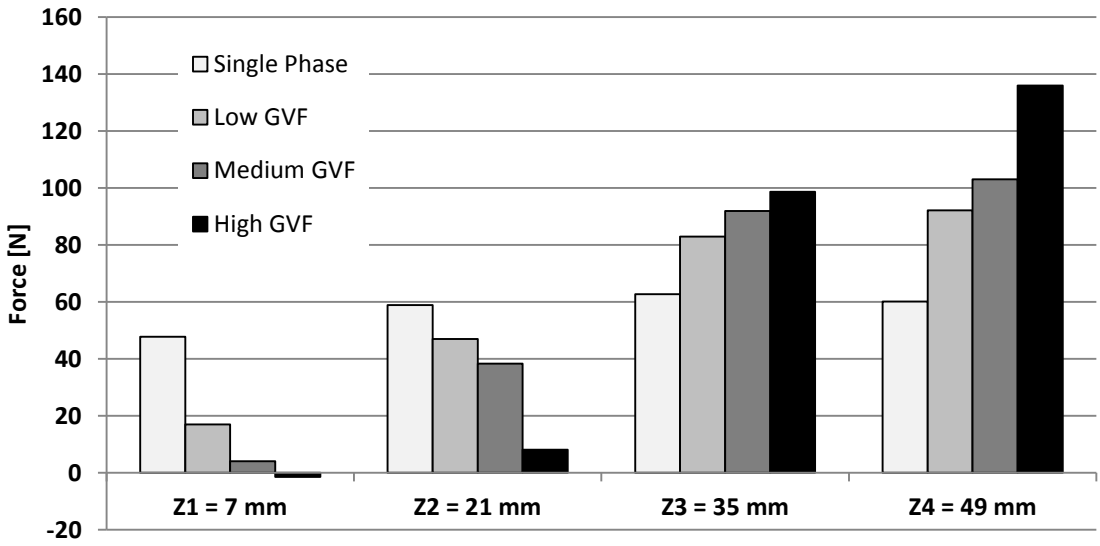

Figure 120 Predicted vertical static force axial distribution

Figure 121 compares the measured versus predicted static deflection at mid span for single phase, low, medium and high GVF ratio cases. The measured static deflection values at the mid span are close to each other in all four operating conditions. The slightly higher deflection in the case of high GVF is due to shift of the effective force to the mid span of the rotor. The model consistently under predicts the measurements by ~8%.

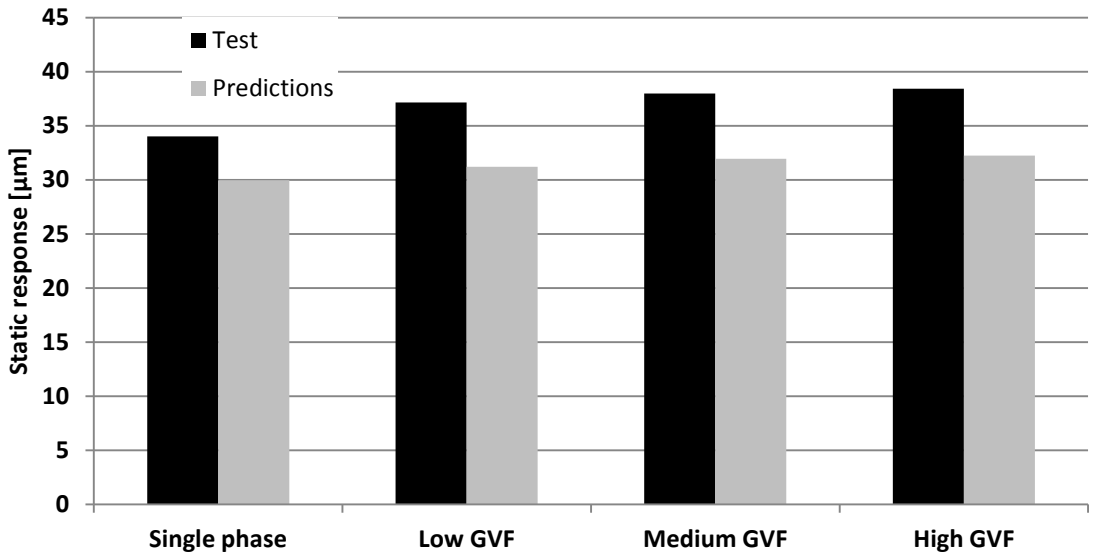

Figure 121 Vertical mid span static deflection measurements versus predictions

Figure 122 shows the predicted horizontal static force at the four axial locations along the length of the screw in the four operating conditions. The forces closer to the suction is predicted in the negative direction pushing the screws away from each other, while the forces closer to the discharge are predicted in the positive direction pushing the screws closer to each other. As mentioned earlier, the combined effects of low magnitude and the change in the force sign from a negative at suction to a positive at discharge, result in a static deflection in the horizontal direction smaller than in the vertical direction.

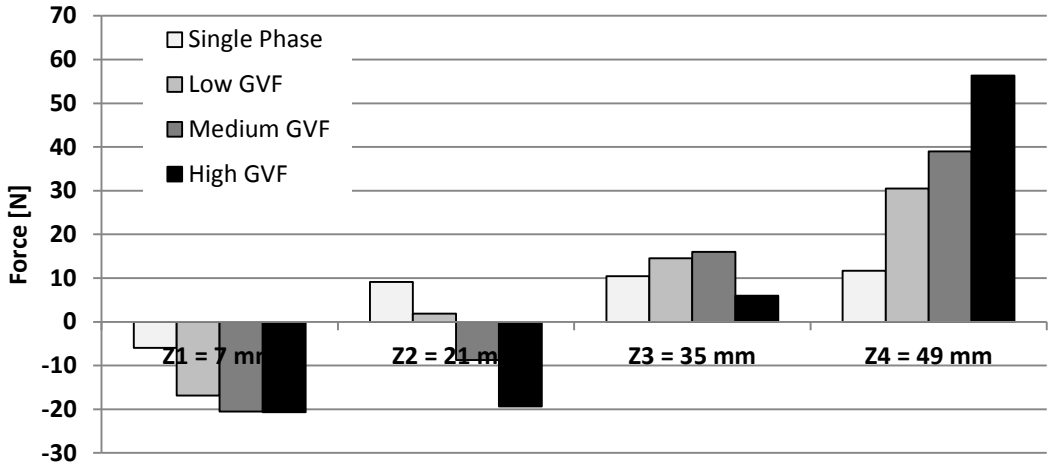

Figure 122 Predicted horizontal static force axial distribution

Figure 123 compares the measured to the predicted horizontal static deflection values at the four operating conditions. The model predicted the measured horizontal static deflection closely in the single-phase flow, while for all multiphase flow conditions the static deflection was consistently under predicted.

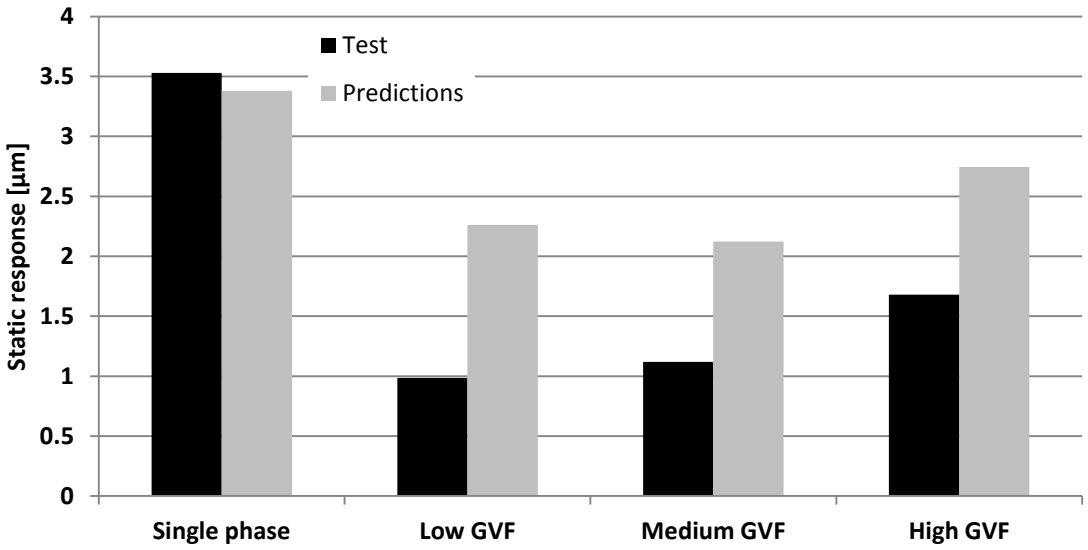

Figure 123 Horizontal mid span static response measurements versus predictions

5.2.4 Dynamic response measurements versus predictions

This section presents the dynamic results of the multiphase operation. First, the predicted dynamic forces are shown for the vertical and horizontal directions. The spectra of the dynamic forces are not shown for brevity. Then, the vertical and horizontal dynamic response measurements are compared to predictions along with their spectrum. Finally, the measured and predicted orbits are presented. The results are shown for the low, medium, and high GVF ratios.

Figure 124 shows the predicted forces in the horizontal and vertical directions. The forces at the suction side (Z1) show less oscillation than in the case of single phase in Figure 94. This reduced force oscillation at the suction is consistent in all three GVF ratios. It is due to the reduced pressure difference between the suction and the first chamber because of the parabolic buildup of pressure in case of multiphase operation.

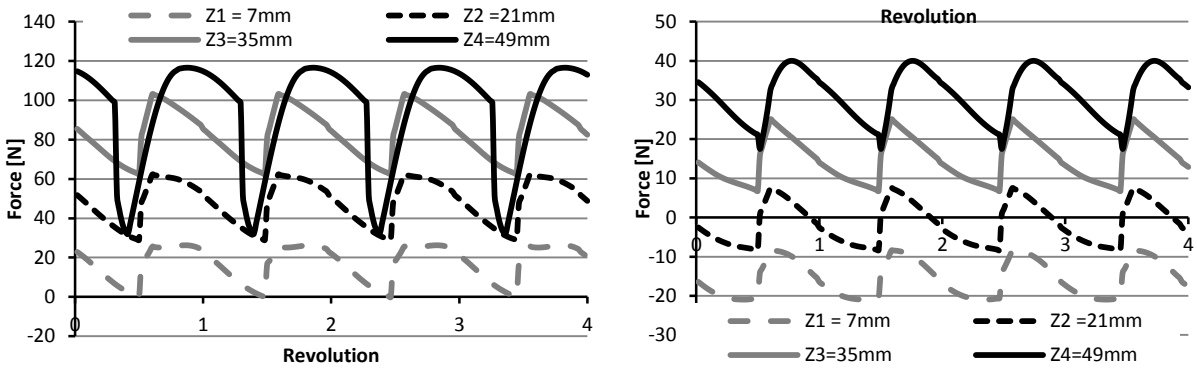

Vertical Force Horizontal Force

Figure 124 Predicted dynamic force components at four axial locations (Low GVF)

Figure 125 compares the measured and predicted response at the rotor mid span in the vertical and horizontal directions. In the vertical direction, the synchronous response is well predicted by the model, while the rest of the harmonics are under-predicted. The predictions are slightly larger than the measurements in the horizontal direction.

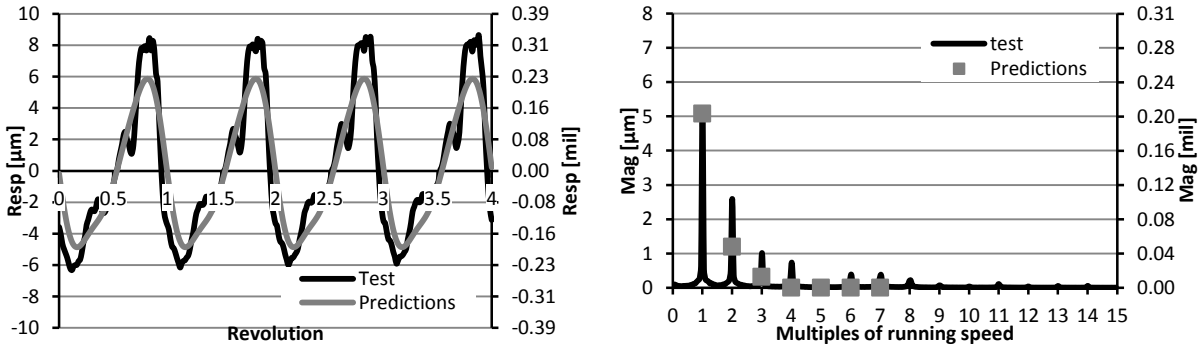

Vertical Response

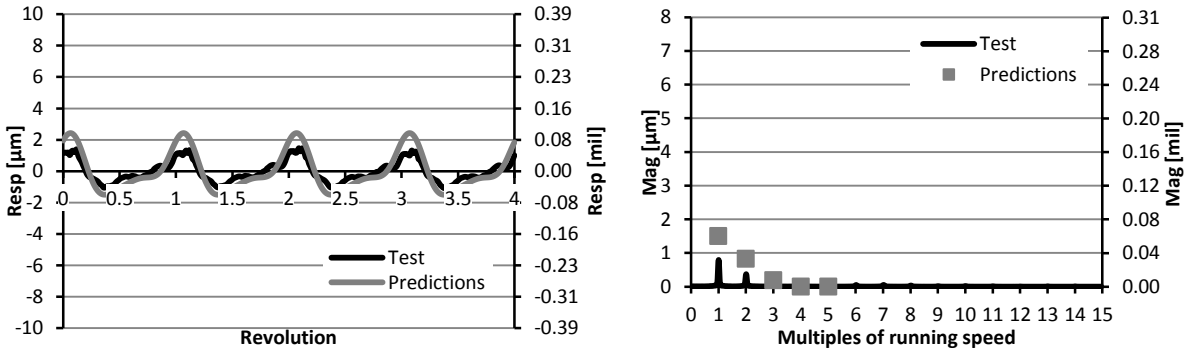

Horizontal Response

Figure 125 Measured versus predicted response at the rotor mid span (Low GVF)

Figure 126 compares the predicted to measured orbit at the low GVF at the mid span of the rotor. The range of the measured vibrations in the vertical direction is ~14 [µm], while the range of the measured vibration in the horizontal direction is ~3 [µm]. The model predicts the general shape of the orbit closely.

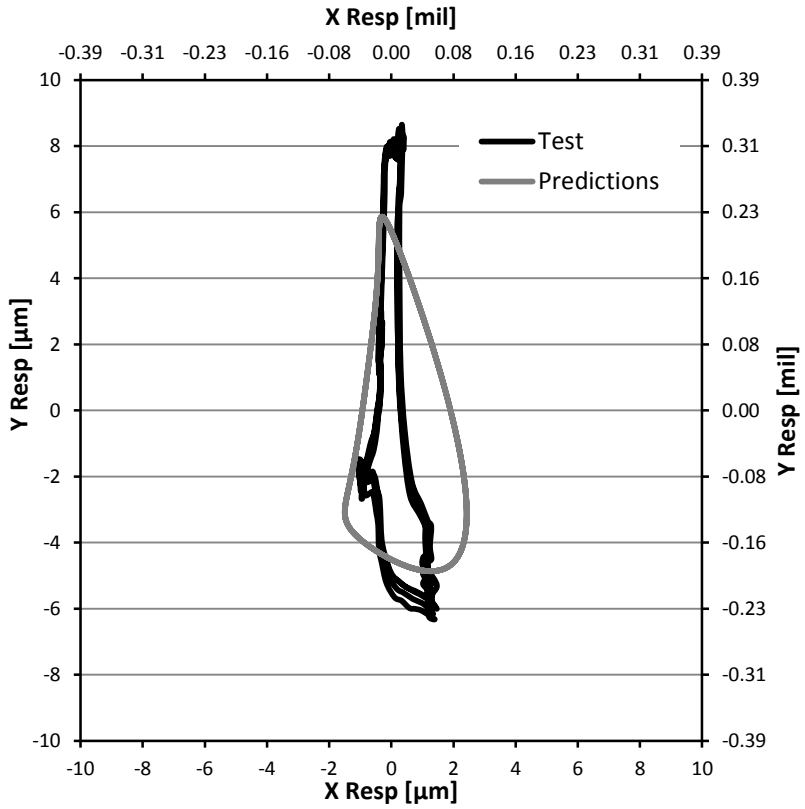

Figure 126 Measured versus predicted orbit at the rotor mid span (Low GVF)

Similar to the GVF, predicted dynamic force components for medium GVF are shown in Figure 127. The oscillations of the forces show the effect of the parabolic axial pressure buildup. The forces closer to discharge at Z4 and Z3 show a larger range of oscillation in the vertical direction than the forces closer to suction at Z1 and Z2.

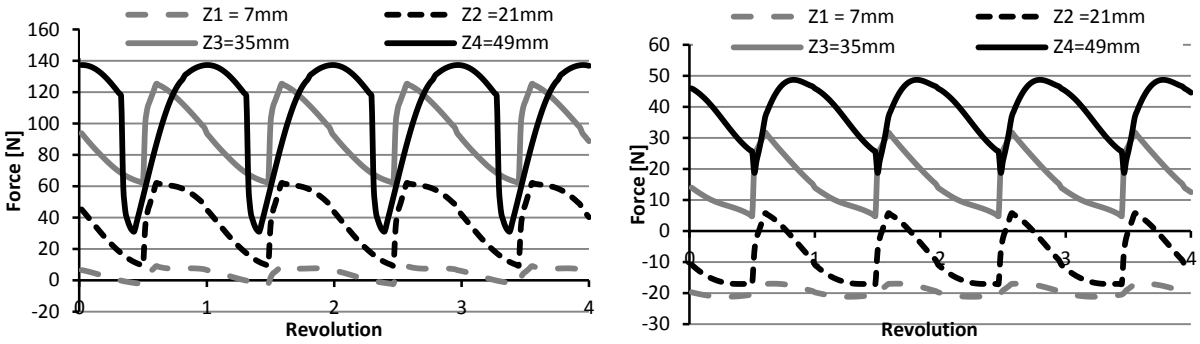

Vertical Force Horizontal Force

Figure 127 Predicted dynamic force components at four axial locations (Medium GVF)

Figure 128 compares the predicted to the measured response in the vertical and horizontal directions at the rotor mid span in the time and frequency domain for the medium GVF ratio. Similar to previous single-phase and multiphase results, the vertical synchronous response component is predicted accurately by the model, while the 2x response component is under predicted. The model does not show significant 3x response component.

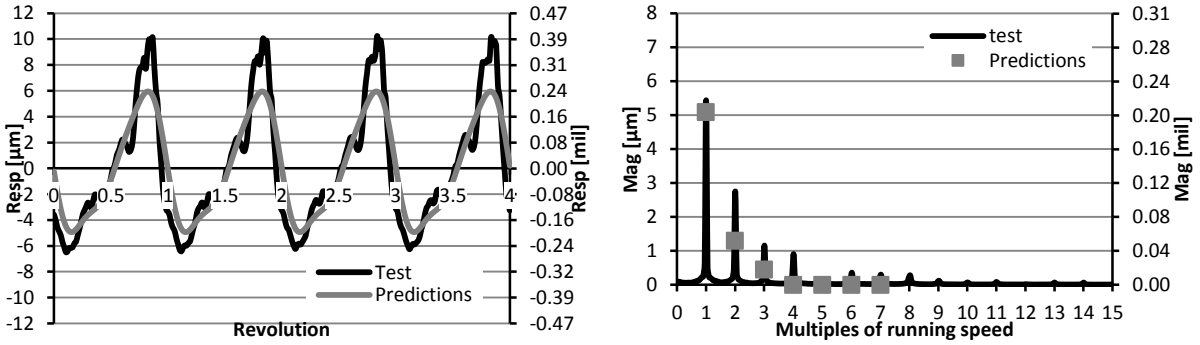

Vertical Response

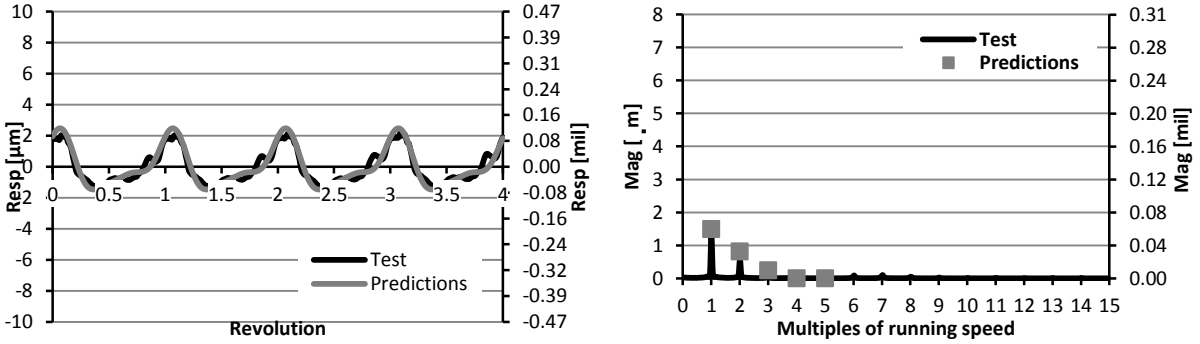

Horizontal Response

Figure 128 Measured versus predicted response at the rotor mid span (Medium GVF)

Figure 129 compares the predicted to the measured orbit at the mid span for the medium GVF ratio. The vertical range of the measured vibration is ~16 [µm]. The predicted vertical range of vibration is ~12 [µm]. The model predicts the shape of the orbits closely.

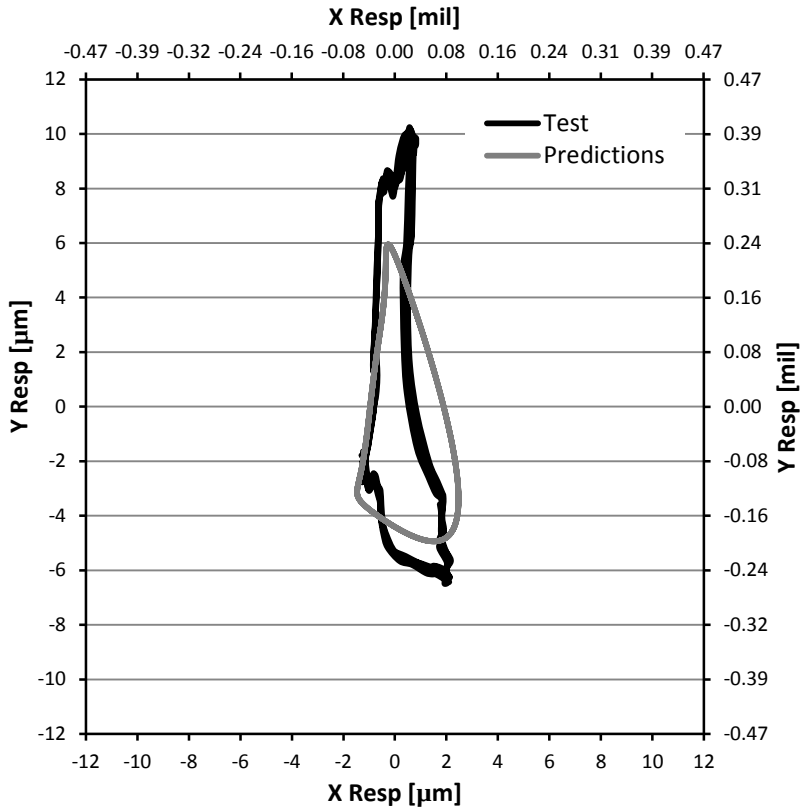

Figure 129 Measured versus predicted orbit at the rotor mid span (Medium GVF)

The measurements and predictions of the high GVF ratio is consistent with the trend for the low and medium GVF. Similar to Figures 124 and 127, the predicted dynamic forces at high GVF ratio shown in Figure 130 show large oscillations closer to the discharge (at Z4 and Z3) compared to the forces closer to suction (at Z2 and Z1) in the vertical and horizontal directions due to the increased parabolic axial pressure buildup.

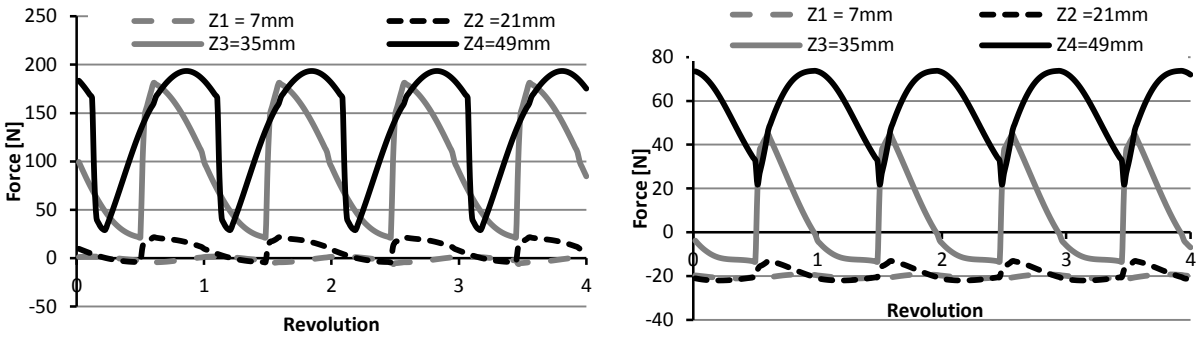

Vertical Force Horizontal Force

Figure 130 Predicted dynamic force components at four axial locations (High GVF)

Figure 131 compares the predicted to measured responses in the vertical and horizontal directions at the rotor's mid span at high GVF ratio. Similar to the predictions of the low and medium GVF shown in Figures 125 and 128 respectively, the vertical predictions match the measured synchronous response closely, but under-predicts the $2x$ component.

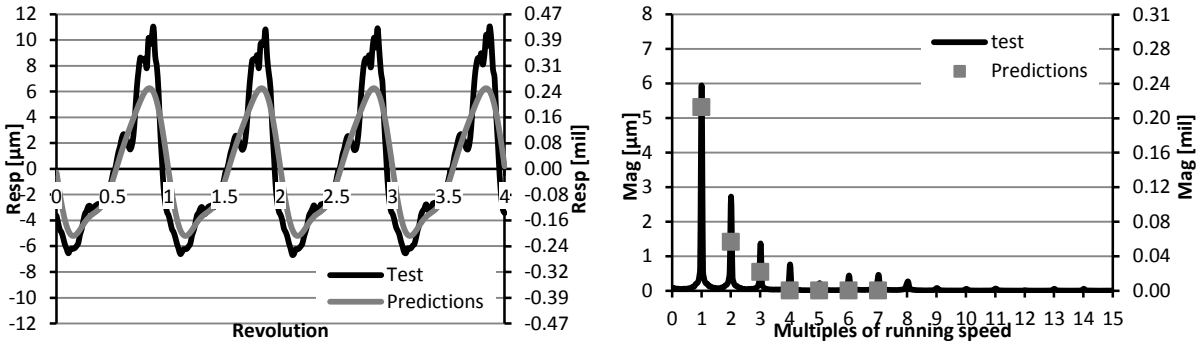

Vertical Response

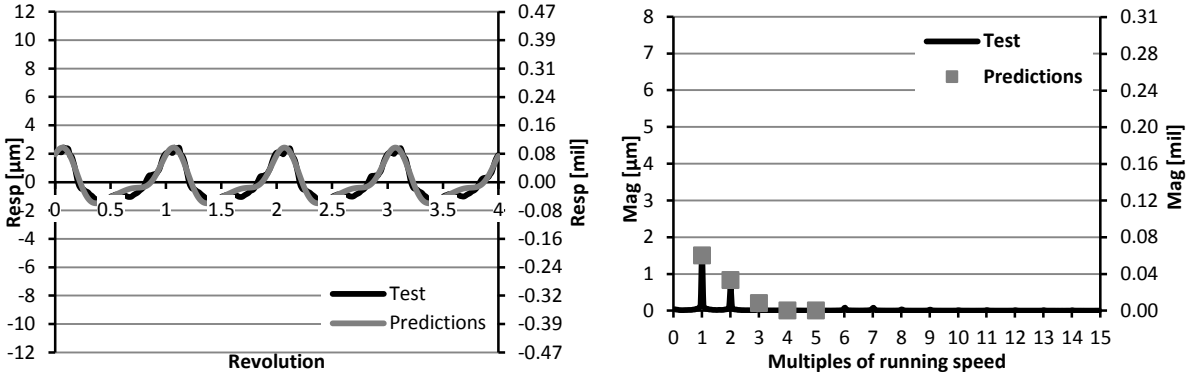

Horizontal Response

Figure 131 Measured versus predicted response at the rotor mid span (High GVF)

Figure 132 compares the predicted to measured orbit at the rotor's mid span for the high GVF ratio. The measured range of vibration in the vertical direction is ~17 $[\mu m]$ and the measured range of vibration in the horizontal direction is ~4 $[\mu m]$. The model predicts the measured orbits satisfactorily.

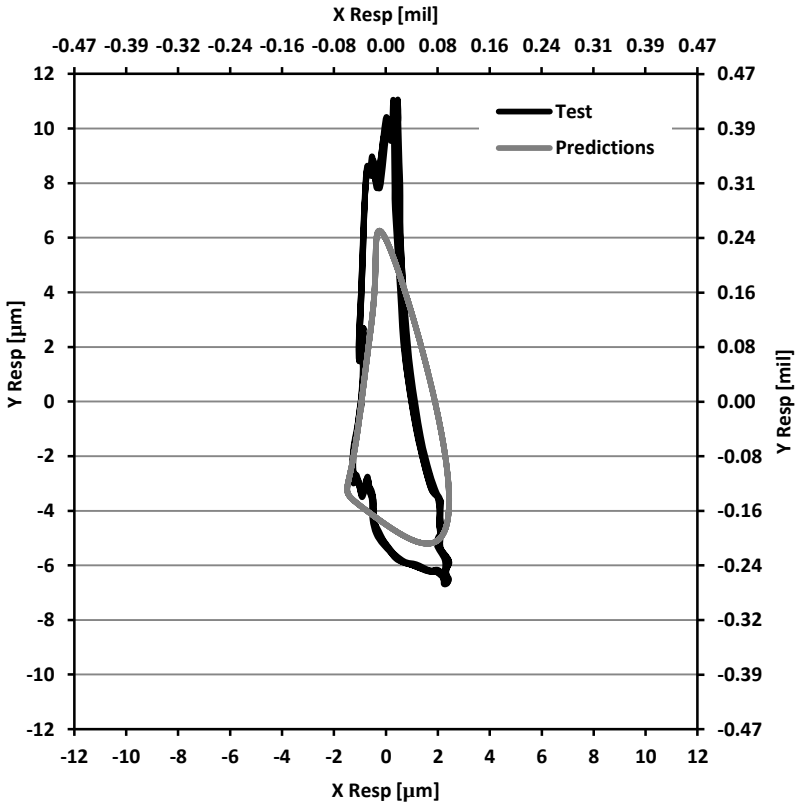

Figure 132 Measured versus predicted orbit at the rotor mid span (High GVF)

5.3 Results summary

This section presents a summary of the results in a tabular format for reference and comparison. The predicted and experimental synchronous dynamic pressure components are compared in Table 10 for the sensors in the horizontal plane and in Table 11 for the sensors in the vertical plane. Similarly, the predicted and experimental 2 times running speed dynamic pressure components are compared in Table 12 for the sensors in the horizontal plane and in Table 13 for sensors in the vertical plane. These are the same results presented and discussed earlier in this chapter, they are provided here for reference.

Table 10 Dynamic pressure component at 1x running speed of sensors in horizontal plane

	1x Dynamic pressure [Pa]					
	Horizontal Suction		Horizontal Middle		Horizontal Discharge	
	Test	Predictions	Test	Predictions	Test	Predictions
Single phase	7.91E+04	7.70E+04	5.78E+04	5.94E+04	5.49E+04	7.19E+04
Low GVF	2.07E+04	4.45E+04	3.82E+04	4.13E+04	6.79E+04	1.00E+05
Medium GVF	2.07E+04	2.35E+04	3.82E+04	4.32E+04	6.79E+04	1.05E+05
High GVF	1.78E+04	4.59E+03	9.78E+03	3.87E+04	7.76E+04	1.08E+05

Table 11 Dynamic pressure component at 1x running speed of sensors in vertical plane

	1x Dynamic pressure [Pa]			
	Vertical Suction		Vertical Middle	
	Test	Predictions	Test	Predictions
Single phase	1.04E+05	7.53E+04	7.52E+04	8.17E+04
Low GVF	1.25E+05	1.07E+05	1.22E+05	1.11E+05
Medium GVF	1.25E+05	1.03E+05	1.22E+05	1.23E+05
High GVF	1.23E+05	1.09E+05	1.22E+05	1.43E+05

Table 12 Dynamic pressure component at 2x running speed of sensors in horizontal plane

	2x Dynamic pressure [Pa]					
	Horizontal Suction		Horizontal Middle		Horizontal Discharge	
	Test	Predictions	Test	Predictions	Test	Predictions
Single phase	2.15E+04	6.13E+03	3.58E+04	2.66E+04	2.78E+04	2.25E+04
Low GVF	6.52E+03	1.58E+04	2.42E+04	1.04E+04	3.37E+04	3.15E+04
Medium GVF	6.52E+03	8.95E+03	2.42E+04	1.14E+04	3.37E+04	3.47E+04
High GVF	9.50E+03	2.65E+03	5.28E+03	1.37E+04	4.73E+04	6.14E+04

Table 13 Dynamic pressure component at 2x running speed of sensors in vertical plane

	2x Dynamic pressure [Pa]			
	Vertical Suction		Vertical Middle	
	Test	Predictions	Test	Predictions
Single phase	4.63E+04	3.31E+04	3.96E+04	2.20E+04
Low GVF	6.61E+04	6.26E+03	5.81E+04	2.62E+04
Medium GVF	6.61E+04	7.26E+03	5.81E+04	3.01E+04
High GVF	6.58E+04	8.10E+03	6.09E+04	4.05E+04

The model's response consistently under-predicts the test response by a 5-10%. However, in general it can be concluded that the model successfully shows the basic phenomena of the rotordynamic behavior of the twin screw pumps in single and multiphase operation. The static and synchronous responses for the four different operating conditions are shown in Table 14 for the response in the vertical direction and Table 15 for the response in the horizontal direction.

Table 14 Vertical response

	Static Response [μm]		1X Response [μm]	
	Test	Predictions	Test	Predictions
Single phase	34.02	29.96	5.38	5.15
Low GVF	37.15	31.93	5.32	5.02
Medium GVF	37.99	32.25	5.54	5.62
High GVF	38.42	32.54	5.94	5.45

Table 15 Horizontal responses

	Static Response [μm]		1x Response [μm]	
	Test	Predictions	Test	Predictions
Single phase	3.53	3.38	1.13	0.89
Low GVF	0.99	2.02	0.80	0.67
Medium GVF	1.12	2.12	1.16	0.86
High GVF	1.68	2.75	1.50	1.34

6. CONCLUSION AND FUTURE RESEARCH

The research presented in here is a first step to understand the rotordynamic behavior of twin screw pumps and possibly provide a gateway to understand the rotordynamic behavior of other screw machines like screw compressors. Twin-screw pumps present a range of challenging dynamic behavior. First, the structure of the screw thread does not lend itself to the traditional axisymmetric rotordynamic analysis. Chapter 2 addressed this issue by introducing an equivalent axisymmetric structural model to adequately represent the screw section. Second, the fluid structure interaction forces are complicated by the thread geometry including the chambers, the different types of clearances, and the rotation of the screw. Chapter 3 addressed this issue by extending the steady state twin-screw pump models to predict the pressure field variation with the rotational angle of the screw. Third, no experimental results are available for the dynamic response of twin-screw pumps. Chapters 4 and 5 address this issue by running a basic experiment on a clear-casing twin screw pump.

While the size and range of operation of the clear-casing pump is not on par with industrial-size twin-screw pumps, the results showed the various dynamic phenomena of the pump including: (1) the linear axial pressure buildup for single phase, (2) the parabolic axial pressure buildup for multiphase, (3) the spectrum of the dynamic pressure composed of several distinct harmonics of the running speed, (4) the constant pressure throughout the chambers, (5) the rotor' static deflection due to the unbalanced pressure field, (6) the dynamic response with harmonics up to 8 times the running speed, (7) the response X-Y orbit dominated by the vertical response. All these phenomena were satisfactorily predicted by the model.

The dynamic response results showing excitations at multiples of running speeds confirm the need of accurate rotordynamic modeling if twin-screw pumps are desired to operate in environments where reliability is a prime concern, such as in oil and gas business in general, and subsea applications in particular.

In the author's judgment, this work opens the door to different directions for future research. The rotordynamic model of the twin-screw pump can be improved by building a first-order stiffness-mass-damping (KCM) model to account for forces at the circumferential clearance. Circumferential clearances in twin-screw pumps have clearance to radius ratios

similar to annular seals and, like seals, they separate two zones of different pressures. The CFD study in Appendix B showing the pressure distribution across the circumferential clearance for concentric (Figure 137) and 80% eccentricity (Figure 138) suggests that the circumferential clearance can develop a Lomakin-effect-type restoring forces as with annular seals. The analysis however, will have to account for the helix angle and the portion of the circumference that is not exposed to the circumferential clearance (the portion between $-\beta$ and $+\beta$ as was shown in Figure 23). The analysis will also have to answer the question of where to position the KCM model for clearance axially, since the circumferential-clearance axial location will change due to the 360^o rotation of the screw thread.

Another direction for future research is building an experimental set-up with an industrial-size twin-screw pump that can be shaken externally to excite its natural frequencies. External shaking of the rotor-bearing system would indicate the damping provided by the fluid and the added mass. The pump could be excited in dry, wet, and operating conditions. A similar external-excitation technique was adopted in [38].

The interaction of the twin-screw pump with the discharge downstream of the screws is another aspect that could be studied in a future work. For the clear-casing pump model employed in this work, the dynamic pressure at the discharge of the pump remained largely constant (Figure 80 (b)). However, given the high oscillation and the pulsation nature of the screw pump discharge, an interaction of the screw-pump with the downstream piping might raise some acoustic concerns. In that case, a complete model of the pump would have to include the acoustic dynamics of the downstream piping and its effect on the pressure perturbation at the screw.

REFERENCES

[1] Parker, D. B., 1998, "High Temperature Twin-screw Pumps", Proceedings of the 15th International Pump Users Symposium, Turbomachinery Laboratory, Texas A&M University, College Station, TX. pp. 139-142.

[2] Neumann, W., 1991, "Efficient Multiphase Pump Station for Onshore Application and Prospects for Offshore Application," Proceedings of the 8th International Pump User Symposium, Turbomachinery Laboratory, Texas A&M University, College Station, TX, pp. 43-48.

[3] XU, J. 2008, "Modeling of Wet Gas Compression in Twin-Screw Multiphase Pump," Ph.D. dissertation, Petroleum Engineering Department, Texas A&M University, College Station, TX.

[4] Vetter, G., and Wincek, M., 1993, "Performance Prediction of Twin-Screw Pumps for Two-Phase Gas/Liquid Flow," Proceedings of the Fluid Engineering Conference (FED), Pumping Machinery, ASME, Washington, D.C., Vol. 154, pp. 331-340.

[5] Rabiger, K., 2009, "Fluid Dynamic and Thermodynamic Behavior of Multiphase Screw Pumps Handling Gas-Liquid Mixtures with Very High Gas Volume Fractions," Ph.D. thesis, University of Glamorgan, Treforest, UK.

[6] Shippen, M. E., and Scott, S. L., 2002, "Multiphase Pumping as an Alternative to Conventional Separation, Pumping and Compression", Proceedings of the 34th PSIG Conference, SPE Reprint, Portland, OR, Vol. 58.

[7] Prang, A. J., and Cooper, P., 2004, "Enhanced Multiphase Flow Predictions in Twin-Screw pumps," Proceedings of the 21st International Pump User Symposium, Turbomachinery Laboratory, Texas A&M University, College Station, TX. pp. 69-76.

[8] Prang, A. J., and Cooper, P., 2004, "Improved Performance Prediction Methods for Multiphase Twin-Screw Pumps," Proceedings of the 4thNorth American Conference on Multiphase Technology, BHR Group, Banff, Canada, pp. 239-249.

[9] Singh, A., 2003, "Modeling Twin-Screw Multiphase Pump Performance during Periods of High Gas Volume Fraction," M.S. thesis, Petroleum Engineering Department, Texas A&M University, College Station, TX.

[10] Ryazantsev, V. M., 2001, "Radial forces and Screw Rigidity of Two-Screw Multiphase Pumps," Chemical and Petroleum Engineering, **37**(11), pp. 617-622.

[11] Rausch, T., Vauth, Th., Brandt, J-U., and Mewes, D., 2004, "A Model for the Delivering Characteristic of Multiphase Pumps," Proceedings of the 4th Annual North American Conference on Multiphase Technology, pp. 313-325.

[12] Rabiger, K., Maksoud, T.M.A, Ward, J. and Hausmann, G., 2008, "Theoretical and Experimental Analysis of a Multiphase Screw pump, Handling Gas–Liquid Mixtures with Very High Gas Volume Fractions," Experimental Thermal and Fluid Science, **32**, pp. 1694-1701.

[13] Martin, A.M., 2003, "Multiphase Twin-Screw pump Modeling for the Oil and Gas Industry", Ph.D. dissertation, Petroleum Engineering, Texas A&M University, College Station, TX.

[14] Nakashima, C.Y., Junior, S.O., 2002, "Thermodynamic Model of a Twin-Screw Multiphase Pump," Proceedings of the ASME Engineering Technology Conference on Energy, Houston.

[15] Feng, C., Yueyuan, P., Ziwen, X., Pengcheng, S., 2001, "Thermodynamic Performance Simulation of a Twin-Screw Multiphase Pump," Proceedings of the Institution of Mechanical Engineers, Part E: Journal of Process Mechanical Engineering, **215**(2), pp. 157-163.

[16] Feng, C., Gao, T., Jiao, J., Pan, T., Xing, Z., 2009, "Study of a Screw Rotor With Different Stocks and Leads for a Twin-Screw Multiphase Pump," Journal of Mechanical Engineering Science, **223**(11), pp. 2637-2645.

[17] Stosic, N., Smith, I. K., Kovacevic, A. and Mujic, E., 2006, "Vacuum and Multiphase Screw pump Rotor Profiles and Their Calculation Models," VDI BERICHTE, 1932, pp. 53-68.

[18] Nakashima, C.Y., Oliveira, S., Caetano, E.F., 2006, "Heat Transfer in a Twin-Screw Multiphase pump: Thermal Modeling and one Application in the Petroleum Industry," Energy, **31**(15), pp. 3415-3425.

[19] Schan, A., Rausch, T., et al., 2006, "Performance and Application Range of Multiphase Twin-Screw Pumps with Declining Pitch," Proceedings of the 5th North

American Conference on Multiphase Technology, BHR Group, Banff, Canada, pp. 63-77.

[20] Egashira, K., Shoda, S., Tochikawa, T., Furukawa, A., 1998, "Backflow in Twin-Screw Type Multiphase Pump," SPE Production & Facilities, **13**(1), pp. 64-69.

[21] Vetter, G., Wirth, W., Korner, H., and Pregler, S., 2000, "Multiphase Pumping with Twin-Screw Pumps - Understand and Model Hydrodynamics and Hydroabrasive Wear," Proceedings of the 17th International Pump User Symposium, Turbomachinery Laboratory, Texas A&M University, College Station, TX, pp. 153-169.

[22] Jones, A.B., 1960, "A General Theory for Elastically Constrained ball and Radial Roller Bearings Under Arbitrary Load and Speed Conditions", Journal of Basic Engineering, **82**(2), pp. 309-320.

[23] Rao, J. S., Shiau, T. and Chang, J., 1998, "Theoretical Analysis of Lateral Response due to Torsional Excitation of Geared Rotors," Mechanism and Machine Theory, **33**(6), pp. 761-783.

[24] Lee, A. S., Ha, J. W., and Choi, D.-H., 2003, "Coupled Lateral and Torsional Vibration Characteristics of a Speed Increasing Geared Rotor-Bearing System," Journal of Sound and Vibration, **263**(4), pp. 725-742.

[25] Childs, D., 1993, *Turbomachinery Rotordynamics Phenomena, Modeling & Analysis*, John Wiley & Sons, New York.

[26] Hirs, G.G., 1973, "A Bulk-Flow Theory for Turbulence in Lubricant Films," Journal of Lubrication Technology, **95**(2), pp. 137-145.

[27] Tao, L.N. and Donovan, W.F., 1955,"Through Flow in Concentric and Eccentric Annuli of Fine Clearance With and Without Relative Motion of the Boundaries." Trans-ASME. , **77**, pp. 1291-1301.

[28] Muhammed, A. R. A., Childs, D., 2012, "Rotordynamics of a 2-Phase Flow Twin-Screw Pump," Proceedings of ASME Turbo Expo 2012, Copenhagen, Denmark.

[29] Childs, D., 1991. "Fluid-Structure Interaction Forces at Pump-Impeller-Shroud Surfaces for Axial Vibration," Journal of Vibration and Acoustics, **113**(1), pp. 108-115.

[30] Manring, N.D., 2000, "The Discharge Flow Ripple of an Axial-Piston Swash-Plate Type Hydrostatic Pump," ASME Journal of Dynamic Systems, Measurement, and Control, **122**(2), pp. 263-268.

[31] Cho, B.H., Lee, H.W. and Oh J.S., 2000, "Estimation Technique of Air Content in Automatic Transmission Fluid by Measuring Effective Bulk Modulus," FISITA World Automotive Congress, Seoul, Korea.

[32] Tullis, J. 1989, *Hydraulics of Pipeline: Pumps, Valves, Cavitation, Transients*, John Wiley & Sons, New York.

[33] Martino, G., Fontana, N. and Giugni, M., 2008, "Transient Flow Caused by Air Expulsion Through an Orifice," Journal of Hydraulic Engineering, **134**(9), pp. 1395-1399.

[34] Karassik, I.J., Messina, J.P., Cooper, P., Heald, C., Eds, 2001, *Pump Handbook, 3rd ed*. McGraw-Hill, New York, NY.

[35] Nelson, H.D., 1980, "A Finite Rotating Shaft Element Using Timoshenko Beam Theory," ASME Journal of Mechanical Design, **102**(4), pp. 793-803.

[36] Kramer, E., 1993, *Dynamics of Rotors and Foundations*, Springer-Verlag, Berlin, Germany.

[37] Prang, A.J., Cooper, P., 2002, "Optimizing Multiphase Equipment for Actual Field Conditions," Proceedings of the 3rd North American Conference on Multiphase Technology, BHR Group, Banff, Canada.

[38] Kanki, H., Fujii, A. Hizume, T. Ichimura, and T. Yamamoto, 1986, "Solving Nonsynchronous Vibration Problems of Large Rotating Machineries by Exciting Test in Actual Operating Condition ," Proceedings of the IFToMM International Conference on Rotordynamics, Tokyo, Japan, pp. 221-226.

APPENDIX A

GLOSSARY OF TWIN-SCREW PUMP TERMINOLOGY

Chamber	The cavity enclosed between the screw thread walls, the screw rotor, and the pump liner
Circumferential clearance	The radial gap between the screw outer diameter and the pump liner
Discretized mesh	The two dimensional mesh of rectangular element representing the spatial field (axial and circumferential) around the screw
Flank Clearance	The clearance between the walls of the screws
Liner	The part of the casing surrounding the screws. The liner is separated from the screws by the circumferential clearance gap
Liner edge	The axial line of the liner along the intersection of the two liner circles housing the screws
Liner annular space	The cross section of the liner encircling the screws
Line of centers	The line going through the centers of the two rotors
Orifice	The orifice opening to discharge outlined by the space between the rotor, the screw thread terminal edge, the meshing line and the pump liner
Parallel axis	The axis perpendicular to the centers axis in the screw radial plane.
Thread terminal edge angle	The angle between the line of centers and the screw thread terminal edge
Screw land	The surface of the screw thread separated from the pump liner by the circumferential clearance
Screw thread	The helix around the screw rotor
Screw section	The section of the rotor over which the screw thread extends.
Screw thread helix angle	The inclination of the helix on the horizontal axis
Slip flow	The total back flow from one chamber to the chamber upstream (leakage from circumferential, radial and flank clearances). The pump slip is the slip between the first chamber and the pump suction.
Screw thread terminal edge	The edge of the screw profile end

APPENDIX B

CFD STUDY OF ECCENTRIC LEAKAGE THROUGH CIRCUMFERENTIAL CLEARANCE IN TWIN SCREW PUMPS

The purpose of the CFD study in this appendix is to validate the applicability of the eccentric leakage model in [27] to the circumferential clearance in twin-screw pumps.

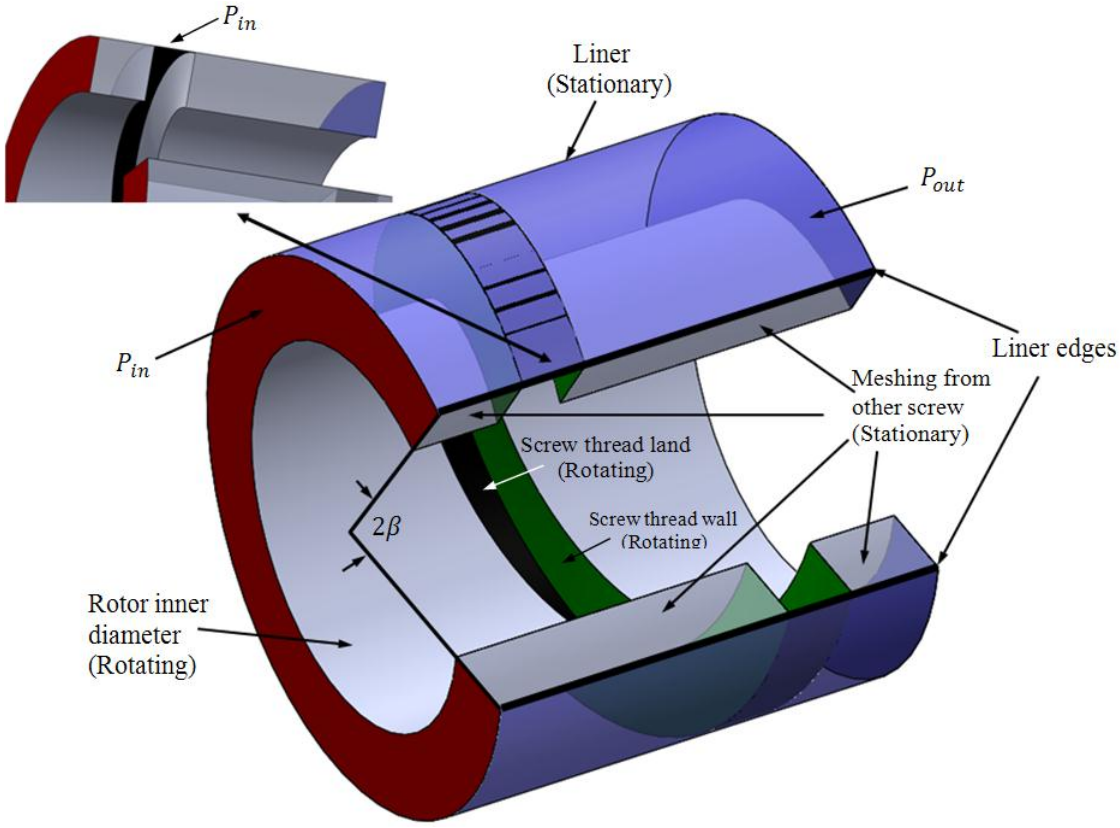

Figure 133 CFD fluid path for leakage flow across circumferential clearance

The fluid path shown in Figure 133 is for a single clearance separating two chambers on a screw. Including the chambers in the fluid path insures developing constant pressure zones upstream and downstream from the clearance to account for the entrance loss phenomena. The boundary conditions and the wall rotations are listed in Figure 133. The model's boundary conditions are the pressures in the chambers (P_{in} and P_{out} faces in Figure 133). The model's output is the mass flow rates through the input and output faces. The liner and the faces labeled "meshing from other screw" are stationary walls, while the inner

diameter, the screw land and the screw walls are all assigned a rotational speed equal to the pump speed. The faces representing the mating with the other screws are an approximation. The actual geometry should follow the curvature of the outer diameter of the mating screw, and should be rotating at an equal but opposite speed to the other rotating walls. The commercial CFD package used only handles symmetric rotating surfaces. The effect of the wall rotation is generally marginal with respect to leakage and pressure distribution.

Five cases were studied (concentric, 20%, 40%, 60% and 80% eccentricity). Eccentricity is modeled by displacing the liner surface a distance equal to the static deflection e calculated from the eccentricity ratio.

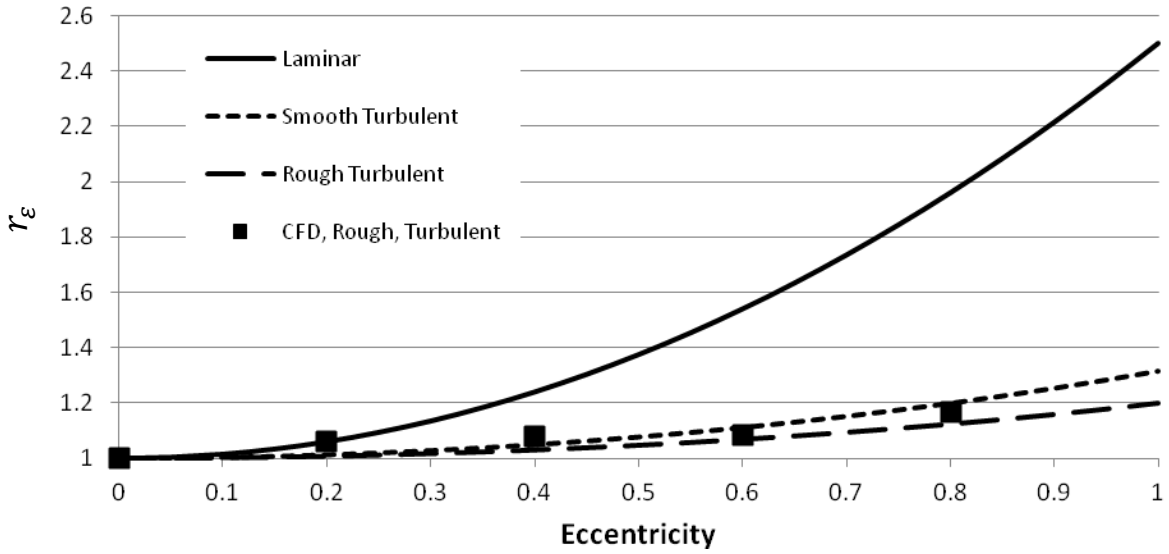

Figure 134 Eccentricity effect on leakage (CFD versus [27])

Figure 134 compares the ratio of the concentric to eccentric leakage from the CFD study to the model in [27].

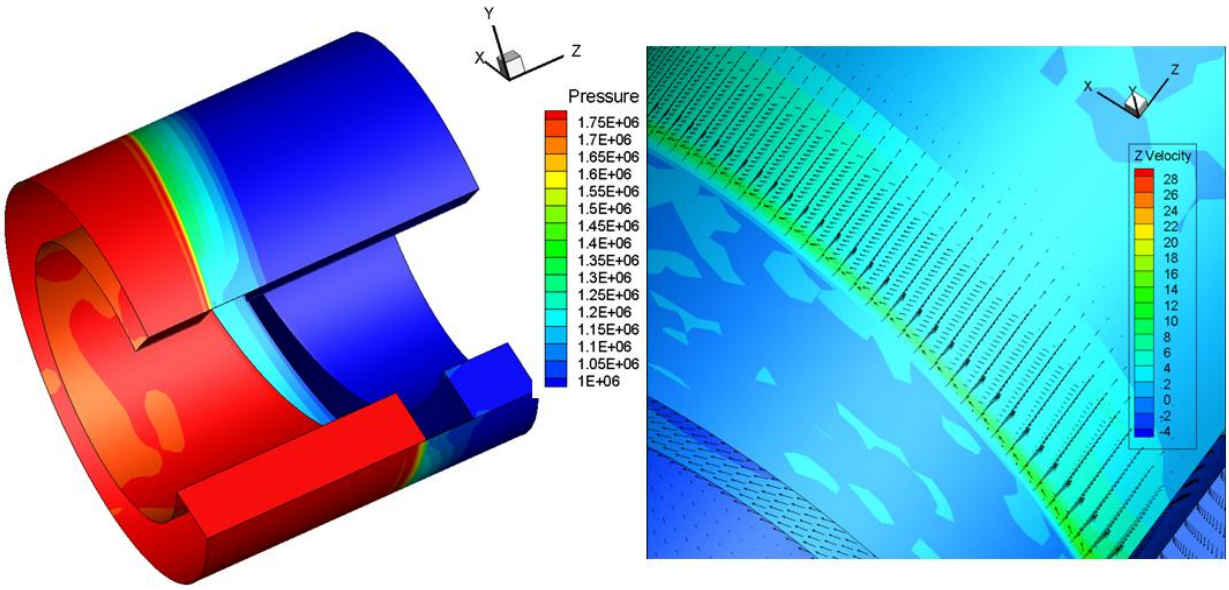

Figure 135 Pressure and velocity field CFD results for leakage across circumferential clearance

A 3D representation of the pressure field and the velocity field across the circumferential clearance are shown in Figure 135. The constant pressure chamber is clearly shown in the pressure field, while the dominance of the axial flow is shown in the velocity field.

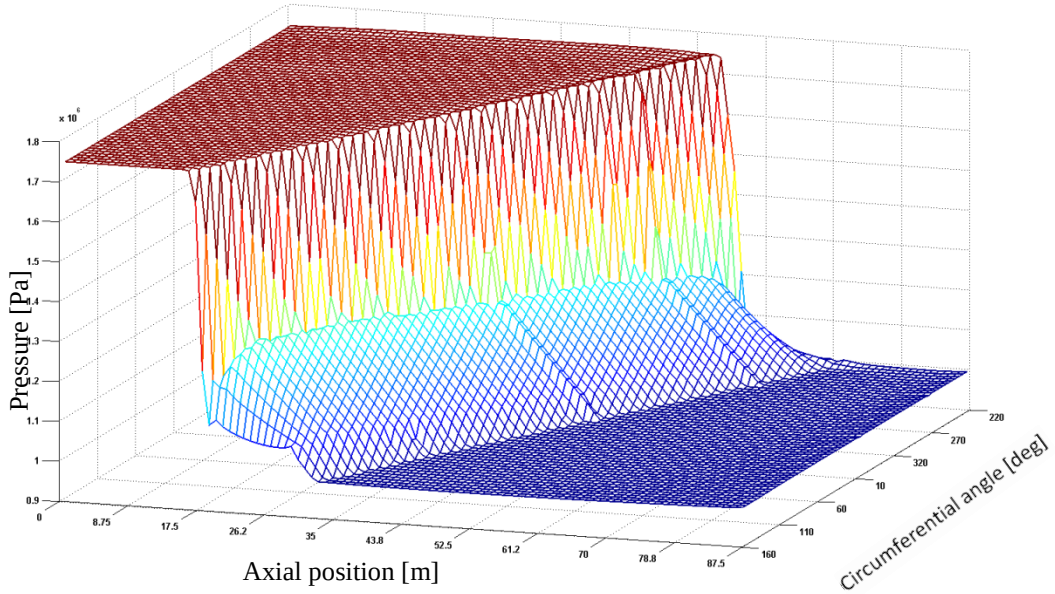

Figure 136 Pressure field (concentric)

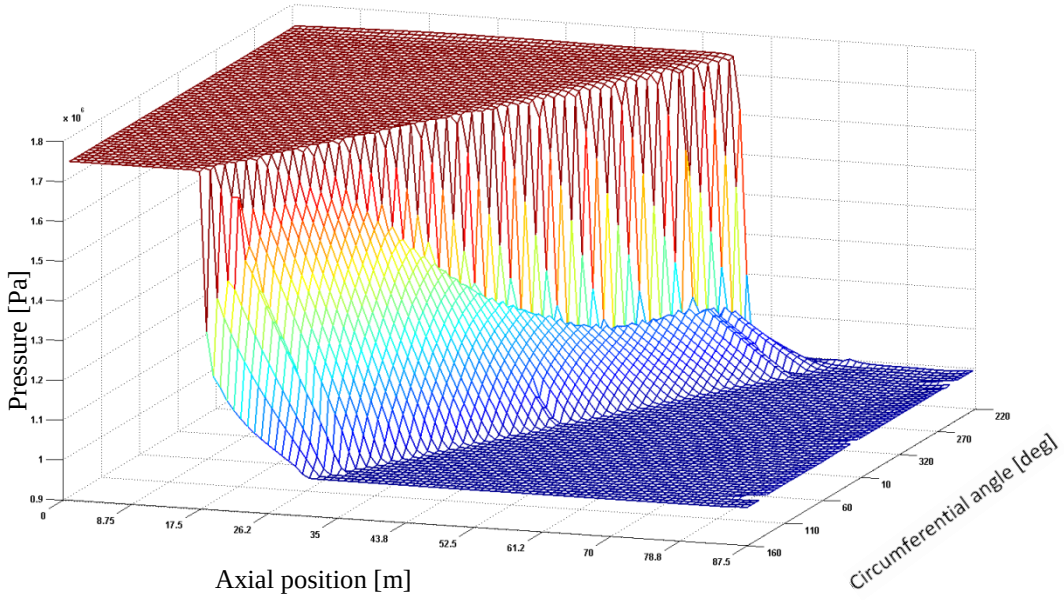

Figure 137 Pressure field (80% eccentricity)

Figure 136 and Figure 137unwraps the geometry of the fluid path to show the pressure field distribution on a 3D plot, with the axial and circumferential directions as the X and Y coordinates and the pressure value as the Z coordinate. The unwrap geometry helps appreciate the importance of the entrance loss which takes around 60% of the pressure drop for the concentric case. In Figure 137 (80% eccentricity) the entrance loss effect is accentuated at the loose side of the circumference (the portion of the circumference where the eccentric clearance is greater than the concentric clearance), while disappearing at the tight side of the circumference (the portion of the circumference where the eccentric clearance is less than the concentric clearance). The difference between the two is the origin of the restoring forces in seals known as Lamakin effect. The physical explanation of this behavior is due to the higher flow rate going through the loose side, which according to Eq. (31) would locally increases the effect of the entrance loss.

APPENDIX C

VISUALIZATION OF SCREW THREAD ORIENTATION AND THE VARIATION OF THE DYNAMIC PRESSURE MEASUREMENTS

The orientation of the screw and the location of the screw thread with respect to the pressure sensors can be traced through the clear casing. The pressure measurements and the thread orientation can be correlated through the phase mark placed on the shaft. To this end, 10 pictures were taken for the rotor in full rotation, with the first picture taken at the angle where the phasor fires its signal. The rest of the pictures are taken with an increment 36^{o} in the direction of shaft rotation. In this appendix the focus is on the middle vertical sensors. The response of the remaining sensors can be explained in the same manner.

Figure 138 shows the vertical and horizontal middle sensors readings in 2 full rotations. The instants in time corresponding to the screw positions of the pictures shown in Figures 139-148 are marked 1 through 10.

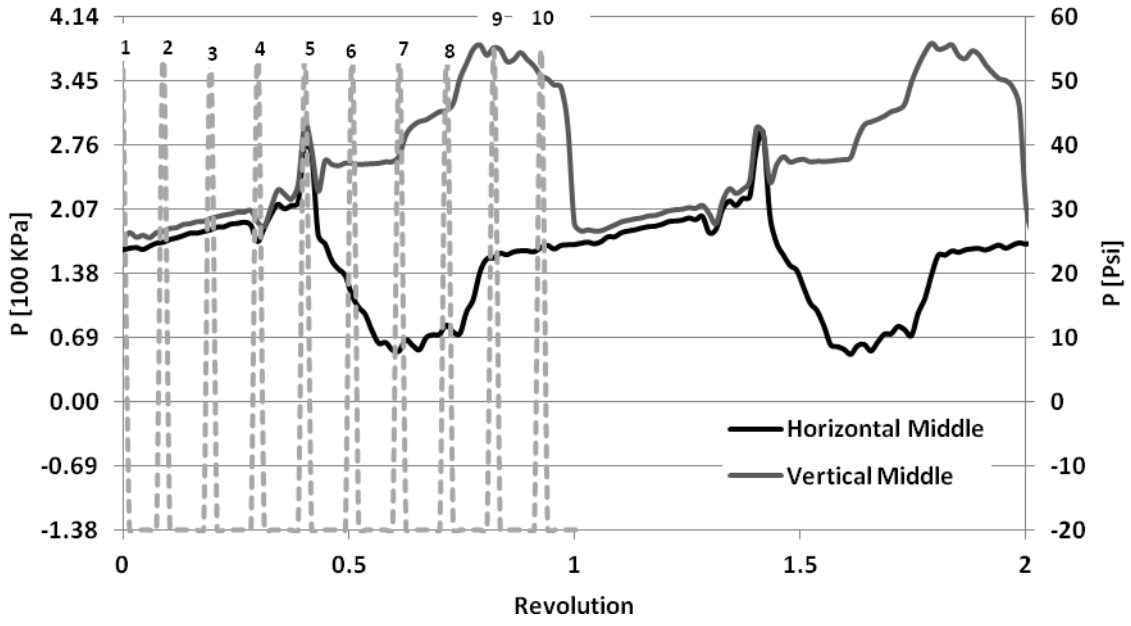

Figure 138 Pressure measurement corresponding to screw thread positions 1-10 (pictures of screw thread are shown in Figures 139-148)

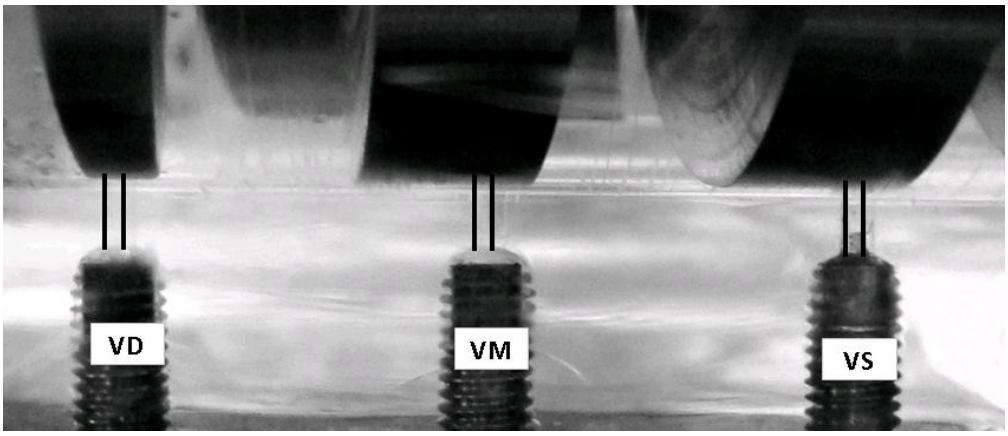

Figure 139 Screw position (1)

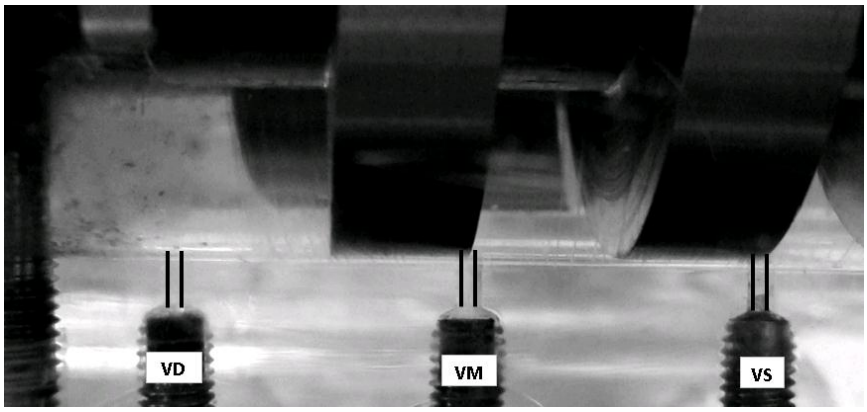

Figure 140 Screw position (2)

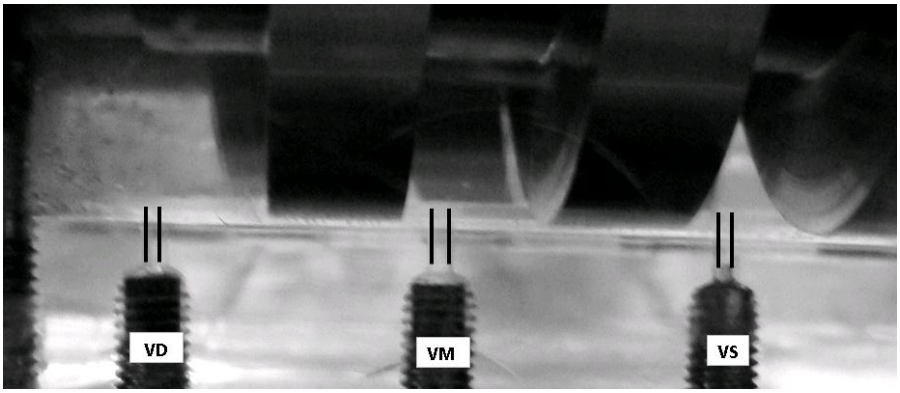

Figure 141 Screw position (3)

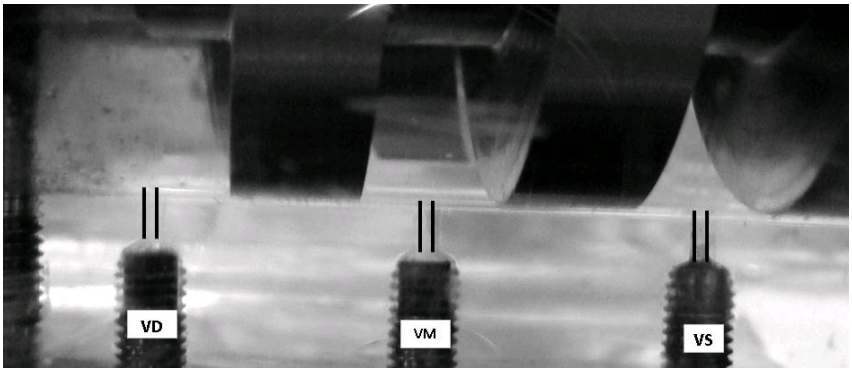

Figure 142 Screw position (4)

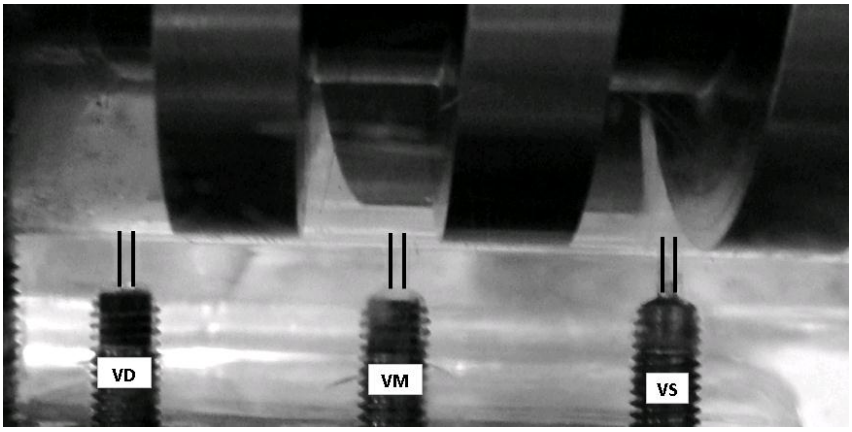

Figure 143 Screw position (5)

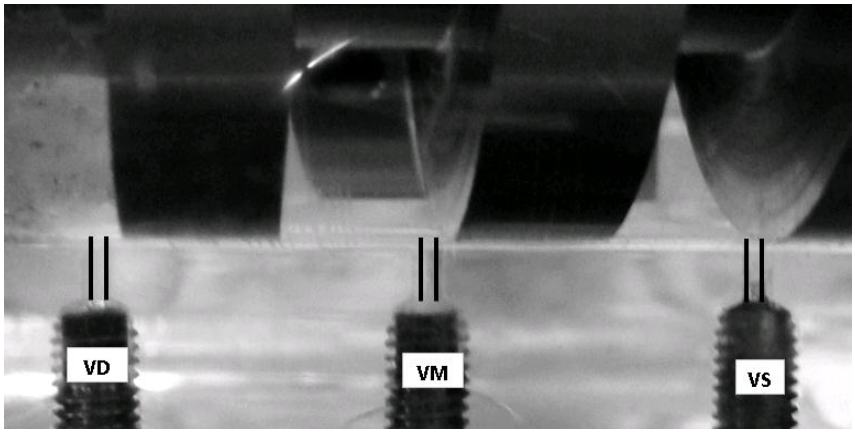

Figure 144 Screw position (6)

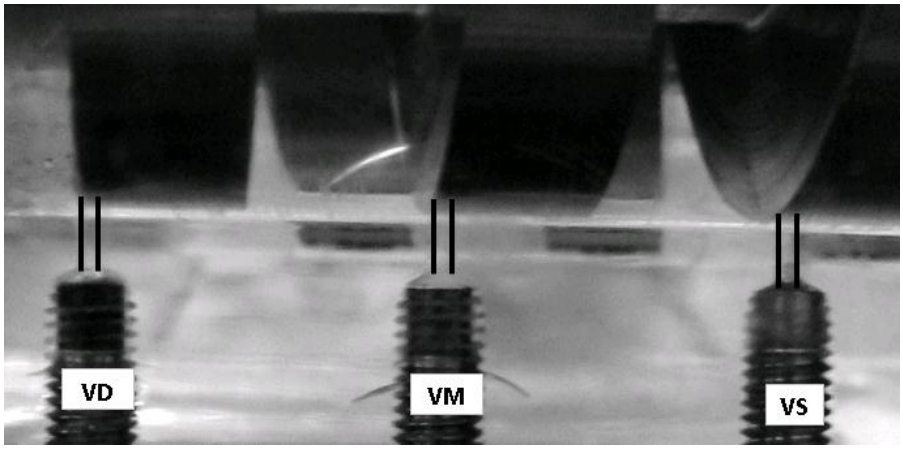

Figure 145 Screw position (7)

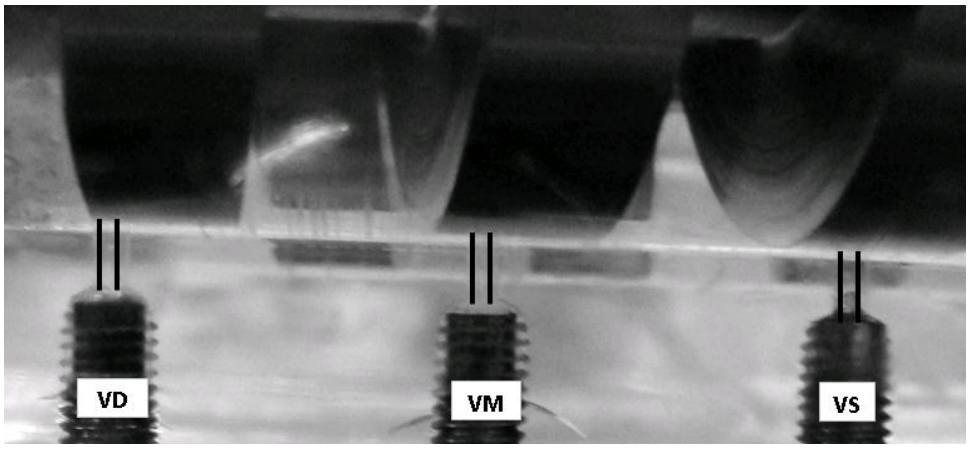

Figure 146 Screw position (8)

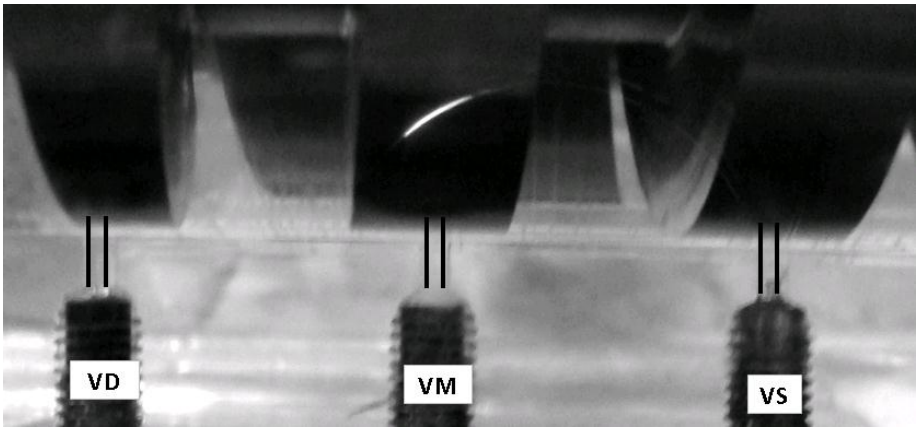

Figure 147 Screw position (9)

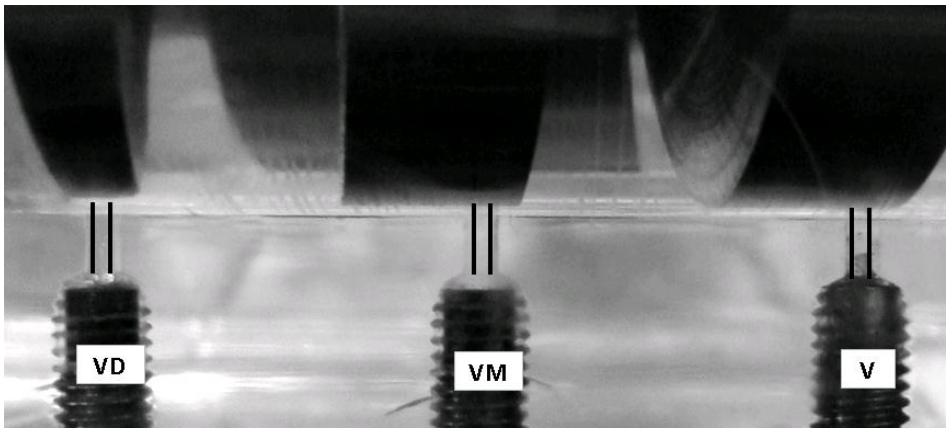

Figure 148 Screw position (10)

In position 1 in Figure 139 shows the Vertical Middle (VM) sensor at the trailing edge of the screw land separating the discharge from the chamber upstream. At this position the sensor is on the verge of 'seeing' the chamber upstream of discharge.

In position 2 through 4 in Figures 140 - 142 the VM sensor is exposed to the chamber upstream of discharge. The pressure readings in Figure 138 labeled 1 through 4 show a 'constant' pressure since the chamber is completely isolated from discharge. In addition, the vertical and horizontal middle sensors (VM and HM) both record the same pressure values. Because the horizontal pressure sensors are displaced a distance equal to the screw land width *B* (Figure 67), both VM and HM see the same chamber pressure for half the revolution.

In position 5 (Figure 143) the HM sensor starts to 'see' the second screw land separating the two chambers upstream of discharge. Therefore, the HM sensor pressure starts to drop. On the other hand the VM sensor still sees the pressure of the chamber upstream of discharge. In positions 6 and 7 (Figures 144 and 145) the chamber is about to open to discharge, the pressure rises due to the reduced length of the screw land separating the chamber from discharge. In positions 8-10 (Figures 146 - 148) an orifice opens to discharge, and the chamber starts to be exposed to the discharge pressure, while the sensor starts to 'see' the screw land. The pressure values of the VM sensors at position 8-10 in Figure 138 are larger than the discharge pressure. In the author's judgment the rise of the dynamic pressure reading of the VM sensor above the discharge pressure might be due to the sudden exposure

of the chamber to discharge pressure. The difference in pressure between the two zones causes a flow through the last chamber. This flow is then stopped at the second screw land shown in Figure 146 converting the velocity head into a pressure head and causing a transient increase in the dynamic pressure above the discharge pressure. This transient effect is not captured in the model.